

THE DEVELOPMENT OF A CONTINUOUS AND CONTROLLED FREEZE-DRYING CONCEPT FOR BIOPHARMACEUTICAL UNIT DOSES

Apr. Pieter-Jan Van Bockstal

Thesis submitted in fulfilment of the requirements for the degree of
Doctor in Pharmaceutical Sciences - 2018

Promotor: Prof. dr. Thomas De Beer



THE DEVELOPMENT OF A CONTINUOUS AND CONTROLLED FREEZE-DRYING CONCEPT FOR BIOPHARMACEUTICAL UNIT DOSES

Apr. Pieter-Jan Van Bockstal

Thesis submitted in fulfilment of the requirements for the degree of
Doctor in Pharmaceutical Sciences - 2018

Promotor: Prof. dr. Thomas De Beer



Examination committee: Prof. dr. Stefaan De Smedt
Chairman
Department of Pharmaceutics
Ghent University, Belgium

Prof. dr. Chris Vervaet
Department of Pharmaceutics
Ghent University, Belgium

Dr. Stéphanie Passot
Joint Research Unit of Microbiology and Food Process
Engineering
INRA–AgroParisTech, France

Dr. Raf De Dier
Pharmaceutical Development & Manufacturing Sciences
Janssen–Cilag AG, Switzerland

Dr. Erwan Bourles
Technical Research and Development Drug Product
GlaxoSmithKline Biologicals S.A., Belgium

Prof. dr. Ingmar Nopens
Department of Mathematical Modelling, Statistics
and Bioinformatics
Ghent University, Belgium

Promoter: Prof. dr. Thomas De Beer
Department of Pharmaceutical Analysis
Ghent University, Belgium

Dean: Prof. dr. Jan Van Bocxlaer

Rector: Prof. dr. Rik Van de Walle

Dutch translation of the title:

De ontwikkeling van een continu en gecontroleerd vriesdroogconcept voor biofarmaceutische eenheidsdosissen

Please refer to this work as follows:

Pieter-Jan Van Bockstal (2018). *The development of a continuous and controlled freeze-drying concept for biopharmaceutical unit-doses*, PhD Thesis, Department of Pharmaceutical Analysis, Ghent University, Ghent, Belgium.

The author and the promoter give the authorization to consult and to copy parts of this thesis for personal use only. Any other use is limited by the Laws of Copyright, especially concerning the obligation to refer to the source whenever results are cited from this thesis.

Ghent, December 5th, 2017

The author

The promotor

Pieter-Jan Van Bockstal

Prof. dr. Thomas De Beer

Voorwoord

Alvorens het wetenschappelijke te belichten, neem ik graag de tijd om mijn enorme dank en appreciatie te betuigen aan een heleboel mensen, zonder wiens hulp dit werk nooit tot stand zou gekomen zijn. Elk op hun manier droegen ze hun steentje bij, iets wat ik nooit zal vergeten.

Als eerste in het rijtje wil ik Prof. Thomas De Beer bedanken. Thomas, jij gaf me vier jaar geleden als promotor de kans om aan deze rit te beginnen en zonder jou had ik nooit gestaan waar ik nu sta. Je aanpak was me perfect op het lijf geschreven: je liet enorm veel vrijheid, maar je deur stond steeds open, voor eender wat. Bedankt voor de vele kansen en uitdagingen die je me hebt geboden, en nog steeds biedt. Bedankt ook voor de mogelijkheid om naar verschillende congressen te gaan, wat ik steeds als enorm leerrijk heb beschouwd. De vele momenten onderweg leenden zich steeds voor geanimeerde gesprekken, al dan niet werk gerelateerd. Het congres in Havana vormde hierbij een echt hoogtepunt en zal ik nooit vergeten, hoewel er zo wel meerdere momenten zijn. Kortom, de voorbije vier jaar was het gewoonweg een plezier om samen te werken. Ik kijk er dan ook enorm naar uit om deze samenwerking de komende jaren verder te zetten.

Ook een enorme dankjewel voor ir. Jos Corver. Als bedenker van het continue concept, was hij het die me introduceerde tot de wereld van het vriesdrogen. Jos, het was steeds een plezier om samen te werken. Je enthousiasme werkte enorm aanstekelijk en van de vele discussies, waarvoor je elk moment klaar stond, was het onmogelijk om niets op te steken. Het was dan ook heel fijn om de technologie de afgelopen jaren samen te hebben zien groeien. Ik kijk enorm uit naar het vervolg! De fijne en leerrijke trip samen naar het congres in Breckenridge was een ervaring die ik niet snel zal vergeten, met onder meer de autorit in de bergen van Colorado en de gezellige avonden. Hartelijk dank Jos!

Heel erg bedankt ook aan Prof. Chris Vervaet, Prof. Jean-Paul Remon, Prof. Bruno De Geest, Prof. Ingmar Nopens en Prof. Krist Gernaey voor de fijne tijd in het labo en de nuttige, opbouwende input bij het uitvoeren van het onderzoek en het nalezen van het wetenschappelijke werk. Ook bij jullie kon ik steeds terecht met vragen, wat ik enorm apprecieerde.

De werkplek kan je bijna als een tweede thuis beschouwen als je het genoeg hebt om zulke fijne collega's rondom je te hebben. Als er laat of in het weekend te werken viel, kon je er zeker van zijn dat je met Simon of Lutz steeds aangenaam gezelschap had. Die late uurtjes werden dan achteraf ook dubbel en dik beloond: een terrasbezoek aan de Geus van Gent, een spaghetti bij De Kastart of de Loge, of gewoon een geanimeerde babbel, al dan niet werk gerelateerd. De leuke herinneringen zijn te talrijk om allemaal op te noemen. De roadtrip met Simon in de zomer van 2015 was dan weer een zeer welgekomen vakantie in een drukke periode. Bedankt voor al deze fijne momenten beide!

Bedankt aan Maxim, Nils en Wouter van de 'Vuilen Hoek'. De term collega's doet hier tekort, want door de jaren heen zijn we een hechte vriendengroep geworden. Er ging geen dag voorbij zonder de gebruikelijke grappen en grollen, elkaar steeds scherp houdend. Toch werd er in de eerste plaats flink werk geleverd, waarbij elk steeds bereid was om de ander te helpen. Dit zorgde steeds voor een opperbeste sfeer op onze bureau. Ik kan me moeilijk voorstellen dat deze sfeer op een andere werkplek ooit geëvenaard kan worden. De vele bezoeken van Alexander, Glenn, Jens en Wesley droegen hier ook zeker aan bij en waren steeds een leuke afleiding. Ook bedankt aan de collega's van de minivoetbal, met een speciale vermelding voor Jeroen, bij wie de voetbalmicrobe nog steeds kriebelt.

Bedankt aan Séverine, Laurens, Brecht, Joris en Gaby, de collega's van het lyo team, voor de hulp en de wetenschappelijke discussies. In het bijzonder wil ik *monsieur* Laurent bedanken: jij was het eerste aanspreekpunt bij al mijn vragen, waarbij ik enorm veel heb opgestoken. Je PAT en industriële ervaringen hebben me enorm vooruit geholpen. Twee jaar na je vertrek uit het labo kan ik nog steeds bij jou terecht, wat ik enorm apprecieer.

Bedankt aan alle collega's van het PAT en Pharm Tech labo voor de toffe sfeer en de leuke momenten: de teambuildings en andere uitjes waren steeds een succes! In het bijzonder wil ik Christine, Ilse, Katharine en Tania bedanken: jullie maken het ons een heel stuk gemakkelijker in het labo.

De voorbije vier jaar heb ik het genoeg gehad om met heel fijne mensen samen te werken in het kader van hun bezoek aan de universiteit. Het was heel interessant om met andere onderzoeksaspecten buiten het eigen domein geconfronteerd te worden en hier aan te proberen bijdragen. In het bijzonder wil ik hier Aleksandar, Henri, Irene, Tu en Ward vermelden.

Mijn dank gaat ook naar Davy, Marc, Mario, Joris, Theo en Tim van de werkplaats. Zij hebben elk een enorme bijdrage geleverd aan ons werk. Met technische problemen konden we bij hen terecht waarbij ze steeds klaar stonden om hun ideeën en ervaring te delen.

Bedankt aan al mijn vrienden die voor de nodige steun en afleiding hebben gezorgd: Stan, Delphine, Tim, Steph, Jonas, Kim, Reinout, Sara, Jolien, Wouter, Dries, Nathalie, Kyrill, Steven, Manon, Nico en Nina.

Mijn enorme dank gaat ook uit naar mijn familie en in het bijzonder mijn ouders, mijn schoonouders, mijn zus Mieke en mijn broer Manuel. Jullie steun, jullie vertrouwen, jullie raad en al de kansen die jullie mij steeds hebben gegeven waren van onschatbare waarde, zaken die ik nooit zal vergeten.

Mijn grootste dank gaat echter uit naar Heleen, ik zou niet weten waar eerst te beginnen. Steeds sta je klaar voor mij, momenten wanneer het wat minder ging was jij daar om me op te fleuren en de weg te wijzen. Dank je wel voor je onvoorwaardelijk steun bij alles wat ik deed. Dank je wel voor al die dingen die mijn leven elke dag veel aangenamer maken.

Pieter-Jan Van Bockstal

5 december 2017

Contents

Voorwoord	i
Contents	v
List of Abbreviations	ix
List of Symbols	xi
List of Figures	xvii
List of Tables	xxiii
1 Introduction	1
1.1 Introduction to pharmaceutical freeze-drying	1
1.2 Conventional pharmaceutical freeze-drying of unit doses	1
1.3 Disadvantages related to batch freeze-drying of unit doses	4
2 Objectives and outline	11
3 Quantitative risk assessment via Uncertainty Analysis in combination with error propagation for the determination of the dynamic Design Space of the primary drying step during batch freeze-drying	13
3.1 Introduction	13
3.2 Materials and methods	16
3.2.1 Freeze-drying model	16
3.2.2 Uncertainty analysis	20
3.2.3 Determination of the vial heat transfer coefficient	22
3.2.4 Determination of the critical product temperature	23

3.2.5	Experimental verification of the dynamic Design Space	24
3.3	Results	26
3.3.1	Experimental determination of the vial heat transfer coefficient . . .	26
3.3.2	Dynamic Design Space for Risk of Failure of 1%	27
3.3.3	Comparison of dynamic Design Space for different Risk of Failure levels	31
3.3.4	Experimental verification of the dynamic Design Space	32
3.4	Discussion	37
3.5	General conclusion	39
4	Application of a Global Sensitivity Analysis for the identification of the most influential process parameters of the primary drying step during batch freeze-drying	45
4.1	Introduction	45
4.2	Materials and methods	47
4.2.1	Freeze-drying model	47
4.2.2	Global Sensitivity Analysis	47
4.2.3	Experimental design methodology	50
4.3	Results	53
4.3.1	Determination of the required number of simulations for the GSA .	53
4.3.2	Gathering process knowledge using graphical tools	58
4.3.3	GSA using a regression- and variance-based technique	58
4.3.4	Analysis of experimental design	60
4.4	Discussion	63
4.5	General conclusion	65
5	Continuous pharmaceutical freeze-drying	71
5.1	Batch versus continuous pharmaceutical manufacturing	71
5.2	History of continuous freeze-drying	72
5.3	Innovative continuous and controlled freeze-drying concept for unit doses .	75
6	Non-contact infrared-mediated heat transfer during continuous freeze- drying of unit doses	81
6.1	Introduction	81
6.2	Materials and methods	82
6.2.1	Experimental set-up	82

6.2.2	Experimental design methodology	84
6.2.3	NIR spectroscopy	89
6.2.4	Multivariate data analysis	89
6.3	Results and Discussion	90
6.3.1	Analysis of DoE 1	90
6.3.2	Analysis of DoE 2	94
6.4	General conclusion	101
7	Mechanistic modelling of infrared mediated energy transfer during the primary drying step of a continuous freeze-drying process	107
7.1	Introduction	107
7.2	Materials and methods	109
7.2.1	Development of primary drying model for continuous drying of spin frozen vials via radiation	109
7.2.2	View factor computation	113
7.2.3	Temperature calibration of the IR heaters	117
7.2.4	Verification of radiation energy contributed by the surroundings	118
7.2.5	Model validation	120
7.2.6	Determination of the critical product temperature	121
7.2.7	NIR spectroscopy	122
7.2.8	Multivariate data analysis	122
7.2.9	Karl Fischer	123
7.3	Results and Discussion	123
7.3.1	View factor for a flat radiator with a cylindrical target	123
7.3.2	IR heater calibration	124
7.3.3	Verification of radiation contribution from surroundings	126
7.3.4	Mechanistic primary drying model predictions	128
7.3.5	Experimental model validation	129
7.4	General conclusion	133
8	Evaluation of thermal imaging as a non-contact in-line process analytical tool for product temperature monitoring during continuous freeze-drying	139
8.1	Introduction	139
8.2	Model-based design of thermal camera set-up	142
8.3	Materials and methods	144
8.3.1	Experimental freeze-drying set-up	144

8.3.2	Thermal imaging	145
8.3.3	Experimental determination of transmittance of germanium IR window	146
8.3.4	Calculation of temperature gradient over glass wall and ice layer . .	146
8.3.5	Determination of dried product mass transfer resistance	148
8.3.6	NIR spectroscopy	150
8.3.7	Multivariate data analysis	150
8.3.8	Determination of the glass transition temperature	151
8.4	Results and discussion	151
8.4.1	Transmittance of germanium IR window	151
8.4.2	Analysis of thermal images	152
8.4.3	Temperature monitoring	154
8.4.4	Temperature gradient over glass wall and ice layer	157
8.4.5	Dried product mass transfer resistance	158
8.5	General conclusion	159
9	Summary and general conclusion	165
10	Broader international context, relevance, and future perspectives	169
10.1	Broader international context and relevance	169
10.2	Future perspectives	173
10.2.1	Research initiatives	173
10.2.2	Valorization	174
	Nederlandse samenvatting	179
	Curriculum vitae	185

List of Abbreviations

CAGR compound annual growth rate.

CIP Cleaning-in-Place.

CLT Central Limit Theorem.

CPP Critical Process Parameter.

CQA Critical Quality Attribute.

CSM Contribution to Sample Mean.

CSV Contribution to Sample Variance.

DoE Design of Experiments.

EMA European Medicines Agency.

FDA Food and Drug Administration.

GMP Good Manufacturing Practice.

GSA Global Sensitivity Analysis.

IR infrared.

MDSC Modulated Differential Scanning Calorimetry.

MLR Multiple Linear Regression.

NETD Noise Equivalent Temperature Difference.

NIR near-infrared.

PAT Process Analytical Technology.

PC principal component.

PCA Principal Component Analysis.

QbD Quality-by-Design.

RMSECV Root Mean Square Error of Cross-Validation.

RoF Risk of Failure.

rpm rotations per minute.

RTD resistance temperature detector.

SIP Sterilization-in-Place.

SNV Standard Normal Variate.

SRC Standardized Regression Coefficient.

UA Uncertainty Analysis.

List of Symbols

α	Constant describing K_v in function of P_c (J/(m ² sK))
β	Constant describing K_v in function of P_c (J/(m ² sKPa))
ΔH_s	Latent sublimation heat of ice
Δl	Increase in dried layer thickness (m)
ΔL_{tot}	Deviation to the average thickness of the spin frozen layer (m)
Δm	Mass of sublimed ice (kg)
ΔT	Temperature difference across the ice layer (T)
Δt	Time step during primary drying (s)
$\dot{m}_{sub,chok}$	Maximum sublimation rate avoiding choked flow (kg/s)
\dot{m}_{sub}	Sublimation rate (kg/s)
ϵ	Emission coefficient of the emitting surface (-)
η	infrared (IR) heater efficiency (-)
γ	Constant describing K_v in function of P_c (1/Pa)
κ	Ratio of specific heats (-)
λ	Wavelength (m)
ω	Angular velocity (rad/s)
ϕ	Volume fraction of ice (-)

ρ_{ice}	Density of ice (kg/m ³)
ρ_{wv}	Density of water vapour (kg/m ³)
σ	Stefan-Boltzmann constant (5.67 10 ⁻⁸ W/(m ² K ⁴))
a	Absorptivity of the target surface (-)
A_p	Product area available for sublimation (m ²)
A_v	Outer vial area (m ²)
A_{R_p}	Constant describing R_p in function of l (1/s)
A_{rad}	Area of the emitting surface (m ²)
B_λ	Spectral radiance (W/sr/m ³)
B_{R_p}	Constant describing R_p in function of l (1/m)
c	Speed of sound for an ideal gas (m/s)
CV	Coefficient of variation (-)
d	Diameter of cylinder for view factor computation (m)
dL	Increment length for view factor computation (m)
F	View factor (-)
g	Gravitational acceleration (9.81 m/s ²)
h	Height of the radiating plane for view factor computation (m)
k	Height of the spin frozen product (m)
k_B	Boltzmann constant (1.38 x 10 ⁻²³ J/K)
K_v	Vial heat transfer coefficient (J/(m ² sK))
k_{glass}	Thermal conductivity of glass (1.05 W/(m K))
k_{ice}	Thermal conductivity of ice (2.18 W/(m K))
L	Initial length of generated ray for view factor computation (m)

l	Dried layer thickness for spin frozen vials (m)
L_{dried}	Dried layer thickness for batch frozen vials (m)
L_{total}	Total thickness of the product layer (m)
M	Molecular weight (kg/mol)
N	Number of samples/simulations (-)
N_{base}	Number of base samples/simulations (-)
n_{par}	Number of parameters included in GSA (-)
n_{vials}	Number of vials (-)
P_c	Chamber pressure (Pa)
P_e	Electric power (W)
P_{rad}	Power provided by IR heater to spin frozen vial (W)
P_{sur}	Power provided by surroundings to spin frozen vial (W)
P_{tot}	Total power required for ice sublimation (W)
$P_{w,c}$	Partial vapour pressure in the drying chamber (Pa)
$P_{w,i}$	Vapour pressure at the sublimation interface (Pa)
R	Gas constant (8.3144621 J/(K mol))
R_Y^2	Model coefficient of determination (-)
R_p	Dried product mass transfer resistance (m/s)
r_d	Equivalent radius corresponding to duct opening between chamber and condenser (m)
$R_{p,0}$	Constant describing R_p in function of l (m/s)
$r_{p,i}$	Radius from the centre of the vial to the border of the spin frozen layer (m)
$r_{v,i}$	Inner radius of the glass vial (m)

$r_{v,n}$	Equivalent radius corresponding to vial neck opening (m)
$r_{v,o}$	Outer radius of the glass vial (m)
s	Distance between radiating plane and center of cylinder for view factor computation (m)
S_i	First order effect (-)
S_{Ti}	Total order effect (-)
t	Primary drying time (h)
T_B	Spectral transmittance (-)
T_b	Ice temperature at bottom of the vial (K)
T_c	Collapse temperature (K)
T_e	Eutectic temperature (K)
T_g	Glass transition temperature of the freeze-dried product (K)
T'_g	Glass transition temperature of the maximum freeze-concentrated formulation (K)
T_i	Product temperature at sublimation front (K)
T_r	Temperature of the water vapour (K)
T_s	Shelf fluid inlet temperature (K)
$T_{i,crit}$	Critical product temperature (K)
T_{rad}	Temperature of the IR heater (K)
$T_{v,i}$	Temperature at the inner side of the vial wall
$T_{v,o}$	Temperature at the outer side of the vial wall (K)
V	Filling volume (mL)
w	Width of the radiating plane for view factor computation (m)
x_{ray}	Length of generated ray for x dimension (m)

x_{shift} Shift parameter in x dimension for view factor computation (m)

y_{ray} Length of generated ray for y dimension (m)

z_{ray} Length of generated ray for z dimension (m)

z_{shift} Shift parameter in z dimension for view factor computation (m)

List of Figures

1.1	Temperature-controlled shelves loaded with vials in the drying chamber of a pilot-scale batch freeze-dryer	2
1.2	Illustration of the progress of primary drying with the gradual downward movement of the sublimation front	3
1.3	Illustration of glass vials containing the freeze-dried end product	4
1.4	Continuous filling and (partially) stoppering of glass vials	5
1.5	Industrial-scale batch freeze-dryer	5
1.6	Illustration of the difference in degree of supercooling and the impact on the resulting ice crystal size and sublimation rate	6
1.7	Sublimation rate of individual vials containing pure ice as illustration of the uneven heat transfer depending on the position on the freeze-dryer shelf	7
3.1	Illustration of the uncertainty on the shelf fluid inlet temperature T_s during temperature ramp	22
3.2	Illustration of the computation of the primary drying endpoint with a certainty of 99%	26
3.3	Vial heat transfer coefficient K_v plotted as function of chamber pressure P_c for edge (Squares) and centre vials (Circles)	27
3.4	Determination of the optimal values for chamber pressure P_c and shelf fluid inlet temperature T_s	28
3.5	Evolution of dried layer thickness L_{dried} for an RoF acceptance level of 1%	29
3.6	Optimal values for shelf fluid inlet temperature T_s (Top) and chamber pressure P_c (Bottom) for an RoF acceptance level of 1%	30
3.7	Uncertainty level on dried layer thickness L_{dried} ($S_{L_{dried}}$) for an RoF acceptance level of 1%	31

3.8	Uncertainty level on shelf fluid inlet temperature T_s for an RoF acceptance level of 1% for the model formulation	32
3.9	Optimal values for shelf fluid inlet temperature T_s (Top) and the evolution of the product temperature at the sublimation front T_i (Bottom) for an RoF acceptance level of 1%, 25%, 50% and 99%	33
3.10	Optimal values for chamber pressure P_c for an RoF acceptance level of 1%, 25%, 50% and 99%	34
3.11	Experimental product temperature at the sublimation front T_i for an RoF acceptance level of 1%, 25%, 50% and 99% and the critical product temperature $T_{i,crit}$ for an edge (Top) and centre (Bottom) vial	35
3.12	Cakes yielded after experimental verification runs for RoF of 1% (Left), 25% (Middle left), 50% (Middle right) and 99% (Right)	36
4.1	Mean of the quotient of two successive SRC values (Top) and the R_Y^2 -value (Bottom) for increasing number of Monte Carlo simulations performed on the primary drying model for the product temperature at the sublimation interface T_i as output variable of the regression-based GSA	55
4.2	Coefficient of variation CV for the SRC for an increasing number of base samples N performed on the primary drying model for the product temperature at the sublimation interface T_i (Top) and the sublimation rate \dot{m}_{sub} (Bottom) as output variable of the regression-based GSA	56
4.3	Mean of the SRC in function of the number of base samples N performed on the primary drying model for the product temperature at the sublimation interface T_i (Top) and the sublimation rate \dot{m}_{sub} (Bottom) as output variable of the regression-based GSA	57
4.4	Coefficient of variation CV for the S_{T_i} in function of the number of base samples N performed on the primary drying model for the product temperature at the sublimation interface T_i (Top) and the sublimation rate \dot{m}_{sub} (Bottom) as output variable of the variance-based GSA	59
4.5	Scatter plot for the freeze-drying model with $N = 10,000$ for P_c with T_i as output variable (Left) and α_{Rp} with \dot{m}_{sub} as output variable (Right) after 1 h	60
4.6	S_{T_i} for the primary drying model with $N = 5,000$ for the product temperature at the sublimation front T_i (Top) and the sublimation rate \dot{m}_{sub} (Bottom) as output variable at different time steps	61
4.7	Extended coefficient plot, response: Sublimation rate	62

5.1	The CONRAD™ freeze-drying plant from GEA Group	73
5.2	Illustrative overview of the continuous freeze-drying concept proposed by Oughton et al.	74
5.3	Illustration of the spin freezing step	76
5.4	Illustration of the IR assisted continuous primary drying of spin frozen vials, rotating along their longitudinal axis in front of individual IR heaters . . .	77
5.5	Parallel lines in the continuous freeze-drying technology avoiding scale-up re-optimization and validation	78
6.1	Illustration of IR mediated primary drying of spin frozen vials	82
6.2	Experimental drying set-up with in-line NIR monitoring	83
6.3	Extended coefficient plot DoE 1	91
6.4	Interaction plot 'Electrical power P^* '*Distance between IR heaters and vial Dis'	93
6.5	Score scatter plot including the explanation of the chronological trends . .	95
6.6	Loading line plot of PC1 (black) and PC2 (blue)	95
6.7	Visualization of drying progress with collected NIR spectra	97
6.8	PC1 in function of time	98
6.9	Extended coefficient plot DoE 2, response: total drying time	99
6.10	Extended coefficient plot DoE 2, response: primary drying time	100
6.11	Extended coefficient plot DoE 2, response: secondary drying time	101
7.1	Illustration of the IR assisted continuous primary drying of spin frozen vials, rotating along their longitudinal axis in front of individual IR heaters . . .	108
7.2	The three situations for a cylindrical target parallel to the plane of the radiator (Target in black)	113
7.3	The direction of the generated ray to determine the view factor	114
7.4	The orientation of the radiator plane versus the cylindrical target: parallel (Left) and perpendicular (Right). The variables which are essential for the model to calculate the view factor, i.e., k , d , h , s and w , are indicated in the figure (Target in black)	115
7.5	Experimental IR assisted drying set-up with in-line NIR monitoring	121
7.6	Determination of optimal number of samples N for Monte Carlo simulation of the view factor F	124
7.7	The rays which hit (Black) and miss (Gray) the cylindrical target (Red) for the radiator set-up (Blue) (parallel case) in different planes	125

7.8	The rays which hit (Black) and miss (Gray) the cylindrical target (Red) for the radiator set-up (Blue) (perpendicular case) in different planes	126
7.9	Mass of sublimed ice Δm and temperature of IR heater T_{rad} in function of electric power P_e	127
7.10	View factor F in function of the distance between the IR heater and the centre of the spin frozen vial s	127
7.11	IR heater temperature T_{rad} and dried layer thickness l in function of primary drying time t	129
7.12	Scores scatter plot including the explanation of the chronological trends . .	130
7.13	Loading line plot of PC1 (black dotted) and PC2 (blue solid)	130
7.14	Mannitol solid state of the freeze-dried product evaluated via Raman spectroscopy	131
7.15	Product appearance of final dried product yielded after the validation runs	133
8.1	Illustration of the compatibility of thermal imaging with batch (top) and continuous (bottom) freeze-drying	141
8.2	Illustration of the IR camera set-up (top view) during primary drying with the rotating spin frozen vial and the IR heater inside the vacuum chamber and the IR camera positioned outside measuring through an IR window at an angle of 90°	143
8.3	The spectral radiance B_λ emitted by glass vials in function of the wavelength λ for a vial temperature varying from -50°C to 50°C , in the absence (top left) and presence (bottom) of the germanium IR window between the vial and the IR camera; the transmission of the germanium window in function of the wavelength $T_B(\lambda)$ is plotted on the top right	144
8.4	Illustration of a cross section of a spin frozen vial during primary drying with specified temperatures and radii	147
8.5	Spectral transmittance T_B of the germanium IR window in function of the vial temperature $T_{v,o}$	152
8.6	Thermal images of a spin frozen vial just before activation of the IR heaters (top left), after 20 min (top right) and after 100 min of primary drying (bottom)	153
8.7	The temperature at the outer vial wall $T_{v,o}$ in function of drying time t . .	155
8.8	The temperature at the outer vial wall $T_{v,o}$ (dashed line) and the temperature at the sublimation front T_i (solid line) in function of primary drying time t	157

8.9	The dried product mass transfer resistance R_p (m/s) in function of the dried layer thickness l (m); the R_p data on the right side of the vertical line were not included to the fitting of the curve	159
10.1	FDA-approved protein, peptide, vaccines (including viral and bacterial), oligonucleotide, and cell-based products grouped according to dosage form	170
10.2	'GMP-like' prototype of the continuous freeze-drying technology	175
10.3	'GMP' prototype of the continuous freeze-drying technology	176

List of Tables

3.1	Nominal values of the parameters of the model describing the primary drying step	19
3.2	Uncertainty level for the input factors of the UA	21
3.3	The experimentally determined primary drying time for the centre vials for different RoF acceptance levels compared with the computed primary drying endpoint with 99% certainty	37
4.1	Nominal values of the parameters of the model describing the primary drying step	48
4.2	Uncertainty level for the input factors	49
4.3	Overview factors DoE with lowest and highest level	51
4.4	Overview experiments DoE, the experiments in bold were performed twice (centre points)	52
6.1	Overview factors DoE 1 with lowest and highest level	84
6.2	Overview experiments DoE 1, the experiments in bold were performed twice (centre points)	85
6.3	Overview of the five model formulations included as a qualitative factor in DoE 1 and 2	86
6.4	Overview factors DoE 2 with lowest and highest level	87
6.5	Overview experiments of DoE 2, the experiments in bold were performed twice (centre points)	88
6.6	Regression coding of the five-level qualitative factor <i>Formulation</i> (For)	89
7.1	Nominal values of input parameters for view factor F computation, calculation power contribution by surroundings and calculation dynamic temperature profile	119

7.2 Overview of the comparison between the computed and experimental primary drying time; Computed primary drying time: 50 minutes 132

CHAPTER 1

Introduction

1.1 Introduction to pharmaceutical freeze-drying

Since biological therapeutics are considered the key driver of growth, the focus of the pharmaceutical industry is shifting from small molecules towards these macromolecules [1]. However, biopharmaceuticals often have a limited stability in aqueous solution due to several water-mediated degradation pathways, e.g., deamidation, aggregation, oxidation or hydrolysis of proteins [2]. The Food and Drug Administration (FDA) and European Medicines Agency (EMA) list with approved biopharmaceutical drug products (> 300) contains approximately 50% freeze-dried products [3, 4]. This indicates the importance of freeze-drying (lyophilization) in stabilizing biopharmaceutical drug products which are unstable when formulated as an aqueous solution, despite the high cost and energy consumption as well as the long processing time. The largest fraction of freeze-dried biological drug products are therapeutic protein formulations and vaccines. The economic importance of the lyophilization process is supported by the presence of three drug products (i.e., Enbrel®[®], Remicade®[®] and Herceptin®[®]) in the top ten of most profitable drugs for the year 2016 [5].

1.2 Conventional pharmaceutical freeze-drying of unit doses

Conventional pharmaceutical freeze-drying is a batch-wise process during which all vials of each batch are processed through a sequence of consecutive steps (i.e., freezing, primary drying and secondary drying) until the dried end product is obtained. Glass vials are aseptically filled with the aqueous drug formulation (i.e., unit doses) and loaded onto



Figure 1.1: Temperature-controlled shelves loaded with vials in the drying chamber of a pilot-scale batch freeze-dryer

temperature-controlled shelves in the drying chamber (Figure 1.1). At the start of the freezing stage, these shelves are gradually cooled until approximately $-45\text{ }^{\circ}\text{C}$, depending on the formulation characteristics. The temperature of the aqueous drug formulation decreases until ice nucleation takes place and part of the water is converted into ice. While ice crystal growth proceeds upon further freezing, the solutes gradually concentrate between these crystals [6]. Freeze-concentration continues until at the eutectic temperature T_e a saturated solution is obtained. From this point forward, water and solutes (e.g., mannitol, NaCl, glycine) start to crystallize simultaneously leading to the formation of a fully crystalline matrix. Amorphous products (e.g., sucrose, trehalose, proteins) behave differently during freeze-concentration as they form a supersaturated solution, without crystallization of the solutes. Due to the gradual increase in viscosity associated with this supersaturation, ice crystallization slows down until maximum freeze-concentration is achieved at the glass transition temperature T'_g . At this characteristic temperature, the viscosity has raised to such an extent that no further freezing occurs [6]. Hence, ice crystallization is interrupted prematurely, explaining the presence of residual unfrozen water in the amorphous glass. At the end of the freezing step, the shelf temperature, and consequently the product temperature, reach a value well below T_e or T'_g for crystalline or amorphous products, respectively, resulting in complete solidification of the product. To allow full crystallization of crystalline components or to enhance the batch uniformity of the ice crystal size, an annealing

step can be added to the freezing stage ([7–9]). Here, the shelf temperature at the end of the freezing step is raised to a temperature above T'_g , but below T_e . This temperature is maintained for several hours before re-establishing the final freezing temperature, below T'_g .

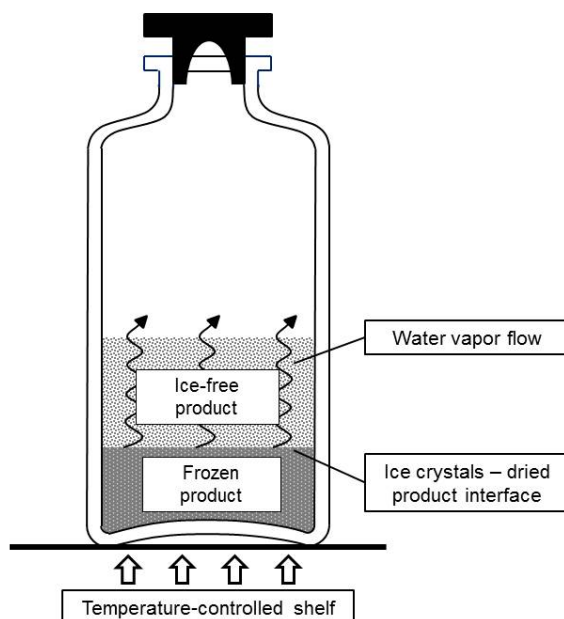


Figure 1.2: Illustration of the progress of primary drying with the gradual downward movement of the sublimation front [10]

The primary drying step, which is in general the most time-consuming of the whole freeze-drying process, is initiated by lowering the chamber pressure, conventionally to a value between 5 and 30 Pa. When the desired pressure is reached, the shelf temperature is raised to promote ice sublimation. The sublimation front, i.e., the interface separating ice-free product from the ice crystal matrix, moves gradually downward with the progress of primary drying (Figure 1.2). When ice sublimation is completely finished, the shelf temperature is further raised during the secondary drying step, supporting the desorption of unfrozen water in the amorphous matrix and/or the removal of hydrate water in crystalline material until the desired residual moisture content of the end product is obtained. At the end of the lyophilization process, the aqueous solution of the (heat-)labile biopharmaceutical is transformed into a solid, dry cake with an increased shelf-life (Figure 1.3).



Figure 1.3: Illustration of glass vials containing the freeze-dried end product

1.3 Disadvantages related to batch freeze-drying of unit doses

Conventional pharmaceutical batch freeze-drying is inherently associated with several disadvantages. The process is inefficient and time- and energy-consuming [2]. Cycle times can vary from 1 to even 7 days, depending on several factors like formulation characteristics (e.g., T'_g and dried product mass transfer resistance), filling volume and vial dimensions. The processing of industrial batches, often containing thousands of vials, leads to operational risks, mainly during loading and unloading of the drying chamber due to complicated handling of the vials. The handling equipment in the steps before (i.e., filling and (partially) stoppering) and after (i.e., capping and packaging) freeze-drying is continuously operated by nature (Figure 1.4). Therefore, buffer systems are required to bridge the time until the start of the upcoming cycle, which highly increases the risk of product contamination. Additionally, the handling equipment and buffer systems take up an enormous space which must meet the class 100 clean room standards, mandatory in the sterile production of (injectable) biopharmaceuticals [11]. These strict requirements in terms of sterility and cleanliness strongly increase energy consumption and production costs.

The huge size of industrial batches is impractical for cycle development. The initial development of freeze-drying cycles is performed in lab-scale equipment. Subsequent steps in the development process demand scale-up from lab-scale to pilot-scale and, finally, to industrial-scale freeze-dryers (Figure 1.5). Differences in heat and mass transfer between each equipment scale require re-optimization and re-validation of these cycles ([12, 13]).

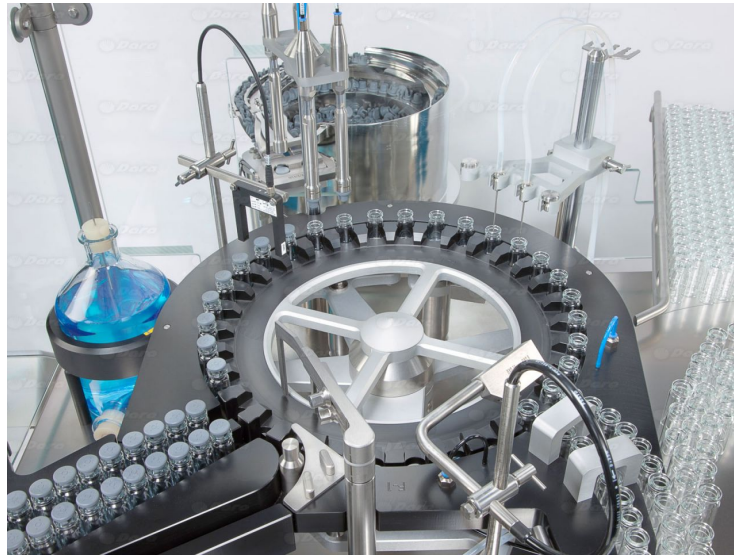


Figure 1.4: Continuous filling and (partially) stoppering of glass vials

Also, in general, the freeze-drying equipment is designed and optimized to process the maximum applicable amount of vials. Often, the required batch size is smaller than the maximum load, leading to inefficient use of the equipment. Additionally, re-validation of the freeze-drying cycle is mandatory in case the batch size is modified.



Figure 1.5: Industrial-scale batch freeze-dryer

During the freezing stage in batch freeze-drying, ice nucleation generally does not occur at the equilibrium freezing point of the solution. Retaining the liquid state below the equilibrium freezing temperature is a phenomenon termed supercooling [6]. Ice nucleation during traditional batch freeze-drying is a stochastic event, resulting in different degrees of supercooling for each vial in the batch. A higher degree of supercooling leads to a higher rate of ice nucleation and a faster effective freezing rate [6]. This way, a high number of small ice crystals is obtained (Figure 1.6). In turn, a lower degree of supercooling results in a lower number of large ice crystals. The stochastic nature of ice nucleation during batch freeze-drying leads to different sizes of ice crystals in each vial of the batch. The ice crystal size in the frozen matrix corresponds to the final pore size in the dried layer during the sublimation process. As a reduced pore size is associated with a higher dried product mass transfer resistance and vice versa, the sublimation rate during primary drying is highly influenced by the pore size in the dried layer [13]. Eventually, the uncontrolled freezing step causes vial-to-vial variability of the sublimation rate within a batch and between batches [14].

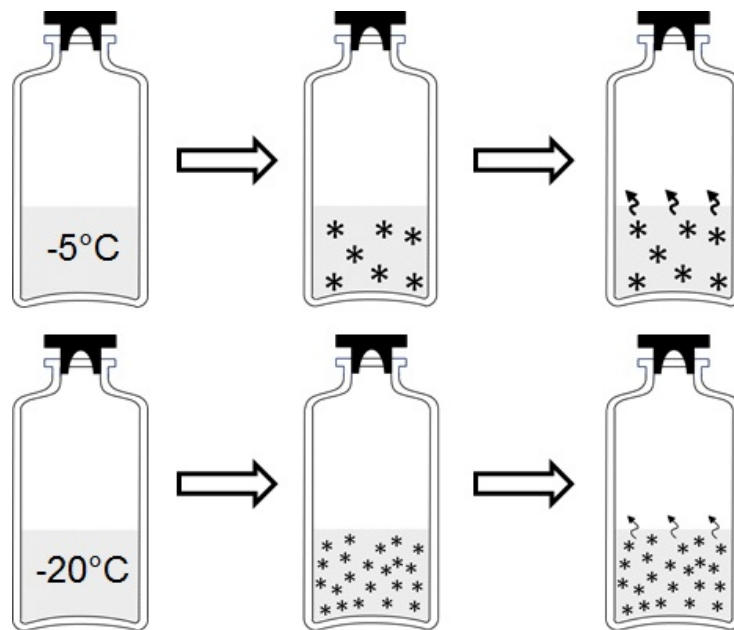


Figure 1.6: Illustration of the difference in degree of supercooling and the impact on the resulting ice crystal size and sublimation rate: the temperature in the vials indicates the temperature at which ice nucleation occurs, the size of the asterisks represents the size of the ice crystals and the thickness of the arrows in the vials at the right is related to the sublimation rate

Primary drying requires an appropriate and sufficient energy supply to the vial, necessary for ice sublimation (endothermic process) [2]. In traditional batch freeze-drying, this energy is provided via thermal conduction from the silicone heat transfer fluid in the shelves to the vial by increasing the temperature of this fluid. Vials placed at the edge of the shelves receive additional energy radiated from the warmer surroundings (e.g., the door and walls of the drying chamber) (Figure 1.7) [15]. This results in a higher temperature of these vials, associated with faster drying rates and a higher risk for collapse [12]. Both the uncontrolled freezing and the uneven heat transfer lead to different process conditions for each individual vial in the batch [6, 16]. Product quality is only determined on a limited fraction of vials, before releasing the complete batch. The uncontrolled vial-to-vial variation and quality approach do not meet the most recent guidelines issued by the regulatory authorities regarding Quality-by-Design (QbD) and Process Analytical Technology (PAT) which state that quality should be guaranteed by building it into the product instead of elaborate off-line testing [17].

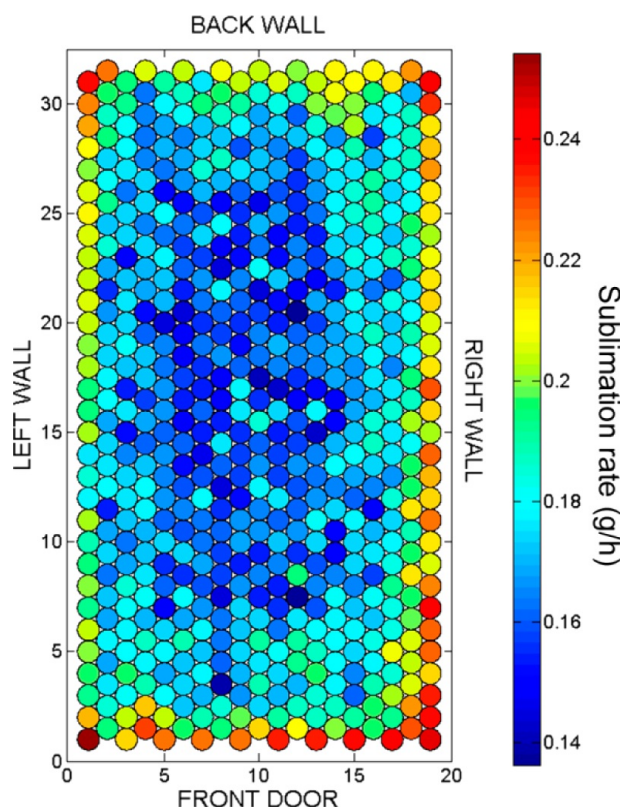


Figure 1.7: Sublimation rate of individual vials containing pure ice as illustration of the uneven heat transfer depending on the position on the freeze-dryer shelf [15]

Bibliography

- [1] J. C. Kasper, G. Winter, and W. Friess. Recent advances and further challenges in lyophilization. *Eur. J. Pharm. Biopharm.*, 85:162–169, 2013.
- [2] T. Jennings. *Lyophilization: Introduction and basic principles*. Informa healthcare, New York, 2008.
- [3] L. Burns. The biopharmaceutical sector’s impact on the US economy: Analysis at the national, state and local levels. Technical report, 2009.
- [4] H. Gieseler. Insights in lyophilization. In *Current best practices & research trends*, Antwerp, 2012.
- [5] Top drugs by sales in 2016: Who sold the blockbuster drugs?, 2017.
- [6] J. C. Kasper and W. Friess. The freezing step in lyophilization: Physico-chemical fundamentals, freezing methods and consequences on process performance and quality attributes of biopharmaceuticals. *Eur. J. Pharm. Biopharm.*, 78:248–263, 2011.
- [7] J. A. Searles, J. F. Carpenter, and T. W. Randolph. Annealing to optimize the primary drying rate, reduce freezing-induced drying rate heterogeneity, and determine Tg’ in pharmaceutical lyophilization. *J. Pharm. Sci.*, 90(7):872–887, 2001.
- [8] A. Hawe and W. Friess. Impact of freezing procedure and annealing on the physico-chemical properties and the formation of mannitol hydrate in mannitol-sucrose-NaCl formulations. *Eur. J. Pharm. Biopharm.*, 64(3):316–325, 2006.
- [9] X. Lu and M. J. Pikal. Freeze-drying of mannitol-trehalose-sodium chloride-based formulations: the impact of annealing on dry layer resistance to mass transfer and cake structure. *Pharm. Dev. Technol.*, 9(1):85–95, 2004.
- [10] S. Mortier, P. J. Van Bockstal, J. Corver, I. Nopens, K. Gernaey, and T. De Beer. Uncertainty analysis as essential step in the establishment of the dynamic Design Space of primary drying during freeze-drying. *Eur. J. Pharm. Biopharm.*, 103:71–83, 2016.
- [11] W. Tschudi, K. Benschine, S. Fok, and P. Rumsey. Cleanroom Energy Benchmarking In High-Tech and Biotech Industries. In *ACEEE Summer Study on Energy Efficiency in Industry*, Tarrytown, New York, 2001.

-
- [12] S. Rambhatla and M. J. Pikal. Heat and mass transfer scale-up issues during freeze-drying, I: atypical radiation and the edge vial effect. *AAPS PharmSciTech*, 4:22–31, jan 2003.
- [13] S. Rambhatla, R. Ramot, C. Bhugra, and M. J. Pikal. Heat and mass transfer scale-up issues during freeze drying: II. Control and characterization of the degree of supercooling. *AAPS PharmSciTech*, 5:54–62, 2004.
- [14] J. A. Searles, J. F. Carpenter, and T. W. Randolph. The ice nucleation temperature determines the primary drying rate of lyophilization for samples frozen on a temperature-controlled shelf. *J. Pharm. Sci.*, 90:860–871, 2001.
- [15] A. Kauppinen, M. Toiviainen, O. Korhonen, J. Aaltonen, J. Paaso, M. Juuti, and J. Ketolainen. In-Line Multipoint Near-Infrared Spectroscopy for Moisture Content Quantification during Freeze-Drying. *Anal. Chem.*, 85:2377–2384, 2013.
- [16] A. A. Barresi, R. Pisano, V. Rasetto, D. Fissore, and D. L. Marchisio. Model-Based Monitoring and Control of Industrial Freeze-Drying Processes: Effect of Batch Nonuniformity. *Drying Technol.*, 28:577–590, 2010.
- [17] Food and Drug Administration. International Conference on Harmonisation Q8, 2004.

CHAPTER 2

Objectives and outline

The overall objective of this thesis is twofold. The initial chapters (Chapter 3 and 4) describe the optimization of the primary drying step of a batch freeze-drying process through mechanistic modelling. The aim is to maximize the primary drying efficiency while obtaining a freeze-dried end product which meets all Critical Quality Attributes (CQAs). However, due to the inherent disadvantages related to batch freeze-drying, as elaborately discussed in **chapter 1**, the second part (Chapter 5 to 8) focuses on the main objective of this thesis: the development of a continuous alternative for the current state-of-the-art batch freeze-drying process of unit doses. The different research aspects towards these objectives are outlined in the next paragraphs.

Chapter 3 describes the determination of the dynamic Design Space of the primary drying step during batch freeze-drying. A mechanistic model is developed to quantify the heat and mass transfer, which allows to maximise the sublimation efficiency while simultaneously minimising and controlling the risk of cake collapse. The impact of the uncertainty of the model input variables and process parameters on the model output is estimated via an Uncertainty Analysis (UA) on this primary drying model. In addition, the propagation of error on the estimation of the dried layer thickness is included in the UA. The computed dynamic Design Space, i.e., the optimal dynamic settings for shelf temperature and chamber pressure in function of process time, is experimentally verified. In **chapter 4**, a Global Sensitivity Analysis (GSA) is applied on the same mechanistic primary drying model to evaluate how the uncertainty in the output of this model can be apportioned to different sources of uncertainty in the model input, which allows the determination of the most influential process parameters of the primary drying step. The results of the GSA were experimentally verified via a Design of Experiments (DoE) approach.

In **chapter 5**, the incentives for the pharmaceutical industry to shift to continuous processing and the history of continuous freeze-drying are summarized. In addition, the proposed continuous freeze-drying concept for biopharmaceutical unit doses, resolving the disadvantages related to the batch process, is elaborately described. This continuous concept is based on spinning the vials during freezing and on optimal energy transfer via non-contact IR radiation during drying. In **chapter 6**, the feasibility of the IR mediated energy transfer during the processing of spin frozen vials is evaluated. Empirical models are constructed via a DoE approach to determine the influence of various process parameters on the primary drying behaviour of different model formulations. In addition, a near-infrared (NIR) spectroscopy method is developed for in-line monitoring of the drying progress of spin frozen vials, which allows the detection of the endpoint of both the primary and secondary drying step. Similar to batch freeze-drying, the heat and mass transfer during continuous IR mediated primary drying is quantified via mechanistic modelling. The development and experimental verification of this model is extensively described in **chapter 7**. The mechanistic model computes the optimal dynamic temperature of the IR heaters in function of process time. As the standard temperature sensors currently used in batch freeze-drying are invasive and incompatible with the proposed continuous technology, **chapter 8** focuses on the evaluation of the feasibility of non-contact IR thermography as innovative PAT tool for in-line monitoring of the temperature at the sublimation front during primary drying. Additionally, a method is developed to estimate the dried product mass transfer resistance of spin frozen vials. A summary and the general conclusions of this thesis are outlined in **chapter 9**. Finally, **chapter 10** provides a detailed outline of the social and economic context in which the research of this thesis fits, with a focus on the future challenges of the pharmaceutical industry and the valorization potential of the proposed continuous freeze-drying technology.

CHAPTER 3

Quantitative risk assessment via Uncertainty Analysis in combination with error propagation for the determination of the dynamic Design Space of the primary drying step during batch freeze-drying

Redrafted from: Van Bockstal P.J., Mortier S.T.F.C., Corver J., Nopens I., Gernaey K.V., De Beer T. (2017) *Quantitative risk assessment via uncertainty analysis in combination with error propagation for the determination of the dynamic Design Space of the primary drying step during freeze-drying*. European Journal of Pharmaceutics & Biopharmaceutics, 121, 32-41.

3.1 Introduction

One of the CQAs of lyophilized biopharmaceutical products, defined as product properties or characteristics that should meet defined standards to ensure the desired quality (ICH Q8), is the cake appearance [1]. Loss of cake structure (collapse) should be avoided throughout the lyophilization process to ensure reconstitution of the drug product within an appropriate timing and for aesthetic purposes [2]. For this reason, the product temperature at the sublimation front T_i should be maintained below the critical product temperature $T_{i,crit}$ during the entire primary drying step. $T_{i,crit}$ is characteristic for each formulation and identified as the collapse temperature T_c or the eutectic temperature T_e for amorphous and crystalline products, respectively. In general, T_c lies a few degrees above the glass transition temperature of the maximum freeze-concentrated formulation T'_g because the viscosity

near T'_g is sufficiently high to limit viscous flow [3]. During secondary drying, the product temperature should be kept below the glass transition temperature of the dried product T_g to avoid molecular motion and loss of cake structure. The value of T_g is much higher compared to T'_g of the freeze-concentrate and is highly influenced by the residual moisture content, due to the plasticizing effect of water [2]. In general, the shelf temperature ramp during the transition of the primary to secondary drying step is rather conservative, due to the potential high residual moisture content immediately after primary drying. However, several approaches have been developed to optimize this transition phase [4, 5].

The freeze-drying process is characterized by two adaptable process variables, i.e. the shelf fluid inlet temperature T_s and chamber pressure P_c . Combinations of both parameters are set in function of time, specific for each process step. During primary drying, the settings of T_s and P_c should result in a value for T_i associated with maximum sublimation efficiency, while maintaining an appropriate cake structure. Mechanistic models based on the fundamental understanding of the underlying physical mechanisms of the sublimation process, allow the determination of the optimal combination of T_s and P_c during primary drying and their calibration for a formulation to be freeze-dried [6, 7]. The development of these mechanistic models only requires a limited amount of experiments, compared to data-driven empirical models associated with a high experimental load. Mechanistic modelling assists in cycle development and optimization by computing T_i for different combinations of T_s and P_c , eventually leading to the construction of the Design Space for primary drying [8–10]. The Design Space is defined as the multidimensional combination and interaction of input variables and process parameters leading to an acceptable product quality with a controlled probability (ICH Q8) [1]. For primary drying, the Design Space is demarcated by the equipment limitations, the sublimation efficiency and the specific CQA for the lyophilized biopharmaceutical product, in this case the dried cake appearance [11–13]. All combinations of T_s and P_c within these limits lead to a lyophilized product with an appropriate cake appearance that is achieved within an acceptable time-frame. Model input variables can change with the progress of primary drying, such as the thickness of the dried product layer L_{dried} . Upon an increase in L_{dried} , the path of the water vapour originating from the sublimation interface through the pores of the above dried product layer becomes longer, associated with an increase in the dried product mass transfer resistance R_p . Therefore, the heat transfer to the product should be gradually lowered, to avoid an increase in T_i . As a consequence, the optimal combination of T_s and P_c changes in time to maintain T_i below $T_{i,crit}$, leading to a dynamic Design Space [8, 9].

The mechanistic models are a mathematical approximation of the sublimation process during the primary drying stage. Inherent to model development, a few assumptions and simplifications are included in these primary drying models (e.g., a planar sublimation front and steady-state system are assumed). In addition, the model input variables and process parameters are in some cases an estimation of the real value. Some input variables (i.e., R_p and the vial heat transfer coefficient K_v) are quantified by one global value for the entire batch, while they can differ from vial to vial (inter-vial variability). For these reasons, the computational model predictions are associated with a degree of uncertainty, through which they can deviate from the actual (experimental) drying behaviour. By including this parameter uncertainty into the mechanistic primary drying model, the uncertainty on the model predictions can be determined leading to the quantitative estimation of the Risk of Failure (RoF) (i.e., risk of cake collapse) for each combination of the adaptable process variables, P_c and T_s , in the dynamic Design Space. Only a limited number of studies have been conducted focusing on quantitative risk assessment. The uncertainty of two input variables, R_p and K_v , can be compensated by assuming a Gaussian distribution of the values around their mean [6, 14]. Alternatively, the impact of the variation in R_p and K_v was assessed by determining the variance for these parameters and their influence on the primary drying time [15]. In both approaches, only R_p and K_v were considered as uncertain parameters. This work presents the use of a dedicated uncertainty analysis (UA) in which the uncertainty on *each* uncertain input variable and process parameter is estimated and quantified. L_{dried} is both an input and output variable of the mechanistic primary drying model. As the value of L_{dried} is computed throughout the simulation, the uncertainty on this input parameter results from the other uncertain input variables and, in addition, the uncertainty increases with the drying progress due to the accumulation of error. Therefore, the dedicated UA is refined and extended with a strategy to incorporate the accumulation of error into the primary drying model. The combination of the dedicated UA with the time dependent process variables results in the dynamic Design Space with the ultimate aim of quantifying and controlling the risk of cake collapse and reducing the risk of batch rejection, while maximizing the drying efficiency.

3.2 Materials and methods

3.2.1 Freeze-drying model

The mechanistic primary drying model consists of two stages, the start-up phase and the actual primary drying stage. During the start-up phase, the chamber pressure is gradually decreased till the calculated sublimation rate \dot{m}_{sub} becomes positive. An exponential decrease of the chamber pressure P_c from 100,000 Pa to 10 Pa in 10 minutes is assumed based on the equipment constraints. During this pressure decrease, it is assumed that the shelf fluid inlet temperature T_s remains constant at the final freezing phase temperature and that the product temperature at the sublimation interface T_i equals T_s . Moreover, the initial temperature difference across the ice layer ΔT is fixed at 0 K. As long as the calculated sublimation rate is lower than zero, \dot{m}_{sub} is set to zero. The second stage, the primary drying step, starts when \dot{m}_{sub} is higher than zero. From this moment, the dried layer thickness L_{dried} gradually increases as sublimation proceeds.

The full mathematical model describing the sublimation process consists of a set of equations of which some have to be solved simultaneously as they are interdependent. The model calculates the product temperature at the sublimation interface T_i (K), the sublimation rate \dot{m}_{sub} (kg/s) and the evolution of the dried layer thickness L_{dried} (m) as function of time. For a fixed set of input values, T_i and the temperature difference across the ice layer ΔT (K) are calculated using the following equations [8, 9, 16–18]:

$$\begin{aligned} & e^{9.550426 - 5723.265/T_i + 3.53068 \ln(T_i) - 0.00728332 T_i} \\ & = - \frac{(-A_p \Delta H_s P_{w,c} - A_v K_v R_p M T_s + A_v K_v R_p M T_i + A_v K_v R_p M \Delta T)}{A_p \Delta H_s} \end{aligned} \quad (3.1)$$

$$\Delta T = \frac{889200 \frac{(L_{total} - L_{dried})(P_{w,i} - P_{w,c})}{R_p} - 0.0102 (L_{total} - L_{dried}) (T_s - T_i)}{1 - 0.0102 (L_{total} - L_{dried})} \quad (3.2)$$

with A_p the product area available for sublimation (m^2), ΔH_s the latent heat of ice sublimation (J/mol), $P_{w,c}$ the partial vapour pressure in the drying chamber (Pa), A_v the outer vial area (m^2), K_v the vial heat transfer coefficient (J/(m^2sK)), R_p the dried product mass transfer resistance (m/s), M the molecular weight of water (0.018 kg/mol), L_{total} the total thickness of the product layer (m) and $P_{w,i}$ the vapour pressure at the sublimation interface (Pa). $P_{w,c}$ is assumed to be equal to P_c (Pa), as during primary drying the gas composition in the drying chamber consists almost entirely of water vapour [8].

The latent sublimation heat of ice ΔH_s is given by [17]:

$$\Delta H_s = 46782.5 + 35.8925T_i - 0.07414T_i^2 + 541.5e^{-\left(\frac{T_i}{123.75}\right)^2} \quad (3.3)$$

The vial heat transfer coefficient K_v is calculated by [8]:

$$K_v = \alpha + \frac{\beta P_c}{1 + \gamma P_c} \quad (3.4)$$

with α (J/(m²sK)), β (J/(m²sKPa)) and γ (1/Pa) constants describing K_v quantitatively in function of P_c , which are determined by fitting experimental data [19]. K_v is characteristic for the vial type, because the contact area with the shelf differs due to the shape of the bottom and the size of the vial. The equipment can also influence K_v , as the radiation provided by the surroundings to the (edge) vials is dependent on the geometry of the equipment [20]. Additionally, the ratio of vials exposed to this radiative heat is much higher in the small laboratory scale freeze-dryers, in comparison with the much larger manufacturing scale freeze-dryers.

The dried product resistance R_p is given by [8]:

$$R_p = R_{p,0} + \frac{A_{Rp}L_{dried}}{1 + B_{Rp}L_{dried}} \quad (3.5)$$

with $R_{p,0}$ (m/s), A_{Rp} (1/s) and B_{Rp} (1/m) constants describing R_p quantitatively in function of L_{dried} . These constants are formulation specific and are determined by fitting experimental data [19]. Theoretically, $R_{p,0}$ is the product resistance at the start of primary drying, because L_{dried} is equal to zero. A_{Rp} and B_{Rp} describe the progress of the product resistance with the increase of L_{dried} .

Once T_i is known, the vapour pressure at the sublimation interface $P_{w,i}$ can be calculated using the following relation [17]:

$$P_{w,i} = e^{9.550426 - 5723.265/T_i + 3.53068\ln(T_i) - 0.00728332T_i} \quad (3.6)$$

The sublimation rate \dot{m}_{sub} can be calculated using [8, 16]:

$$\dot{m}_{sub} = A_p \frac{(P_{w,i} - P_{w,c})}{R_p} \quad (3.7)$$

The evolution of the dried layer thickness L_{dried} is then given by [18]:

$$L_{dried} = \frac{\Delta m}{\rho_{ice}\phi A_p} \quad (3.8)$$

with Δm the mass of sublimed ice (kg), ρ_{ice} the density of ice (kg/m³) and ϕ the volume fraction of ice (-). Δm based on \dot{m}_{sub} and the used time step Δt in the iteration, i.e. $\Delta m_{t+1} = \Delta m_t + \dot{m}_{sub}\Delta t$.

The total thickness of the product layer L_{total} is calculated based on the amount of liquid that is filled in the vial:

$$L_{total} = \frac{V10^{-6}}{\pi r_i^2} \quad (3.9)$$

with V the filling volume for one vial (mL) and r_i the inner vial radius (m).

The nominal values of the model input parameters are listed in table 3.1. The coefficients describing K_v were experimentally determined, as explained in section 3.2.3. The coefficients describing R_p for the model formulation were taken from literature [21]. The aqueous model formulation contained 30 mg/mL of sucrose (Sigma-Aldrich, Saint-Louis, MO, USA). $T_{i,crit}$ was assumed to be equal to T'_g of the model formulation, which was determined using Modulated Differential Scanning Calorimetry (MDSC) (Section 3.2.4). A planar sublimation interface was assumed for the model. Finally, the system was considered to be at steady-state, i.e., the transferred energy was only used for ice sublimation.

To limit the computational load, the grid for P_c and T_s for the grid-search was limited. As the optimal value for the chamber pressure is seldom increasing after reaching the vacuum conditions, the limits for P_c were set at [10 Pa; 14 Pa] after the exponential pressure decrease at the start of primary drying [9]. The lower boundary was chosen based on the lower limit that can be reached by the equipment. The upper boundary was initially set based on expert knowledge. In case this upper boundary was reached during the grid-search, the upper limit was extended. The grid boundaries for T_s changed during the process, and the range was based on the maximum temperature ramp that can be supported by the freeze-dryer, i.e., 1 °C/min. The time step used for the calculations increased with the progress of primary drying. Consequently, the width of the range for T_s changed accordingly throughout the calculations based on the value of T_s for the previous time step and the maximum ramp of T_s , e.g., for a value of -20 °C for T_s and a time step of 5 minutes, the range is [-25 °C; -15 °C].

The sublimation rate during primary drying can be limited by the choked flow phenomenon [13]. The gas flow rate in the duct connecting the chamber and the condenser is restricted by an upper limit, and as such the maximum sublimation rate is restricted by the capacity

Table 3.1: Nominal values of the parameters of the model describing the primary drying step

Parameter		Numerical value
Inner radius of 10R vial	$r_{v,i}$	0.011 m
Outer radius of 10R vial	$r_{v,o}$	0.012 m
Radius of the vial neck	$r_{v,n}$	0.0063 m
Radius of the duct of the dryer	r_d	0.08 m
K_v -coefficient	α	11.18 J/(m ² sK)
K_v -coefficient	β	1.435 J/(m ² sKPa)
K_v -coefficient	γ	0.04008 1/Pa
R_p -coefficient	$R_{p,0}$	6.926 10 ⁴ m/s
R_p -coefficient	A_{Rp}	9.124 10 ⁶ 1/s
R_p -coefficient	B_{Rp}	0 1/m
Critical product temperature	$T_{i,crit}$	-32.5 °C
Filling volume	V	2.5 mL
Density of ice	ρ_{ice}	919.4 kg/m ³
Volume fraction of ice	ϕ	0.97
Ratio of the specific heat for water	κ	1.33
Molecular weight of water	M	0.018015 kg/mol

of the freeze-dryer. Once the gas flow rate approaches the velocity of sound (Mach I), a further rise in mass flow leads to an increased vapour density, as is expressed by a higher value for P_c . The increased amount of water vapour molecules will in turn enhance the thermal energy transfer to the vial and product thereby enhancing ice sublimation. At this point during primary drying, the process is out of control. The ever increasing pressure and corresponding thermal energy transfer eventually leads to a situation where the sublimation rate cannot increase any further when the maximum mass transfer resistance in the dried product is reached and due to the reduced pressure difference between $P_{w,i}$ and $P_{w,c}$. As a consequence, more energy is supplied to the product than can be extracted by subliming ice, resulting in an increase of T_i , eventually leading to collapse of the product and loss of the batch.

The optimal process settings were determined on both vial and dryer-level. On vial-level, only choked flow at the vial neck is taken into account, as it is the most narrow point for

the mass transfer, which is calculated using the following relation [13]:

$$\dot{m}_{\text{sub,chok,vial}} = \frac{0.3 r_{v,n}^2 \pi \sqrt{\frac{\kappa T_r R}{M}} M}{R T_r} P_c \quad (3.10)$$

with $\dot{m}_{\text{sub,chok,vial}}$ the maximum sublimation rate avoiding choked flow at vial level (kg/s), $r_{v,n}$ the equivalent radius corresponding with the most narrow lumen at the stopper placed upon the vial neck opening (m), κ the ratio of the specific heat for water (1.33), T_r the temperature of the water vapour (K), R the gas constant (8.3144621 J/(K mol)) and M the molecular weight of water (kg/mol).

The choked flow at dryer-level, where the valve in the duct connecting the drying chamber and the condenser is the limiting factor, is given by [13]:

$$\dot{m}_{\text{sub,chok,dryer}} = \frac{0.3 r_d^2 \pi \sqrt{\frac{\kappa T_r R}{M}} M}{R T_r} \frac{P_c}{n_{\text{vials}}} \quad (3.11)$$

with $\dot{m}_{\text{sub,chok,dryer}}$ the maximum sublimation rate avoiding choked flow at dryer level (kg/s), r_d the equivalent radius corresponding with the most narrow lumen at the valve connecting the drying chamber and condenser (m) and n_{vials} the theoretical maximum number of vials that can fit in the drying chamber of the freeze-dryer (1,140). Here, r_d is defined for the used equipment, equipped with a butterfly valve. For other types of equipment, r_d can be defined as the radius of the duct connecting drying chamber and condenser itself.

3.2.2 Uncertainty analysis

The UA on the freeze-drying model leading to the dynamic Design Space was conducted using the sampling-based approach [22]. For this method, the model is run for different combinations of input variables and process parameters, based on their uncertainty range. Next, the uncertainty on the model output is estimated from the predictions at these sample points. The input matrix containing 10,000 samples (i.e., the sampling scheme) was constructed using the Sobol sampling technique [23].

The UA was conducted for 8 factors that were considered to be uncertain. $T_{i,\text{crit}}$ was assumed to be equal to T'_g of the model formulation. In general, T'_g is a few degrees lower than T_c , the temperature at which collapse actually occurs. This should provide a sufficient safety margin to avoid cake collapse. For this reason, $T_{i,\text{crit}}$ was not considered as one of the uncertain factors. The uncertainty levels for each factor are given in table 3.2. For

most factors, the uncertainty was not implemented as a percentage of the nominal value as the range is highly dependent on the magnitude of the factor. For these factors (i.e., T_s , P_c , $r_{v,i}$ and $r_{v,o}$), the uncertainty was defined by an absolute range, based on experimental data or data provided by the supplier.

Table 3.2: Uncertainty level for the input factors of the UA

Factor	Uncertainty level	Reason of inclusion in UA
L_{dried}	-	Error propagation
R_p	20%	Based on experimental data
K_v	5%	Based on experimental data
$r_{v,i}$	10^{-4} m	Process variable with inherent error
$r_{v,o}$	10^{-4} m	Process variable with inherent error
V	1%	Process variable with inherent error
T_s	2.5-10 °C	Based on experimental data
P_c	1 Pa	Process variable with inherent error

L_{dried} was calculated for each time step throughout the process, based on the other (uncertain) model input variables. Therefore, there is uncertainty about the exact value of this state variable due to the uncertainty of the initial conditions and the model parameters. In addition, the uncertainty on L_{dried} increases throughout the simulation due to the accumulation of error in the previous steps. The uncertainty level was determined by calculating the standard deviation on a fixed number of samples, i.e., 1,000 samples, by varying the values of the model parameters within their specified ranges.

K_v is described in function of P_c via equation 3.4. R_p is described in function of L_{dried} via equation 3.5. The uncertainty on these coefficients is lumped by introducing an uncertainty on the entire parameter, i.e., R_p and K_v . The uncertainty on the inner and outer radius of the vials, $r_{v,i}$ and $r_{v,o}$, is based on data provided by the supplier of the 10R vials (Schott AG, Mainz, Germany). The filling volume V was included in the analysis because of the inherent error during the filling stage. The error on P_c is based on the maximum allowed deviation of the feedback pressure control system.

Depending on the location of the vial on the shelf, T_s can be somewhat higher or lower than the set value. This error has been experimentally determined for both a constant value of T_s and during a shelf temperature ramp. The uncertainty level for T_s is based on

these preliminary experiments. When T_s is kept constant, the uncertainty level on T_s is fixed at 2.5°C . During a shelf temperature ramp, it was revealed that T_s reaches the set value with a delay due to thermal inertia of the shelves, leading to a broadening of the uncertainty range. When T_s is set to increase, the upper uncertainty level remains fixed at 2.5°C , while the lower level linearly increases from 2.5°C until a maximum of 10°C at the same rate as the temperature ramp (Figure 3.1). The lower limit remains 10°C as long as T_s increases, until the set value is reached and the uncertainty on T_s gradually vanishes within 15 minutes. Vice versa, when T_s is set to decrease, the lower level of the uncertainty range remains constant while the upper level increases.

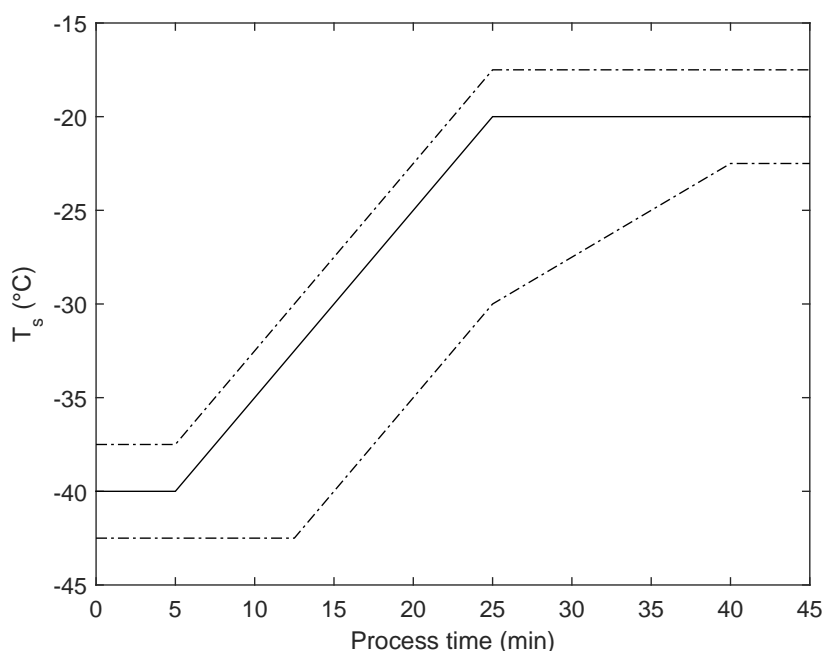


Figure 3.1: Illustration of the uncertainty on the shelf fluid inlet temperature T_s during temperature ramp: set value of T_s (Solid line) with uncertainty levels (Dash dotted line) in function of process time

3.2.3 Determination of the vial heat transfer coefficient

K_v was determined via a gravimetric method [19]. A total of 100 type I glass vials, each filled with 2.5 mL of deionized water, were placed on the precooled shelves (3°C) in the drying chamber. The shelves were further cooled until -45°C at a rate of $1^\circ\text{C}/\text{min}$. This

temperature was maintained for 1 hour. Next, the pressure was lowered until the desired value, after which the temperature was linearly increased until $-20\text{ }^{\circ}\text{C}$ in 25 minutes. After 6 hours of primary drying, ice sublimation was interrupted by aerating the drying chamber with dry nitrogen and subsequently closing the vials. Each individual vial was weighed before and after primary drying. The value of K_v changes in function of P_c , therefore, this cycle was repeated at six different pressure levels: 5, 10, 15, 20, 25 and 30 Pa. Type-K thermocouples (Conrad Electronic, Hirschau, Germany) were placed inside four different vials, which were randomly distributed at the border and the centre of the batch, against the bottom in the centre of the vial, to monitor the ice temperature during primary drying [24].

K_v was calculated at each pressure level according to equation 3.12 [8]:

$$K_v = \frac{\Delta m \Delta H_s}{\Delta t (T_s - T_b) A_v M} \quad (3.12)$$

with Δm the mass of sublimed ice (kg), Δt the primary drying time interval (s) and T_b the ice temperature at the bottom of the vial (K). For each pressure level, equation 3.12 was fitted to the value of K_v via non-linear regression to obtain these coefficients.

Because of the difference in radiation energy coming from the surrounding walls, discrimination was made between vials situated in the centre and at the edge of the batch. The first group consisted of vials which were at all four sides surrounded by other vials (centre vials). The second group consisted of vials situated at the edge of the shelf, with at least one side directed towards the door or the walls of the drying chamber (edge vials). The parameters α , β and γ describing K_v in function of P_c , were determined separately for both groups. This implies that K_v combines both the radiative and conductive energy transfer. The total energy transfer to the edge vials is higher compared to the centre vials (Section 3.3.1), which is associated with a higher risk of cake collapse for the vials situated at the border of the batch. Because they are the limiting factor, α , β and γ for the edge vials were selected as input variables for the freeze-drying model to compute the dynamic Design Space.

3.2.4 Determination of the critical product temperature

$T_{i,crit}$ of the model formulation was determined via MDSC using a differential scanning calorimeter Q2000 (TA instruments, New Castle, DE, USA). Hermetically sealed aluminum pans (TA instruments, New Castle, DE, USA) were filled with approximately 12 mg of the

model formulation, containing 30 mg/mL sucrose. The DSC cell was constantly purged with dry nitrogen at a flow rate of 50 mL/min. Initially, the sample was rapidly cooled until -90°C . This temperature was maintained for 5 minutes. Subsequently the temperature was linearly increased until 0°C at a heating rate of $2^{\circ}\text{C}/\text{min}$. The modulation amplitude and period were set at 0.212°C and 40 seconds, respectively. The analysis was performed in triplicate. The thermograms were analyzed with TA Instruments Universal Analysis 2000 version 4.7A (TA Instruments, New Castle, DE, USA).

3.2.5 Experimental verification of the dynamic Design Space

Four experimental runs were conducted to verify the dynamic Design Space for the model formulation under study. The settings of the adaptable process parameters T_s and P_c were computed for different RoF acceptance levels (1%, 25%, 50% and 99%). The RoF acceptance level is defined as the chance of batch rejection due to macroscopic cake collapse in one or more vials. The experiments were conducted in a laboratory scale freeze-dryer Lyobeta 25 (Telstar, Terrassa, Spain) equipped with four shelves, each with a heatable area of 0.16 m^2 , in the vacuum-tight drying chamber with a volume of 0.2 m^3 . The system contains a condenser with 35 kg of ice capacity and a vacuum pump to evacuate the drying chamber. Chamber pressure control was performed via a Baratron Type 626A capacitance manometer (MKS Instruments, Andover, MA, USA). Comparative pressure measurements were conducted using a Pirani Type PSG-502-S thermal conductivity gauge (Inficon, Bad Ragaz, Switzerland). Temperature control of shelf and condenser was based on Pt100 thermal sensors (WIKA Instruments, Klingenberg, Germany) measurements.

The freezing step for each verification run was identical to the freezing procedure used to determine R_p of the model formulation [21]. A total of 100 glass vials, each filled with 2.5 mL of the model formulation, was placed on the precooled shelves (3°C) in the drying chamber. The shelves were chilled at a rate of $1^{\circ}\text{C}/\text{min}$ until -45°C . This temperature was maintained for 1 hour. An annealing step was included in the freezing procedure, during which T_s was increased in 25 minutes until -20°C and kept at this value for 2 hours. After re-establishing the final freezing temperature of -45°C at a rate of $1^{\circ}\text{C}/\text{min}$, T_s was kept for another hour at this value, before the condenser was cooled and the vacuum pump was activated. The primary drying settings were characteristic for each verification run and the corresponding RoF acceptance level. When the endpoint of primary drying was detected, secondary drying was conducted at 20°C , after ramping the temperature at $1^{\circ}\text{C}/\text{min}$ starting from the final T_s at the end of primary drying. The value of P_c during

secondary drying was kept equal to the one during primary drying. At the end of each run, the vials were stoppered under a controlled nitrogen atmosphere.

The dynamic Design Space was computed based on the coefficients describing K_v for the edge vials (Table 3.1). As compensation for the slower sublimation rate in the centre vials (Section 3.3.1), the primary drying phase of each verification run was prolonged by maintaining the final optimal combination of T_s and P_c for a few additional hours, on top of the predicted dynamic primary drying trajectory for the edge vials. The total drying time for the complete batch, including the centre vials, was predicted based on the coefficients describing K_v for these centre vials. The computed optimal dynamic settings of T_s and P_c were used as input for the primary drying model to calculate the sublimation rate \dot{m}_{sub} using equation 3.7. The nominal values of the input parameters (Table 3.1) and uncertainty levels (Table 3.2) required for the calculation of the total primary drying time were equal to the ones used for the calculation of the dynamic Design Space, with the coefficients describing K_v for the centre vials instead of the edge vials. The propagation of errors on L_{dried} was not included for the computation of the total drying time, as the primary drying endpoint was based upon complete sublimation of the ice mass instead of correlating L_{dried} with the total layer thickness to avoid an overestimation of the drying time. For each verification run, the primary drying endpoint was computed with a certainty of 99% based on the uncertainty level of each parameter, as illustrated in figure 3.2, ensuring the batch is completely dry.

The end of primary drying was detected based on the ratio of the Pirani thermal conductivity gauge and the Baratron capacitance manometer. The capacitance manometer measures the absolute pressure, while the relative pressure measurement of the thermal conductivity gauge changes with the gas composition in the drying chamber. The gas composition changes from mainly water vapour during primary drying to mostly nitrogen towards the end of primary drying, when ice sublimation is complete. Primary drying was considered finished at the midpoint of the drop in Pirani pressure [25]. As this comparative pressure measurement method monitors the entire batch, the endpoint is only reached when the last vials of the batch are dry.

T_i was constantly monitored via thermocouples in contact with the bottom of the vials, to evaluate whether $T_{i,\text{crit}}$ was exceeded during primary drying or not. Vials situated in the centre and at the edge of the batch were monitored, which allowed the comparison in drying behaviour between these two positions. After freeze-drying, the cake appearance of each vial was visually evaluated to look for signs of macroscopic collapse. Slight shrinkage

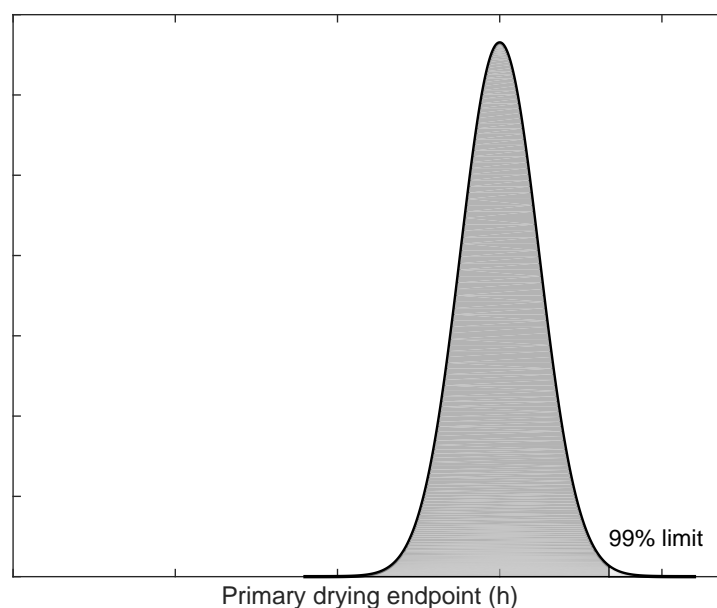


Figure 3.2: Illustration of the computation of the primary drying endpoint with a certainty of 99%

of the cake was attributed to the amorphous characteristics of the sucrose formulation and was not considered as macroscopic collapse [26].

3.3 Results

3.3.1 Experimental determination of the vial heat transfer coefficient

K_v as function of P_c is displayed in figure 3.3. Higher values of P_c are associated with a significant increase in K_v , as reported before [9, 19, 27]. Sub-optimal contact between the stainless steel shelf and the bottom of the glass vials leads to an enhanced conductive heat flux for an increased gas molecule density between both surfaces. Furthermore, K_v is higher for vials situated at the edge of the batch due to the significantly higher contribution of radiation energy coming from the surroundings, compared to vials in the centre of the batch [9, 19, 27]. Therefore, discrimination was made between these two groups of vials. The relation between K_v and P_c is described by equation 3.4. For both groups of vials, non-linear regression was applied to fit equation 3.4 to the data, resulting in the parameters describing K_v as function of P_c . For the centre vials, $\alpha = 6.11 \text{ J}/(\text{m}^2\text{sK})$ (95% CI [5.21,7.01]), $\beta =$

1.54 J/(m²sKPa) ([1.31,1.78]) and $\gamma = 0.046$ 1/Pa ([0.037,0.055]) were obtained. For the edge vials, $\alpha = 11.16$ J/(m²sK) (95% CI [10.16,12.16]), $\beta = 1.44$ J/(m²sKPa) ([1.20,1.69]) and $\gamma = 0.040$ 1/Pa ([0.031,0.050]) were obtained. As the edge vials receive additional radiation energy, the risk of cake collapse is higher in these vials compared to the centre vials. For this reason, the parameters describing K_v as function of P_c for the edge vials were selected as input factors for the mechanistic model. Consequently, the predicted drying time will be underestimated for the centre vials. To assure primary drying is finished for all vials, the total drying time was prolonged by maintaining the final optimal combination of T_s and P_c for a few additional hours on top of the optimal dynamic trajectory for the edge vials, based on the coefficients describing K_v for these centre vials (Section 3.3.4).

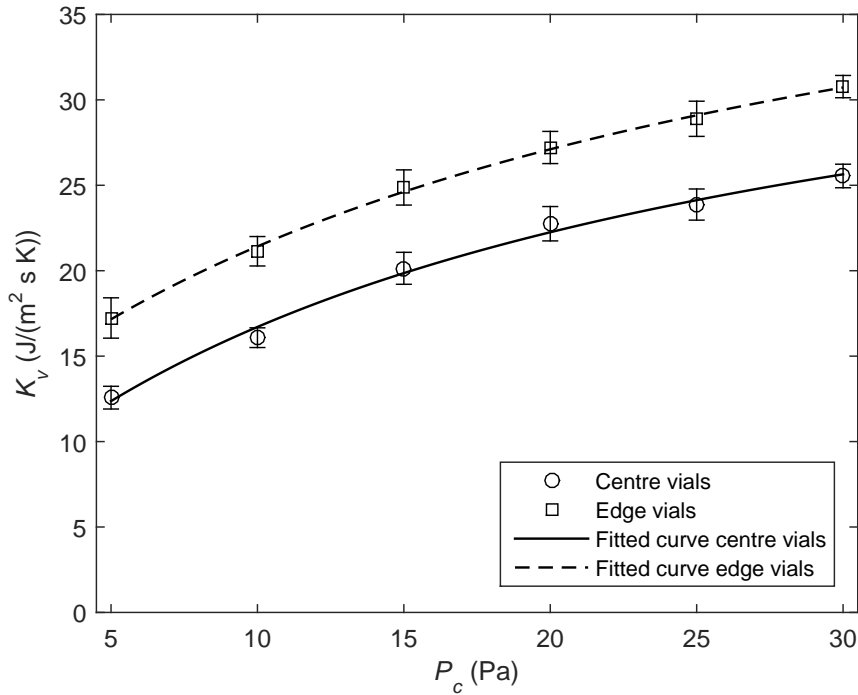


Figure 3.3: Vial heat transfer coefficient K_v plotted as function of chamber pressure P_c for edge (Squares) and centre vials (Circles)

3.3.2 Dynamic Design Space for Risk of Failure of 1%

The procedure to determine the optimal combination of P_c and T_s is presented in figure 3.4. The coloured rectangle in the figures represents the grid used at the current time step. The full range of P_c is explored, while the range for T_s is based on the maximum temperature

ramp which can be obtained by the shelves of the freeze-dryer. As the time step is small at the start of the calculations, the range of T_s is also small. With the increase of the time step throughout the simulation, the width of the range of T_s also increases. On the left side of the figure, the calculated sublimation rate \dot{m}_{sub} is given for each combination of P_c and T_s in the explored range. In the figure in the centre, the product temperature T_i is plotted, while the black line indicates $T_{i,crit}$. Below this black line the critical value is not exceeded. The right part of figure 3.4 indicates for which P_c - T_s -combinations the choked flow criterion is exceeded, both at vial and dryer-level, which is never the case here. After determining the optimal combination of T_s and P_c , which is indicated with a black dot in the left figure, the uncertainty level on L_{dried} is calculated using an UA.

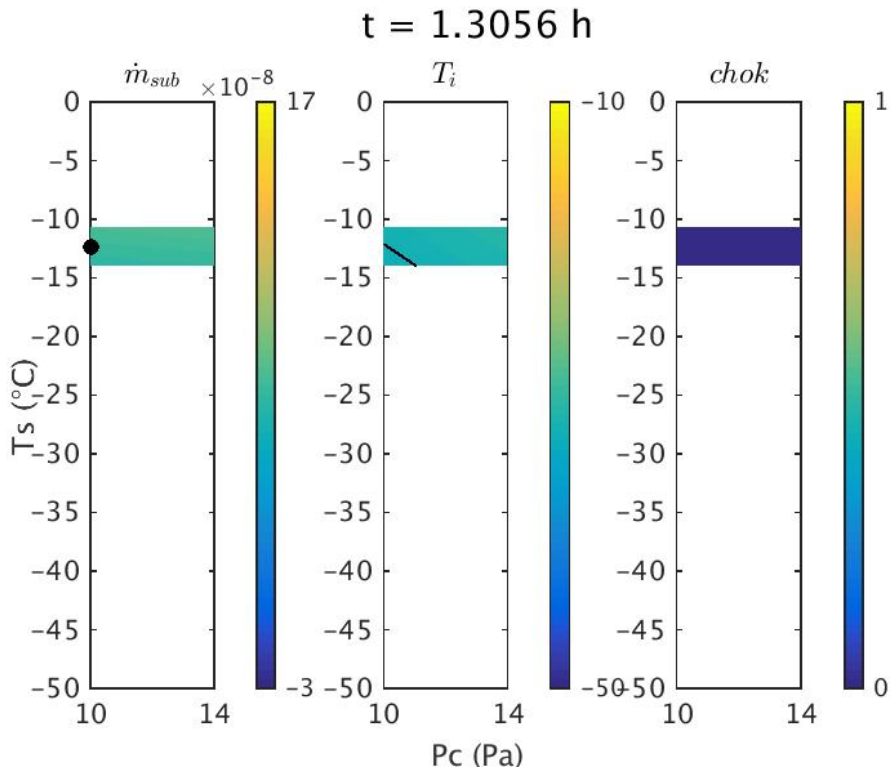


Figure 3.4: Determination of the optimal values for chamber pressure P_c and shelf fluid inlet temperature T_s (e.g., at $t = 1.31$ h): In the left figure, \dot{m}_{sub} is plotted for each combination of P_c and T_s where the optimal $T_s P_c$ combination is indicated with a black dot. In the middle figure, T_i is plotted for each combination of P_c and T_s with the black line indicating $T_{i,crit}$; below this line $T_{i,crit}$ is not exceeded. In the right figure, the choked flow criterion is evaluated: the result is either 0, i.e., not exceeding the limit, or 1, i.e., exceeding the limit.

The evolution of L_{dried} for an RoF of 1% is given in figure 3.5. Initially, P_c is equal to the ambient pressure, the condition used during the freezing step. At this high pressure, the sublimation rate is zero and L_{dried} remains at zero, until P_c becomes lower than the ice vapour pressure and sublimation starts. Later on, during primary drying, the increase in L_{dried} is almost linear.

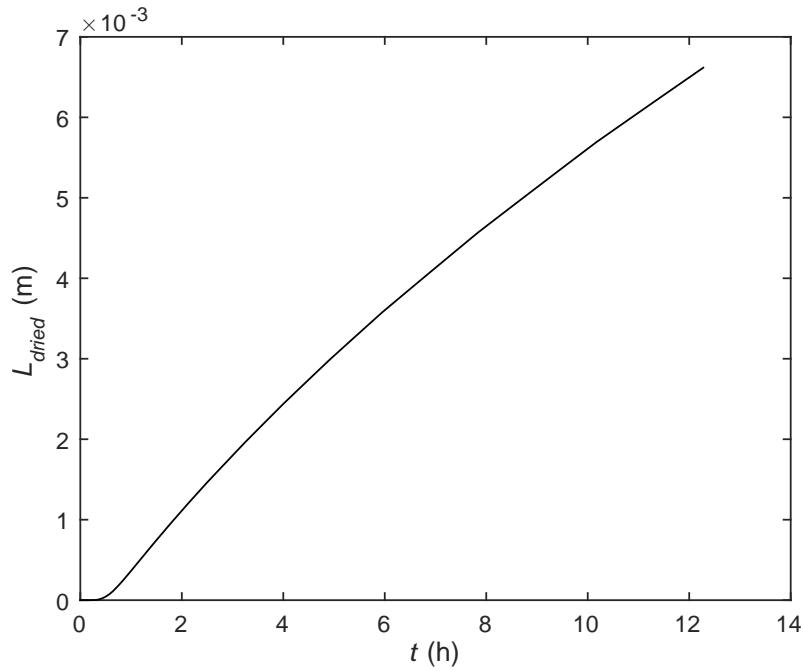


Figure 3.5: Evolution of dried layer thickness L_{dried} for an RoF acceptance level of 1%

In figure 3.6, the optimal values for T_s and P_c are presented. Initially, T_s equals -45°C , the temperature used during the freezing step. As soon as sublimation starts, the optimal value of T_s increases at the maximum rate which can be obtained by the freeze-dryer. After approximately 1 h, the optimal value starts to decrease again due to the limitation of $T_{i,crit}$. P_c is lowered at the start of primary drying and, after reaching vacuum conditions, the optimal value is hardly ever changing.

In figure 3.7 the uncertainty level on L_{dried} ($S_{L_{dried}}$ is plotted in function of L_{dried} . The increase of the uncertainty on L_{dried} with the drying time is obvious, i.e. the error is based on deviations in the previous steps, which leads to a cumulative effect: error propagation.

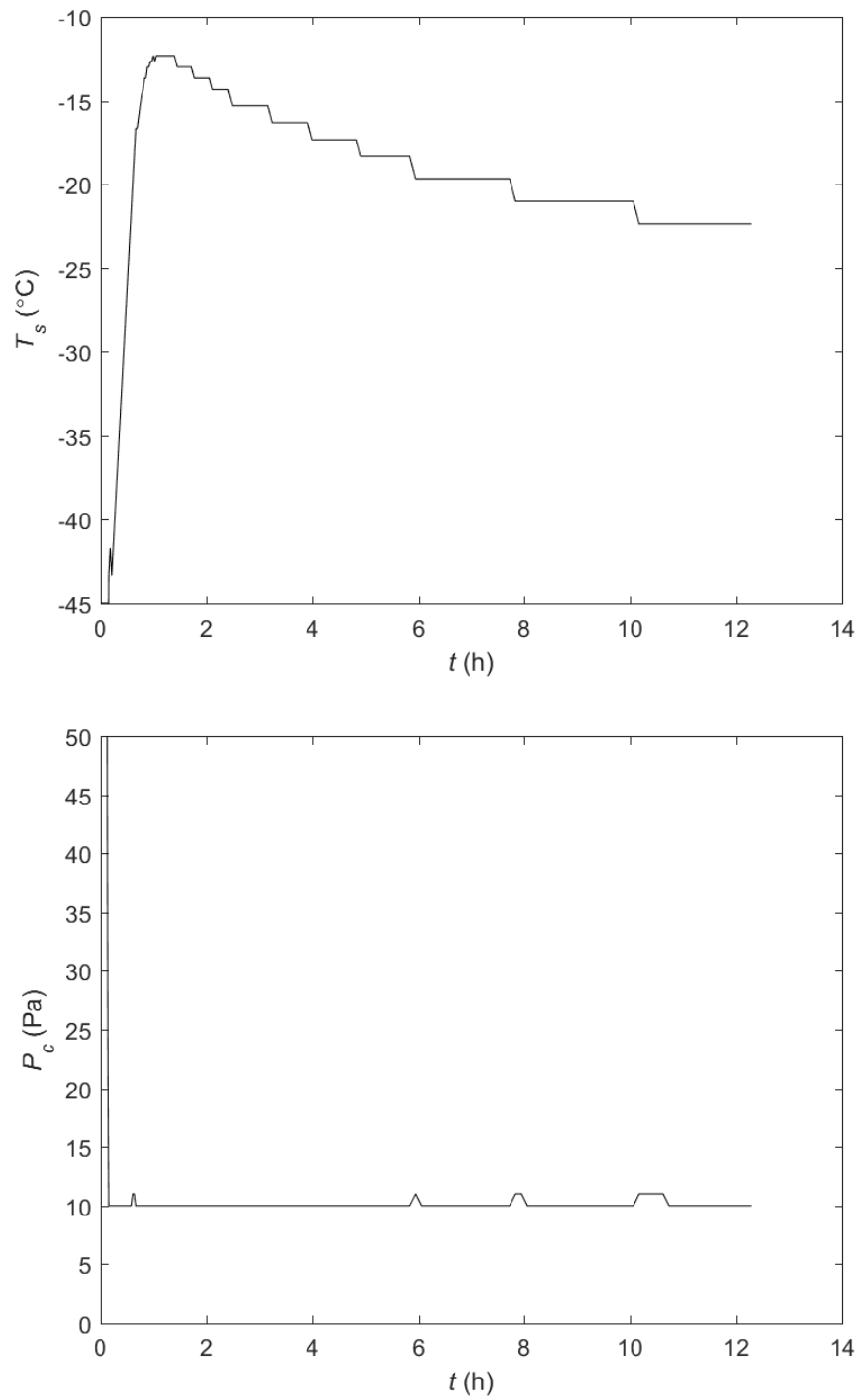


Figure 3.6: Optimal values for shelf fluid inlet temperature T_s (Top) and chamber pressure P_c (Bottom) for an RoF acceptance level of 1%

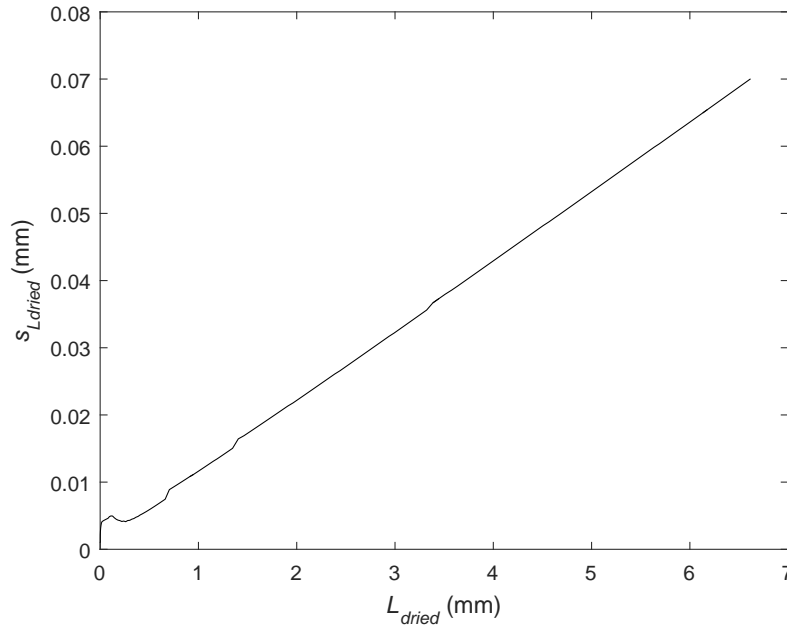


Figure 3.7: Uncertainty level on dried layer thickness L_{dried} ($S_{L_{dried}}$) for an RoF acceptance level of 1%

Figure 3.8 presents the uncertainty level on T_s which is asymmetric. When the T_s is increasing, i.e. the first 1 h, the actual value runs behind due to thermal inertia of the shelves, and therefore, the uncertainty is higher at the lower boundary compared to the upper boundary. The opposite is true when the temperature starts to decrease, i.e., after 1 h.

3.3.3 Comparison of dynamic Design Space for different Risk of Failure levels

In the top part of figure 3.9, T_s is plotted in function of t for four different RoF acceptance levels. A higher RoF allows the use of less conservative settings, therefore, T_s is obviously higher compared to lower RoF levels. The difference in the maximum value of T_s is around 17°C between an RoF-value of 99% and 50%. Between 1% and 99% this difference is about 29°C . The corresponding evolution of T_i is given in the right part of figure 3.9. It is obvious that T_i is higher for higher RoF levels. When the RoF-value is higher than 50%, the chance that $T_{i,crit}$ is exceeded is higher than 50%. Therefore, $T_{i,crit}$ is evolving after the start-up phase towards the nominal value of the T_i , i.e., -32.5° when the RoF is 50%. For an RoF of 99%, T_i is evolving towards -30° , which is higher than $T_{i,crit}$. For an RoF of 1% and 25%, T_i is evolving to respectively -34.5° and -33° , both lower than $T_{i,crit}$.

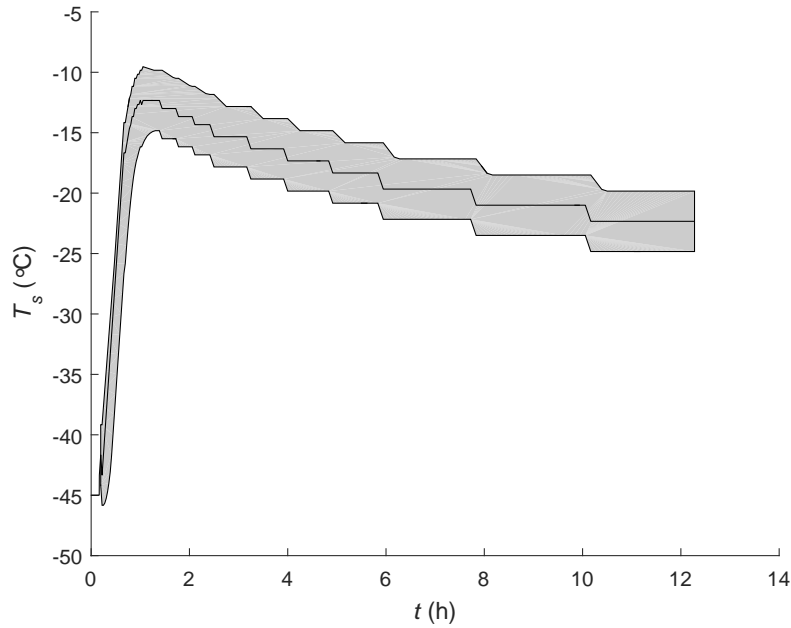


Figure 3.8: Uncertainty level on shelf fluid inlet temperature T_s for an RoF acceptance level of 1% for the model formulation

The difference in P_c for different values of RoF is negligible (Figure 3.10). At the start, P_c is decreasing to vacuum conditions, while an increase is noted after around 0.6 h. This increase is higher for a higher RoF level. It is clear that the total value of t is larger when the RoF is lower. The computed drying time for the edge vials is 12.28 h, 9.97 h, 9.05 h and 6.67 h for an RoF of 1%, 25%, 50% and 99%, respectively. It has to be remarked that these drying times are computed based on the coefficients describing K_v for the edge vials. As compensation, the total drying time for the complete batch is prolonged by maintaining the final optimal combination of T_s and P_c for a few additional hours on top of the optimal dynamic trajectory for the edge vials as calculated based on the coefficients describing K_v for the centre vials (Section 3.3.4).

3.3.4 Experimental verification of the dynamic Design Space

In figure 3.11, the monitored T_i is plotted in function of t for an RoF acceptance level of 1%, 25%, 50% and 99%, while the horizontal line represents $T_{i,crit}$. Immediately after introducing the vacuum, T_i was very low (below -40 °C). With the progress of drying, L_{dried} and R_p simultaneously started to increase. Consequently, the mass transfer of water vapour

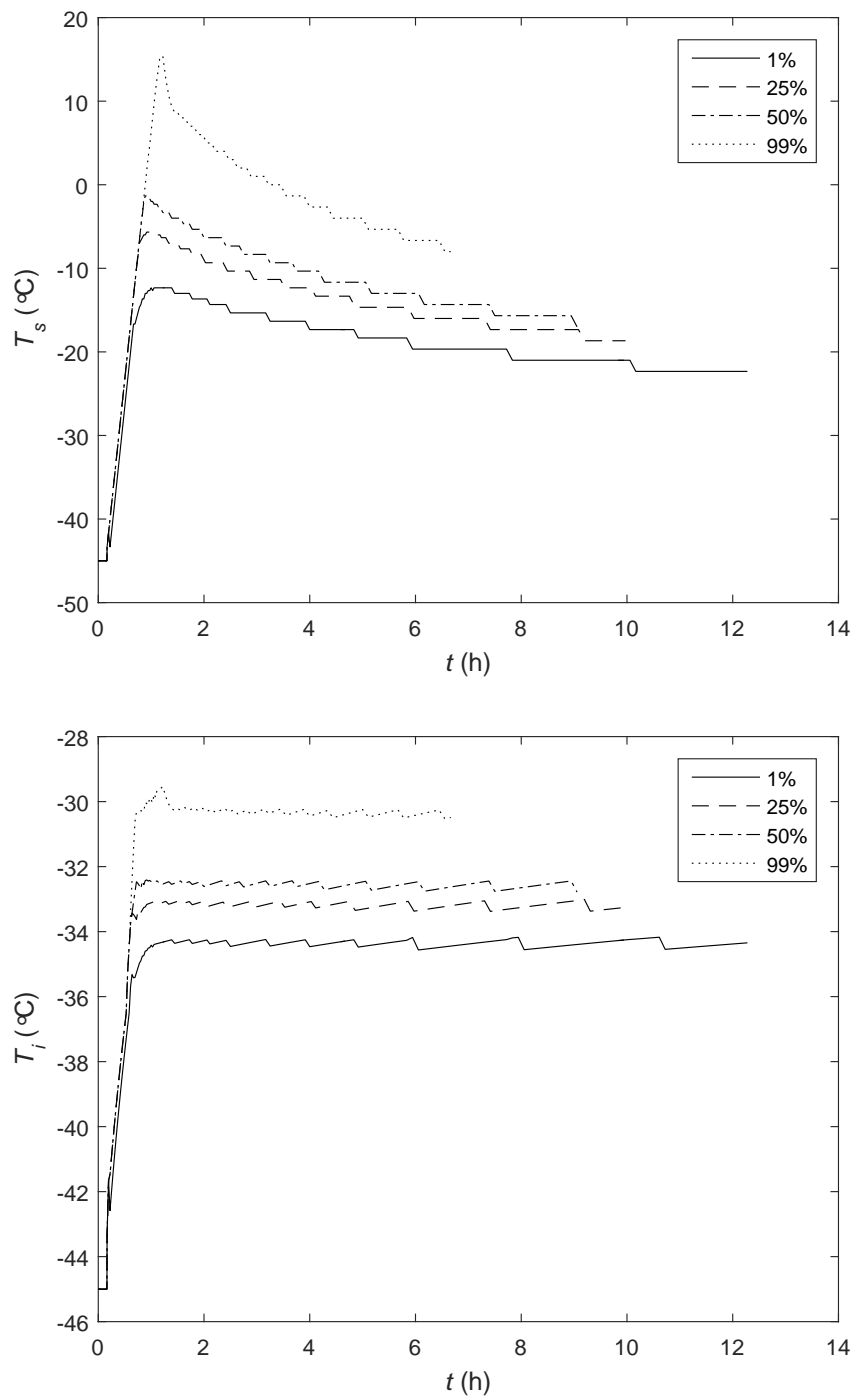


Figure 3.9: Optimal values for shelf fluid inlet temperature T_s (Top) and the evolution of the product temperature at the sublimation front T_i (Bottom) for an RoF acceptance level of 1%, 25%, 50% and 99%

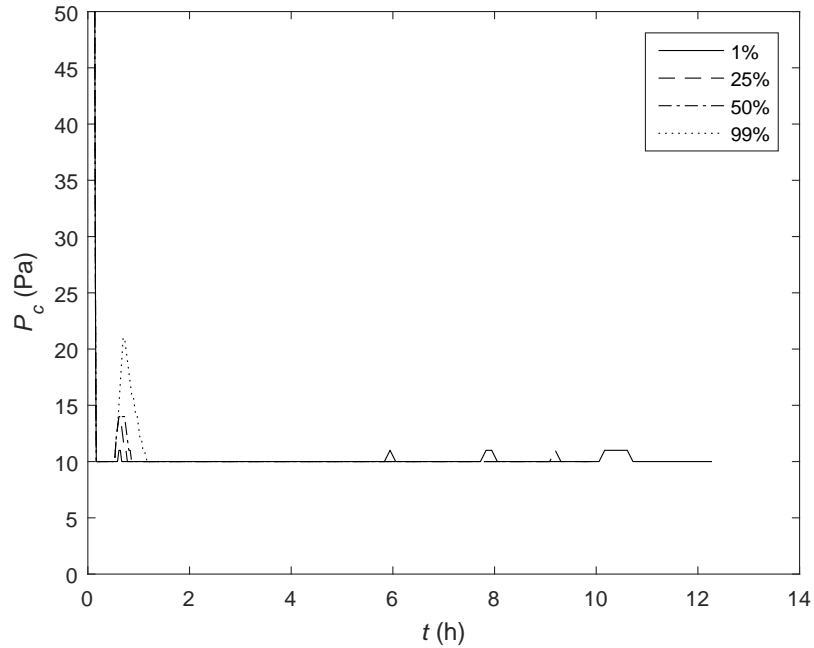


Figure 3.10: Optimal values for chamber pressure P_c for an RoF acceptance level of 1%, 25%, 50% and 99%

through the dried layer got more obstructed, associated with a local pressure rise at the sublimation front and, hence, an increase in T_i , eventually leading to a gradual limitation of T_s . T_i was measured at the bottom of the vial, while there is a (small) temperature gradient across the frozen product layer between the sublimation front and the bottom of the vial. In general, the temperature measured at the bottom of the vial is slightly higher compared to the sublimation front. As the sublimation interface gradually moved downwards during primary drying, this temperature gradient became smaller, which might explain the gradual decrease in T_i . This observed decrease is mostly relevant for the more aggressive cycles with a higher RoF. Therefore, this feature might be linked to the occurrence of collapse at the ice-dried product interface due to the exceedance of $T_{i,crit}$. The increased pore size in the dried product layer might reduce R_p and in turn T_i [28, 29]. Near the end of primary drying, when the ice in contact with the thermocouple was completely sublimated, T_i increased drastically, as more energy was transferred to the vial than was removed via ice sublimation.

The measured value of T_i was obviously higher with the increase in RoF acceptance level (Figure 3.11), as T_s was set at a higher (mean) value for each corresponding verification run

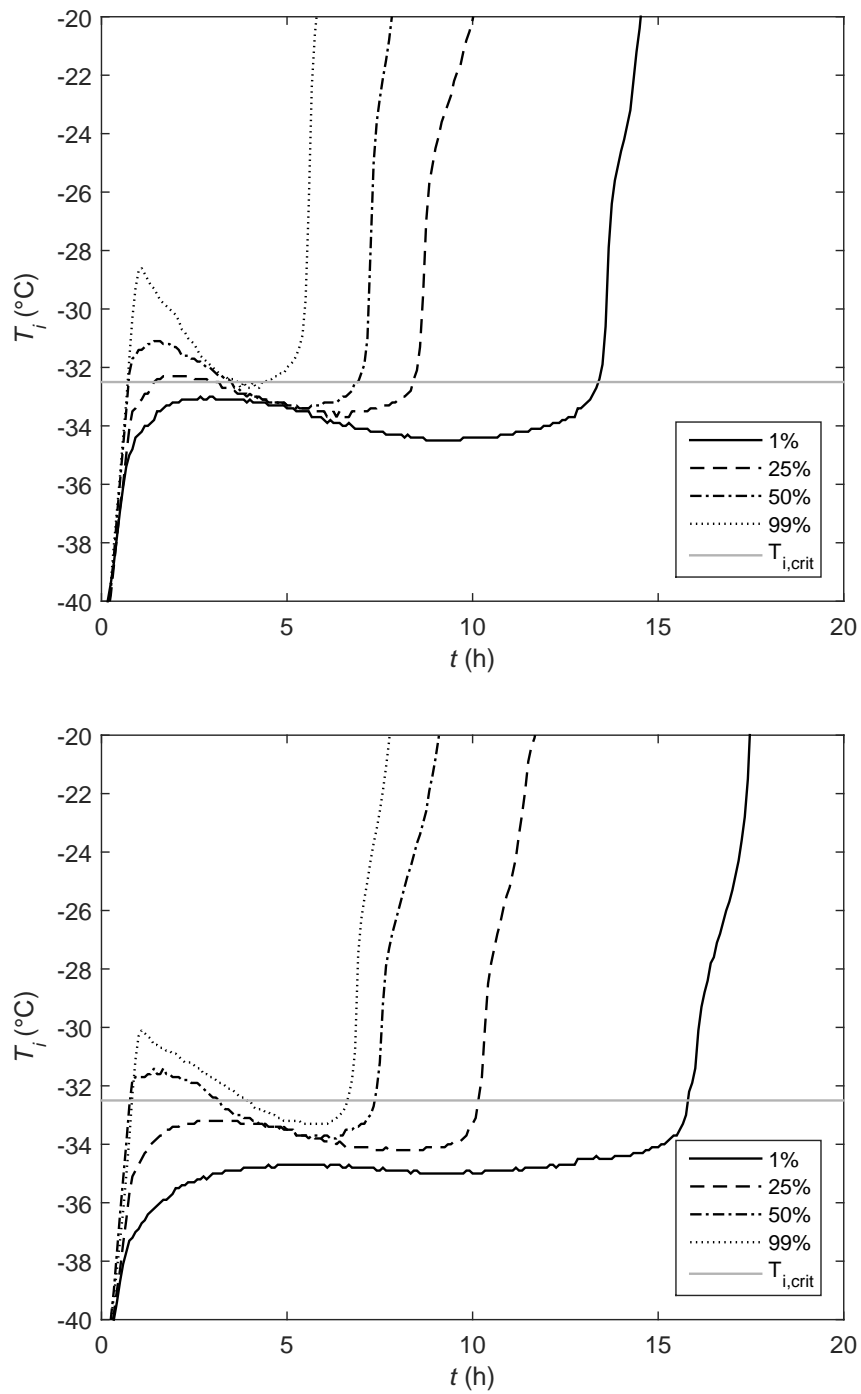


Figure 3.11: Experimental product temperature at the sublimation front T_i for an RoF acceptance level of 1%, 25%, 50% and 99% and the critical product temperature $T_{i,crit}$ for an edge (Top) and centre (Bottom) vial

(Figure 3.9). T_i was also higher for edge vials compared to centre vials during the same RoF verification run, due to the additional radiation energy originating from the surroundings received by the edge vials (Section 3.3.1). During the experimental verification run based on an RoF acceptance level of 50% and 99%, T_i exceeds $T_{i,crit}$ in both the edge and centre vials. For an RoF of 25%, T_i remains below $T_{i,crit}$ in the centre vials, while T_i is slightly above $T_{i,crit}$ in the edge vials. For an RoF of 1%, T_i remains below $T_{i,crit}$ in both the edge and centre vials. These temperature data can be related to the resulting cake appearance after each verification run. Macroscopic cake collapse was observed in a significant part of the batch for an RoF acceptance level of 50% and 99%, as $T_{i,crit}$ was greatly exceeded during primary drying (Figure 3.12). The degree of collapse was more severe for a higher RoF. The majority of the vials where loss of structure occurred, was situated at the edge of the batch, due to the additional energy transfer (Section 3.3.1). The vials obtained during the verification run with an RoF of 25% did not show any sign of (macroscopic) collapse. Despite (just) exceeding $T_{i,crit}$ in the edge vials, T_i remained below T_c . $T_{i,crit}$ was assumed to be equal to T'_g of the model formulation (Section 3.2.2). Because the viscosity near T'_g is sufficiently high to prevent viscous flow, no macroscopic collapse was observed. $T_{i,crit}$ was never exceeded during the verification run for an RoF of 1%. Logically, an acceptable cake appearance was obtained at the end of this run (Figure 3.12). Due to the amorphous characteristics of the product, partial cake shrinkage of approximately 10% was observed for all non-collapsed vials in the batch.

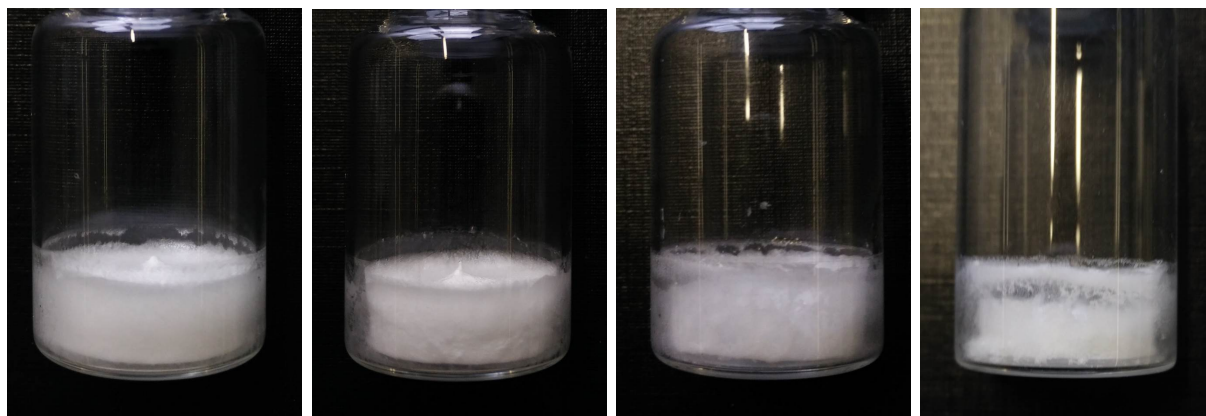


Figure 3.12: Cakes yielded after experimental verification runs for RoF of 1% (Left), 25% (Middle left), 50% (Middle right) and 99% (Right)

For each RoF acceptance level, the computed primary drying endpoint with a certainty of 99%, based on the coefficients describing K_v for the centre vials, is listed in table 3.3. These predictions are in accordance with the experimentally determined primary drying

endpoint, determined via the ratio of the relative and absolute pressure measurement. For each RoF acceptance level, the experimental endpoint was situated below the computed limit, indicating that primary drying was finished before the shelf temperature ramp to secondary drying was started.

Table 3.3: The experimentally determined primary drying time for the centre vials for different RoF acceptance levels compared with the computed primary drying endpoint with 99% certainty

Risk of Failure	Computed primary drying endpoint (h)	Experimental value (h)
1%	17.61	16.83
25%	14.19	13.59
50%	12.61	11.72
99%	9.22	9.09

3.4 Discussion

Conventionally, the primary drying step of a freeze-drying process is characterized by fixed settings for the adaptable process parameters T_s and P_c . These suboptimal process conditions lead to the prolongation of the primary drying time, associated with an increase in production costs and inefficient usage of the equipment. Alternatively, mechanistic modelling is a cost-effective and efficient approach for the development and optimization of freeze-drying cycles, via the construction of the Design Space for the primary drying step. Because some model input variables change with the primary drying progress, e.g. the gradual increase in L_{dried} corresponds to an increase in R_p (Section 3.1), the optimal combination of T_s and P_c also changes throughout the process. Instead of a static Design Space, this leads to the construction of a dynamic Design Space, associated with an increased processing efficiency. Because model input variables and process parameters are often an estimation of the real value and due to the fact that several assumptions and resulting simplifications were included in the model, an UA was conducted to quantitatively estimate the risk of cake collapse for each combination of the adaptable process parameters T_s and P_c in the dynamic Design Space. In addition, experimental verification of the Design Space is required before conclusions can be drawn with the final aim of implementing the Design Space in production processes.

The experimental run based on the nominal values of the input parameters (i.e., RoF of 50%) led to cake collapse in a significant number of vials, mainly situated at the edge of the batch, which would in practice lead to rejection of the complete batch. This observation indicates the necessity of including the parameter uncertainty during Design Space construction via the UA. The nominal values of the input variables are often associated with a certain degree of uncertainty. For instance, R_p is characterized by one global set of coefficients describing R_p in function of L_{dried} . However, this parameter is inherently associated with a high inter-vial variability due to the stochastic nature of ice nucleation leading to differences in ice crystal size, which is linked to the final pore size in the dried product [3]. As the pore size impacts the mass flow dynamics through the dried layer, R_p is subject to an immense vial-to-vial variability [30]. The inclusion of an annealing step improves the inter-vial homogeneity in pore size [31]. However, an assessment of the uncertainty on R_p is still required, as indicated during the experimental verification of the dynamic Design Space.

The observation that cake collapse mainly occurred in the vials situated at the edge of the batch was attributed to the additional radiation energy transfer to these vials (Section 3.3.1). As K_v is highly different between the edge and centre vials [9, 19, 27], which is inherent to the design of the freeze-dryer, a global value for the quantification of K_v for the whole batch would be associated with a very high uncertainty for each individual vial. This issue was addressed by dividing the batch in two groups, based on whether radiation from the surroundings contributed to the energy transfer or not (Section 3.2.3). This way, the uncertainty on K_v was reduced as within each individual group the variability was much smaller. However, due to local differences in energy transfer to the individual vials of each group depending on the location of the vial in the drying chamber, the shape of the vial bottom and temperature differences across the shelves, K_v should still be included in the UA. In addition, the inherent inter-vial variability in both R_p and K_v also yields a potential increased variability in final product quality, which however is difficult to avoid due to the design of the equipment.

As the total energy transfer to the edge vials is significantly higher compared to the centre vials, this group was considered for the construction of the dynamic Design Space, while the centre vials were the limiting factor regarding the computation of the primary drying endpoint. The endpoint of primary drying was experimentally verified based on the pressure ratio measurement between a Pirani gauge and a capacitance manometer. To avoid the introduction of secondary drying before primary drying is finished, the one-sided 97.5%

confidence limit is considered as the most relevant and safe parameter in estimating the primary drying endpoint. An even better approach, which would fit the PAT initiative issued by the FDA, would be to monitor the pressure ratio real-time and in-line and to start the secondary drying ramp-up when a predefined threshold value is reached [32].

The parameters which should be included in the UA and their respective uncertainty level should be considered very carefully, as they impact the Design Space [9]. Preferably, the uncertainty level is based on experimental data, e.g., T_s , K_v , $r_{v,i}$ or $r_{v,o}$. In case experiments do not give an indication about the degree of uncertainty, the uncertainty level should be estimated based on expert knowledge. This estimation should be conservative, associated with rather broad uncertainty levels, otherwise this could lead to collapse of the product, even for very low risk of failure acceptance levels.

3.5 General conclusion

The dynamic Design Space for the primary drying step of the freeze-drying process was constructed, allowing the determination of the optimal combination of the adaptable process parameters T_s and P_c in function of the primary drying time. The inclusion of the UA extended with the error propagation, lead to the quantification and control of the risk of cake collapse and rejection of the batch. The dynamic Design Space was verified with experimental data for different risk of failure acceptance levels. The experimental run based on the nominal values of the input variables (i.e., RoF of 50%) resulted in cake collapse for a significant part of the batch. An acceptable cake appearance was only obtained for a minimum risk of failure acceptance level of 25%. This study demonstrates that the UA is an essential step in the establishment of the dynamic Design Space, with a controlled risk of cake collapse.

Bibliography

- [1] L. X. Yu. Pharmaceutical quality by design: Product and process development, understanding, and control. *Pharm. Dev. Technol.*, 25:781–791, 2008.
- [2] M. J. Pikal. Freeze drying. In *Encyclopedia of pharmaceutical technology*, pages 1299–1326. Marcel Dekker, New York, 2002.
- [3] J. C. Kasper and W. Friess. The freezing step in lyophilization: Physico-chemical fundamentals, freezing methods and consequences on process performance and quality attributes of biopharmaceuticals. *Eur. J. Pharm. Biopharm.*, 78:248–263, 2011.
- [4] D. Fissore, R. Pisano, and A. A. Barresi. Monitoring of the Secondary Drying in Freeze-Drying. *J. Pharm. Sci.*, 100:732–742, 2011.
- [5] R. Pisano, D. Fissore, A. A. Barresi, R. Pisano, D. Fissore, and A. A. Barresi. Quality by Design in the Secondary Drying Step of a Freeze-Drying Process. *Dry. Technol.*, 30:1307–1316, 2012.
- [6] A. Giordano, A. A. Barresi, and D. Fissore. On the use of mathematical models to build the design space for the primary drying phase of a pharmaceutical lyophilization process. *J. Pharm. Sci.*, 100:311–324, 2011.
- [7] L. N. Mockus, T. W. Paul, N. A. Pease, N. J. Harper, P. K. Basu, E. A. Oslos, G. A. Sacha, W. Y. Kuu, L. M. Hardwick, J. J. Karty, M. J. Pikal, E. Hee, M. A. Khan, and S. L. Nail. Quality by design in formulation and process development for a freeze-dried, small molecule parenteral product: a case study. *Pharm. Dev. Technol.*, 16:549–576, 2011.
- [8] D. Fissore, R. Pisano, and A. A. Barresi. Advanced approach to build the design space for the primary drying of a pharmaceutical freeze-drying process. *J. Pharm. Sci.*, 100:4922–4933, 2011.
- [9] S. Mortier, P. J. Van Bockstal, J. Corver, I. Nopens, K. Gernaey, and T. De Beer. Uncertainty analysis as essential step in the establishment of the dynamic Design Space of primary drying during freeze-drying. *Eur. J. Pharm. Biopharm.*, 103:71–83, 2016.
- [10] V. R. Koganti, E. Y. Shalaev, M. R. Berry, T. Osterberg, M. Youssef, D. N. Hiebert, F. A. Kanka, M. Nolan, R. Barrett, G. Scalzo, G. Fitzpatrick, N. Fitzgibbon,

- S. Luthra, and L. Zhang. Investigation of design space for freeze-drying: use of modeling for primary drying segment of a freeze-drying cycle. *AAPS PharmSciTech*, 12:854–861, 2011.
- [11] S. L. Nail and J. A. Searles. Elements of Quality by Design in development and scale-up of freeze-dried parenterals. *BioPharm Int.*, 21:44–52, 2008.
- [12] L. Hardwick, C. Paunicka, and M. Akers. Critical Factors in the Design and Optimisation of Lyophilisation Processes. *IPT*, 26:70–74, 2008.
- [13] S. M. Patel, S. Chaudhuri, and M. J. Pikal. Choked flow and importance of Mach I in freeze-drying process design. *Chem. Eng. Sci.*, 65:5716–5727, 2010.
- [14] S. Bosca, D. Fissore, and M. Demichela. Risk-Based Design of a Freeze-Drying Cycle for Pharmaceuticals. *Ind. Eng. Chem. Res.*, 54:12928–12936, 2015.
- [15] R. Bogner and M. J. Pikal. The Incredible Shrinking Design Space: Using Risk Tolerance to Define Design Space for Primary Drying. *Notes of Freeze Drying of Pharmaceuticals and Biologicals Conference, Garmisch-Partenkirchen*, pages 184–198, 2010.
- [16] D. Fissore, R. Pisano, and A. A. Barresi. On the methods based on the pressure rise test for monitoring a freeze-drying process. *Drying Technol.*, 29:73–90, 2011.
- [17] D. M. Murphy and T. Koop. Review of the vapour pressures of ice and supercooled water for atmospheric applications. *Q. J. R. Meteorol. Soc.*, 131:1539–1565, 2005.
- [18] X. C. Tang, S. L. Nail, and M. J. Pikal. Evaluation of manometric temperature measurement, a process analytical technology tool for freeze-drying: Part II Measurement of dry-layer resistance. *AAPS PharmSciTech*, 7:E77–E84, 2006.
- [19] R. Pisano, D. Fissore, A. A. Barresi, P. Brayard, P. Chouvinc, and B. Woinet. Quality by design: optimization of a freeze-drying cycle via design space in case of heterogeneous drying behavior and influence of the freezing protocol. *Pharm. Dev. Technol.*, 18:280–295, 2013.
- [20] R. Pisano, D. Fissore, and A. A. Barresi. Heat Transfer in Freeze-Drying Apparatus. In *Developments in Heat Transfer*, pages 91–114. InTech, Rijeka, 2011.

- [21] W. Y. Kuu, L. M. Hardwick, and M. J. Akers. Rapid determination of dry layer mass transfer resistance for various pharmaceutical formulations during primary drying using product temperature profiles. *Int. J. Pharm.*, 313:99–113, 2006.
- [22] F. Graziani. *Uncertainty and Sensitivity Analysis for Models of Complex Systems*. Springer, Berlin, 2008.
- [23] I. M. Sobol'. On quasi-Monte Carlo integrations. *Math. Comput. Simulat.*, 47:103–112, 1998.
- [24] S. Nail, S. Tchessalov, E. Shalaev, A. Ganguly, E. Renzi, F. Dimarco, L. Wegiel, S. Ferris, W. Kessler, M. Pikal, G. Sacha, A. Alexeenko, T. N. Thompson, C. Reiter, J. Searles, and P. Coiteux. Recommended Best Practices for Process Monitoring Instrumentation in Pharmaceutical Freeze Drying 2017. *AAPS PharmSciTech*, 18:2379–2393, 2017.
- [25] S. M. Patel, T. Doen, and M. J. Pikal. Determination of end point of primary drying in freeze-drying process control. *AAPS PharmSciTech*, 11:73–84, 2010.
- [26] S. Rambhatla, J.-P. Obert, S. Luthra, C. Bhugra, and M. J. Pikal. Cake shrinkage during freeze drying: a combined experimental and theoretical study. *Pharm. Dev. Technol.*, 10:33–40, 2005.
- [27] S. Rambhatla and M. J. Pikal. Heat and mass transfer scale-up issues during freeze-drying, I: atypical radiation and the edge vial effect. *AAPS PharmSciTech*, 4:22–31, jan 2003.
- [28] A. Konstantinidis, W. Kuu, L. Otten, S. Nail, and R. Sever. Controlled Nucleation in Freeze-drying: Effects on Pore Size in the Dried Product Layer, Mass Transfer Resistance, and Primary Drying Rate. *J. Pharm. Sci.*, 100:3453–3470, 2011.
- [29] W. Kuu, K. O'Brien, L. Hardwick, and T. Paul. Product mass transfer resistance directly determined during freeze-drying cycle runs using tunable diode laser absorption spectroscopy (TDLAS) and pore diffusion model. *Pharm. Dev. Technol.*, 16:343–357, 2011.
- [30] S. Rambhatla, R. Ramot, C. Bhugra, and M. J. Pikal. Heat and mass transfer scale-up issues during freeze drying: II. Control and characterization of the degree of supercooling. *AAPS PharmSciTech*, 5:54–62, 2004.

-
- [31] J. A. Searles, J. F. Carpenter, and T. W. Randolph. Annealing to optimize the primary drying rate, reduce freezing-induced drying rate heterogeneity, and determine T_g' in pharmaceutical lyophilization. *J. Pharm. Sci.*, 90(7):872–887, 2001.
- [32] Food and Drug Administration. Guidance for Industry PAT: A Framework for Innovative Pharmaceutical Development, Manufacturing, and Quality Assurance, 2004.

CHAPTER 4

Application of a Global Sensitivity Analysis for the identification of the most influential process parameters of the primary drying step during batch freeze-drying

Redrafted from: Van Bockstal P.J., Mortier S.T.F.C., Corver J., Nopens I., Gernaey K.V., De Beer T. (2017) *Global Sensitivity Analysis as Good Modelling Practices tool for the identification of the most influential process parameters of the primary drying step during freeze-drying*. European Journal of Pharmaceutics & Biopharmaceutics, 123, 108-116.

4.1 Introduction

The primary drying step during batch-wise freeze-drying is extensively described through mechanistic modelling [1–3]. These models allow the determination of the optimal combination of the adaptable process variables, i.e., shelf fluid inlet temperature T_s and chamber pressure P_c , in function of the primary drying time, to achieve a dried product without any signs of cake collapse in a minimum time frame. The appearance of the dried product is one of the CQAs of freeze-dried products, as structural loss of the cake is undesirable because of aesthetic purposes and the negative impact on the reconstitution time [4]. Cake collapse occurs when the product temperature at the sublimation front T_i exceeds the critical product temperature $T_{i,crit}$ during the primary drying stage [5]. $T_{i,crit}$ depends on the formulation characteristics and is identified as the eutectic temperature T_e or the collapse temperature T_c for crystalline and amorphous products, respectively. In general, T_c is a few

degrees higher than the glass transition temperature of the maximum freeze-concentrated formulation T'_g because viscous flow is limited near T'_g due to the sufficiently high viscosity of the amorphous solid [5].

As the mechanistic primary drying models are a mathematical approximation of the sublimation process, inherently a few assumptions and simplifications are included (e.g., a planar sublimation front and a steady-state system are assumed). In addition, the model input parameters are often an estimation of the real value, while other input variables (i.e., the dried product mass transfer resistance R_p and the vial heat transfer coefficient K_v) are quantified by one global value for the entire batch, despite the inter-vial variability. Because of these reasons, the computational model output can be correlated with a degree of uncertainty, which could lead to a deviation from the actual (experimental) primary drying behaviour. This parameter uncertainty can be included in the model leading to the quantitative estimation of the RoF, i.e., the risk of cake collapse, for each combination of the adaptable process parameters, T_s and P_c [6–9]. This quantitative risk assessment is essential for the construction of the Design Space, defined as the multidimensional combination and interaction of input variables and process parameters leading to the expected product specifications with a controlled (i.e., high) probability [10]. In this way, the optimal combination of T_s and P_c can be determined to maximize the process efficiency for an accepted RoF. The progression of primary drying and the corresponding increase in dried layer thickness leads to a continuous change of dependent process parameters (e.g., R_p). Therefore, the optimal combination of T_s and P_c changes in time, which results in a dynamic Design Space [3]

The determination of the impact of several process parameters and input variables on the primary drying behaviour would require a lot of time-consuming experiments, even via a DoE approach. The information gathered via experimental designs leads to the development of empirical models, which provide some, but no full physical insight in the primary drying dynamics. Mechanistic modelling can offer an alternative as it allows the identification of critical process parameters. In this respect, the application of a Global Sensitivity Analysis (GSA) on the model is recommended for appropriate model building according to the Good Modelling Practices [11]. A sensitivity analysis is the study of how the uncertainty in the output of a model (numerical or otherwise) can be apportioned to different sources of uncertainty in the model input (or model structure, parameters) [12]. In combination with the theoretical and physical background used for the development of the mechanistic model, a lot of process knowledge is obtained in an efficient way. Other

incentives to perform a sensitivity analysis, can be model calibration, model reduction and prediction of uncertainty [13]. In this study, a regression-based and variance-based GSA were conducted on a, previously validated, mechanistic primary drying model to estimate the impact of several model input parameters on two output variables, the product temperature at the sublimation front T_i and the sublimation rate \dot{m}_{sub} .

4.2 Materials and methods

4.2.1 Freeze-drying model

The detailed description of the (validated) mechanistic model describing the primary drying step of a batch freeze-drying process and the computation of the dynamic Design Space is given in chapter 3. The nominal values of the model input parameters are listed in table 4.1. The aqueous model formulation contained 30 mg/mL sucrose (Sigma-Aldrich, Saint-Louis, MO, USA). The coefficients describing R_p for this formulation were obtained from literature [14]. $T_{i,crit}$, which was assumed to be equal to T'_g of the model formulation, and the coefficients describing K_v were experimentally determined in the previous chapter. The mechanistic primary drying model assumes both a planar sublimation front and a steady-state system, i.e., the supplied energy was only consumed for ice sublimation.

4.2.2 Global Sensitivity Analysis

A GSA was conducted on two model outputs, i.e., the product temperature at the sublimation front T_i and the sublimation rate \dot{m}_{sub} . The sensitivity of the parameters was calculated after different primary drying times, i.e., after 1, 2, 3 and 4 h. Initially, the model is run for different combinations of input variables based on their uncertainty range, i.e., Monte Carlo simulations. The sample matrix required for the calculation of the output vector, is generated using the Sobol sampling technique. The number of Monte Carlo simulation runs has an influence on the sensitivity indices. For this reason, the optimal number of samples was determined in a first step, before the regression-based and variance-based GSA methods were conducted.

The parameters involved in the GSA, their uncertainty level and the reason for their inclusion are listed in table 4.2. The estimation of the uncertainty level for each parameter and the reason for their inclusion is described in chapter 3. For most factors, the uncertainty was not implemented as a percentage of the nominal value, as the range is highly

Table 4.1: Nominal values of the parameters of the model describing the primary drying step

Parameter		Numerical value
Inner radius of 10R vial	$r_{v,i}$	0.011 m
Outer radius of 10R vial	$r_{v,o}$	0.012 m
Radius of the vial neck	$r_{v,n}$	0.0063 m
Radius of the duct of the dryer	r_d	0.08 m
K_v -coefficient	α	11.18 J/(m ² sK)
K_v -coefficient	β	1.435 J/(m ² sKPa)
K_v -coefficient	γ	0.04008 1/Pa
R_p -coefficient	$R_{p,0}$	6.926 10 ⁴ m/s
R_p -coefficient	A_{Rp}	9.124 10 ⁶ 1/s
R_p -coefficient	B_{Rp}	0 1/m
Critical product temperature	$T_{i,crit}$	-32.5 °C
Filling volume	V	2.5 mL
Density of ice	ρ_{ice}	919.4 kg/m ³
Volume fraction of ice	ϵ	0.97
Ratio of the specific heat for water	k	1.33
Molecular weight of water	M	0.018015 kg/mol

dependent on the magnitude of the factor. For these factors (i.e., T_s , P_c , inner vial radius $r_{v,i}$ and outer vial radius $r_{v,o}$), the uncertainty was defined by an absolute range, based on experimental data or data provided by the supplier. In this study, the uncertainty on the dried layer thickness L_{dried} was assumed to be constant. However, it has to be remarked that the uncertainty on L_{dried} can also be calculated based on the other (uncertain) model input variables (i.e., error propagation), as demonstrated in the previous chapter for the UA. K_v is described in function of P_c via [9]:

$$K_v = \alpha + \frac{\beta P_c}{1 + \gamma P_c} \quad (4.1)$$

with α (J/(m²sK)), β (J/(m²sKPa)) and γ (1/Pa) constants describing K_v quantitatively in function of P_c (Table 4.1). R_p is described in function of L_{dried} via [9]:

$$R_p = R_{p,0} + \frac{A_{Rp} L_{dried}}{1 + B_{Rp} L_{dried}} \quad (4.2)$$

with $R_{p,0}$ (m/s), A_{Rp} (1/s) and B_{Rp} (1/m) constants describing R_p quantitatively in function of L_{dried} (Table 4.1). The uncertainty on these coefficients is lumped by introducing

an uncertainty on the entire parameter, i.e., α_{Rp} and α_{Kv} . The uncertainty on $r_{v,i}$ and $r_{v,o}$ is based on data provided by the supplier of the 10R glass vials (Schott AG, Mainz, Germany) used during the experimental validation (Section 4.2.3). The filling volume V was included in the analysis because of the inherent error that is made during the filling stage. Depending on the location of the vial on the shelf, T_s can be higher or lower than the set value. This error has been experimentally determined in the previous chapter for both a constant value of T_s and during a shelf temperature ramp. The error on P_c is based on the maximum allowed deviation of the feedback pressure control system of the freeze-dryer.

Table 4.2: Uncertainty level for the input factors

Factor	Uncertainty level	Reason of inclusion in GSA
L_{dried}	5%	Error propagation
R_p	20%	Based on experimental data
K_v	20%	Based on experimental data
$r_{v,i}$	10^{-4} m	Process variable with inherent error
$r_{v,o}$	10^{-4} m	Process variable with inherent error
V	10%	Process variable with inherent error
T_s	2.5 °C	Based on experimental data
P_c	1 Pa	Process variable with inherent error

Regression-based sensitivity analysis

The use of the regression-based GSA technique allows the sensitivity ranking to be determined based on the relative magnitude of the Standardized Regression Coefficients (SRCs). Therefore, the ranking is based on a linear regression model on the output of the Monte Carlo simulations via least square computation, not on the original model [15, 16]. For this method, it is assumed that no correlation exists between the different input factors. The linear regression is evaluated via the model coefficient of determination R_Y^2 which is equal to the fraction of variance of the original data, i.e., the results of the Monte Carlo simulation, explained by the regression model [15]. Ideally, for all regression-based methods, R_Y^2 approximates 1, meaning that most of the model output variance is present in the sensitivity ranking [16]. A low value for R_Y^2 indicates non-linear model behaviour where the SRCs fail to provide an adequate ranking [17]. The minimum criterion for the linear regression is a value of 0.7 for R_Y^2 . The disadvantage of the regression-based method is

that it is computationally expensive, because many samples are required. However, after simulation of the model, the analysis is fast and all measures can be calculated using the same sample and model. The obtained SRCs can only be used to assess the importance of a given parameter. Moreover, it is difficult to determine the number of samples to obtain valuable results.

Variance-based sensitivity analysis

Variance-based methods are very popular nowadays, and the obtained indices are much more informative compared to the SRCs. These indices are defined from the decomposition of the total output variance into the contribution of the input factors [12, 16, 18]. Two sensitivity measures are calculated by the variance-based GSA, i.e., the first order effect S_i and the total order effect S_{Ti} . S_i indicates the actual fraction of variance accounted for by each factor, whereas S_{Ti} represents the total effect of factor i , i.e., the sum of the first order effects and all interactions with other factors [17]. Different designs are known to calculate these sensitivity indices [19, 20]. The design proposed by Saltelli et al. was applied in this study [21].

Determination of sample size

The Central Limit Theorem (CLT) was used to determine the optimal number of samples N required for both the regression-based and variance-based GSA, i.e., the number of samples required to achieve a normal distribution of the composite [22]. Therefore, for an increasing number of base samples (different values for N), R replicas were taken and the corresponding sensitivity measures were calculated, i.e., the SRCs for the regression-based technique and S_i and S_{Ti} for the variance-based technique. For each N value, this leads to R values for each sensitivity measure. The mean and the coefficient of variation CV were calculated. According to the CLT, R should be at least 30, however, in this contribution 100 replicas were used [22].

4.2.3 Experimental design methodology

The results of the GSA were experimentally validated via a DoE approach for one specific response, i.e., the sublimation rate \dot{m}_{sub} . The parameters used for the GSA were included as factors in the experimental design (Table 4.3), except for the vial dimensions $r_{v,i}$ and $r_{v,o}$, which were kept constant as we did not deem these variables to provide more scientific insight in this stage. The centre points for each factor of the DoE were derived from the

nominal values of the model parameters used for the computation of the dynamic Design Space for an aqueous 30 mg/mL sucrose formulation (Table 4.1), except for T_s and P_c , which were based on the output of this model (Chapter 3). The lowest and highest level for the quantitative factors T_s , P_c and V were based on their corresponding uncertainty level in the GSA (Table 4.2). Both R_p and K_v were treated as two level qualitative factors which approach the relative uncertainty of 20% on the nominal value, as included in the GSA (Table 4.2). Specifically, the uncertainty on R_p was incorporated in the design by including an aqueous 30 mg/mL lactose formulation, i.e., formulation 2 (Fagron, Waregem, Belgium), for which the R_p profile in function of L_{dried} was approximately 20% higher compared to the nominal value for the 30 mg/mL sucrose model formulation, i.e., formulation 1 [14]. The uncertainty on K_v was incorporated by comparing the sublimation rate for the edge vials and centre vials. A fractional factorial screening design consisting of 16 experiments, expanded with two double centre points, was constructed using MODDE Pro (Version 11.0.0, Umetrics, Umeå, Sweden). An overview of all individual experiments is given in table 4.4.

Table 4.3: Overview factors DoE with lowest and highest level

Factors	Level		Unit
	-	+	
<i>Quantitative</i>			
T_s	-18.5	-13.5	°C
P_c	9	11	Pa
V	2.25	2.75	mL
<i>Qualitative</i>			
R_p	Formulation 1–2		
K_v	Edge vials - Centre vials		

The response \dot{m}_{sub} was gravimetrically determined. The experiments were conducted in a laboratory scale freeze-dryer Lyobeta 25 (Telstar, Terrassa, Spain) equipped with four shelves, each with a heatable area of 0.16 m², in the vacuum-tight drying chamber with a volume of 0.2 m³. The system contains a condenser with 35 kg of ice capacity and a vacuum pump to evacuate the drying chamber. Chamber pressure control was performed via a Baratron Type 626A capacitance manometer (MKS Instruments, Andover, MA, USA). Comparative pressure measurements were conducted using a Pirani Type PSG-502-S thermal conductivity gauge (Inficon, Bad Ragaz, Switzerland). Temperature control of shelf and condenser was based on Pt100 thermal sensors (WIKA Instruments, Klingenberg, Ger-

Table 4.4: Overview experiments DoE, the experiments in bold were performed twice (centre points)

Experiment number	T_s (°C)	P_c (Pa)	V (mL)	K_v	R_p
1	-18.5	9	2.75	Formulation 1	Edge vial
2	-13.5	9	2.25	Formulation 1	Edge vial
3	-18.5	11	2.25	Formulation 1	Edge vial
4	-13.5	11	2.75	Formulation 1	Edge vial
5	-18.5	9	2.25	Formulation 2	Edge vial
6	-13.5	9	2.75	Formulation 2	Edge vial
7	-18.5	11	2.75	Formulation 2	Edge vial
8	-13.5	11	2.25	Formulation 2	Edge vial
9	-18.5	9	2.25	Formulation 1	Centre vial
10	-13.5	9	2.75	Formulation 1	Centre vial
11	-18.5	11	2.75	Formulation 1	Centre vial
12	-13.5	11	2.25	Formulation 1	Centre vial
13	-18.5	9	2.75	Formulation 2	Centre vial
14	-13.5	9	2.25	Formulation 2	Centre vial
15	-18.5	11	2.25	Formulation 2	Centre vial
16	-13.5	11	2.75	Formulation 2	Centre vial
17	-16	10	2.5	Formulation 1	Edge vial
18	-16	10	2.5	Formulation 2	Edge vial

many) measurements. For each individual experiment of the DoE, 10 vials were filled with a certain volume of the specified formulation, as defined by the DoE (Table 4.4). The vials were placed on a precooled shelf (3 °C) in the drying chamber, randomly distributed at the edge or centre of the batch. The batch was expanded with dummy vials containing 2.5 mL of water to a total of 100 vials. The size and arrangement of the batch was equal to the experimental determination of K_v (Chapter 3). The freezing step for each validation run was equal to the freezing procedure used to determine R_p of the model formulation [14]. The shelves were chilled at a rate of 1 °C/min until -45 °C and maintained at this temperature for 1 hour. An annealing step was included in the freezing procedure, during which T_s was increased in 25 minutes until -20 °C and kept at this value for 2 hours. After re-establishing the final freezing temperature of -45 °C at a rate of 1 °C/min, T_s was kept for another hour at this value, before the condenser was cooled and the vacuum pump was activated. The settings of T_s and P_c during primary drying were characteristic for each

individual DoE experiment. Primary drying was interrupted after approximately 7 to 8h, to avoid ice sublimation was completely finished. The vials were weighed before and after freeze-drying, allowing the calculation of the mean value of \dot{m}_{sub} .

MODDE Pro was used for the analysis of the experimental design. A regression model for the response was calculated via Multiple Linear Regression (MLR). All factors were scaled and centred, which makes the regression coefficients for the different factors comparable. Each quantitative factor was set to +1 and -1 for their highest and lowest value, respectively. Qualitative factors require an alternative approach via a mathematical re-expression (regression coding). A k-level qualitative parameter will be expanded into k-1 artificial categorical variables. Each expanded term results in one regression coefficient, which in our case led to one coefficient for level 2 (regular mode). In addition, the level 1 coefficient is equal to the negative coefficient of the expanded term of level 2 (extended mode). The regression coefficient of a specific factor represents the quantitative change in response value when this factor is increased from its average to its high level, keeping all other factors at their average value. The effect of a specific factor is defined as the quantitative change in response value when this factor is increased from its low to its high level, keeping all other factors at their average value. Based on these definitions, the effect of a factor is twice the corresponding coefficient. The constant term is related to the response value at the design centre point, with all factors at their nominal value. For all regression coefficients the 95% confidence interval was calculated. Factors or interactions between factors were considered significant if the 95% confidence interval of the corresponding regression coefficient did not contain zero.

4.3 Results

4.3.1 Determination of the required number of simulations for the GSA

To determine the number of samples required for the GSA, the convergence of the sensitivity measures was verified for a base scenario, i.e., the output after 1,800 s. This could be done on a graphical basis, by visually checking the convergence. However, a more objective evaluation was conducted using a technique based on CLT [22].

For the regression-based GSA, the coefficient of determination R_Y^2 should be higher than 0.7. Only when R_Y^2 is higher than 0.7, the SRCs can be used to rank the parameters of the mechanistic primary drying model. It was possible to perform the analysis for both

output variables, i.e., T_i and \dot{m}_{sub} , as R_Y^2 was above 0.7, without the need for a rank transformation. In the top part of figure 4.1, the mean of the quotient of two successive SRC values is presented for an increasing number of simulations N for T_i as output variable. For each parameter, the quotient of two successive SRC values should converge to 1 for an increasing value of N , therefore, the mean over all parameters should also converge towards one. However, the question arises for which N the value is close enough to 1. Therefore, a more in-depth method has been used to objectively determine the optimal number of samples, i.e., CLT. Besides the mean quotient of two successive SRC values, the R_Y^2 -value also converges for an increasing number of Monte Carlo simulations (Bottom part of figure 4.1).

In figure 4.2 (Top), CV is plotted in function of the number of base samples N for T_i as output variable. From the graph it can be concluded that this coefficient decreases for a higher number of base samples. After 10,000 samples, the solution seems to be converged, but the optimal number of samples is determined graphically and is not exact. There exists no quantitative method in order to determine the optimal number. From this figure it is apparent that CV is remarkable higher for V and L_{dried} compared to the other parameters. CV in function of N for the sublimation rate \dot{m}_{sub} as output variable is presented in figure 4.2 (Bottom). CV is much higher for this output variable, and moreover, the behaviour for L_{dried} is different compared to the other parameters. Based on these results, and given the fact that it has no impact on the mean of the SRCs (Figure 4.3), it was decided to use 10,000 samples for the regression-based GSA.

The same approach was applied for the variance-based technique. The results for the total sensitivity indices S_{T_i} are presented in figure 4.4 for the temperature at the sublimation front T_i and the sublimation rate \dot{m}_{sub} . It should be noted that the actual number of model runs is presented on the x -axis. Dependent on the formulas used to calculate S_i and S_{T_i} , the actual number of model runs varies according to the set sample size. Here, the scheme proposed by Saltelli et al. was used [21]. This means that the actual number of models runs equals $(n_{par} + 2)N_{base}$ with n_{par} the number of parameters included in the sensitivity analysis and N_{base} the base sample size.

The variance-based sensitivity technique does not require a linear model as input, therefore, the method has a broader applicability. To have a converged result for the temperature at the sublimation front T_i (Top part of figure 4.4), a sample size of 5,000 seems to be needed. The same is valid for the sublimation rate \dot{m}_{sub} (Bottom part of figure 4.4). Therefore,

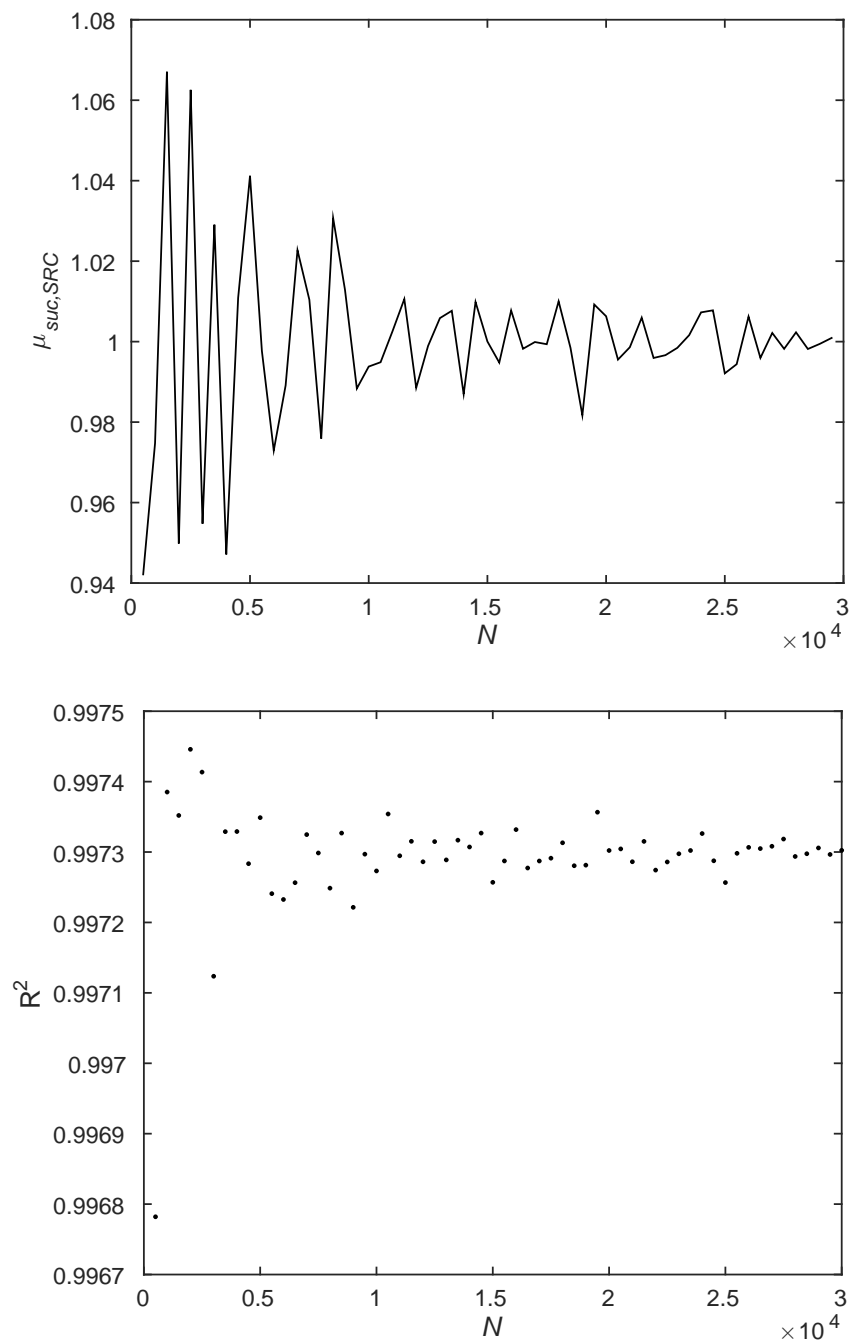


Figure 4.1: Mean of the quotient of two successive SRC values (Top) and the R^2 -value (Bottom) for increasing number of Monte Carlo simulations performed on the primary drying model for the product temperature at the sublimation interface T_i as output variable of the regression-based GSA

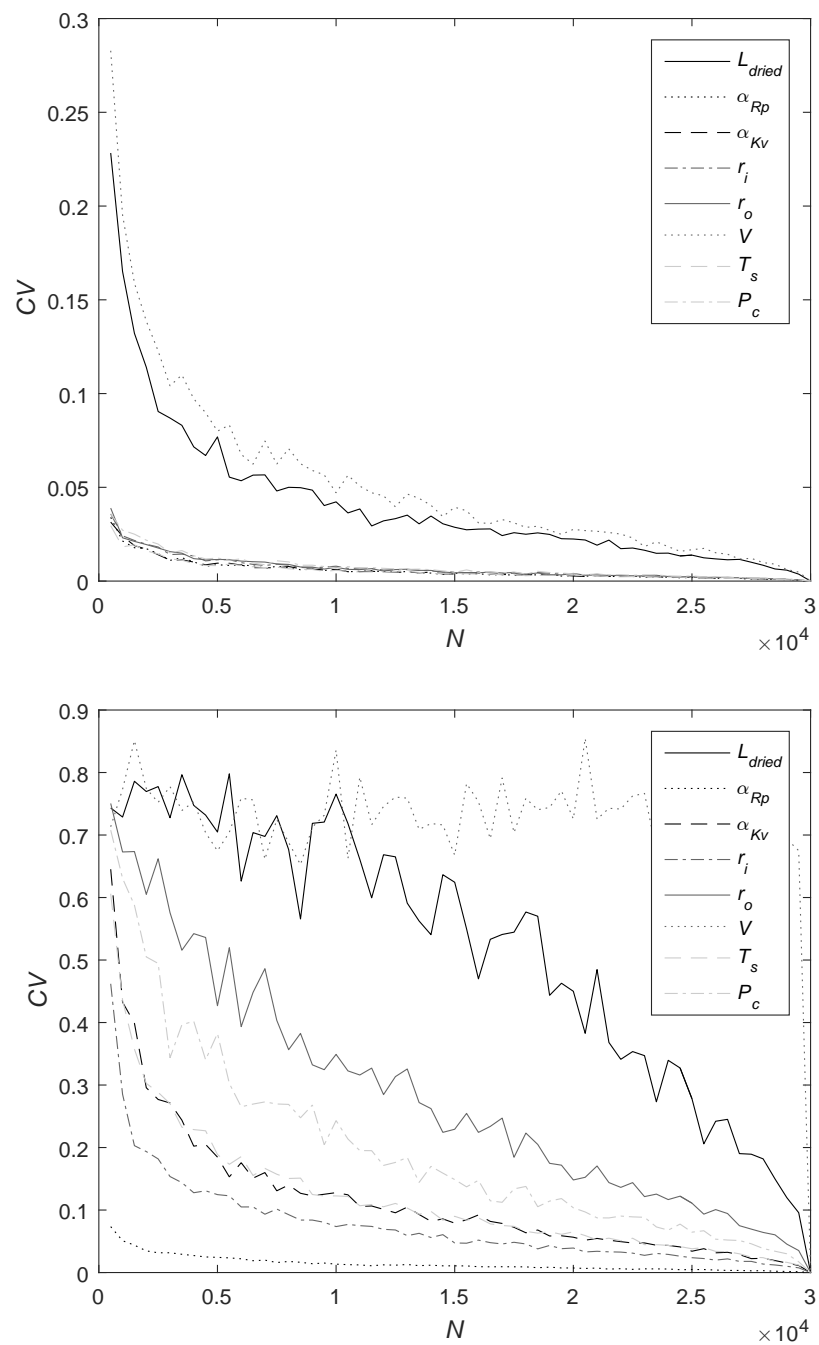


Figure 4.2: Coefficient of variation CV for the SRC for an increasing number of base samples N performed on the primary drying model for the product temperature at the sublimation interface T_i (Top) and the sublimation rate \dot{m}_{sub} (Bottom) as output variable of the regression-based GSA

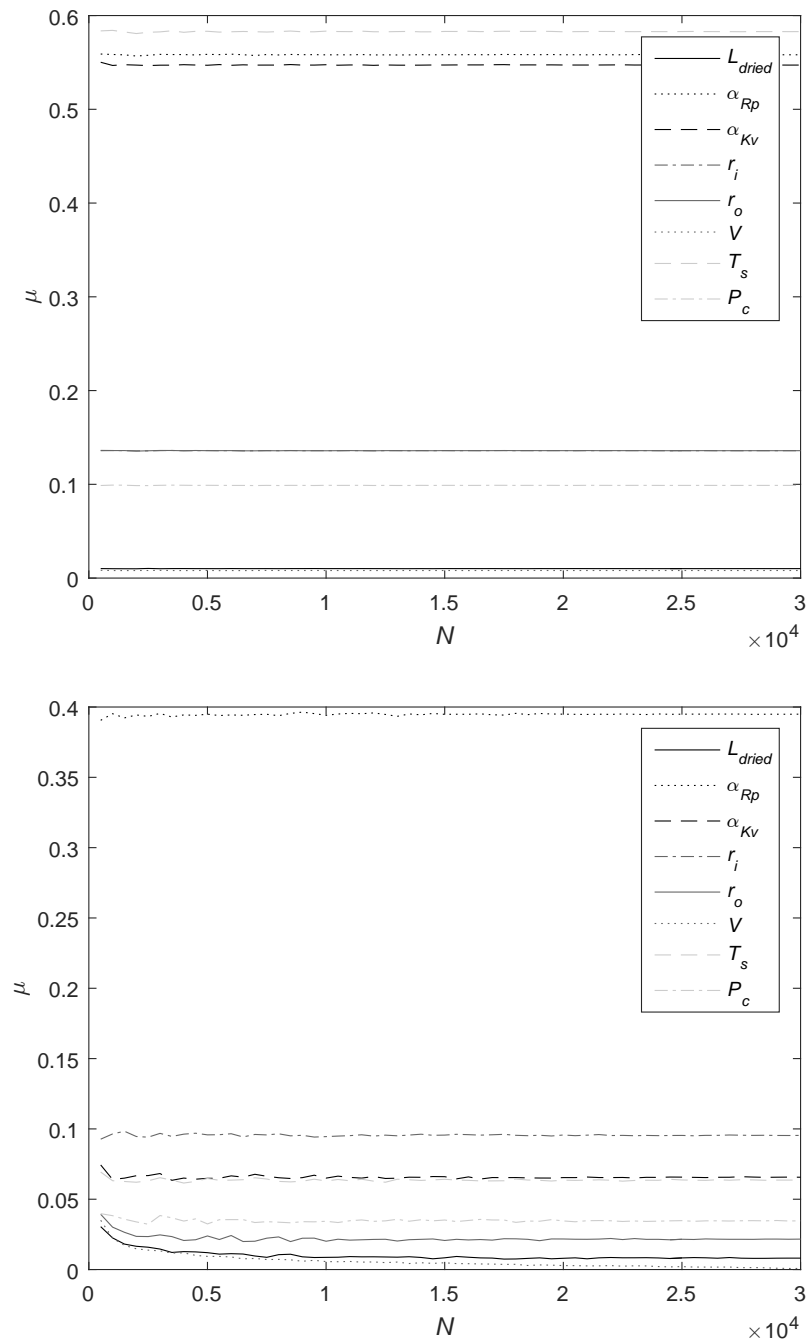


Figure 4.3: Mean of the SRC in function of the number of base samples N performed on the primary drying model for the product temperature at the sublimation interface T_i (Top) and the sublimation rate \dot{m}_{sub} (Bottom) as output variable of the regression-based GSA

a 500 base samples, i.e., 5,000 divided by $n_{par} + 2$, were chosen to perform the further analysis.

4.3.2 Gathering process knowledge using graphical tools

Graphical sensitivity analysis tools, which are qualitative techniques (i.e., scatter plots or Contribution to Sample Mean (CSM)/Contribution to Sample Variance (CSV) plots), are interesting to detect the relationship between uncertain model inputs and the resulting output [23]. The scatter plots are presented for three different parameters with a different behaviour, after 1 h of simulated process time (Figure 4.5). From the scatter plot of T_s it can be concluded that the deviation from the nominal value of T_s is not similarly reflected in deviation of the T_i (note that the deviation in the nominal value of T_s is presented on the x -axis). For low values of T_s , T_i is also lower due to the decreased energy input. If the difference with the nominal value of T_s is between -1 and 1, the effect on T_i is rather limited, because T_i is stable when equilibrium is achieved between energy input and ice sublimation. The influence of P_c on T_i is rather limited, as the same value of T_i can be obtained for each value of the chamber pressure. The effect of α_{Rp} on the sublimation rate (Bottom part of figure 4.5) is obvious, for lower values of α_{Rp} the sublimation rate is higher.

4.3.3 GSA using a regression- and variance-based technique

To rank the parameters it is suggested to perform a regression- or variance-based GSA technique, where quantitative sensitivity measures are obtained. The GSA was performed for different time steps during the primary drying process. In figure 4.6, S_{T_i} values for the different parameters are presented for different time steps. Focusing at the results after 1 h for T_i as output variable (Top part of figure 4.6), it can be concluded that T_s is the most influential parameter, followed by P_c . The significance of T_s is important as this is one of the adaptable process parameters of the freeze-drying process. The other process variable, i.e., P_c , has a rather limited influence. Looking at the results for the whole drying process, it is obvious that T_s has the most influence on T_i . The influence of P_c is somewhat decreasing over time. The influence of α_{Rp} and α_{Kv} is clearly increasing over time.

On the bottom part of figure 4.6, the results for S_{T_i} with \dot{m}_{sub} as output variable are presented. Again T_s is the most influential parameter, followed by α_{Rp} . The influence of T_s is decreasing and the influence for P_c is increasing, but for the other parameters the

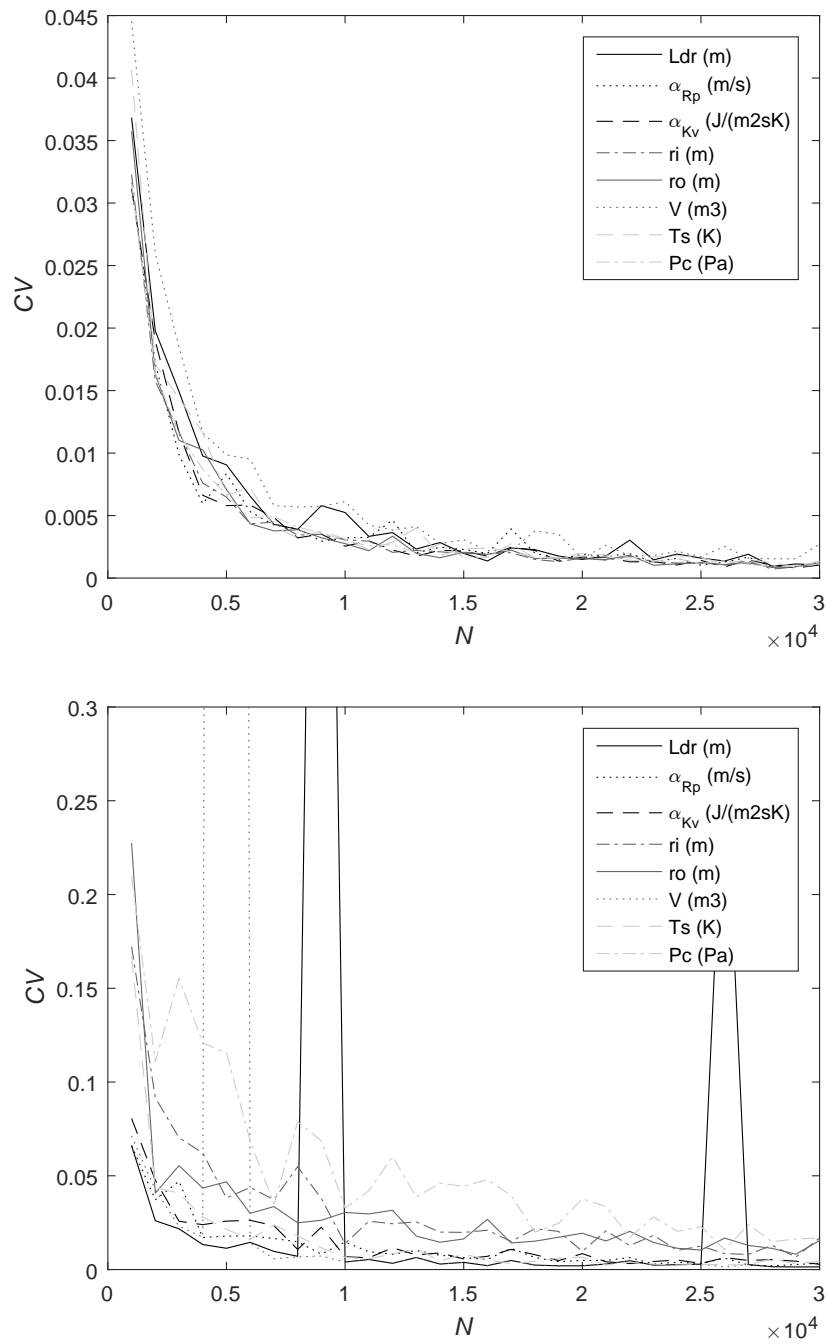


Figure 4.4: Coefficient of variation CV for the S_{T_i} in function of the number of base samples N performed on the primary drying model for the product temperature at the sublimation interface T_i (Top) and the sublimation rate \dot{m}_{sub} (Bottom) as output variable of the variance-based GSA

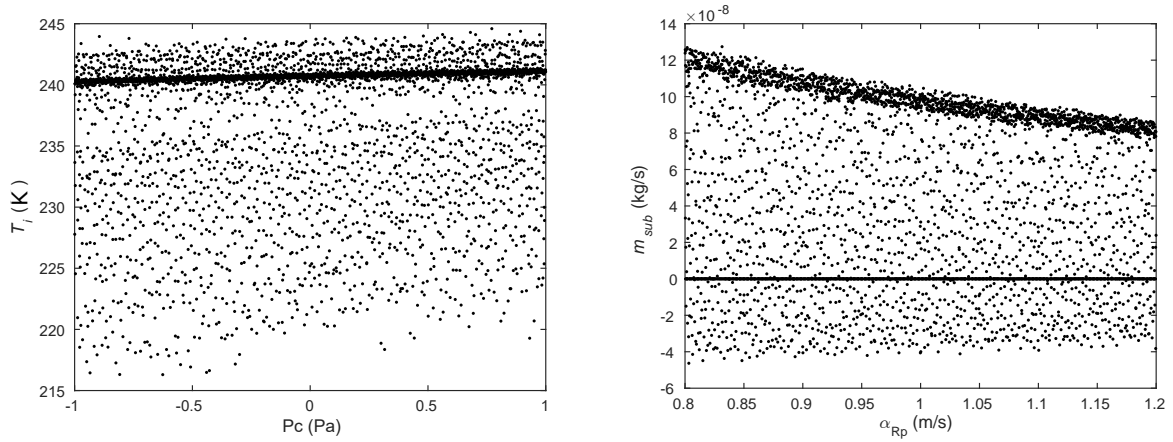


Figure 4.5: Scatter plot for the freeze-drying model with $N = 10,000$ for P_c with T_i as output variable (Left) and α_{Rp} with \dot{m}_{sub} as output variable (Right) after 1 h

value for S_{T_i} is similar over the whole time range. The results using the regression-based analysis with the SRCs are similar.

4.3.4 Analysis of experimental design

The mean sublimation rate \dot{m}_{sub} for the individual experiments of the experimental design (Table 4.4) ranged from approximately 0.15 g/h up to 0.27 g/h. For the filling volume of 2.5 mL, assuming an ice mass of 2.5 g, this would correspond to an estimated primary drying time ranging from approximately 16.67 h to 9.25 h. Evaluation of the raw data indicated that there were no peculiarities in the results: the variability in \dot{m}_{sub} between the repetitions (i.e., centre points) was less than the overall variability for the individual experiments. The response data were normally distributed, hence, data transformation before regression analysis was not needed. The regression coefficients, computed via MLR fitting, are displayed for each factor and factor interaction, including their 95% confidence interval, in the extended coefficient plot in Figure 4.7.

The position of the vial in the batch, i.e., K_v (Edge vial) and K_v (Centre vial), was identified as the factor with the highest influence on \dot{m}_{sub} , with a regression coefficient of 0.0317 g/h (Figure 4.7). For a vial situated at the edge of the shelf, \dot{m}_{sub} increases with 0.0635 g/h compared to a centre vial, keeping all other factors at their average level, hence, decreasing the primary drying time with approximately 27% from 14.53 h to 10.61 h for a 2.5 mL filling volume. The shelf fluid inlet temperature T_s had a positive impact on the response

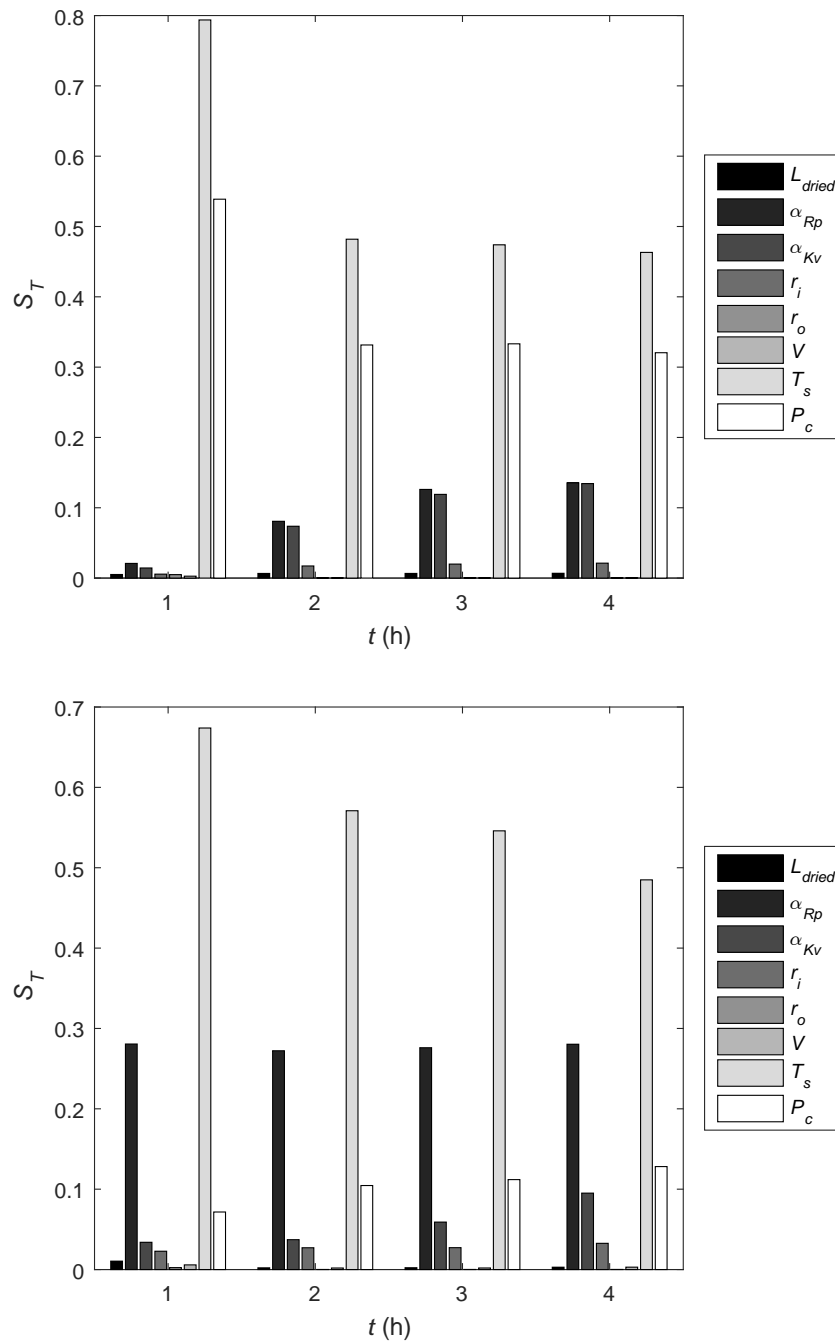


Figure 4.6: S_{T_i} for the primary drying model with $N = 5,000$ for the product temperature at the sublimation front T_i (Top) and the sublimation rate \dot{m}_{sub} (Bottom) as output variable at different time steps

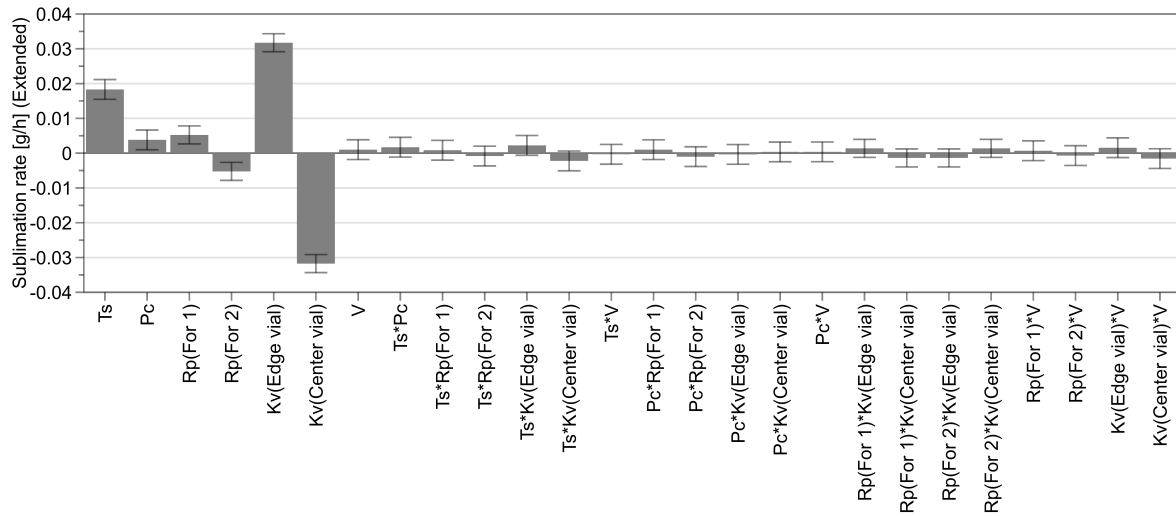


Figure 4.7: Extended coefficient plot, response: Sublimation rate: Regression coefficients displayed including 95% confidence interval, with shelf fluid inlet temperature T_s , chamber pressure P_c , filling volume V , the expanded model terms related to the qualitative factor R_p ($R_p(\text{For1})$ and $R_p(\text{For2})$ being the sucrose and lactose formulation, respectively) and the expanded model terms related to the qualitative factor K_v ($K_v(\text{Edge vial})$ and $K_v(\text{Centre vial})$)

variable (regression coefficient 0.0183 g/h). An increase in T_s from -16°C to -13.5°C , keeping all other factors at their average level, is associated with a decrease in drying time of approximately 1 h from 12.26 h to 11.25 h. The difference in dried product mass transfer resistance R_p , represented by the two different formulations, i.e., $R_p(\text{For1})$ and $R_p(\text{For2})$, was small with a regression coefficient of 0.00524 g/h. Primary drying of the lactose formulation would take 5% or 38 min longer compared to the sucrose formulation with a primary drying time of 12.59 h and 11.96 h, respectively, keeping all other factors at their average level. With a regression coefficient of 0.00382 g/h, the chamber pressure P_c had a very small impact on \dot{m}_{sub} . An increase of P_c from 10 Pa to 11 Pa, keeping all other factors at their average level, is associated with a decrease in drying time of approximately 13 min from 12.26 h to 12.04 h. The filling volume V had no significant impact on the response \dot{m}_{sub} (regression coefficient 0.001003 g/h). In addition, none of the factor interactions was significant.

4.4 Discussion

The results of the GSA on the mechanistic primary drying model, i.e., the significance ranking S_{T_i} for both T_i and \dot{m}_{sub} , should be interpreted considering the physical basis of the sublimation process. As one of the adaptable process variables, T_s had the largest impact on both T_i and \dot{m}_{sub} (Figure 4.6). The shelves provide the energy transfer to the glass vials which impacts both T_i and \dot{m}_{sub} . Therefore, T_s is the process parameter with the highest influence on these output variables. The experimental results confirm the significant impact of T_s on \dot{m}_{sub} (Figure 4.7). The relative impact of T_s decreases when the primary drying process progresses (Figure 4.6) due to the dynamic nature of the optimized cycle as R_p increases in function of time, requiring a gradual decrease in energy input to avoid cake collapse [3]. The other adaptable parameter of the primary drying process, P_c , was also identified in the GSA as a factor with a significant impact, mainly on T_i . P_c directly impacts \dot{m}_{sub} , as the sublimation rate is based on the difference in vapour pressure at the sublimation front and in the drying chamber. Because of the high accuracy of the pressure control system of the freeze-dryer, the uncertainty level for P_c is very narrow, i.e., only 1 Pa, explaining why the impact of P_c on \dot{m}_{sub} is rather limited. Due to the narrow uncertainty range, P_c was identified as a factor with a very limited impact on the experimental \dot{m}_{sub} . In addition, it should be noted that P_c influences the conductive energy transfer. An increase in P_c is related to a higher density of gas molecules in the drying chamber, which enhances the conductive energy transfer from shelf to vial due to the suboptimal contact between vial and shelf [24].

The GSA predicted that the impact of α_{Rp} on T_i and \dot{m}_{sub} was less pronounced compared to T_s (Figure 4.6). However the influence of α_{Rp} is still significant, especially towards \dot{m}_{sub} . R_p directly impacts \dot{m}_{sub} , as the sublimation rate is inversely proportional to the resistance of the dried product layer. This is confirmed by the results of the experimental design, where R_p has a significant, but limited impact. For equal process conditions, the primary drying step lasts 5% longer for the 30 mg/mL lactose formulation compared to the 30 mg/mL sucrose formulation (Section 4.3.4). R_p is highly dependent on the formulation characteristics and the pore size of the dried product layer, which, in turn, depends on the ice crystal size, related to the degree of supercooling before ice nucleation takes place [14, 25]. Therefore, cycle optimization can only be performed for a specific freezing regime. The stochastic nature of ice nucleation and the resulting interval variability in pore size distribution is countered by including a sufficiently high uncertainty level for R_p .

α_{K_v} is the only parameter of which the effect on \dot{m}_{sub} is underestimated by the GSA, compared to the experimental validation. Based on the experimental design, the position of the vial, at the edge of the shelf or in the centre of the vial pack, is the parameter with the highest influence on \dot{m}_{sub} . These experimental findings stroke with the difference in K_v between the edge and centre vials, due to the additional radiative heat transfer coming from the surrounding walls and the door [24, 26]. This uneven energy transfer between both positions is inherent to the design of the pharmaceutical batch freeze-dryer. Therefore, an appropriate freeze-drying cycle operating strategy is required as a compensation. For this reason, the K_v parameter was experimentally determined for separate groups. One group consisted of vials completely surrounded by other vials, i.e., centre vials, while the other group contained vials situated at the edge of the shelf, with at least one side directed towards the door or the walls of the drying chamber, i.e., edge vials (Chapter 3). The dynamic Design Space was computed based on these edge vials, as these vials are the limiting factor in the prevention of cake collapse due to the additional radiative energy transfer. As compensation for the centre vials with a lower energy input, the optimal primary drying trajectory should be prolonged before the start of the secondary drying step (Chapter 3). It should be noted that the ratio of edge to centre vials decreases considerably during upscaling to industrial scale freeze-driers, however, the edge vials will remain the limiting factor and the same strategy should be applied.

The computed impact of $r_{v,i}$, $r_{v,o}$ and V was very limited. Based on the data provided by the supplier, the uncertainty margin on $r_{v,i}$ and $r_{v,o}$ is very small and the GSA indicates that their impact is negligible. The experimental design confirmed the low impact of V on \dot{m}_{sub} .

In general, the experimental validation seems to confirm the results of the GSA, with an exception for α_{K_v} . It is important to note that the results of the GSA are highly dependent on the used uncertainty level. Therefore, the uncertainty ranges for each parameter should be carefully chosen. In addition, the uncertainty range should also be considered when interpreting the results of the GSA. For the experimental validation of the GSA, it is equally important to choose an appropriate level for each factor of the design, correctly reflecting the uncertainty level for each process variable included in the GSA. For quantitative factors, this can be easily done by adapting the input settings, e.g., P_c can be set at a specific value via the pressure control system. However, K_v and R_p could only be included in the design as qualitative factors, which makes it more difficult to approach the quantitative uncertainty range used in the GSA. This might be the reason why the impact

of α_{Kv} is underestimated in the GSA compared to the experimental validation.

As the GSA was conducted on a validated model, essential process knowledge can be extracted. The method allows to determine which uncertain input variables only have a limited influence on the model outcome, even to such extent their uncertainty could be irrelevant. Also, GSA can identify the parameter for which a reduction or elimination of the uncertainty would reduce most of the variance on the output and, hence, lower the risk of cake collapse during primary drying. The experimental DoE was conducted to validate the GSA on the previously validated primary drying model. Once validated, it is no longer required to repeat the post DoE in case different nominal values or uncertainty levels would be used for the model input parameters, e.g., during upscaling or during the optimization of the primary drying cycle for another formulation. This way, similar information can be obtained in a much shorter time frame compared to the labor intensive and more expensive DoE approach. However, freeze-drying cycles designed and optimized via the mechanistic primary drying model, do require a final experimental validation.

4.5 General conclusion

A GSA has been applied on a, previously validated, mechanistic primary drying model in order to gain process knowledge. First, the optimal number of samples has been determined by using CLT. For the regression-based GSA, 10,000 samples was sufficient to obtain converged SRCs. The variance-based GSA required 500 base samples, corresponding to 5,000 samples $((n_{par} + 2)N_{base})$. For both methods, the ranking of the parameters was similar for both output variables of the model, i.e., the temperature at the sublimation front T_i and the sublimation rate \dot{m}_{sub} . The shelf temperature T_s was identified as the factor with the highest impact on both output variables. The chamber pressure P_c has a large influence on T_i , however, the impact on \dot{m}_{sub} is rather limited. The influence of α_{Rp} on \dot{m}_{sub} is significant.

The results of the GSA were largely confirmed by the experimental validation via a DoE approach. Only, the impact of α_{Kv} was underestimated by the GSA, as this parameter was included as a qualitative factor in the experimental design. The level of uncertainty of each process parameter was identified as a major influence on the significance ranking. Therefore, the uncertainty level of each process parameter should be determined with reason and not be chosen randomly. In summary, the results indicated that GSA is a very useful

tool for the evaluation of the impact of different process variables on the model outcome, leading to essential process knowledge, without performing time-consuming experiments.

Bibliography

- [1] S. L. Nail and J. A. Searles. Elements of Quality by Design in development and scale-up of freeze-dried parenterals. *BioPharm Int.*, 21:44–52, 2008.
- [2] L. N. Mockus, T. W. Paul, N. A. Pease, N. J. Harper, P. K. Basu, E. A. Oslos, G. A. Sacha, W. Y. Kuu, L. M. Hardwick, J. J. Karty, M. J. Pikal, E. Hee, M. A. Khan, and S. L. Nail. Quality by design in formulation and process development for a freeze-dried, small molecule parenteral product: a case study. *Pharm. Dev. Technol.*, 16:549–576, 2011.
- [3] D. Fissore, R. Pisano, and A. A. Barresi. Advanced approach to build the design space for the primary drying of a pharmaceutical freeze-drying process. *J. Pharm. Sci.*, 100:4922–4933, 2011.
- [4] V. R. Koganti, E. Y. Shalaev, M. R. Berry, T. Osterberg, M. Youssef, D. N. Hiebert, F. A. Kanka, M. Nolan, R. Barrett, G. Scalzo, G. Fitzpatrick, N. Fitzgibbon, S. Luthra, and L. Zhang. Investigation of design space for freeze-drying: use of modeling for primary drying segment of a freeze-drying cycle. *AAPS PharmSciTech*, 12:854–861, 2011.
- [5] J. C. Kasper and W. Friess. The freezing step in lyophilization: Physico-chemical fundamentals, freezing methods and consequences on process performance and quality attributes of biopharmaceuticals. *Eur. J. Pharm. Biopharm.*, 78:248–263, 2011.
- [6] A. Giordano, A. A. Barresi, and D. Fissore. On the use of mathematical models to build the design space for the primary drying phase of a pharmaceutical lyophilization process. *J. Pharm. Sci.*, 100:311–324, 2011.
- [7] R. Bogner and M. J. Pikal. The Incredible Shrinking Design Space: Using Risk Tolerance to Define Design Space for Primary Drying. *Notes of Freeze Drying of Pharmaceuticals and Biologicals Conference, Garmisch-Partenkirchen*, pages 184–198, 2010.
- [8] S. Bosca, D. Fissore, and M. Demichela. Risk-Based Design of a Freeze-Drying Cycle for Pharmaceuticals. *Ind. Eng. Chem. Res.*, 54:12928–12936, 2015.
- [9] S. Mortier, P. J. Van Bockstal, J. Corver, I. Nopens, K. Gernaey, and T. De Beer. Uncertainty analysis as essential step in the establishment of the dynamic Design

- Space of primary drying during freeze-drying. *Eur. J. Pharm. Biopharm.*, 103:71–83, 2016.
- [10] L. X. Yu, G. Amidon, M. a. Khan, S. W. Hoag, J. Polli, G. K. Raju, and J. Woodcock. Understanding pharmaceutical quality by design. *The AAPS journal*, 16(4):771–83, 2014.
- [11] A. J. Jakeman, R. A. Letcher, and J. P. Norton. Ten iterative steps in development and evaluation of environmental models. *Environ. Modell. Softw.*, 21:602–614, 2006.
- [12] A. Saltelli, S. Tarantola, F. Campolongo, and M. Ratto. *Sensitivity Analysis in Practice: A Guide to Assessing Scientific Models*. John Wiley & Sons, Chichester, 2004.
- [13] S. Mortier, K. V. Gernaey, T. De Beer, and I. Nopens. Global Sensitivity Analysis applied to drying models for one or a population of granules. *AIChE J.*, 60:1700–1717, 2014.
- [14] W. Y. Kuu, L. M. Hardwick, and M. J. Akers. Rapid determination of dry layer mass transfer resistance for various pharmaceutical formulations during primary drying using product temperature profiles. *Int. J. Pharm.*, 313:99–113, 2006.
- [15] A. Saltelli. The critique of modelling and sensitivity analysis in the scientific discourse: An overview of good practices. In *TAUC*, Washington, 2006.
- [16] R. Urbonas, A. Kaliatka, and V. Kopustinskias. Comparative sensitivity study of the RBMK-1500 reactor one group distribution header blockage accident model. *Nucl. Eng. Des.*, 240:3238–3247, 2010.
- [17] T. Homma and A. Saltelli. Importance measures in global sensitivity analysis of nonlinear models. *Reliab. Eng. Syst. Saf.*, 52:1–17, 1996.
- [18] S. Tarantola and W. Becker. A comparison of two sampling methods for global sensitivity analysis. *Comput. Phys. Commun.*, 183:1061–1072, 2012.
- [19] M. D. McKay, R. J. Beckman, and W. J. Conover. A comparison of three methods for selecting values of input variables in the analysis of output from computer code. *Technometrics*, 42:55–61, 2000.
- [20] F. Campolongo, A. Saltelli, and J. Cariboni. From screening to quantitative sensitivity analysis. A unified approach. *Comput. Phys. Commun.*, 182:978–988, 2011.

- [21] A. Saltelli, P. Annoni, I. Azzini, F. Campolongo, M. Ratto, and S. Tarantola. Variance based sensitivity analysis of model output. Design and estimator for the total sensitivity index. *Comput. Phys. Commun.*, 181:259–270, 2010.
- [22] J. Yang. Convergence and uncertainty analyses in Monte-Carlo sensitivity analysis. *Environ. Modell. Softw.*, 26:444–457, 2011.
- [23] S. Tarantola, V. Kopustinskas, R. Bolado-Lavin, A. Kaliatka, E. Ušpuras, and M. Vaišnoras. Sensitivity analysis using contribution to sample variance plot: Application to a water hammer model. *Reliab. Eng. Syst. Saf.*, 99:62–73, 2012.
- [24] R. Pisano, D. Fissore, A. A. Barresi, P. Brayard, P. Chouvenc, and B. Woinet. Quality by design: optimization of a freeze-drying cycle via design space in case of heterogeneous drying behavior and influence of the freezing protocol. *Pharm. Dev. Technol.*, 18:280–295, 2013.
- [25] S. Rambhatla, J.-P. Obert, S. Luthra, C. Bhugra, and M. J. Pikal. Cake shrinkage during freeze drying: a combined experimental and theoretical study. *Pharm. Dev. Technol.*, 10:33–40, 2005.
- [26] S. Rambhatla and M. J. Pikal. Heat and mass transfer scale-up issues during freeze-drying, I: atypical radiation and the edge vial effect. *AAPS PharmSciTech*, 4:22–31, jan 2003.

CHAPTER 5

Continuous pharmaceutical freeze-drying

5.1 Batch versus continuous pharmaceutical manufacturing

Conventional pharmaceutical manufacturing is generally accomplished using inefficient batch processes [1]. Batch-wise manufacturing is characterised by the processing of starting materials through a sequence of segmented unit operations, each with specific process settings, until the final product is obtained [2]. The (off-line) quality assessment of intermediate products after each unit operation strongly delays the production process. Additionally, rejection or reprocessing of the entire batch is required in case product specifications are not met, which has a significant economical impact. With the aim of increasing the process efficiency and encouraged by the regulatory authorities, the pharmaceutical industry is currently shifting from batch-wise production processes to continuous manufacturing. This is illustrated by the recent introduction of two new drugs on the market, i.e., Orkambi® (Vertex Pharmaceuticals) and Prezista® (Johnson & Johnson), which are produced by continuous manufacturing. In continuous processes, all unit operations are integrated in a single production line with continuous feeding of raw materials and the concomitant removal of finished products. This manufacturing approach results in several advantages, like avoiding scale-up issues, reduction of cycle times, reducing production costs, faster product release, increase in flexibility and efficiency, improved product quality (uniformity) and smaller manufacturing installations compared to batch processing.

In the development of continuous alternatives for batch-wise pharmaceutical manufacturing processes, the focus till now was mainly on solid dosage forms. However, continuous processing of therapeutic biologicals, both up- and downstream, is also of major importance [3]. Freeze-drying is often an essential step in the formulation of these biopharmaceuti-

cals to avoid water-mediated degradation during storage and distribution [4]. Hence, the lyophilization process should be integrated in the continuous production chain of biopharmaceutical drug products. In this respect, an innovative continuous freeze-drying concept for unit doses is proposed, resolving the disadvantages related to batch freeze-drying outlined in the introductory chapter [5].

5.2 History of continuous freeze-drying

In the past decades, several attempts have been made towards continuous freeze-drying. Most of the developed technologies were intended for the continuous freeze-drying of bulk material instead of unit doses (e.g., glass vials). These technologies have been described in patents, most of them being filed before 1990 and now expired. In one of the proposed concepts, frozen bulk material is continuously fed onto a vibrating carrier with upward channels to guide the drying material towards the discharge hopper, while providing energy through microwaves or via electric heating of these carriers, all under vacuum [6]. Another system is based on freezing the liquid as a thin sheet which is broken in small particles before being fed onto a chilled conveyor belt in an evacuated chamber with radiant heat sources [7]. For a third system, wet slurry is forced through pores of a chilled plate where it is frozen while sublimation takes place upon exit in a chamber of reduced pressure [8]. As continuous freeze-drying requires a continuously operating cold trap, several adapted condenser systems have been developed based on alternating between two or more refrigerated coils or surfaces [9]. Alternatively, the use of chemical desiccants to sequester the sublimating water vapour has been proposed [10].

The CONRAD™ freeze-dryer (GEA Group) is a commercialized large scale freeze-drying plant which allows the continuous processing of high-volume food products, such as instant coffee [11]. The product is frozen, either fast or slow, and broken into granules which are collected in the buffer tank. The frozen granules are loaded on trays which are brought inside the dryer cabinet through an airlock, where they are stacked. A full stack of trays is moved to the first drying zone. Here, each tray is located between two heating plates through which hot water is circulated. These plates make no contact, hence, energy transfer to the product on the trays takes place by radiation. The dryer cabinet contains multiple of these drying zones in sequence. For each zone, the temperature of the water running through the heatable plates can be adjusted to the required drying characteristics. At the end of the process, the trays exit the dryer cabinet through an airlock and the dried

product is collected from the trays. Inside the cabinet, an alternating condenser system is installed which allows continuous freeze-drying of the food products.



Figure 5.1: The CONRAD™ freeze-drying plant from GEA Group [11]

Despite all the effort, continuous bulk freeze-drying did not break through in the pharmaceutical industry. Continuous pharmaceutical freeze-drying is desired to be conducted in unit doses because of the following reasons:

- **Compatibility with handling equipment:** The currently used handling equipment before (filling) and after (capping and packaging) conventional freeze-drying is designed for unit doses. Filling of freeze-dried bulk powder into unit doses is not straightforward, and less accurate compared to the filling of aqueous solutions.
- **Stringent sterility requirements:** Continuous bulk freeze-drying systems do not allow aseptic processing. Furthermore, it is straightforward to filtrate solutions before filling and maintain the sterility during (continuous) freeze-drying, while sterile filling of powder after bulk freeze-drying would be more challenging.
- **Regulatory requirements:** Tracing and tracking of individual doses is impossible with bulk freeze-drying.

Approximately 20 years ago, the first concept for continuous freeze-drying of unit doses has been proposed [12]. Individual vessels are loaded into racks, with the opening directed downward. The vessels are washed and sterilized using hot air, before they are moved to

the fill and freezing section. Here, vessels are gripped by a multi-fingered robotic arm and rotated horizontally along their longitudinal axis at high velocity. During rotation, the aqueous formulation is filled in the vessels, resulting in a uniform spread product over the inner vial wall. The rotating vessels are moved over nozzles from which cold gas (-150°C) is blown, leading to a frozen shell. The vessels are returned to the rack, which is maintained at sufficiently cold temperature to avoid melting. Optionally, after this step, the vessels can be turned to have the opening directed upward. The racks filled with frozen vials is entered inside the vacuum drying tunnel through an airlock, where they are placed on a conveyor. Heater blocks are lowered over the vessels to provide direct heat over the entire surface of the vessel for ice sublimation. By raising the heater blocks and indexing the conveyor, the racks are moved to the subsequent heater block until the final dried product is obtained. The heater blocks can each be set to a different temperature, hence, the vessels can be dried according to the required drying characteristics. The rack containing dried vessels is removed from the drying tunnel via an airlock, before they are stoppered and capped. The basis of this continuous freeze-drying concept, i.e., shell freezing, was described before in the context of several other freeze-drying technologies [13–16].

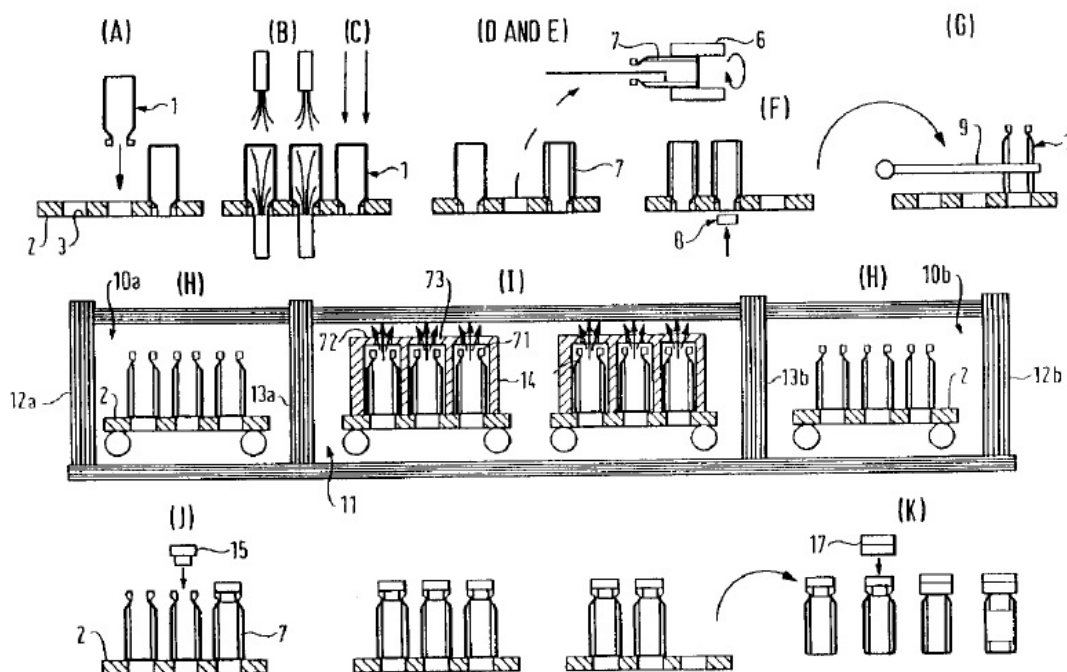


Figure 5.2: Illustrative overview of the continuous freeze-drying concept proposed by Oughton et al. [12]

However, the described technology lacks several important aspects which are indispensable for the continuous freeze-drying of pharmaceutical unit doses:

- Freezing is not possible via a programmed cycle (e.g., a freezing rate and an annealing step, which are crucial steps in pharmaceutical freeze-drying, cannot be set).
- Vials are placed in cartridges and then processed together, hence making individual vial steering and controlled processing impossible.
- Homogeneous energy transfer for sublimation and desorption (i.e., during primary and secondary drying, respectively) is suggested, but no concrete solutions are provided.
- No continuous process monitoring and control solution is implemented in the technology, whereas continuous manufacturing requires continuous process monitoring and control.

Finally, two emerging technologies are worth mentioning. Spray freeze-drying is applied to produce free-flowing powders with different particle sizes and various densities suitable for nasal, pulmonary (low density) and needle-free epidermal applications (high density) [17]. The Active Freeze-Drying technology of Hosokawa Micron B.V. results in fine, dried particles by dynamically freezing the material and by applying forced motion during the sublimation step, however, in a non-continuous way [18].

5.3 Innovative continuous and controlled freeze-drying concept for unit doses

More specific concepts and engineering know-how to design and develop a system for continuous freeze-drying of pharmaceutical unit doses has been developed [5]. At the start of the continuous freeze-drying process, sterile glass vials are aseptically filled with the aqueous drug formulation before they are transferred to the freezing unit. Here, the vials are gripped at their cylindrical walls and rapidly rotated (at approximately 4000 rotations per minute (rpm)) along their longitudinal axis to form a thin layer of product which is spread over the entire inner vial wall (Figure 5.3). When a homogeneous product layer is obtained, the flow of a cold, inert and sterile gas cools the solution, leading to the induction of ice nucleation. Both the temperature and the flow of the gas can be adapted to obtain a specific cooling regime, varying from very fast to slow cooling. At the end of the primary spin freezing step, when the product temperature is below the eutectic temperature T_e or

glass transition temperature T'_g for crystalline or amorphous products, respectively, the product is solidified over the entire inner vial wall resulting in a thin product layer.

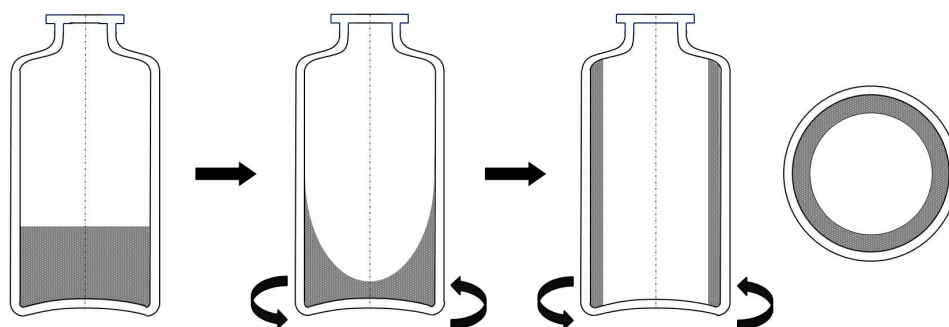


Figure 5.3: Illustration of the spin freezing step: glass vials containing the aqueous drug formulation are rapidly rotated along their longitudinal axis to form a thin layer of product while the flow of a cold, inert and sterile gas cools the solution

The spin frozen vials are continuously transferred to a long belt in a temperature-controlled chamber, which allows further crystallisation and solidification of the solutes under standardized conditions, i.e., annealing. After obtaining the desired morphological structure during this secondary freezing step, the spin frozen vials are further processed to the primary drying unit. Here, the pressure is kept at a constant value between 10 to 30 Pa. The freezing and primary drying unit are separated by an appropriate load-lock system to facilitate the vial transfer without disturbing the specific conditions of pressure and temperature in each chamber, guaranteeing the continuity of the process [19].

Continuous primary drying requires a uniform and adequate energy supply towards the entire vial surface to achieve an efficient and homogeneous drying behaviour. This energy transfer can be provided via conduction, by placing spin frozen vials in individual, close-fitting temperature-controlled pockets. Alternatively, IR radiation could be applied to provide the heat needed for drying of the spin frozen vials. Each spin frozen vial is rotating along its longitudinal axis in front of an individual IR heater, which can be controlled at a specific temperature (Figure 5.4). Rotation of the vials is a prerequisite to obtain a uniform heat transfer. The belt of spin frozen vials moves in discrete steps ensuring that each vial is in a known position, centred in front of a single IR heater. The individual IR heaters allow to individualize and optimize the drying trajectory for each spin frozen vial. Non-contact IR radiation offers some benefits over conduction as energy transfer method

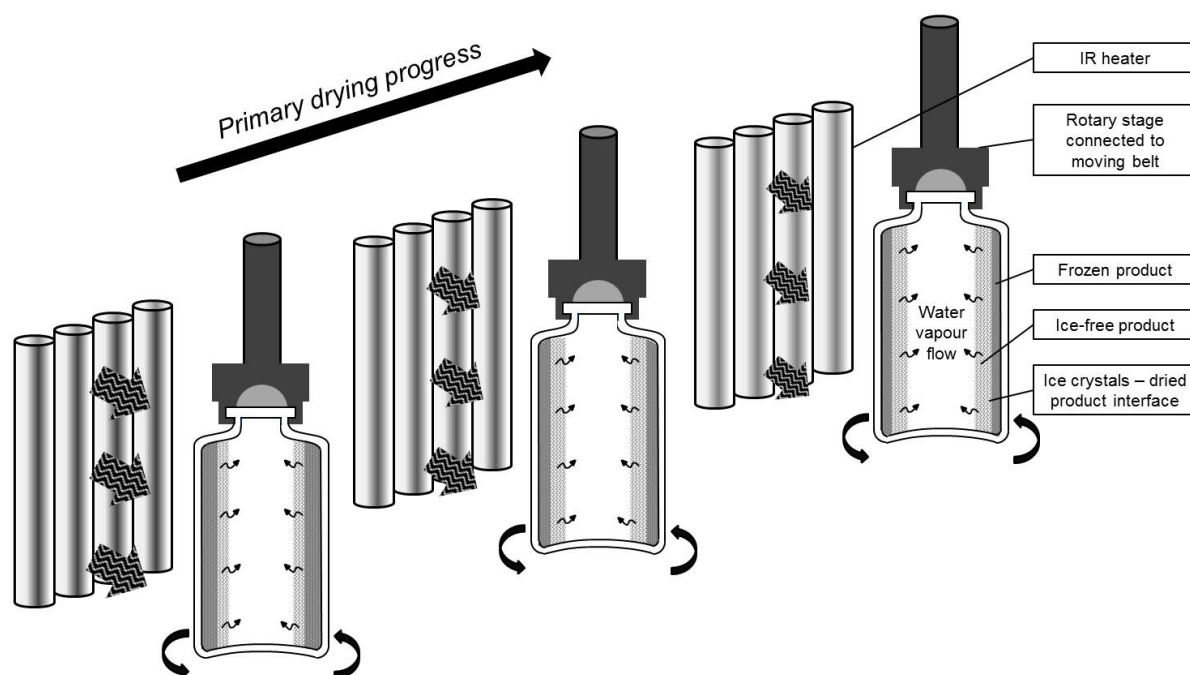


Figure 5.4: Illustration of the IR assisted continuous primary drying of spin frozen vials, rotating along their longitudinal axis in front of individual IR heaters

of preference. A whole range of vial types can be processed without the need to customise the heatable pockets to different vial dimensions. In addition, monitoring and control of the drying behaviour is facilitated in non-enveloped vials. Lastly, the thermal inertia of the heatable pockets is higher compared to the IR heaters, which allows a faster response to changing input parameters.

During the last step of the continuous freeze-drying process, secondary drying, any remaining unfrozen water is removed by desorption until the final dried product with the desired residual moisture content is obtained. Depending on whether secondary drying requires a pressure level different from primary drying, a second continuous drying unit is necessary, separated from the first one by an appropriate load-lock system for vial transport. At the end of the continuous lyophilization process, vials are removed from the vacuum conditions in the drying module via another load-lock system and transferred to the final unit, where stoppering and capping of the processed vials under sterile nitrogen conditions takes place.

Lastly, figure 5.5 shows schematically that increasing the vial throughput (i.e., scale-up) can be simply done by adding parallel lines in the continuous freeze-drying technology modules (i.e., LEGO™ principle).

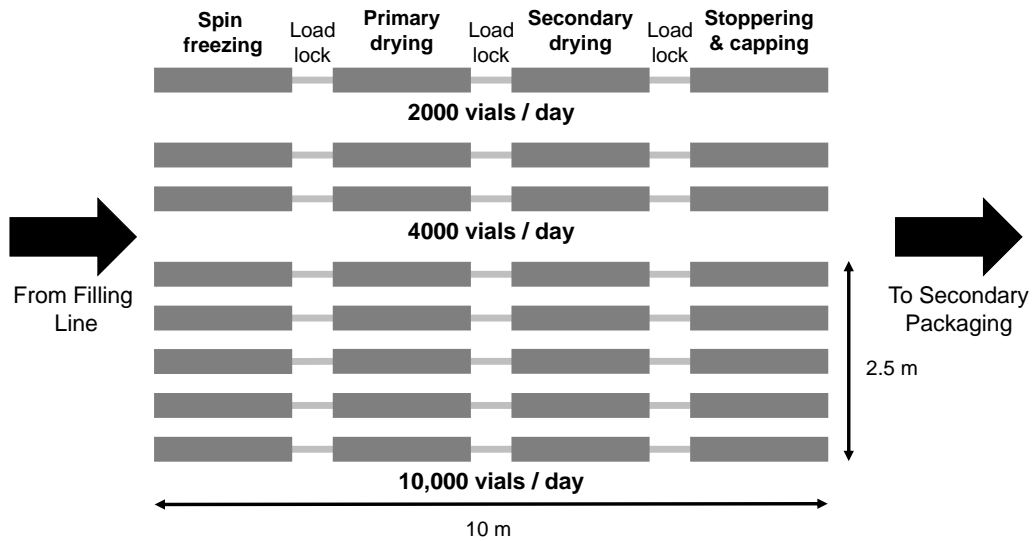


Figure 5.5: Parallel lines in the continuous freeze-drying technology avoiding scale-up re-optimization and validation

Bibliography

- [1] K. Plumb. Continuous processing in the pharmaceutical industry: Changing the mind set. *Chem. Eng. Res. Des.*, 83:730–738, 2005.
- [2] C. Vervaet, J. Verduyck, J. P. Remon, and T. De Beer. Continuous Processing of Pharmaceuticals. In *Encyclopedia of Pharmaceutical Science and Technology*. Taylor and Francis, New York, 2013.
- [3] A. Jungbauer. Continuous downstream processing of biopharmaceuticals. *Trends Biotechnol.*, 31:479–492, 2013.
- [4] T. Jennings. *Lyophilization: Introduction and basic principles*. Informa healthcare, New York, 2008.
- [5] J. Corver. Method and system for freeze-drying injectable compositions, in particular pharmaceutical. WO2013036107, 2013.
- [6] M. Fuentevilla. Method and Apparatus for Continuous Freeze Drying. US3264747, 1966.
- [7] J. L. Mercer and L. A. Rowell. Continuous freeze drying system. US3648379, 1972.
- [8] H. B. Arsem. Continuous freeze drying. US4590684, 1986.
- [9] V. A. Liobis. Freeze drying apparatus. US3516170, 1970.
- [10] M. C. Parkinson. Method and apparatus for continuous freeze drying. US4561191, 1985.
- [11] CONRAD Freeze Dryer, 2017.
- [12] D. M. A. Oughton, P. R. J. Smith, and D. B. A. MacMichael. Freeze-drying process and apparatus. US5964043, 1999.
- [13] F. J. L. Robinson and L. G. Beckett. Improvements in or relating to vacuum freezing and/or vacuum freeze drying methods and apparatus . GB784784, 1956.
- [14] L. M. A. Rieutord. Device for the freezing of a product to be lyophilized and other products. US3195547, 1965.
- [15] S. M. Broadwin. Centrifugal freeze drying apparatus. US3203108, 1965.

-
- [16] M. R. Hilleman and W. M. Hurni. Lyophilization process. EP0048194, 1982.
- [17] S. Wanning, R. Süverkrüp, and A. Lamprecht. Pharmaceutical spray freeze drying. *International Journal of Pharmaceutics*, 488:136–153, 2015.
- [18] A. Touzet, F. Pfefferlé, P. van der Wel, A. Lamprecht, and Y. Pellequer. Active Freeze Drying for production of nanocrystal-based powder: a pilot study. *International Journal of Pharmaceutics*, 2017.
- [19] B. G. Ramsay. Vacuum chamber load lock structure and article transport mechanism. US 6609877 B1, 2003.

CHAPTER 6

Non-contact infrared-mediated heat transfer during continuous freeze-drying of unit doses

Redrafted from: Van Bockstal P.J., De Meyer L., Corver J., Vervaet C., De Beer T. (2017) *Noncontact infrared-mediated heat transfer during continuous freeze-drying of unit doses*. *Journal of Pharmaceutical Sciences*, 106, 71-82.

6.1 Introduction

The continuous processing of spin frozen vials requires an efficient heat transfer during primary drying. Due to the increase of the surface available for sublimation and the corresponding reduction of the layer thickness, the primary and secondary drying efficiency can be highly improved compared to batch freeze-drying. To achieve a homogeneous and efficient drying behaviour, the thin product layer requires an adequate and uniform heat transfer towards the entire vial wall. The energy necessary for sublimation can be provided through conduction by individual pockets for each vial, allowing individual temperature-regulation [1]. Alternatively, non-contact energy provision via IR radiation could offer major benefits as opposed to the inefficient heat transfer during traditional batch freeze-drying. IR radiation is a type of electromagnetic radiation allowing energy transport between two bodies with a different absolute temperature which are not in direct contact [2]. This mechanism could be applied to provide the heat transfer to the spin frozen vials during the primary and secondary drying step of the continuous concept (Figure 6.1). The application of IR radiation offers a major advantage as energy is provided to the vials without direct contact with the heat source. This way it is not necessary to envelop

processed vials by heatable pockets which eases the monitoring of the drying progress at the level of each individual vial. Additionally, several vial types with different dimensions can be processed without the need to adapt the heatable pockets to obtain a homogeneous energy transfer.

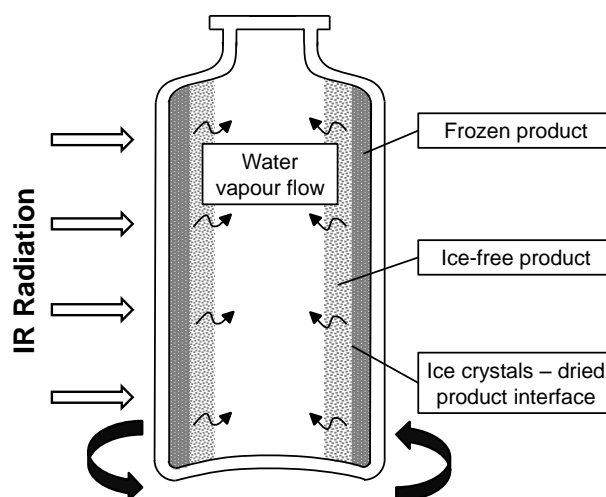


Figure 6.1: Illustration of IR mediated primary drying of spin frozen vials: IR radiation is provided to one side of the vial, which is slowly rotating along its longitudinal axis to assure homogeneous energy transfer

The high potential and added value of IR mediated heat transfer to the continuous freeze-drying concept has to be thoroughly evaluated. The aim of this study was to test whether IR radiation is applicable for the primary and secondary drying of spin frozen vials. The influence of various process and formulation parameters upon the mass of sublimated ice after 15 minutes of primary drying (i.e., sublimation rate) and the total drying time was evaluated. This study is the first step in the evaluation of the feasibility of IR mediated heat transfer in the continuous processing of spin frozen vials.

6.2 Materials and methods

6.2.1 Experimental set-up

A 10 mL type I glass vial (Schott, Müllheim, Germany) containing the required volume of a specific formulation was vertically rotated along its longitudinal axis in a vial holder at approximately 2900 rpm. As a result, the product was spread across the whole vial wall,

after which the rotating vial was immersed into liquid nitrogen for 40 ± 5 s to completely solidify the product. After spin freezing, the vial was transferred from the vial holder to the drying chamber within 15 ± 5 s, ensuring that the glass transition temperature of the maximum freeze-concentrated formulation T'_g or the eutectic temperature T_e of the formulation was never exceeded.

After spin freezing, drying was performed in the drying chamber of an Amsco FINN-AQUA GT4 freeze-dryer (GEA, Köln, Germany) with the shelves pre-cooled at -10 °C. The experimental set-up consisted of two IR heaters (Weiss Technik, Zellik, Belgium) facing each other (Figure 6.2). The spin frozen vial was placed exactly in between these IR heaters at a defined distance. The vial was continuously rotating at a constant velocity of 5 rpm which was necessary to obtain a homogeneous energy transfer from the IR heaters to the vial. Immediately after transferring the vial to the drying chamber, the pressure was decreased until the desired vacuum was reached. Within 5 minutes the pressure in the drying chamber was below the triple point of water, avoiding exceedance of T'_g or T_e of the formulation. After exactly 17 minutes, the time necessary to achieve the desired pressure level, the IR heaters were activated. In a first series of experiments, the system was aerated exactly 15 minutes after activation of the IR heaters. Immediately thereafter, the amount of sublimated ice was determined gravimetrically. In a second series of experiments, the process was stopped after secondary drying was finished.

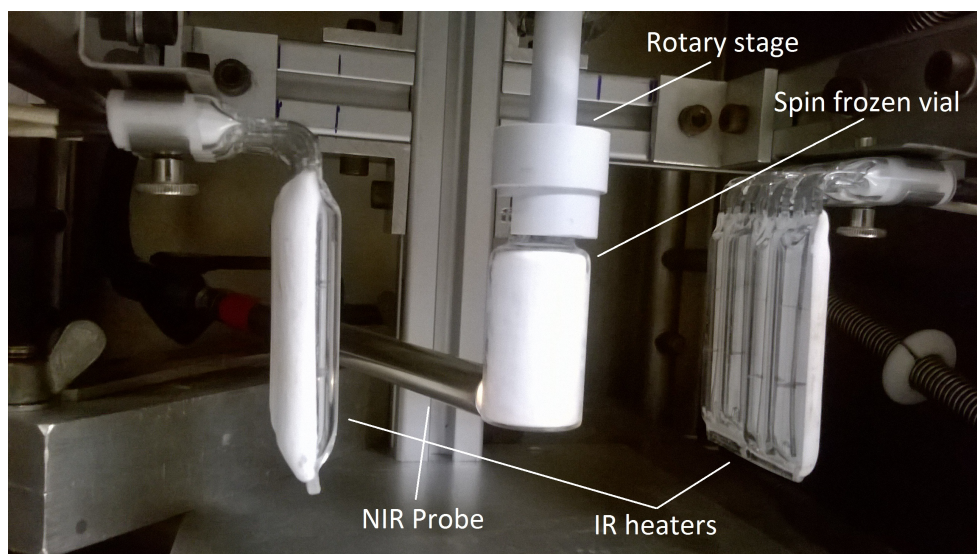


Figure 6.2: Experimental drying set-up with in-line NIR monitoring

6.2.2 Experimental design methodology

A D-optimal interaction screening design consisting of 36 experiments, expanded with 2 double centre points, was developed using MODDE Pro (Version 11.0.0, Umetrics, Umeå, Sweden) to evaluate the first response, i.e., the mass of sublimated ice after 15 minutes of primary drying. The length of this time span was decided during preliminary experiments to make sure sublimation was not finished within this period. The factors examined in this first design, from now on referred to as DoE 1, are listed in Table 6.1, including their examined lowest and highest level, while an overview of all individual experiments is given in Table 6.2. The electrical power supplied to the IR heaters is expressed in units of watt, calculated by the product of the electric current I and the voltage U provided by the voltage source. This value is a measure for the temperature of the IR heaters. The volume of each formulation to obtain the desired layer thickness was calculated based on the dimensions of the 10 mL type I glass vials. A layer thickness of 0.5, 1.0 and 1.5 mm corresponds respectively to a volume of 1.35 mL, 2.65 mL and 3.90 mL. The distance between the IR heaters and the vial is defined from the edge of the vial.

Table 6.1: Overview factors DoE 1 with lowest and highest level

Factors	Level		Unit
	-	+	
<i>Quantitative</i>			
Electrical power	14	36	W
Distance between IR heaters and vial	2	6	cm
Chamber pressure	10	30	Pa
Product layer thickness	0.5	1.5	mm
<i>Qualitative</i>			
Formulation	Formulation 1–5		

The first four variables in Table 6.1 are quantitative factors which can be set according to a continuous scale. The last factor, the five different model formulations used during the experiments, is a qualitative factor. An overview of the different formulations is provided in Table 6.3. These formulations were selected from previous studies because they have a different dried product mass transfer resistance profile in function of the dried layer thickness [3, 4]. Formulations 1 and 5 were used for the centre points of DoE 1. Trehalose was obtained from Cargill (Minneapolis, MN, USA). Polysorbate 20, sodium chloride, lactose and mannitol were purchased from Fagron (Waregem, Belgium). L-Histidine and glycine

Table 6.2: Overview experiments DoE 1, the experiments in bold were performed twice (centre points)

Experiment number	Electrical power (W)	Distance heater-vial (cm)	Chamber pressure (Pa)	Layer thickness (mm)	Formulation
1	14	2	10	0.5	Formulation 1
2	36	6	10	0.5	Formulation 1
3	36	2	30	0.5	Formulation 1
4	14	6	30	0.5	Formulation 1
5	36	2	10	1.5	Formulation 1
6	14	6	10	1.5	Formulation 1
7	14	2	30	1.5	Formulation 1
8	36	6	30	1.5	Formulation 1
9	36	2	10	0.5	Formulation 2
10	14	6	10	0.5	Formulation 2
11	14	2	30	0.5	Formulation 2
12	36	6	30	0.5	Formulation 2
13	14	2	10	1.5	Formulation 2
14	36	6	10	1.5	Formulation 2
15	36	2	30	1.5	Formulation 2
16	14	6	30	1.5	Formulation 2
17	36	2	10	0.5	Formulation 3
18	14	6	10	0.5	Formulation 3
19	14	2	30	0.5	Formulation 3
20	36	6	30	0.5	Formulation 3
21	14	2	10	1.5	Formulation 3
22	36	6	10	1.5	Formulation 3
23	36	2	30	1.5	Formulation 3
24	14	6	30	1.5	Formulation 3
25	36	2	10	0.5	Formulation 4
26	14	6	10	0.5	Formulation 4
27	36	6	30	0.5	Formulation 4
28	36	6	10	1.5	Formulation 4
29	14	2	30	1.5	Formulation 4
30	36	2	30	1.5	Formulation 4
31	36	6	10	0.5	Formulation 5
32	36	2	30	0.5	Formulation 5
33	14	2	10	1.5	Formulation 5
34	14	6	10	1.5	Formulation 5
35	36	2	30	1.5	Formulation 5
36	36	6	30	1.5	Formulation 5
37	25	4	200	1	Formulation 1
38	25	4	200	1	Formulation 5

were acquired from Sigma-Aldrich (Saint Louis, MO, USA). Sucrose was purchased from VWR (Radnor, PA, USA).

Table 6.3: Overview of the five model formulations included as a qualitative factor in DoE 1 and 2

Formulation	Composition	
	Component	Concentration
Formulation 1	Trehalose	45 mg/mL
	Polysorbate 20	0.1 mg/mL
	Histidine	5 mM (pH 6)
Formulation 2	Lactose	30 mg/mL
	Sucrose	3.42 mg/mL
	Glycine	3.75 mg/mL
	NaCl	0.58 mg/mL
Formulation 3	Mannitol	30 mg/mL
	Sucrose	3.42 mg/mL
	Glycine	3.75 mg/mL
	NaCl	0.58 mg/mL
Formulation 4	Lactose	30 mg/mL
Formulation 5	Sucrose	30 mg/mL

Similar to DoE 1, a second D-optimal interaction screening design was developed, resulting in 28 experiments with additional 2 double centre points, to evaluate the primary, secondary and total drying time and the transition width between primary and secondary drying. Comparison of the primary and total drying time will emphasize the differences between the tested model formulations, which allows a more appropriate evaluation of the impact of the dried product mass transfer resistance on the primary drying behaviour. An overview of the examined factors for this second experimental design, from now on referred to as DoE 2, is provided in Table 6.4. All experiments of DoE 2 are listed in Table 6.5. In this design the same factors were examined as in the former one, except for the chamber pressure, which was kept constant at 20 Pa during each experiment. The reason for this will be explained in the results section. Both the endpoint of primary and secondary drying were determined via in-line NIR spectroscopy [5, 6]. Hence, as opposed to DoE 1, the drying process was not interrupted during primary drying, but continued until secondary drying was finished. Similar to DoE 1, formulations 1 and 5 were used for the centre points.

Table 6.4: Overview factors DoE 2 with lowest and highest level

Factors	Level		Unit
	-	+	
<i>Quantitative</i>			
Electrical power	14	36	W
Distance between IR heaters and vial	2	6	cm
Product layer thickness	0.5	1.5	mm
<i>Qualitative</i>			
Formulation	Formulation 1–5		

MODDE Pro was used for the analysis of both experimental designs. Regression models for each response were calculated by MLR. All factors were scaled and centred, which makes the regression coefficients for the different factors comparable. Each quantitative factor was set to +1 and -1 for their highest and lowest value, respectively. Qualitative factors require an alternative approach via a mathematical re-expression (regression coding). A k-level qualitative parameter will be expanded into k-1 artificial categorical variables, as illustrated for the qualitative factor Formulation (*For*) in Table 6.6. Each expanded term results in one regression coefficient, which in our case led to four coefficients for level 2 to level 5 (regular mode). Additionally, the level 1 coefficient can be calculated as the negative sum of the coefficients of the other expanded terms (extended mode).

The regression coefficient of a specific factor represents the quantitative change in response value when this factor is increased from its average to its high level, keeping all other factors at their average value. The effect of a specific factor is defined as the quantitative change in response value when this factor is increased from its low to its high level, keeping all other factors at their average value. Based on these definitions, the effect of a factor is twice the corresponding coefficient. The constant term is related to the response value at the design centre point, with all factors at their average level. For all regression coefficients the 95% confidence interval was calculated. Factor or interactions between factors were considered significant if the 95% confidence interval of the corresponding regression coefficient did not contain zero.

Table 6.5: Overview experiments of DoE 2, the experiments in bold were performed twice (centre points)

Experiment number	Electrical power (W)	Distance heater-vial (cm)	Layer thickness (mm)	Formulation
1	14	2	0.5	Formulation 1
2	36	2	0.5	Formulation 1
3	36	6	0.5	Formulation 1
4	14	2	1.5	Formulation 1
5	36	2	1.5	Formulation 1
6	14	6	1.5	Formulation 1
7	36	6	1.5	Formulation 1
8	14	2	0.5	Formulation 2
9	36	2	0.5	Formulation 2
10	14	6	0.5	Formulation 2
11	36	6	0.5	Formulation 2
12	36	2	1.5	Formulation 2
13	14	6	1.5	Formulation 2
14	14	2	0.5	Formulation 3
15	36	2	0.5	Formulation 3
16	14	6	0.5	Formulation 3
17	14	2	1.5	Formulation 3
18	36	6	1.5	Formulation 3
19	14	2	0.5	Formulation 4
20	36	6	0.5	Formulation 4
21	14	2	1.5	Formulation 4
22	36	2	1.5	Formulation 4
23	14	6	1.5	Formulation 4
24	36	2	0.5	Formulation 5
25	14	6	0.5	Formulation 5
26	14	2	1.5	Formulation 5
27	36	2	1.5	Formulation 5
28	36	6	1.5	Formulation 5
29	25	4	1	Formulation 1
30	25	4	1	Formulation 5

Table 6.6: Regression coding of the five-level qualitative factor *Formulation* (For)

Level of factor	Expanded term			
	<i>For</i> (<i>For2</i>)	<i>For</i> (<i>For3</i>)	<i>For</i> (<i>For4</i>)	<i>For</i> (<i>For5</i>)
<i>For1</i>	−1	−1	−1	−1
<i>For2</i>	1	0	0	0
<i>For3</i>	0	1	0	0
<i>For4</i>	0	0	1	0
<i>For5</i>	0	0	0	1

6.2.3 NIR spectroscopy

Diffuse reflectance NIR spectra were continuously in-line collected with an Antaris™ II Fourier-Transform NIR spectrometer (Thermo Fisher Scientific, Erembodegem, Belgium), equipped with a quartz halogen lamp, a Michelson interferometer and an InGaAs detector. The fibre optic probe was implemented in the drying chamber at a distance of 0.5 ± 0.1 mm near the base of the vial without hampering or disturbing the rotation of the vial (Figure 6.2). As drying progresses from the centre of the vial to the inner vial wall, in-line NIR spectroscopy allowed the detection of complete ice and water removal, i.e. the endpoint of primary and secondary drying, respectively. Every 20 seconds a NIR spectrum was collected in the $4500\text{--}10000\text{ cm}^{-1}$ region with a resolution of 16 cm^{-1} and averaged over 4 scans. The illumination spot size obtained with the NIR probe was approximately 28 mm^2 . Due to rotation of the vial during the measurements, each spectrum was collected at a different position of the cake on a specific height. It was assumed that this monitored part is representative for the whole cake, due to the uniform layer thickness over the entire vial wall.

6.2.4 Multivariate data analysis

The collected NIR spectra were separately analysed for each individual experiment of DoE 2 using the multivariate data analysis software SIMCA (Version 14.0.0, Umetrics, Umeå, Sweden). The NIR spectra collected before activation of the heaters were removed from each dataset. The Savitzky-Golay filter was applied to smooth the spectra: a quadratic polynomial function was fitted to a moving sub-model, each containing fifteen data points. Additionally, Standard Normal Variate (SNV) preprocessing was applied to eliminate the

additive baseline offset variations and multiplicative scaling effects in the spectra which may be caused by small variations in distance between the NIR probe and the rotating glass vial and possible differences in product density [7]. Principal Component Analysis (PCA) was then used for the analysis of the preprocessed and mean-centred NIR spectra.

PCA is an unsupervised multivariate projection method which extracts and displays the variation in the data set [8, 9]. The original variables, e.g. the individual wave numbers of the NIR spectra, are replaced by a new set of latent variables, named principal components (PCs). These PCs are sequentially acquired by an orthogonal, bilinear decomposition of the data matrix. Each component explains most of the remaining variability in the data. PCs are composed of a score and a loading vector. The score vector contains a score value for each spectrum, which describes its quantitative relation to the other spectra. The loading vector provides qualitative information about which spectral features present in the original observations are captured by the corresponding component.

6.3 Results and Discussion

6.3.1 Analysis of DoE 1

The absolute mass of ice sublimated after 15 minutes of primary drying of the individual experiments ranged from approximately 0.5 g up to 1.2 g. This corresponded to a relative amount of 36.5% up to 80% and 15% up to 30% of the total ice mass for the thinnest and thickest product layers, respectively. Evaluation of the raw data (responses) indicated there were no peculiarities in the results: the variability in sublimated ice mass between the repeated experiments was much less than the overall variability of all DoE 1 experiments. Also, data transformation before regression analysis was not needed, due to the normal distribution of the response data. The regression coefficients, computed via MLR fitting, are displayed for each factor and factor interaction, including the 95% confidence interval, in the extended coefficient plot (Figure 6.3).

The electrical power supplied to the IR heaters was the factor with the highest influence on the amount of sublimated ice, with a regression coefficient of 0.13966 g (Figure 6.3). Increasing the electrical power from 14 W to 36 W, keeping all other factors at their average, hence leads to an increase of 0.279 g or 45% in the amount of sublimated ice.

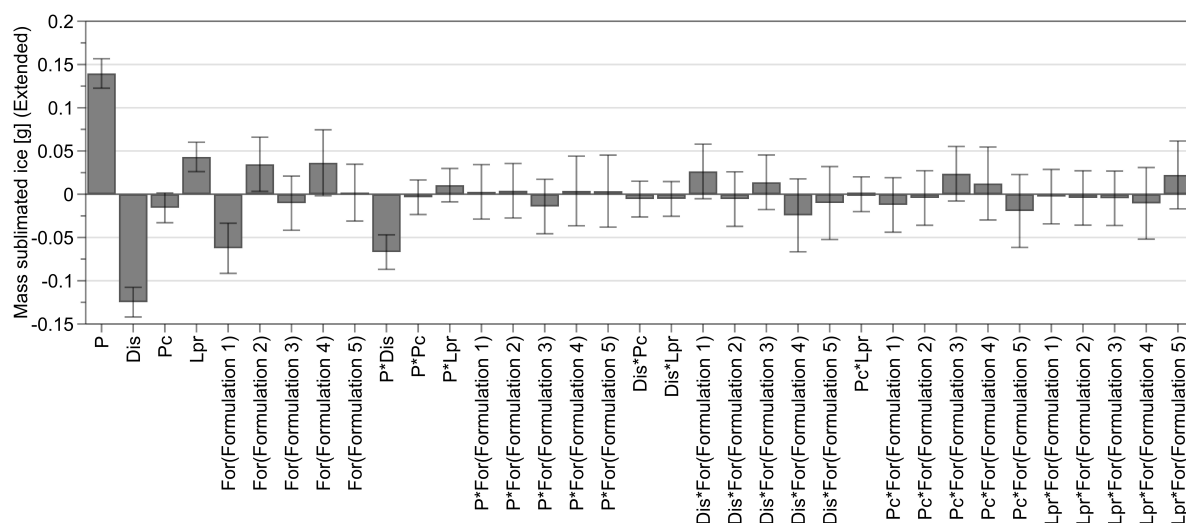


Figure 6.3: Extended coefficient plot DoE 1: Regression coefficients displayed including 95% confidence interval, with electrical power (P), distance between IR heaters and vial (Dis), chamber pressure (Pc), thickness of the product layer (Lpr) and the expanded model terms related to the qualitative factor 'Formulation' ($For(For1)$, $For(For2)$, $For(For3)$, $For(For4)$ and $For(For5)$)

An increase of the electrical power can be associated with a higher temperature of the IR heater. More radiant energy was provided to the spin frozen vial, which explains the faster ice removal. The distance between the IR heaters and the glass vial had a large, negative impact on the response variable (regression coefficient -0.12478 g) (Figure 6.3). Altering the distance between the IR heaters and the glass vial from 2 to 6 cm was associated with a decrease of 0.250 g or 39% in the mass of sublimated ice, with all other factors at their average level. The efficiency with which the IR heaters provided energy to the glass vial was influenced by the view factor. The view factor is a measure of the fraction of radiation emitted by the IR heaters that hits the glass vial [10]. This dimensionless number, between 0 and 1, is only determined by the geometric orientation of both surfaces (i.e., the IR heater and the glass vial). A larger distance between the IR heaters and the glass vial decreased the view factor. Therefore, a smaller part of the emitted energy reached the vial, which resulted in the lower sublimation rate.

The chamber pressure had no significant impact on the response value (regression coefficient -0.015711 g) (Figure 6.3). The energy transfer via IR radiation does not require direct contact and is mainly determined by the temperature difference between the IR

heater and the spin frozen vial, given by the Stefan-Boltzmann equation [10]:

$$P = A_{rad}F\sigma(\epsilon T_{rad}^4 - aT_{v,o}^4) \quad (6.1)$$

with P the power radiated by the IR heater to the spin frozen vial (W), A_{rad} the surface of the IR heater (m^2), F the view factor (-), σ the Stefan-Boltzmann constant ($5.67 \cdot 10^{-8} \text{ W m}^{-2} \text{ K}^{-4}$), ϵ the emissivity of the IR heater (-), T_{rad} the temperature of the IR heater (K), a the absorptivity of the target surface () and $T_{v,o}$ the temperature of the spin frozen vial (K). The energy flux via IR radiation is not influenced by the gas density between the vial and the heat source, which resulted in the insignificant impact of the chamber pressure on the sublimation rate. However, when the energy transfer to spin frozen vials is provided by conduction, the chamber pressure does have a significant impact on the sublimation rate [11]. As opposed to heat transfer by radiation, direct contact is required for conductive heat transfer. Due to suboptimal contact between the stainless steel shelf and the aluminium vial holder and between this vial holder and the spin frozen vial, the conduction heat flux is enhanced with the increase in the amount of gas molecules between these surfaces. Hence the higher heat transfer is responsible for the increased sublimation rate observed at a higher pressure [11]. This phenomenon is also extensively described in batch freeze-drying: poor contact between the shelf and the bottom of the glass vials yields a higher heat transfer coefficient when the chamber pressure is increased [12, 13]. Naturally, improvement of the contact between the vial and the energy source (i.e., adaptable heatable pockets) will result in a conduction heat flux which is independent of the chamber pressure [1].

The layer thickness had a statistically significant impact on the sublimation rate (regression coefficient 0.043128 g) (Figure 6.3). Tripling the layer thickness from 0.5 mm to 1.5 mm was associated with an increase of 0.0863 g or 12% in the mass of sublimated ice, keeping all other factors at their average. Compared to other significant factors, the influence of layer thickness is relatively low, because each experiment was stopped after a fixed drying time (15 minutes) before primary drying was completely finished. Therefore, the small impact of this factor was considered irrelevant. Five different formulations were included in the experimental design, but only Formulation 1 had a small, statistically significant influence, as the sublimation rate was lower in comparison with the other formulations (regression coefficient -0.062509 g) (Figure 6.3). This formulation contained a higher concentration of solutes compared to the four other formulations (Table 6.3), which could be associated with a higher dried product mass transfer resistance and a corresponding lower sublimation rate. These results do not match the product resistance profiles in function of

the dried layer thickness provided from literature [3, 4]. However, these resistance profiles were determined under different process conditions for both freezing and primary drying, which impacts the pore size of the dried cake and therefore the dried product mass transfer resistance [14, 15]. For this reason, the literature values might not be representative for the thin layers, obtained under the applied process conditions. Finally, comparison of the total drying time for each formulation (DoE 2) should allow a more appropriate evaluation of the impact of the dried product mass transfer resistance on the drying behaviour.

Only the interaction between the factors electrical power and the distance between the IR heaters and the vial was statistically significant (regression coefficient -0.066907 g) (Figure 6.3). However, the interaction plot shows that it was only a weak interaction because both lines do not cross and there is only a small difference in slope (Figure 6.4). With the increase of the distance between the glass vial and the IR heaters, the influence of the electrical power provided to the IR heaters (i.e., temperature of the IR heaters) on the sublimation rate was reduced. This interaction is explained by the view factor, which decreased non-linearly with a larger the distance between IR heaters and vial [10].

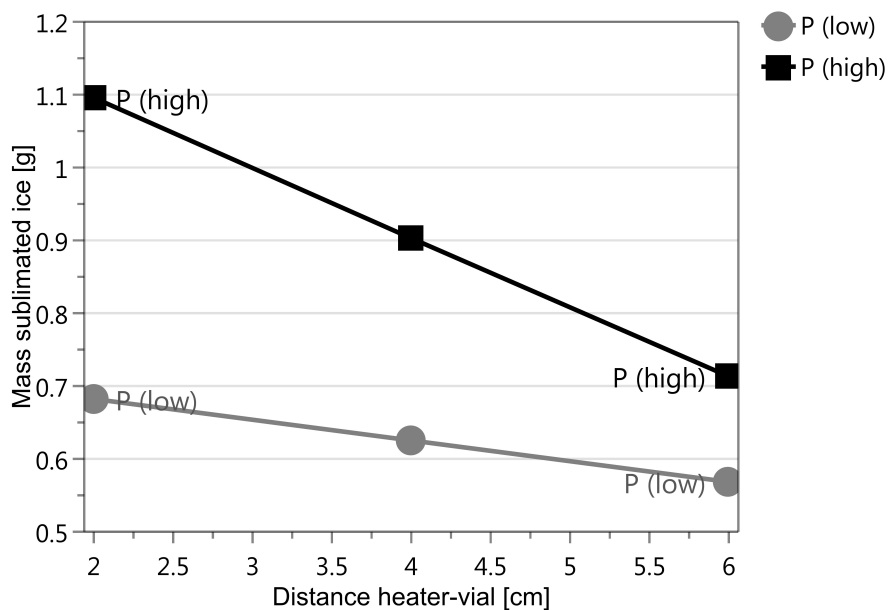


Figure 6.4: Interaction plot 'Electrical power P '*Distance between IR heaters and vial Dis ': response 'Mass of sublimated ice in 15 minutes' plotted in function of 'Distance between IR heaters and vial Dis ' for high (blue) and low (green) level of 'Electrical power P '

6.3.2 Analysis of DoE 2

NIR process analysis

The PC1 versus PC2 score scatter plot obtained after PCA of the preprocessed NIR spectra collected during one of the individual experiments of the second design (Experiment 5 of DoE 2), is shown in Figure 6.5. The main part of the spectral variability (92.6%) was explained by PC1, a smaller part of the variability was explained by PC2 (5.39%). In the loading line plots of both PCs several NIR bands were identified (Figure 6.6). The band near 4760 cm^{-1} in both PC 1 and 2 stems from the combination of O-H bending and C-O stretching of trehalose, the main component of Formulation 1 (Table 6.3) [16]. The band directed downwards near 5130 cm^{-1} in the loading plot of PC 1 originates from O-H stretching and H-O-H bending vibrations of water [17]. Similarly, the band directed upwards near 5130 cm^{-1} in the loading plot of PC 2 could also be assigned to water. The broad band directed downwards between 5500 cm^{-1} and 7000 cm^{-1} in the loading plot of PC 1 represents the change in the ice and water signal. The band directed upwards in the loadings of PC 2 near 6640 cm^{-1} originates from symmetric and asymmetric stretch of the water molecules. The loadings of both PCs clearly represent the changes in ice and water content in the sample. Analysis of the collected spectra allowed the full explanation of the chronological trends in the score plot and the link with the drying behaviour.

The NIR spectra at the start of the primary drying process were dominated by overwhelming ice bands, which indicated the presence of ice in the monitored vial (Figure 6.5 and 6.7(a)). With the progress of primary drying, there is a clear trend in the scores in PC 2, as they move along the vertical axis in the positive direction of PC 2 (Figure 6.5). This trend is visualized in the corresponding spectra (Figure 6.7(a)). The NIR bands near 5100 cm^{-1} and 6640 cm^{-1} gradually increase in intensity and become more distinct in shape with the progression of primary drying. These findings are confirmed by the loading line plot of PC 2, where both these bands are directed upwards (Figure 6.6). Ice sublimation progresses from the centre of the vial towards the inner vial wall, while NIR spectra were collected from the outside of the vial wall. The NIR light only penetrates the sample for a limited distance. Ice signals overwhelm the NIR spectra until the gradual decrease in ice layer thickness allowed the visualisation of the product, specifically the presence of residual water, besides the remaining ice signals. With further drying, the water band near 5130 cm^{-1} became more clear and a characteristic product band near 4760 cm^{-1} (i.e., trehalose) started to appear, as visualized in the spectra situated after the first inflection point in the score plot (Figure 6.5 and 6.7(b)). Simultaneously, ice signals weakened, but

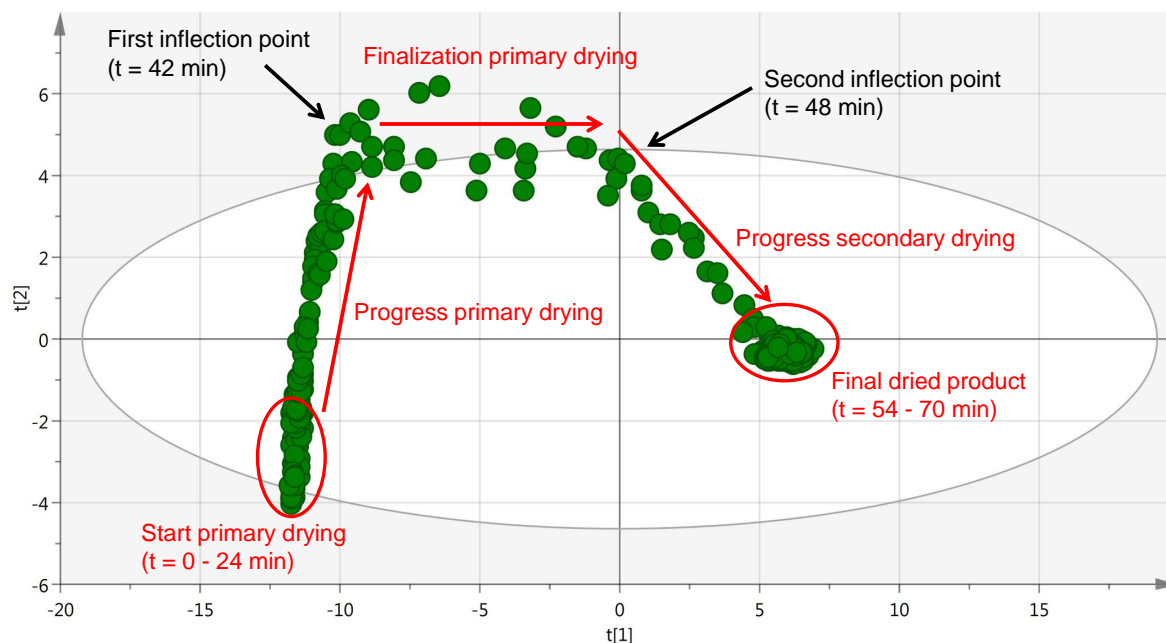


Figure 6.5: Score scatter plot including the explanation of the chronological trends; each point represents one spectrum

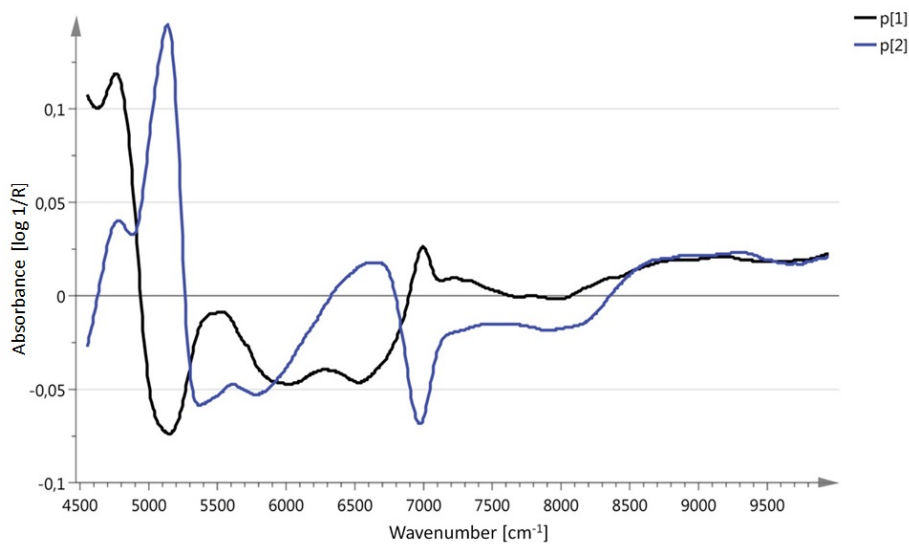


Figure 6.6: Loading line plot of PC1 (black) and PC2 (blue)

they were only completely absent in the NIR spectra displayed after the second inflection point in the score plot (Figure 6.5 and 6.7(c)). So, only at this point all ice crystals were completely sublimated and primary drying was finished at the monitored height of the

vial which is considered to be representative for the whole cake. With the reduction of the ice signals, the trehalose band near 4760 cm^{-1} increased in intensity. The small decrease in the water band near 5130 cm^{-1} is attributed to the fact that secondary drying occurs simultaneously with primary drying in ice-free regions [12]. The loadings of PC 1 confirmed this (Figure 6.6). The band assigned to trehalose is directed in the upwards direction while the bands assigned to water and ice are directed downwards. Therefore, the spectra, represented by scores, situated at the right side along the horizontal axis in the score plot contained less water and ice (Figure 6.5). In the subsequent NIR spectra, the water band at 5130 cm^{-1} gradually decreased along both PC 1 and 2 until the spectra started to cluster (Figure 6.5 and 6.7(d)). At this point the residual moisture stabilized, secondary drying was finished and the final dried product was obtained. This decrease in water content is confirmed by the loading plots of both PC 1 and 2 (Figure 6.6). The water band at 5130 cm^{-1} is directed downwards in the loading plot of PC 1 and the cluster of spectra is situated at the right side along the horizontal axis. The same water band is directed upwards in the loading plot of PC 2 and the cluster of spectra is situated at the bottom along the vertical axis.

In the score scatter plot, NIR spectra were identified in which drying had not progressed as much as in spectra collected earlier in the process. To achieve a homogeneous heat transfer, IR radiation requires the rotation of spin frozen vials during drying. As a result, each spectrum was recorded at a different, horizontal position at one specific height of the vial. This indicated that the drying progress was not completely homogeneous for the whole monitored region, although energy was equally provided. Consequently, primary drying was locally finished at different time points, which is visualized in the PC1 versus time plot (Figure 6.8). This plot shows to which extent the drying behaviour was homogeneous or not. The inhomogeneous primary drying behaviour might be explained by small deviations in layer thickness or by local differences in dried product mass transfer resistance. This effect was not observed at the end of secondary drying.

For all individual experiments the score scatter plot showed the same trends and therefore they were all analysed in a similar way. The several responses studied in the second design (end of primary drying, end of secondary drying, total drying time, transition width between primary and secondary drying) could be determined based on this PCA plot. The primary drying time was defined as the time between the collection of the first spectrum after the onset of the heaters and the spectrum following the last spectrum situated before the second inflection point in the score plot. The total drying time was defined as the time

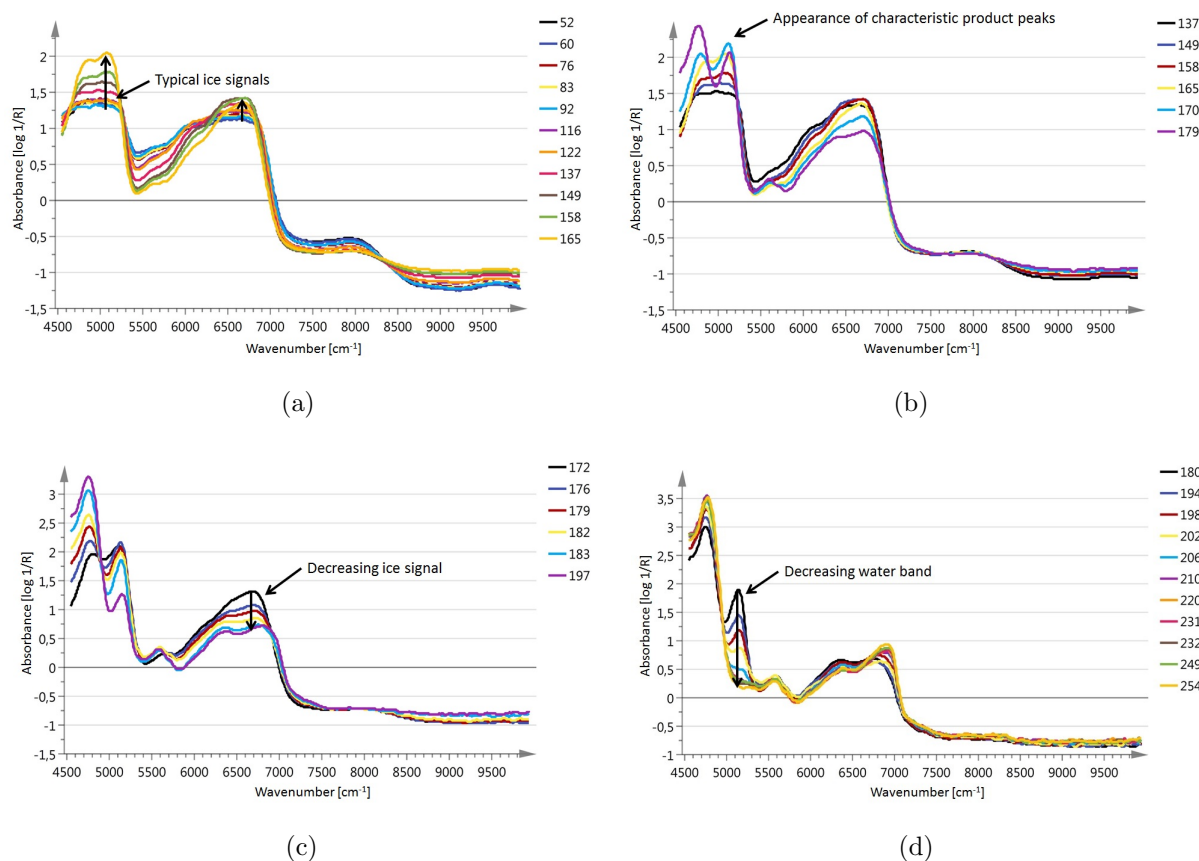


Figure 6.7: Visualization of drying progress with collected NIR spectra: (a) Progress primary drying: overwhelming ice bands until ice-free product became partially visible; (b) Progress primary drying: appearance of bands characteristic for trehalose and water (First inflection in point score plot); (c) Finalizing primary drying: decrease in ice band (Second inflection point in score plot); (d) Progress secondary drying: decrease in water band until completely dried product (Cluster of NIR spectra in score plot)

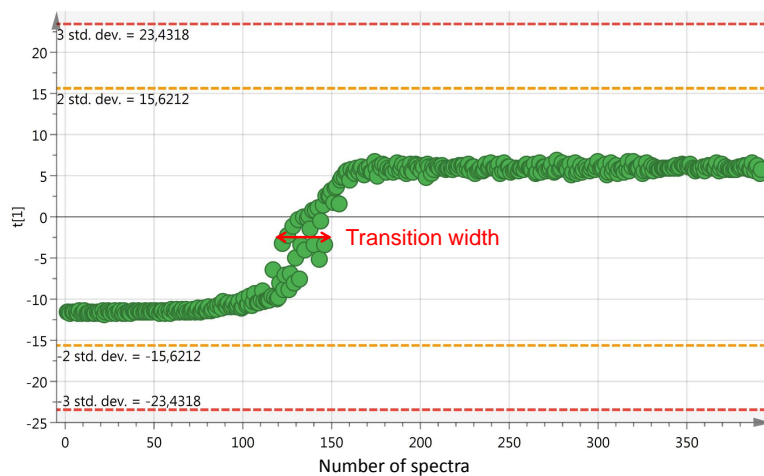


Figure 6.8: PC1 in function of time: time is expressed as number of spectra; one spectrum corresponds to 20 seconds of drying time

between the collection of the first spectrum after the onset of the heaters and the spectrum following the last spectrum situated outside of the cluster where secondary drying is finished. The secondary drying time was computed as the difference between the total drying time and the time necessary for primary drying. Additionally, for each run the PC1 versus time plot was analysed to determine the time between the first monitored position of the cake primary drying was finished and the point sublimation was completely finished. This transition width was added as a response to the analysis of DoE 2 and was defined as the time between the first spectrum after the second inflection point and the spectrum following the last spectrum situated before the second inflection point in the score plot.

Factor and interaction significance analysis

Each response of DoE 2 was analysed in a similar way to the response of DoE 1. There were no peculiarities in the raw data: for each response the variability between the repeated experiments was much less than the overall variability of all DoE 2 experiments. The regression coefficients for each response are shown in the extended coefficient plots (Figure 6.9, 6.10 and 6.11)

The total drying time ranged for the individual experiments from approximately 20 minutes up to 175 minutes. This response was mainly influenced by the thickness of the product layer, with a regression coefficient of 33.78 min (Figure 6.9). Tripling the layer thickness from 0.5 to 1.5 mm was associated with an increase in total drying time of 67 min or 169%,

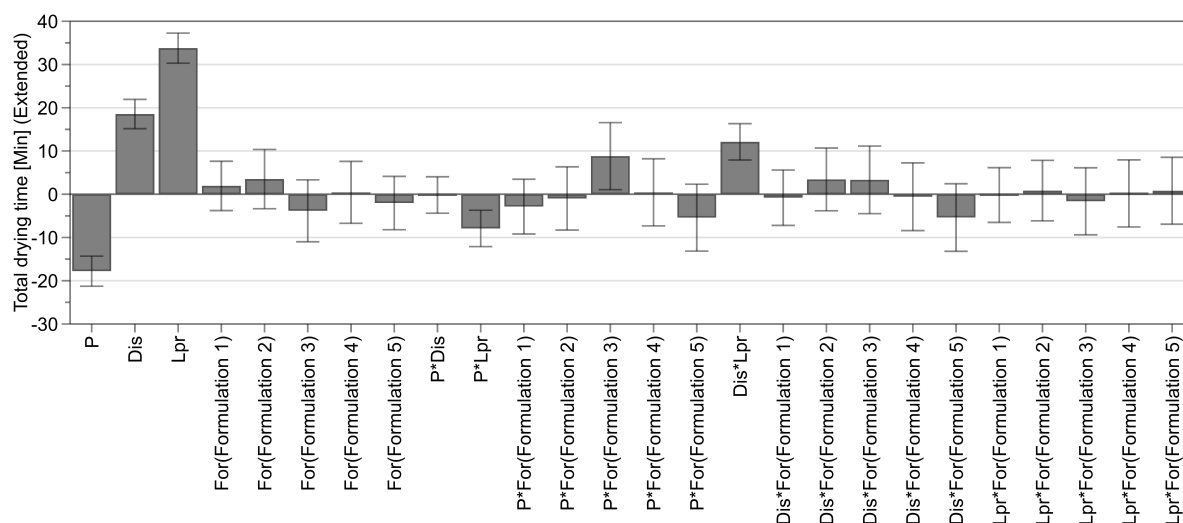


Figure 6.9: Extended coefficient plot DoE 2, response: total drying time: Regression coefficients displayed including 95% confidence interval, with electrical power (P), distance between IR heaters and vial (Dis), thickness of the product layer (Lpr) and the expanded model terms related to the qualitative factor 'Formulation' ($For(For1)$, $For(For2)$, $For(For3)$, $For(For4)$ and $For(For5)$)

keeping all other factors at their average level. The influence of the layer thickness was much larger because the drying process was continued until a dried end product was obtained as opposed to DoE 1, where primary drying was interrupted after 15 minutes. The impact of the electrical power (regression coefficient -17.795 min) and the distance between IR heaters and glass vial (regression coefficient 18.543 min) on the drying progress confirmed the results of DoE 1. Increasing the electrical power from 14 W to 36 W reduced the total drying time with 35 min or 39% and positioning the IR heaters at a distance of 2 cm instead of 6 cm from the glass vial decreased the total drying time with 37 min or 40%, keeping all other factors at their average. Naturally, these three process variables had the same impact on the primary and secondary drying time.

Formulation 4 was the only formulation which had a statistically significant impact on the primary drying rate with a regression coefficient of 5.3987 min (Figure 6.10), although all formulations had a different dried product mass transfer resistance profile according to literature values [3, 4]. Lower primary drying rates for lactose solutions have been reported earlier and could be explained by the formation of a low permeable skin at the top of the

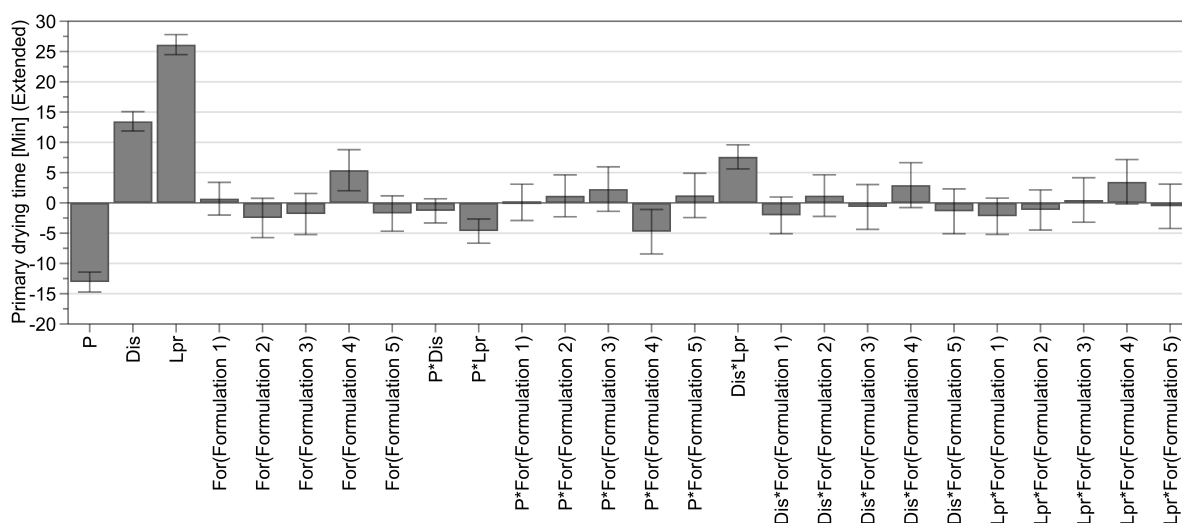


Figure 6.10: Extended coefficient plot DoE 2, response: primary drying time: Regression coefficients displayed including 95% confidence interval, with electrical power (P), distance between IR heaters and vial (Dis), thickness of the product layer (Lpr) and the expanded model terms related to the qualitative factor 'Formulation' ($For(For1)$, $For(For2)$, $For(For3)$, $For(For4)$ and $For(For5)$)

cake which is associated with a high product resistance [11, 18]. Due to the compensation by faster secondary drying of formulation 4, none of the five formulations had a significant impact on the total drying time (Figure 6.9). This confirms the theory that product resistance plays a less crucial role in the primary drying behaviour of spin frozen vials in comparison with traditional freeze-drying due to the thinner product layers [11].

Several significant factor interactions were identified for the total, primary and secondary drying time (Figure 6.9, 6.10 and 6.11). However, based on the analysis of the interaction plots similar to Figure 6.4, we could conclude that there were no strong, relevant interactions between the factors.

The transition width varied from 20 seconds to 17 minutes. Only two factors had a significant impact on this response variable. A larger distance between the IR heaters and the glass vial was associated with a longer transition width (regression coefficient 2.6107 min) as this prolonged the total drying time, which simultaneously increased the transition width. A thicker product layer also significantly impacted the transition width (regression

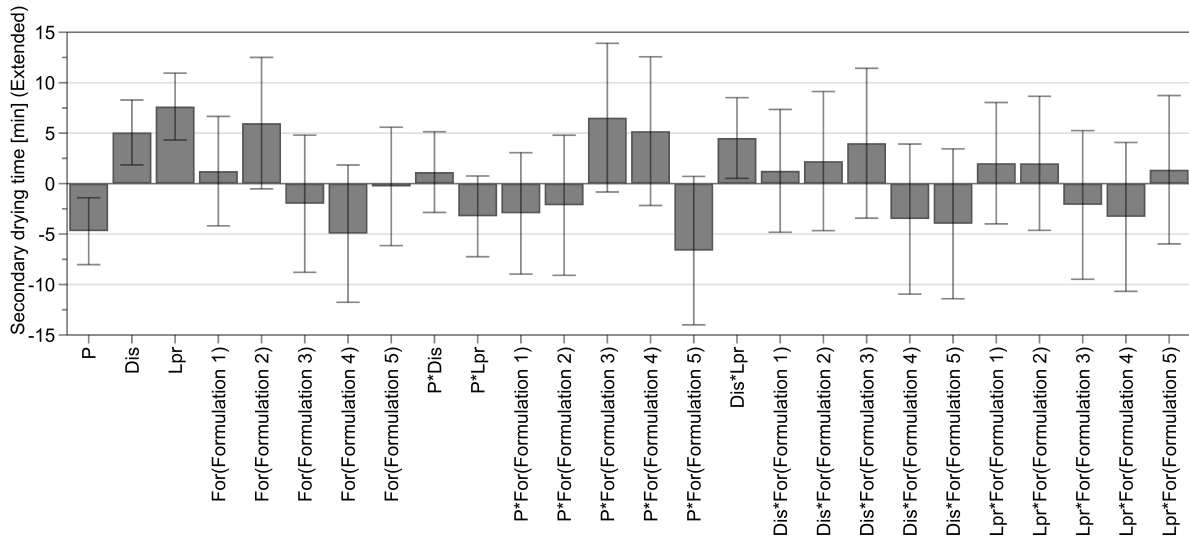


Figure 6.11: Extended coefficient plot DoE 2, response: secondary drying time: Regression coefficients displayed including 95% confidence interval, with electrical power (P), distance between IR heaters and vial (Dis), thickness of the product layer (Lpr) and the expanded model terms related to the qualitative factor 'Formulation' ($For(For1)$, $For(For2)$, $For(For3)$, $For(For4)$ and $For(For5)$)

coefficient 1.7261 min), also linked to a longer drying time.

The aim of DoE 2 was to determine the impact of several process and formulation variables on the drying time. The design was not specifically performed to study the transition width between primary and secondary drying. This response was only added after analysis of the NIR data of the individual experiments of DoE 2. Therefore, the included factors were not optimal to study this response, which might explain why only two factors had a significant impact on this response.

6.4 General conclusion

IR radiation is highly suitable to provide the energy necessary for the continuous processing (i.e., drying) of spin frozen vials. The electrical power supplied to the IR heaters and the distance between the IR heaters and the glass vial, were the most influential factors on the sublimation rate. Additionally, the layer thickness had the largest impact on the total drying time. The pressure in the drying chamber had no significant effect on the sublima-

tion rate in contrast to energy provision via conduction during both batch and continuous freeze-drying. Although several formulations with a different dried product resistance profile were tested, no significant differences in total drying time were observed. This might indicate that dried product mass transfer resistance is less crucial in the primary drying behaviour of spin frozen vials compared to batch freeze-drying, due to the reduced product layer thickness. Further research is necessary to confirm this finding.

A NIR spectroscopy method was developed to monitor the drying behaviour of spin frozen vials. This method allowed the visualisation of the drying progress and the determination of the endpoint of both primary and secondary drying. Additionally, it was possible to determine the homogeneity of the primary drying behaviour within the vial. During traditional batch freeze-drying, only one vial of the batch, or a few vials in case of a multi-point set-up, can be monitored in-line with NIR spectroscopy [19, 20]. Also, the monitored vial(s) are often not representative for the whole batch. A continuous moving belt of spin frozen vials counters these disadvantages and allows the monitoring of each individual vial in a representative way. The NIR measurements were accomplished while the vial was continuously rotating and therefore the spectra cover a large portion of the product. Also, the penetration depth of the light of the NIR probe is only a few tenths of a millimetre and since relatively thin layers are applied in this process, the measurement results are more representative compared to current methods in batch freeze-drying.

Bibliography

- [1] J. Corver. Method and system for freeze-drying injectable compositions, in particular pharmaceutical. WO2013036107, 2013.
- [2] R. Bird, W. Stewart, and E. Lightfoot. *Transport phenomena*. John Wiley & Sons, New York, 2006.
- [3] W. Y. Kuu, L. M. Hardwick, and M. J. Akers. Rapid determination of dry layer mass transfer resistance for various pharmaceutical formulations during primary drying using product temperature profiles. *Int. J. Pharm.*, 313:99–113, 2006.
- [4] D. E. Overcashier, T. W. Patapoff, and C. C. Hsu. Lyophilization of protein formulations in vials: Investigation of the relationship between resistance to vapor flow during primary drying and small-scale product collapse. *J. Pharm. Sci.*, 88:688–695, 1999.
- [5] T. R. M. De Beer, M. Wiggernhorn, R. Veillon, C. Debaq, Y. Mayeresse, B. Moreau, A. Burggraeve, T. Quinten, W. Friess, G. Winter, C. Vervaet, J. P. Remon, and W. R. G. Baeyens. Importance of Using Complementary Process Analyzers for the Process Monitoring, Analysis, and Understanding of Freeze Drying. *Anal. Chem.*, 81:7639–7649, 2009.
- [6] T. R. M. De Beer, P. Vercruyssen, A. Burggraeve, T. Quinten, J. Ouyang, X. Zhang, C. Vervaet, J. P. Remon, and W. R. G. Baeyens. In-Line and Real-Time Process Monitoring of a Freeze Drying Process Using Raman and NIR Spectroscopy as Complementary Process Analytical Technology (PAT) Tools. *J. Pharm. Sci.*, 98:3430–3446, 2009.
- [7] J. Vercruyssen, M. Toiviainen, M. Fonteyne, N. Helkimo, J. Ketolainen, M. Juuti, U. Delaet, I. Van Assche, J. P. Remon, C. Vervaet, and T. De Beer. Visualization and understanding of the granulation liquid mixing and distribution during continuous twin screw granulation using NIR chemical imaging. *Eur. J. Pharm. Biopharm.*, 2013.
- [8] L. Eriksson, E. Johansson, N. Kettaneh-Wold, J. Trygg, C. Wikström, and S. Wold. *Multi- and megavariable data analysis part 1: Basic principles and applications*. Umetrics, Umeå, 2006.
- [9] S. Pieters, Y. Vander Heyden, J. M. Roger, M. D’Hondt, L. Hansen, B. Palagos, B. De Spiegeleer, J. P. Remon, C. Vervaet, and T. De Beer. Raman spectroscopy and

- multivariate analysis for the rapid discrimination between native-like and non-native states in freeze-dried protein formulations. *Eur. J. Pharm. Biopharm.*, 85:263–271, 2013.
- [10] G. F. Nellis and S. A. Klein. Radiation. In *Heat Transfer*. Cambridge University Press, Cambridge, 2009.
- [11] L. De Meyer, P. J. Van Bockstal, J. Corver, C. Vervaet, J. P. Remon, and T. De Beer. Evaluation of spin freezing versus conventional freezing as part of a continuous pharmaceutical freeze-drying concept for unit doses. *Int. J. Pharm.*, 496:75–85, 2015.
- [12] T. Jennings. *Lyophilization: Introduction and basic principles*. Informa healthcare, New York, 2008.
- [13] R. Pisano, D. Fissore, A. A. Barresi, P. Brayard, P. Chouvinc, and B. Woinet. Quality by design: optimization of a freeze-drying cycle via design space in case of heterogeneous drying behavior and influence of the freezing protocol. *Pharm. Dev. Technol.*, 18:280–295, 2013.
- [14] D. Fissore, R. Pisano, and A. A. Barresi. Advanced approach to build the design space for the primary drying of a pharmaceutical freeze-drying process. *J. Pharm. Sci.*, 100:4922–4933, 2011.
- [15] S. Rambhatla, R. Ramot, C. Bhugra, and M. J. Pikal. Heat and mass transfer scale-up issues during freeze drying: II. Control and characterization of the degree of supercooling. *AAPS PharmSciTech*, 5:54–62, 2004.
- [16] J. Workman and L. Weyer. *Practical Guide to Interpretive Near-Infrared Spectroscopy*. CRC Press, Boca Raton (FL), 2007.
- [17] S. Pieters, T. De Beer, J. C. Kasper, D. Boulpaep, O. Waszkiewicz, M. Goodarzi, C. Tistaert, W. Friess, J. P. Remon, C. Vervaet, and Y. Vander Heyden. Near-infrared spectroscopy for in-line monitoring of protein unfolding and its interactions with lyoprotectants during freeze-drying. *Anal. Chem.*, 84:947–955, 2012.
- [18] R. Chen, N. K. H. Slater, L. A. Gatlin, T. Kramer, and E. Y. Shalaev. Comparative rates of freeze-drying for lactose and sucrose solutions as measured by photographic recording, product temperature, and heat flux transducer. *Pharm. Dev. Technol.*, 13:367–374, 2008.

-
- [19] T. De Beer, A. Burggraeve, M. Fonteyne, L. Saerens, J. P. Remon, and C. Vervaet. Near infrared and Raman spectroscopy for the in-process monitoring of pharmaceutical production processes. *Int. J. Pharm.*, 417:32–47, 2011.
- [20] A. Kauppinen, M. Toiviainen, O. Korhonen, J. Aaltonen, J. Paaso, M. Juuti, and J. Ketolainen. In-Line Multipoint Near-Infrared Spectroscopy for Moisture Content Quantification during Freeze-Drying. *Anal. Chem.*, 85:2377–2384, 2013.

CHAPTER 7

Mechanistic modelling of infrared mediated energy transfer during the primary drying step of a continuous freeze-drying process

Redrafted from: Van Bockstal P.J., Mortier S.T.F.C., De Meyer L., Corver J., Vervaet C., Nopens I., De Beer T. (2017) *Mechanistic modelling of infrared mediated energy transfer during the primary drying step of a continuous freeze-drying process*. European Journal of Pharmaceutics & Biopharmaceutics, 114, 11-21.

7.1 Introduction

Spin freezing of glass vials and the corresponding decrease in layer thickness strongly increases the drying efficiency compared to conventional batch freeze-drying. The study in the previous chapter showed the feasibility of IR radiation in providing the latent sublimation energy to the spin frozen vials. The IR mediated primary drying process is illustrated in figure 7.1. Each spin frozen vial is rotating along its longitudinal axis in front of an individual IR heater, which can be controlled at a specific temperature. Rotation of the vials is necessary to obtain a uniform heat transfer. To obtain an as high as possible throughput, it is furthermore necessary to maximise the drying efficiency by providing sufficient radiation energy to the spin frozen vials during its entire drying process. On the other hand, product appearance is an important CQA of freeze-dried products and cake collapse should be avoided at all cost to ensure fast reconstitution of the dried product and for aesthetic purposes [1, 2]. Therefore, the product temperature during primary drying should never

exceed the eutectic temperature T_e or the collapse temperature T_c of the formulation for crystalline or amorphous materials, respectively. In general, T_c is a few degrees higher than T_g' because the viscosity near T_g' is still sufficiently high to prevent molecular motion [1]. The thickness of the dried product layer increases with the primary drying progress. The dried product mass transfer resistance R_p also raises, associated with a gradual increase in product temperature. To maintain the product temperature below the critical value during the entire process, the optimal radiation energy transfer to the spin frozen vial is rather dynamic instead of static.

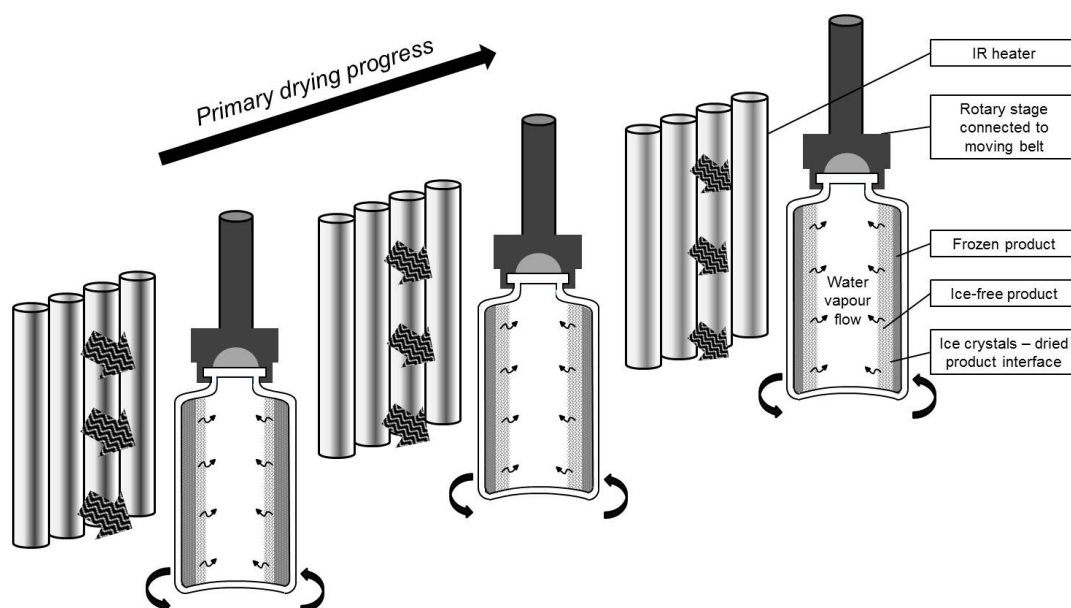


Figure 7.1: Illustration of the IR assisted continuous primary drying of spin frozen vials, rotating along their longitudinal axis in front of individual IR heaters

Mechanistic modelling of the primary drying step in conventional batch freeze-drying has already been extensively described [3–8]. These models allow the computation of the adaptable process parameters, shelf temperature and chamber pressure, maximising the sublimation rate while preventing cake collapse. Additionally, inclusion of the uncertainty on each process and formulation parameter of the primary drying model leads to the construction of the (dynamic) Design Space for a specific lyophilized formulation, allowing qualitative assessment of the risk of cake collapse [9]. Besides increasing process efficiency, mechanistic modelling also offers fundamental process knowledge which contributes to the understanding of the lyophilisation process.

In chapter 6, a DoE approach was used to determine the impact of several radiation drying related process parameters on the drying behaviour of spin frozen formulations. However, no fundamental insight in the underlying physics of the process was obtained via this approach. In addition, the resulting empirical models are only valid for the different formulations and parameter ranges included in this DoE. Because of both these reasons, it is clear that the continuous freeze-drying concept would benefit from mechanistic models (similar to conventional batch freeze-drying) which describe the primary drying behaviour of spin frozen vials. The aim of this paper is the development and validation of a mechanistic model which computes the optimal, dynamic IR heater temperature in function of the drying progress of a formulation in a spin frozen vial, maximising the drying efficiency while maintaining an elegant product structure. Additionally, the primary drying model allows the determination of the amount of sublimed ice at each time point and the computation of the primary drying endpoint.

7.2 Materials and methods

7.2.1 Development of primary drying model for continuous drying of spin frozen vials via radiation

Initially, the maximum allowable sublimation rate \dot{m}_{sub} is calculated as several limitations need to be considered. First, \dot{m}_{sub} is restricted by the dried product mass transfer resistance R_p as only a limited amount of water vapour can escape the sublimation interface through the pores of the dried product. If more water vapour is generated at the sublimation interface, the mass transfer through the dried layer will be obstructed, leading to a local pressure increase at this interface. Since the product temperature at the sublimation front T_i is in equilibrium with the vapour pressure $P_{w,i}$, naturally, T_i will also increase. However, during the entire primary drying process, T_i should be maintained below the critical value, T_e or T_c , to avoid collapse of the product. Therefore, \dot{m}_{sub} is limited to a maximum to avoid that the critical product temperature $T_{i,\text{crit}}$ is exceeded during the primary drying stage. Consequently, as ice sublimation is an endothermic process, the energy transfer during primary drying is also limited.

The sublimation rate during primary drying \dot{m}_{sub} (kg/s) is calculated by:

$$\dot{m}_{\text{sub}} = \frac{A_p(P_{w,i} - P_{w,c})}{R_p} \quad (7.1)$$

where A_p is the product area available for sublimation (m^2), $P_{w,i}$ the vapour pressure of ice at the sublimation interface (Pa), $P_{w,c}$ the partial pressure of water in the drying unit (Pa) and R_p the dried product mass transfer resistance (m/s). $P_{w,c}$ is assumed to be equal to the overall pressure in the drying unit P_c , as during primary drying the gas composition in the drying unit consists almost entirely of water vapour, similar to batch freeze-drying [7].

$P_{w,i}$ is calculated by the following empirical equation [10]:

$$P_{w,i} = 133.322 \cdot 2.7 \cdot 10^{10} e^{-\frac{6145}{T_i}} \quad (7.2)$$

where T_i is the product temperature at the sublimation interface (K). To maximise the drying efficiency and simultaneously avoid loss of cake structure, T_i is set at the critical product temperature $T_{i,crit}$

R_p depends on the thickness of the dried product layer l (m). This relation is given by the following empirical equation:

$$R_p = R_{p,0} + \frac{A_{R_p} l}{1 + B_{R_p} l} \quad (7.3)$$

where $R_{p,0}$ (m/s), A_{R_p} (1/s) and B_{R_p} (1/m) are constants, determined by the fitting of experimental data [8]. R_p is formulation specific and is strongly influenced by the pore size of the dried product, which is mainly determined by the degree of supercooling during the freezing step [11, 12]. In general, R_p increases with the primary drying progress and the corresponding increase in l . As a consequence, the energy input needs to be decreased so all generated water vapour can escape the sublimation front to avoid an increase in $P_{w,i}$ and T_i , associated with a decrease in \dot{m}_{sub} (Equation (7.1)).

Spin freezing leads to a thin product layer, uniformly spread over the entire inner vial wall (Figure 7.1). Hence, A_p is calculated by:

$$A_p = 2\pi(r_{p,i} + l)k \quad (7.4)$$

with k the height of the spin frozen product (m) and $r_{p,i}$ the radius from the centre of the vial to the border of the spin frozen layer (m), which is given by:

$$r_{p,i} = \sqrt{r_{v,i}^2 - \frac{V}{\pi k}} \quad (7.5)$$

where $r_{v,i}$ is the inner radius of the glass vial (m) and V is the filling volume (m^3). During primary drying, the sublimation front gradually moves from the inside of the vial towards

the vial wall. For this reason, A_p increases simultaneously with the increase of l .

The increase in the dried layer thickness Δl (m) for a specified time interval Δt (s) is calculated by:

$$\Delta l = \frac{\dot{m}_{\text{sub}} \Delta t}{A_p \rho_{\text{ice}} \phi} \quad (7.6)$$

with ρ_{ice} the density of ice (kg/m^3) and ϕ the volume fraction of ice (-).

Secondly, the maximum value of \dot{m}_{sub} is limited by the choked flow phenomenon [13]. The gas flow rate to the condenser is restricted by an upper limit near the narrowest point in the processing equipment. In batch freeze-drying, the duct connecting the drying chamber with the condenser is considered the most critical point where choked flow can occur. In continuous freeze-drying, the amount of vials being processed at the same time is much smaller, which makes the occurrence of choked flow at the duct in the continuous drying unit unlikely. On the other hand, spin freezing results in a significant increase of A_p in comparison with batch freeze-drying, which allows a much higher sublimation rate in each individual vial. For this reason, it is necessary to evaluate the risk of choked flow at the vial neck, being the narrowest point during sublimation. Choked flow occurs once the vapour flow rate through the vial neck approaches the speed of sound (Mach I), where a further increase in mass flow would result in an elevated vapour density, leading to a local pressure increase inside the vial. The difference between $P_{w,i}$ and $P_{w,c}$ becomes smaller, resulting in a decrease of the sublimation rate (Equation (7.1)), while the energy input is maintained at the same level. Consequently, more energy is provided to the spin frozen vial than can be removed through ice sublimation (maximum R_p), resulting in an increase in T_i . Eventually, T_i will exceed $T_{i,\text{crit}}$, leading to loss of cake structure and rejection of the product. In general, choked flow is most likely to occur during the processing of a formulation characterized by a high value for $T_{i,\text{crit}}$ or a low R_p profile, especially at the onset of primary drying.

Evaluation of the choked flow criterion requires the calculation of the speed of sound c (m/s) for an ideal gas [13]:

$$c = \sqrt{\frac{\kappa R T_r}{M}} \quad (7.7)$$

with κ the ratio of specific heats (adiabatic index) for water (1.33), R the gas constant (8.31 J/(K mol)), T_r the temperature of the water vapour (K) and M the molecular weight of water (0.018 kg/mol). The maximum sublimation rate avoiding choked flow $\dot{m}_{\text{sub, chok}}$

(kg/s), is given by [14]:

$$\dot{m}_{\text{sub,chok}} = c\pi r_{v,n}^2 \rho_{wv} \quad (7.8)$$

with $r_{v,n}$ the radius of the vial neck (m) and ρ_{wv} the density of water vapour (kg/m³), which is given by the following equation for the calculation of the density of an ideal gas [14]:

$$\rho_{wv} = \frac{P_c M}{T_r R} \quad (7.9)$$

After computing the maximum allowable sublimation rate, the radiation energy required to support this sublimation rate \dot{m}_{sub} is calculated by:

$$P_{\text{tot}} = \frac{\dot{m}_{\text{sub}} \Delta H_s}{M} \quad (7.10)$$

where P_{tot} is the total power that should be provided to the spin frozen vial (W) and ΔH_s is the latent heat of ice sublimation (51139 J/mol). The system was assumed to be at steady-state, i.e., the radiation energy was only used for ice sublimation.

It should be taken into account that a significant part of the required power is provided by the surroundings, as the walls and door of the vacuum chamber are at a higher temperature than the spin frozen vial. Therefore, P_{tot} is compensated for the radiation energy contributed by these surrounding surfaces:

$$P_{\text{rad}} = P_{\text{tot}} - P_{\text{sur}} \quad (7.11)$$

where P_{rad} is the power that should be provided by the IR heater to the spin frozen vial (W) and P_{sur} is the power provided by the surroundings to the spin frozen vial (W).

Both P_{sur} and the temperature of the IR heater necessary to provide sufficient energy to achieve the optimal sublimation rate are calculated via the Stefan-Boltzmann law:

$$P = A_{\text{rad}} F \sigma (\epsilon T_{\text{rad}}^4 - a T_{v,o}^4) \quad (7.12)$$

where A_{rad} is the area of the emitting surface (i.e., IR heater or chamber wall) (m²), F is the view factor (-), σ the Stefan-Boltzmann constant (5.67 10⁻⁸ W/(m² K⁴)), ϵ is the emission coefficient of the emitting surface (-), T_{rad} is the temperature of the emitting surface (K), a is the absorptivity of the target surface (-) and $T_{v,o}$ is the temperature of the spin frozen vial (K). P is equal to P_{rad} when the IR heater is the emitting surface or P_{sur} when the chamber wall or door is the emitting surface. In general, a is estimated as the value of ϵ for the target surface [14]. In this chapter, $T_{v,o}$ is assumed to be equal to T_i . The computation of the view factor F is described in the next section.

7.2.2 View factor computation

The computation of the view factor F for this specific situation is based on the Monte Carlo method described by Brenner [15]. Both the IR heater and the walls of the drying chamber are considered diffuse emitters, meaning, these surfaces emit radiation uniformly in all directions. Consequently, F only depends on the relative geometric orientation of the emitting surface (i.e., IR heater or chamber wall) to the spin frozen vial, represented by a flat plate and a cylinder, respectively. The Monte Carlo method is a simulation approach in which a defined amount of rays N is propagated from random positions on the radiator surface at randomly chosen angles [16]. For each generated ray, it is evaluated whether it will directly hit the target surface or not. F is estimated by the ratio of the number of rays that strike the target surface, M , to the total amount of emitted rays, N .

First, the principles to determine the view factor for a plane surface as radiator with a cylindrical target are presented. There are three situations for a parallel orientation of the cylindrical target to the radiator plane, illustrated in figure 7.2. On the left side, the situation with a cylindrical target smaller than the radiator is given, therefore, the width of the radiator w is larger than the diameter of the cylinder d . On the right side, the other extreme case is illustrated, where $w < d$. A clear distinction between these situations is important during the computation of the view factor.

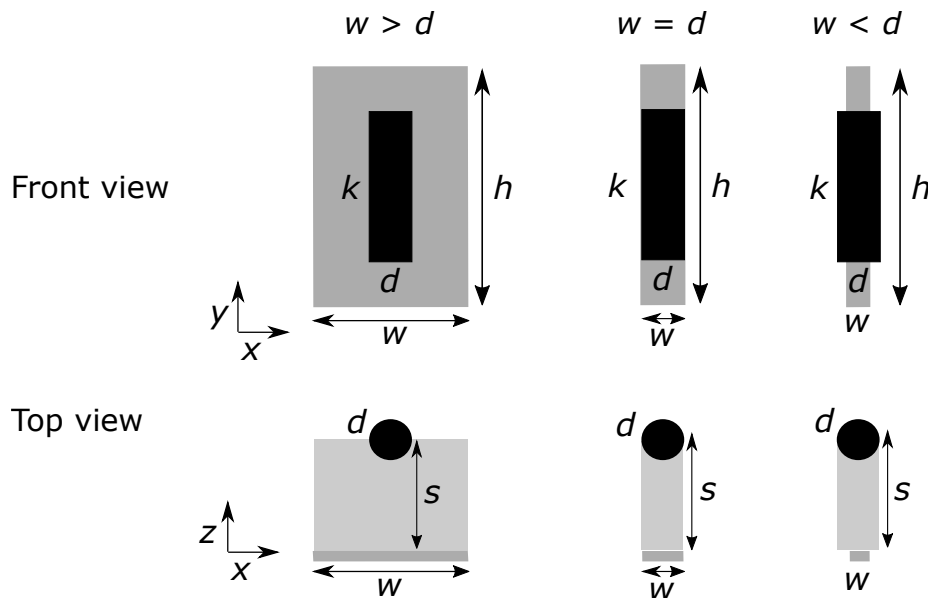


Figure 7.2: The three situations for a cylindrical target parallel to the plane of the radiator (Target in black)

Two characteristics for each generated ray need to be defined: the starting position from the radiator surface and the direction. The starting position of the generated ray is determined by selecting a random number between 0 and 1 for both dimensions of the surface, which is then multiplied by the length h and the width w of the surface, respectively. Therefore, the origin of each generated ray is described by two coordinates. To select a random direction of the generated ray, two angles are defined: the polar angle θ and the azimuthal angle ϕ (Figure 7.3). For each angle, a random number between 0 and 1 is generated, p_θ and p_ϕ [15]. The corresponding angles are determined using [15]:

$$\theta = \arcsin \sqrt{p_\theta} \quad (7.13)$$

$$\phi = 2\pi p_\phi \quad (7.14)$$

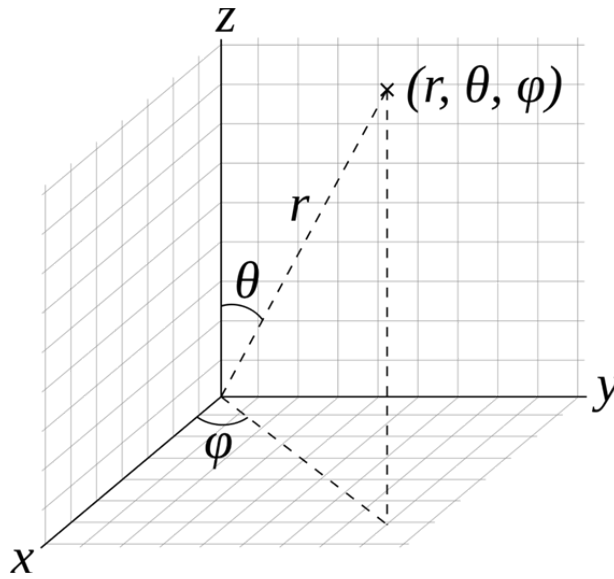


Figure 7.3: The direction of the generated ray to determine the view factor

The length of the generated ray L is gradually increased by the sequential addition of increments, dL , until it hits the target or till it is impossible to hit the target from the end-position of the ray. The length of the generated ray is determined by [15]:

$$x_{ray} = x + L \cos \phi \sin \theta \quad (7.15)$$

$$y_{ray} = y + L \sin \phi \sin \theta \quad (7.16)$$

$$z_{ray} = L \cos \theta \quad (7.17)$$

for each dimension of the coordinate system. The length of the ray is increased by adding an increment dL . The length of dL is dependent on the orientation of the cylinder with respect to the radiator. Two cases are distinguished, i.e., the cylinder is oriented parallel or perpendicular to the plane (Figure 7.4). For the parallel case, dL is determined as the diameter of the cylinder d divided by 10 [15]. In some cases it is recommended to divide d by 100 or more. The value of this parameter is further denoted as α_{dL} . The initial length of the ray L is determined as the distance between the surface and the border of the cylinder minus the length of dL : $s - d/2 - dL$ [15]. In the case where the axis of the cylinder is perpendicular to the plane of the radiator, the initial length of the ray is equal to $s - k/2 - dL$ with dL equal to k divided by 10 or more.

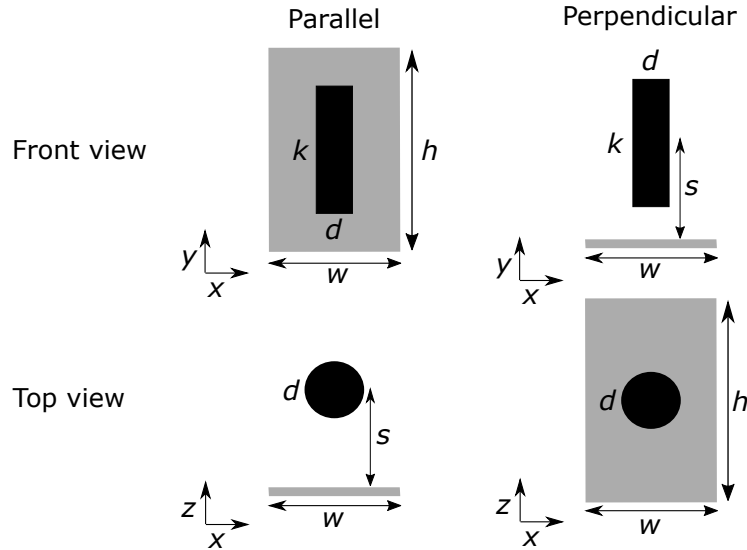


Figure 7.4: The orientation of the radiator plane versus the cylindrical target: parallel (Left) and perpendicular (Right). The variables which are essential for the model to calculate the view factor, i.e., k , d , h , s and w , are indicated in the figure (Target in black)

The end-position of the ray should be within the position of the target in order to have a hit, therefore, the following constraints are verified in case of a parallel orientation of the cylinder to the plane:

$$\begin{cases} \frac{h-k}{2} \leq y_{ray} \leq \frac{h-k}{2} + k \\ \sqrt{(x_{ray} - x_{shift} - w/2)^2 + (z_{ray} - z_{shift} - s)^2} \leq d/2 \end{cases} \quad (7.18)$$

with h and w the length and width of the flat radiator plane, respectively, s the distance between the centre of the cylinder and the radiator plane, d the diameter of the cylinder and k the height of the cylinder. If the end-position of the ray is not situated within the cylinder, the length of the ray is incremented. In case it is impossible for the ray to ever hit the target, independent from the number of increments which is added, a next ray is generated, but the counter which tracks the number of hits is not incremented. Therefore, the following equations are evaluated, depending on the size of the target with respect to the size of the radiator:

$$w \geq d \implies \begin{cases} 0 \leq x_{ray} - x_{shift} \leq w \\ 0 \leq y_{ray} \leq h \\ 0 \leq z_{ray} - z_{shift} \leq s + d/2 \end{cases} \quad (7.19)$$

$$w < d \implies \begin{cases} -(d-w)/2 \leq x_{ray} - x_{shift} \leq w + (d-w)/2 \\ 0 \leq y_{ray} \leq h \\ 0 \leq z_{ray} - z_{shift} \leq s + d/2 \end{cases} \quad (7.20)$$

If the end-point of the ray exceeds the box, defined by equation 7.19 or 7.20, the ray is not categorized as a hit.

For the perpendicular case, the conditions to have a hit are given by:

$$\begin{cases} s - k/2 \leq y_{ray} \leq s + k/2 \\ \sqrt{(x_{ray} - x_{shift} - w/2)^2 + (z_{ray} - z_{shift} - h/2)^2} \leq d/2 \end{cases} \quad (7.21)$$

The conditions for a further increase of the length of the ray are:

$$w \geq d \implies \begin{cases} 0 \leq x_{ray} - x_{shift} \leq w \\ 0 \leq y_{ray} \leq s + k/2 \\ 0 \leq z_{ray} - z_{shift} \leq h \end{cases} \quad (7.22)$$

$$w < d \implies \begin{cases} -(d-w)/2 \leq x_{ray} - x_{shift} \leq w + (d-w)/2 \\ 0 \leq y_{ray} \leq s + k/2 \\ 0 \leq z_{ray} - z_{shift} \leq h \end{cases} \quad (7.23)$$

The parameters to calculate the view factor for the specific experimental set-up are listed in table 7.1. The first five parameters identify the stationary geometric situation. For the purpose of future use of the model, in cases where the vials moves with respect to the radiators, the shift parameters are included in the calculations. Furthermore, these parameters are used to calculate the potential interference between two neighbouring radiators.

7.2.3 Temperature calibration of the IR heaters

The temperature of the IR heater T_{rad} was determined in function of electric power P_e , delivered by the Voltcraft PPS-11360 power supply (Conrad Electronic, Hirschau, Germany). A 10 mL type I glass vial (Schott, Müllheim, Germany) filled with 3.9 mL of water was spin frozen according to the procedure described in the previous chapter. The glass vial was placed in a vial holder and vertically rotated along its longitudinal axis at approximately 2900 rotations per minute (rpm). Consequently, the liquid was spread uniformly across the entire vial wall. The rotating vial was then immersed into liquid nitrogen for 40 ± 5 s to completely solidify the product. Within 15 ± 5 s after spin freezing, the vial was transferred from the liquid nitrogen to the drying chamber of an Amsco FINN-AQUA GT4 freeze-dryer (GEA, Köln, Germany), herewith avoiding exceedance of the melting point of ice. The shelves in the drying chamber were set at a constant temperature of -10 °C. The spin frozen vial was presented to one IR heater (Weiss Technik, Zellik, Belgium) at a distance of 4 cm measured from the centre of the vial until the heated filament of the IR heater. No contact was made with the shelf. The vial was continuously rotating at 5 rpm which was necessary for a homogeneous energy transfer from the IR heater to the vial. Immediately after placing the vial in the drying chamber, the pressure was lowered to 13.3 Pa. Within 5 minutes, the pressure in the drying chamber was below the triple point of water, hence avoiding any melting of ice. After exactly 17 minutes, the time necessary to achieve the desired pressure level, the IR heaters were activated. During each individual experiment, primary drying was conducted at a different level of P_e (7 W, 18 W, 32 W, 49 W and 69 W), provided by the power supply. The temperature of the wall of the glass vial was continuously monitored with a type-K thermocouple (Conrad Electronic, Hirschau, Germany). The drying chamber was aerated with nitrogen 20 min after activation of the IR heaters to interrupt ice sublimation after which the sublimed ice mass was immediately determined gravimetrically, including a correction for the amount of ice sublimed during the introduction of the vacuum in the drying chamber and for the computed value of P_{sur} , as described in section 7.2.4. T_{rad} is calculated with the help of equations (7.10), (7.11) and (7.12) in function of P_e . In addition, using the same equations, the efficiency of the IR heater η was calculated by taking the ratio of the net power provided to the spin frozen vial P_{rad} and P_e :

$$\eta = \frac{P_{rad}}{P_e} \quad (7.24)$$

Linear regression using the least squares approach was applied to describe T_{rad} in function of P_e . Both a linear and a quadratic empirical model were developed to describe this

relation. The significance of the regression coefficients of both equations was statistically evaluated via a t -test ($\alpha = 5\%$) using SPSS (Version 23.0, IBM, Armonk, IL, USA). For each regression coefficient the null hypothesis, stating that a coefficient was equal to zero, was tested. Acceptance of the null hypothesis for a specific regression coefficient indicated that the corresponding term was not significant. In addition, the Root Mean Square Error of Cross-Validation (RMSECV) was calculated for the linear and quadratic model to compare the predictive power of both models.

7.2.4 Verification of radiation energy contributed by the surroundings

The power radiated by the surroundings was calculated individually for each plane surface contributing to the IR energy transfer to the spin frozen vial: the acrylic glass door, the three stainless steel chamber walls, the stainless steel shelf located above and below the experimental set-up and the inactivated IR heater. The view factor F was computed for each of these surfaces via Monte Carlo simulation to determine the fraction of radiation which reaches the spin frozen vial [15]. A defined number of rays is propagated from randomly chosen positions on the emitting surface (i.e., the door, the chamber walls, the shelf and the IR heater) at random angles. For each simulated ray, the conditions are evaluated whether the target surface (i.e., the spin frozen vial) is hit or not. F is equal to the ratio of the number of hits to the amount of simulated rays. The net power contribution was then calculated with the help of equations (7.10) and (7.12). The nominal values of the model parameters required for the computation of both the view factor and the power contributed by the surroundings are listed in table 7.1.

The computed IR energy contribution radiated by the surroundings to the spin frozen vial was verified with experimental data. A 10 mL type I glass vial filled with 3.9 mL of water was spin frozen and transferred to the drying chamber as described in section 7.2.3. The amount of ice sublimed during the initial pressure decrease, i.e. the 17 minutes lasting period immediately after activation of the vacuum pump, was determined gravimetrically. In a second experiment, the vacuum was maintained for another 20 minutes after reaching the desired pressure (13.3 Pa), i.e. 37 minutes in total, without activation of the IR heater. After this period, the sublimed ice mass was determined gravimetrically. Both experiments were conducted in triplicate. With the help of equation (7.10), the power corresponding to this sublimation rate was calculated. The difference in power between both experiments reflects the energy provided through radiation from the surroundings to the spin frozen vial.

Table 7.1: Nominal values of input parameters for view factor F computation, calculation power contribution by surroundings and calculation dynamic temperature profile

Parameter	Nominal value
<i>Input parameters view factor computation:</i>	
Length radiator	0.045 m
Width radiator	0.045 m
Width chamber door	0.478 m
Height chamber door	0.523 m
Length drying chamber	0.557 m
Width drying chamber	0.478 m
Height drying chamber	0.523 m
Length shelf	0.453 m
Width shelf	0.300 m
Outer radius vial $r_{v,o}$	0.0119 m
Vial height k	0.040 m
Distance between centre cylinder and IR heater	0.040 m
Distance between centre cylinder and chamber door	0.150 m
Distance between centre cylinder and left chamber wall	0.270 m
Distance between centre cylinder and top shelf	0.220 m
Distance between centre cylinder and bottom shelf	0.070 m
Number of simulated rays (Monte Carlo simulation)	10^6
Position of cylinder shifted in x -direction x_{shift}	0 mm
Position of cylinder shifted in z -direction z_{shift}	0 mm
<i>Input parameters power contribution surroundings:</i>	
Emissivity quartz glass (IR heater) ϵ	0.93
Emissivity stainless steel ϵ	0.83
Emissivity acrylic glass ϵ	0.86
Temperature chamber door	288.75 K
Temperature chamber wall (left)	288.95 K
Temperature chamber wall (right)	289.15 K
Temperature chamber wall (back)	287.45 K
Temperature shelves	263.15 K

Continued on next page

Table 7.1 – *Continued from previous page*

Parameter	Nominal value
<i>Specific input parameters for calculation dynamic temperature profile:</i>	
Inner radius vial $r_{v,i}$	0.0109 m
Inner radius vial neck $r_{v,n}$	0.0063 m
Product resistance parameter $R_{p,0}$	$1.85 \cdot 10^4$ m/s [12]
Product resistance parameter A_{R_p}	$1.20 \cdot 10^7$ 1/s [12]
Product resistance parameter B_{R_p}	$-6.76 \cdot 10$ 1/m [12]
Filling volume V	3.90 mL
Volume fraction ice ϕ	1
View factor F	0.1484
Critical product temperature $T_{i,crit}$	240.15 K

7.2.5 Model validation

The primary drying model computing the IR mediated heat transfer to the spin frozen vials was validated for a model formulation. This aqueous formulation contained 30 mg/mL mannitol, 3.42 mg/mL sucrose, 3.75 mg/mL glycine and 0.58 mg/mL sodium chloride. Mannitol, sucrose and sodium chloride were purchased from Fagron (Waregem, Belgium). Glycine was acquired from Sigma-Aldrich (Saint Louis, MO, USA). The optimal dynamic IR heater temperature profile in function of primary drying time t was computed as described in section 7.2.1. Similar as for the IR heater calibration, a correction was made for the amount of ice sublimed during the initial pressure decrease (Section 7.2.3). The nominal values of the model parameters required for solving the model equations are listed in Table 7.1. The parameters describing R_p in function of l were taken from literature [12]. $T_{i,crit}$ was assumed to be equal to T'_g of the model formulation. As the model formulation was low concentrated, ϕ was assumed to be equal to 1. The time step Δt was set at 60 s. The calibration of the IR heaters allowed calculating the dynamic P_e profile corresponding to the optimal dynamic IR heater temperature profile.

A 10 mL type I glass vial (Schott, Müllheim, Germany) filled with 3.9 mL of the model formulation was spin frozen according to the procedure described in section 7.2.3. The volume of 3.9 mL corresponded to a thickness of the frozen product layer of 1.63 mm. After spin freezing, the vial was transferred to the drying chamber where primary drying was

conducted as described in section 7.2.3. The experimental drying set-up is shown in figure 7.5. When the desired pressure (13.3 Pa) was achieved, 17 minutes after activation of the vacuum pump, the preprogrammed P_e profile was initiated. At the end of the dynamic profile, the drying process was prolonged by maintaining the IR heater temperature corresponding to the last value of P_e of this profile for 30 minutes to ensure that all ice was sublimed. This validation experiment was repeated 6 times. The entire drying process was continuously monitored with in-line NIR spectroscopy with the aim of determining the primary drying endpoint (Chapter 6).

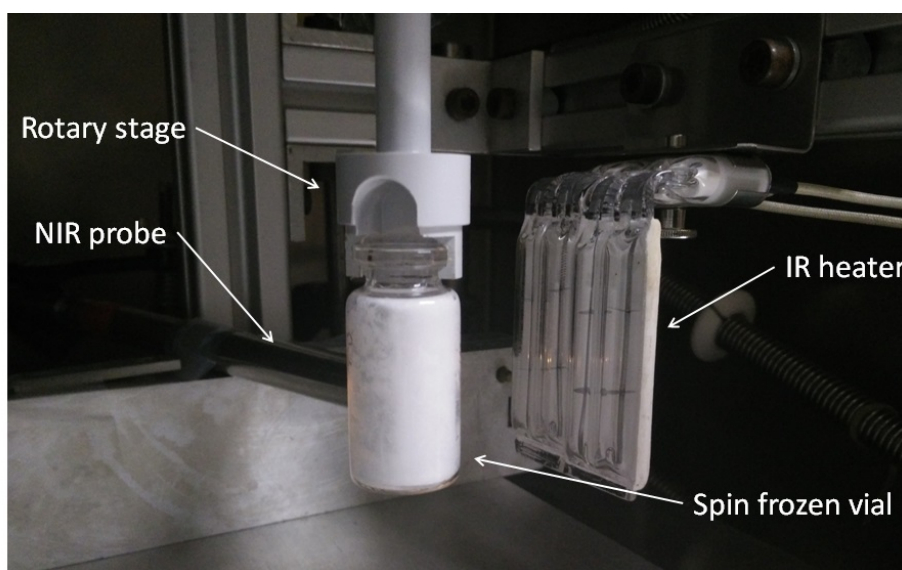


Figure 7.5: Experimental IR assisted drying set-up with in-line NIR monitoring

7.2.6 Determination of the critical product temperature

The critical product temperature $T_{i,crit}$ of the model formulation during primary drying was determined via MDSC using a differential scanning calorimeter Q2000 (TA instruments, Zellik, Belgium). Hermetically sealed aluminium pans (TA instruments, Zellik, Belgium) were filled with approximately 12 mg of the formulation. The DSC cell was constantly purged with dry nitrogen at a flow rate of 50 mL/min. The sample was initially cooled until -90°C . This temperature was maintained for 5 minutes. Subsequently the temperature was linearly increased until 0°C at a heating rate of $2^{\circ}\text{C}/\text{min}$. The modulation amplitude and period were set at 0.212°C and 40 seconds, respectively. The analysis was conducted in

triplicate. The thermograms were analysed with TA Instruments Universal Analysis 2000 version 4.7A (TA Instruments, Zellik, Belgium).

7.2.7 NIR spectroscopy

Diffuse reflectance NIR spectra were continuously in-line collected with an Antaris™ II Fourier-Transform NIR spectrometer (Thermo Fisher Scientific, Erembodegem, Belgium), equipped with a quartz halogen lamp, a Michelson interferometer and an InGaAs detector. The fibre optic probe was implemented in the drying chamber at a distance of 0.5 ± 0.1 mm near the middle of the vial without hampering or disturbing the rotation of the vial (Figure 7.5). As drying progresses from the centre of the vial to the inner vial wall, in-line NIR spectroscopy allowed the detection of complete ice removal, i.e. the endpoint of primary drying. Every 20 seconds a NIR spectrum was collected in the $4500\text{--}10000\text{ cm}^{-1}$ region with a resolution of 16 cm^{-1} and averaged over 4 scans. The illumination spot size obtained with the NIR probe was approximately 28 mm^2 . Due to rotation of the vial during the measurements, each spectrum was collected at a different position of the cake on a specific height. It was assumed that this monitored part is representative for the whole cake.

7.2.8 Multivariate data analysis

The collected NIR spectra during each validation run were analysed with the help of the multivariate data analysis software SIMCA (Version 14.0.0, Umetrics, Umeå, Sweden). The NIR spectra collected before activation of the heaters were removed from each dataset. The Savitzky-Golay filter was applied to smooth the spectra: a quadratic polynomial function was fitted to a moving sub-model, each containing fifteen data points. Additionally, SNV preprocessing was applied to eliminate the additive baseline offset variations and multiplicative scaling effects in the spectra which may be caused by small variations in distance between the NIR probe and the rotating glass vial and possible differences in product density [17]. PCA was then used for the analysis of the preprocessed and mean-centred NIR spectra.

PCA is an unsupervised multivariate projection method which extracts and displays the variation in the data set [18, 19]. The original variables, e.g. the individual wave numbers of the NIR spectra, are replaced by a new set of latent variables, named PCs. These PCs are sequentially acquired by an orthogonal, bilinear decomposition of the data matrix. Each component explains most of the remaining variability in the data. PCs are composed

of a score and a loading vector. The score vector contains a score value for each spectrum, which describes its quantitative relation to the other spectra. The loading vector provides qualitative information about which spectral features present in the original observations are captured by the corresponding component.

7.2.9 Karl Fischer

The residual moisture content of the freeze-dried product obtained from the model validation runs, was determined using Karl Fischer titration as described by Hansen et al. [20]. The freeze-dried product was reconstituted with a known volume of dry methanol (Sigma-Aldrich, Saint Louis, MO, USA) and left to equilibrate for roughly 15 minutes. With the help of a syringe, a known volume of this solution was volumetrically removed from the vial, injected in the titration vessel of the Mettler Toledo V30 volumetric Karl Fischer titrator (Schwerzenbach, Switzerland) and titrated with Hydranal[®] titration solvent (Sigma-Aldrich, Saint Louis, MO, USA). Prior to the measurement of the residual water, the moisture content of the dry methanol was determined in triplicate and subtracted from the result. The residual moisture content of the freeze-dried product was determined for three different validation runs.

7.3 Results and Discussion

7.3.1 View factor for a flat radiator with a cylindrical target

To investigate the influence of the number of rays leaving the radiator plane N , the confidence interval on the view factor is determined for several values of N by repeating the calculation 100 times. In figure 7.6, the intervals between the mean \pm the standard deviation are outlined for an N -value ranging from 10^2 to 10^7 . Obviously, the width of the confidence interval is decreasing with the increase of the N -value. Based on these results, in further analysis, a value of 10^6 was used for N to compute the view factor for different situations.

The view factor for the experimental set-up consisting of a flat radiator with a cylindrical target (i.e., the glass vial) parallel to the plane of the radiator is equal to 0.1484, given the parameter settings as defined in table 7.1. The results for the different planes, i.e., the x - y -, x - z - and y - z -plane, are presented in figure 7.7 for this set-up. It is clear that in the x - y -plane the rays which hit the target (black dots) are within the target boundaries (red

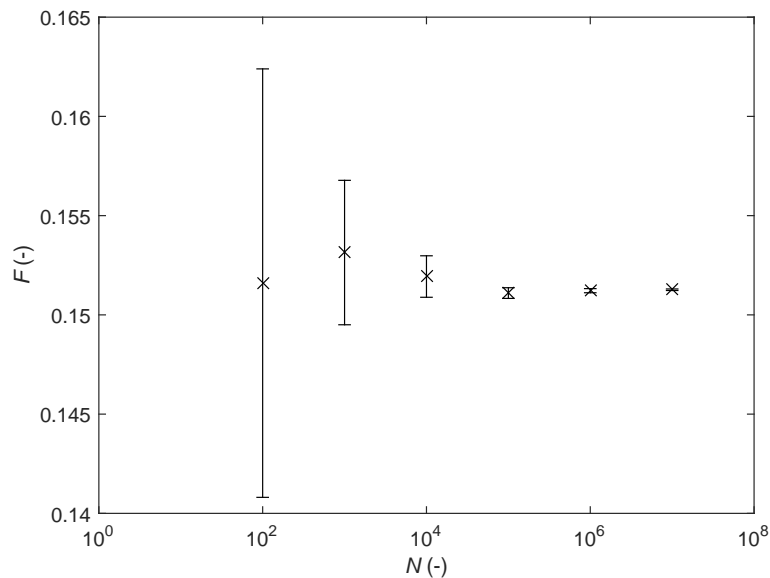


Figure 7.6: Determination of optimal number of samples N for Monte Carlo simulation of the view factor F

frame), while the rays which miss the target (gray dots) are located outside the cylinder. The reason why the endpoints of some rays which missed the target are located within the target boundaries is due to the fact that the third dimension is not presented in these two-dimensional representations. For the perpendicular case, the results are presented in figure 7.8. The view factor equals 0.1212.

7.3.2 IR heater calibration

The mass of sublimed ice Δm (g) after 20 minutes of drying and corrected for the energy contributed by the surroundings and the corresponding IR heater temperature T_{rad} (as calculated from equations (7.10) and (7.12)) are both plotted in function of the applied electric power P_e in figure 7.9. Initially, a linear model was fitted, though, the parabolic distribution of the standardized residuals of the linear model suggested that a quadratic model might be preferred to explain this relation (standardized residual plot not shown). Therefore, a t -test ($\alpha = 5\%$) was conducted to evaluate the statistical significance of the regression coefficients of both the linear and quadratic model. The t -value (-2.474) for the regression coefficient associated with the quadratic term lies between the critical values -3.182 and 3.182 of the t distribution (degrees of freedom = 3) and the corresponding p -value (0.132) is higher than the significance level α . Hence, the null hypothesis is not rejected

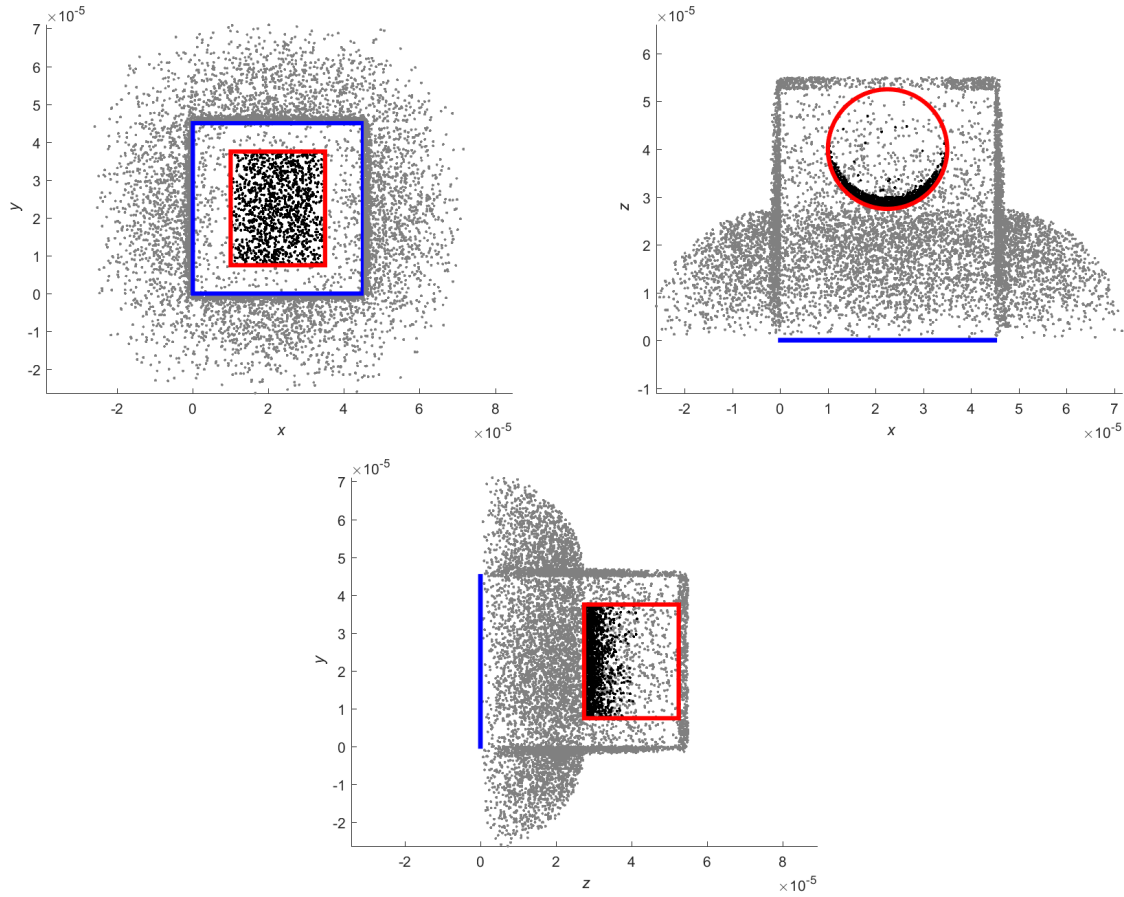


Figure 7.7: The rays which hit (Black) and miss (Gray) the cylindrical target (Red) for the radiator set-up (Blue) (parallel case) in different planes

which means that this regression coefficient is not significant at the 5% significance level. Therefore, a linear model is sufficient (from which all regression coefficients are proven to be significant). In addition, RMSECV for the linear and quadratic model was 35.90 K and 38.67 K, respectively. Hence, the predictive power of the linear model is higher compared to the quadratic model. Based on these findings, the relation between T_{rad} and P_e was described by the following (empirical) linear equation, plotted in figure 7.9:

$$T_{rad} = 5.120P_e + 425.173 \quad (7.25)$$

Comparison of P_e and the net power provided to the spin frozen vial P_{rad} allowed the determination of the IR heater efficiency η (Equation (7.24)). The mean value of η was 6.61%. However, this is not the efficiency inherent to the IR heater itself as only part of the emitted radiation reaches the spin frozen vial. Therefore, it was necessary to include the view factor F in the calculations. F is defined as the percentage of total radiation

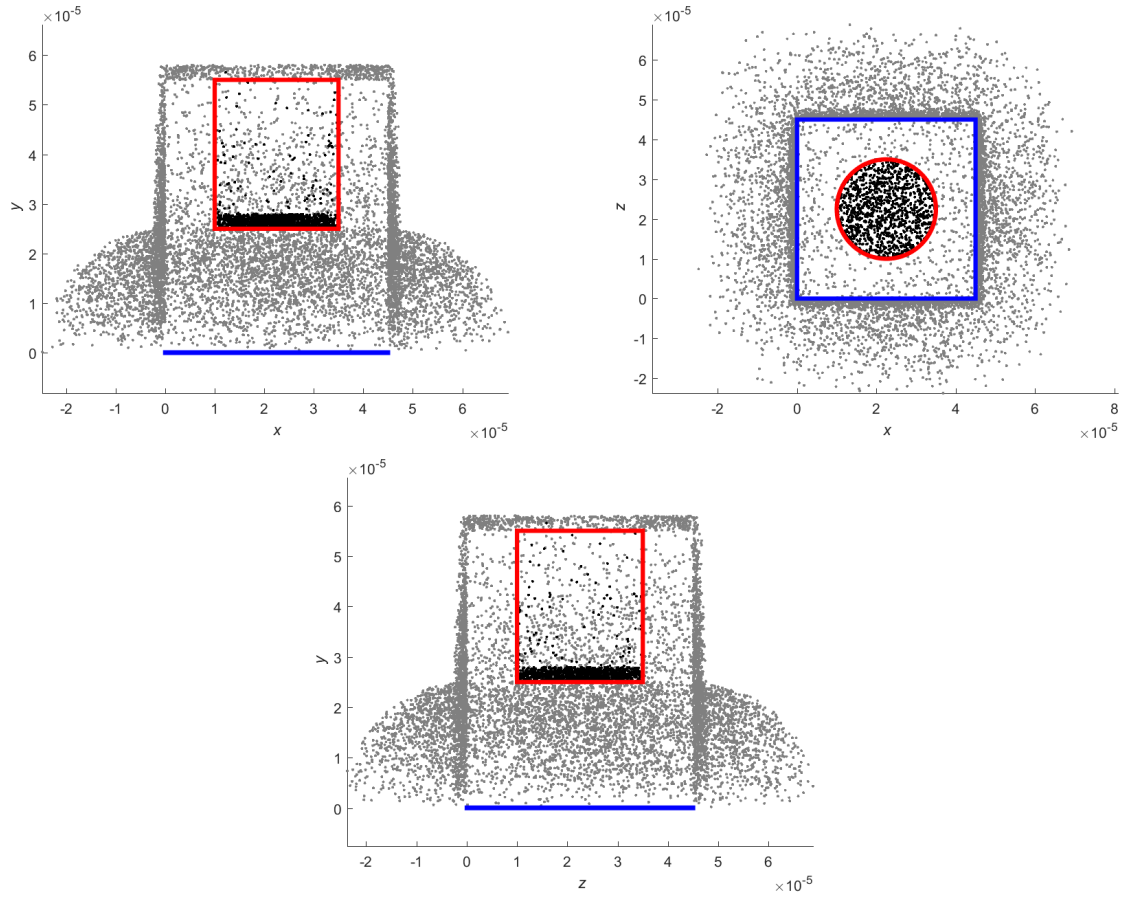


Figure 7.8: The rays which hit (Black) and miss (Gray) the cylindrical target (Red) for the radiator set-up (Blue) (perpendicular case) in different planes

which leaves the IR heater and goes directly to the spin frozen vial [16]. In the current experimental set-up, the vial was located in the middle of the IR heater at a distance of 4 cm, measured from the centre of the vial. The corresponding value of F was 0.1484. Hence, the value of η inherent to the IR heater is 44.54%. The distance between the IR heater and the spin frozen vial (s) has a major impact on F , as illustrated in figure 7.10. F is subject to an exponential decay with the increase of s . η exhibits the same behaviour. Consequently, in order to maintain an equal net energy transfer to the spin frozen vial, P_e needs to be adapted proportionally to the change in s .

7.3.3 Verification of radiation contribution from surroundings

The ice mass sublimed during the verification runs with inactivated heaters was found to be 0.543 ± 0.0395 g ($\dot{m}_{\text{sub}} = 4.53 \cdot 10^{-7}$ kg/s). This value had to be compensated for the

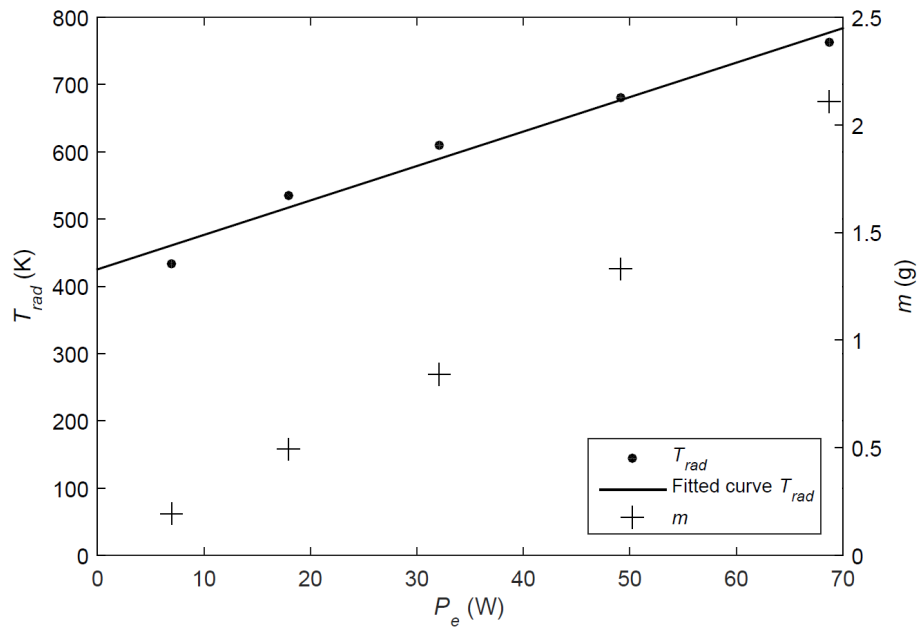


Figure 7.9: Mass of sublimed ice Δm and temperature of IR heater T_{rad} in function of electric power P_e

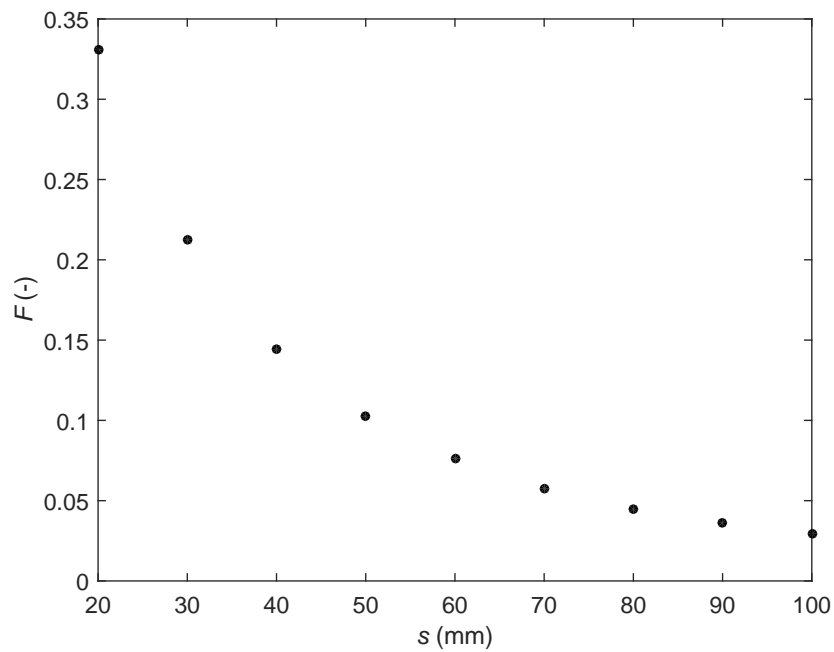


Figure 7.10: View factor F in function of the distance between the IR heater and the centre of the spin frozen vial s

amount of ice sublimed during the initial pressure decrease in the drying chamber, which was 0.219 ± 0.00251 g. Hence, the net sublimed ice mass was 0.324 ± 0.0539 g ($\dot{m}_{\text{sub}} = 2.70 \cdot 10^{-7}$ kg/s) which corresponds to an experimental P_{sur} of 0.766 ± 0.128 W.

The computed value of P_{sur} was 0.649 W, associated with a theoretical \dot{m}_{sub} of $2.29 \cdot 10^{-7}$ kg/s. The power contribution of the surroundings is hence slightly underestimated by the model, with an absolute and relative difference of 0.117 W and 18.0%, respectively. A reason for this underestimation might be that the model only includes the six plane surfaces (the chamber walls and the door of the drying chamber and the shelves above and below the experimental set-up) and the inactive heater in the calculation of the radiation contributed by the surroundings. To reduce the complexity of the model, the parts of the experimental set-up (aluminium frame etc.) were not taken into account which might be responsible for the difference between the experimental and computed P_{sur} . Finally, the absolute value of P_{sur} is very low in comparison to P_{tot} . Therefore, it can be considered that the model provides a good approximation of the radiation energy contributed by the surroundings to the spin frozen vial.

7.3.4 Mechanistic primary drying model predictions

The mechanistic primary drying model (Section 7.2.1) computes the optimal dynamic IR heater temperature profile for the most efficient primary drying without exceeding $T_{i,\text{crit}}$. T_{rad} and l are both plotted in function of the primary drying progress t (Figure 7.11). At the start of the drying process by the heaters, l is predicted to be different from zero, since a significant amount of ice already instantly sublimed during the initial pressure decrease (0.167 ± 0.0143 g). After 50 minutes of primary drying, l is predicted to be equal to the total layer thickness L_{tot} indicating complete ice removal. At the beginning of the process T_{rad} is 728 K, while it slowly decreases until 610 K towards the end of drying. As R_p gradually raises with the increase of l , the energy input should be reduced accordingly with the progress of primary drying, to avoid exceedance of $T_{i,\text{crit}}$ [7]. Therefore, the model predicts T_{rad} to be gradually decreasing as primary drying proceeds. Via equation (7.25), the corresponding P_e profile can be calculated, which is to be used as input for the IR heaters allowing to put the model into practice.

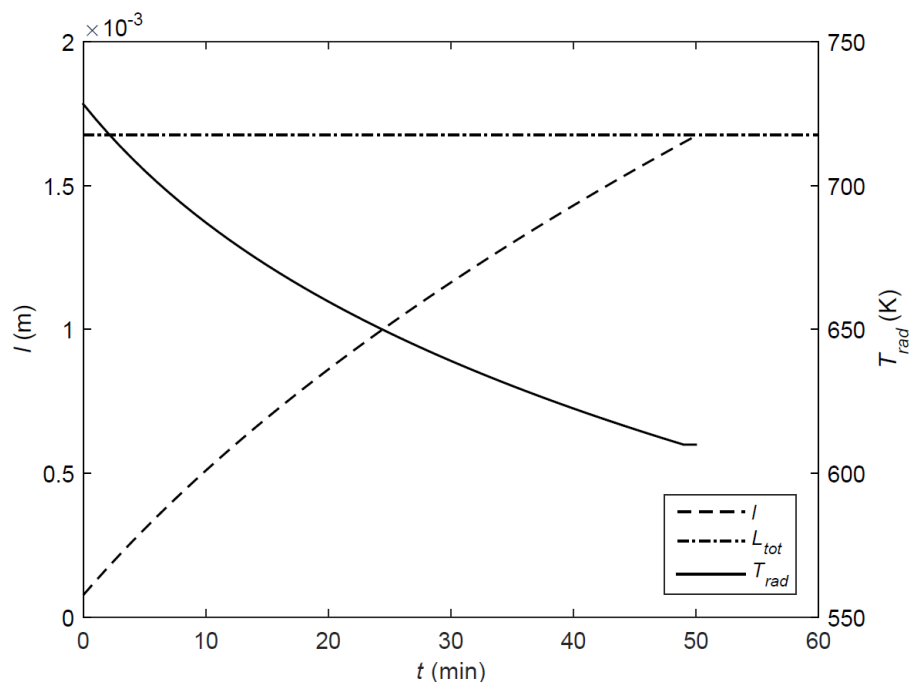


Figure 7.11: IR heater temperature T_{rad} and dried layer thickness l in function of primary drying time t ; the black dash-dotted line represents the total layer thickness of the spin frozen cake L_{tot}

7.3.5 Experimental model validation

Each experimental model validation run ($n = 6$) was continuously monitored with in-line NIR spectroscopy. Via PCA of the preprocessed NIR spectra, the PC1 vs PC2 scores scatter plot was constructed per validation experiment, as illustrated in figure 7.12 for one individual experiment. A significant part of the spectral variability (91.40%) was explained by PC1, a smaller part of the variability was explained by PC2 (6.95%). In the loading line plots of both PCs, some NIR bands were identified (Figure 7.13). The band near 5000 cm^{-1} directed downwards in PC 1 and upwards in PC 2 stems from O-H stretching and H-O-H bending vibrations of ice [21]. The broad band near 6700 cm^{-1} directed downwards in PC 1 and upwards in PC 2 originates from symmetric and asymmetric stretch of ice [21]. Therefore, the loading line plots clearly represent the changes in ice content in the monitored region of the spin frozen vial. These plots assisted in the full explanation of the changing NIR spectra in the scores plot, allowing the determination of the primary drying endpoint (Chapter 6).

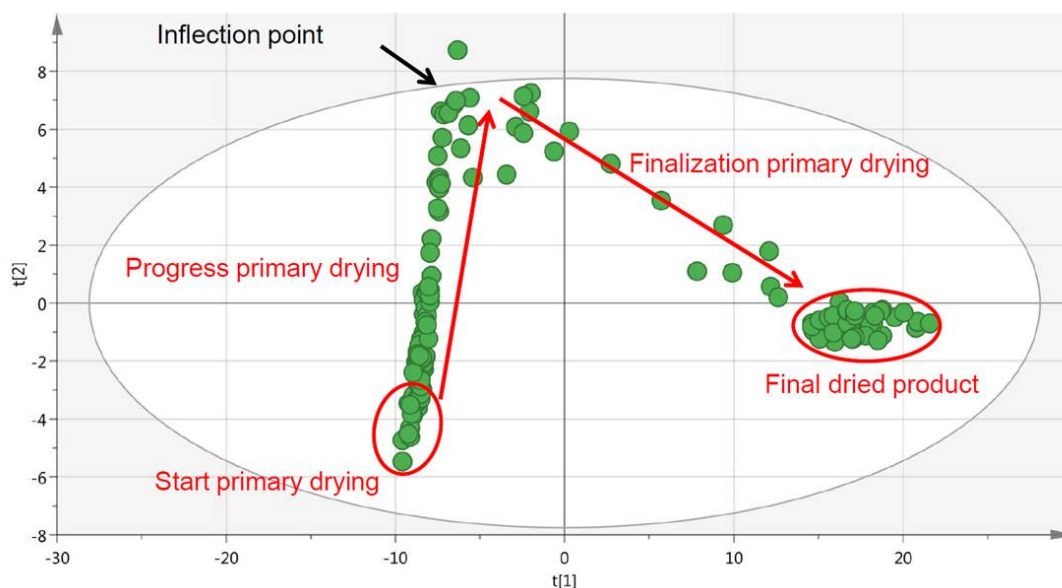


Figure 7.12: Scores scatter plot including the explanation of the chronological trends; each point represents 1 NIR spectrum

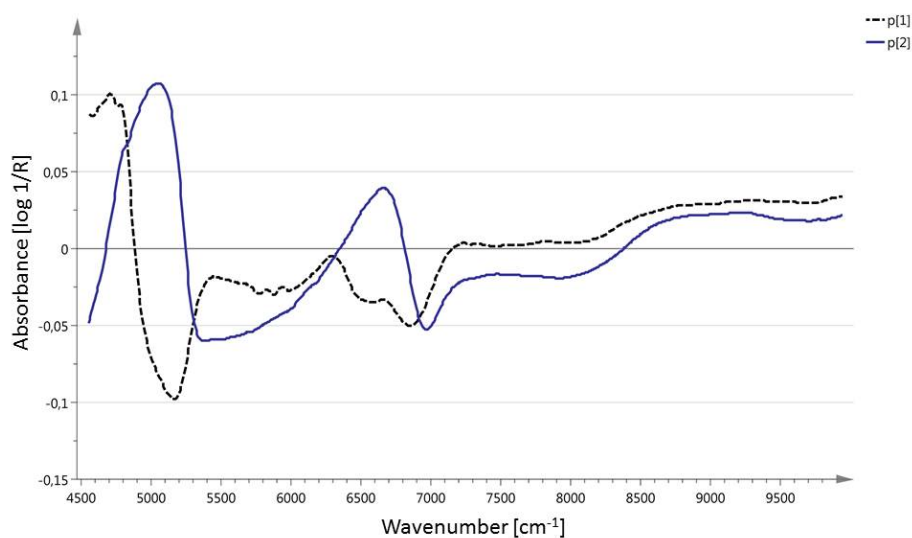


Figure 7.13: Loading line plot of PC1 (black dotted) and PC2 (blue solid)

At the beginning of primary drying, the NIR spectra were completely dominated by overwhelming ice bands. Therefore, the scores of the corresponding NIR spectra were initially clustered in the scores plot (Figure 7.12). At this point, both ice and product were present in the spin frozen vial. With the progression of primary drying, the scores move gradually upwards in the positive direction along PC2 (Figure 7.12). The bands in the NIR spectra

near 5030 cm^{-1} and 6700 cm^{-1} become more distinct in shape (NIR spectra not shown), confirmed by the loading line plot of PC2 where both bands are directed upwards (Figure 7.13). Ice removal proceeds from the centre of the vial in the direction of the glass wall, while NIR spectra were collected from the outer side. The NIR light only has a limited penetration depth into the sample. Hence, ice signals kept dominating the NIR spectra. However, the progress in ice sublimation and the change in the NIR spectra are clearly visible in the scores plot. This trend is probably associated with the reduction in ice layer thickness (Chapter 6). Only after the inflection point in the scores plot (Figure 7.12), characteristic product bands started to appear in the NIR spectra, besides ice specific bands which were still present, but with a lower intensity (NIR spectra not shown). The ice signals only completely disappeared in the NIR spectra in the cluster of scores, situated on the right in the scores plot, illustrated by the characteristic ice bands directed downwards in the loadings of PC1 (Figure 7.12 and 7.13). At this stage, primary drying was completely finished and the final dried product was achieved. In contrast to amorphous products, no removal of residual moisture occurred as the model formulation resulted in a mostly crystalline product identified as β mannitol via Raman spectroscopy, without any traces of mannitol hemihydrate (Figure 7.14).

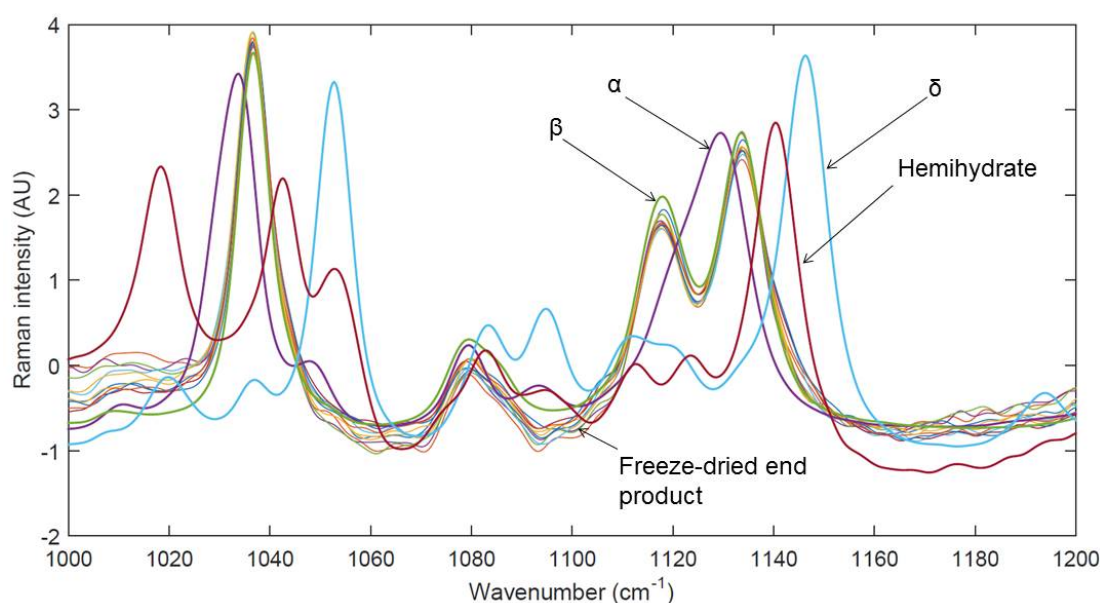


Figure 7.14: Mannitol solid state of the freeze-dried product evaluated via Raman spectroscopy

The spin frozen vial was constantly rotating during primary drying. Hence, each NIR spectrum was collected at a random position at the monitored height of the vial. Despite

the homogeneous energy transfer towards the spin frozen vial, primary drying was locally finished at slightly different time points across the monitored section, which was reflected in the score plot. Primary drying was only considered completely finished, when all ice was sublimated at each position of the monitored height of the spin frozen vial. The experimental primary drying time was defined as the time between the recording of the first spectrum after the onset of the IR heaters and the spectrum following the last spectrum situated outside the cluster in the score plot (Figure 7.12).

For each validation run, the scores scatter plot exhibited the same trends. Each scores plot was analysed as described above to determine the experimental drying time. Comparison was made between the computed and the experimental primary drying time. The results are listed in table 7.2. The experimental drying time was consistent for all repeated

Table 7.2: Overview of the comparison between the computed and experimental primary drying time; Computed primary drying time: 50 minutes

Experiment	Experimental primary drying time (mm:ss)	Ratio experimental to computed primary drying time (-)
1	45:00	0.90
2	47:19	0.95
3	46:00	0.92
4	46:50	0.94
5	43:32	0.87
6	44:09	0.88

runs with an absolute difference of only 3.5 minutes between the two extremes. In addition, there was a fairly good agreement between the predicted (based on the developed model) and the experimentally determined primary drying time, as the mean ratio of both was 0.91 ± 0.025 . The mechanistic model slightly overestimated the primary drying time as for each experiment sublimation was finished before the computed endpoint. This slight deviation could be explained by several hypotheses. Verification of the radiation energy contributed by the surroundings lead to the conclusion that the experimental energy transfer from the chamber walls to the spin frozen vial was higher than estimated by the model (Section 7.3.3). Although the absolute difference was very small, this is a possible reason for the faster primary drying time that was observed. The inertia of the IR heater is another hypothesis that could cause the small deviation between prediction and reality. T_{rad} is gradually decreased with the progress of primary drying to limit the energy transfer

due to the increase in R_p . The power input to the IR heater is lowered in discrete steps until a new level of the computed profile. However, the radiator can not immediately lose all the excess energy at once. T_{rad} decreases steadily until the new equilibrium value is reached, which is associated with a small delay in the response of the IR heater to the power input during the process. This higher value for T_{rad} during (a part of) primary drying might contribute to the higher energy transfer to the spin frozen vial. Finally, some input variables and process parameters of the primary drying model, such as R_p or T_{rad} , are an estimation of the actual value. Inherently, these factors are associated with a certain measurement error. For instance, this was illustrated for T_{rad} via the calculation of RMSECV (Section 7.3.2). This might be the most plausible hypothesis to explain the small deviation between the computed model prediction of the primary drying time and the experimental observations.

Drying of the spin frozen vials following the computed T_{rad} profile resulted in an elegant product appearance without any signs of collapse, visualized in figure 7.15. Finally, the residual moisture content of the dried end product was determined via Karl Fischer titration. The remaining unfrozen water concentration was found to be $0.99 \pm 0.28\%$, which is near the standard target of approximately 1% for batch freeze-dried products [22].



Figure 7.15: Product appearance of final dried product yielded after the validation runs

7.4 General conclusion

The developed mechanistic primary drying model allows the computation of the optimal, dynamic IR heater temperature profile, leading to the optimization of the drying efficiency

of spin frozen vials. The validation experiments indicated a good agreement between the experimental primary drying time and the model predictions (0.91 ± 0.25). In-line NIR spectroscopy allowed the determination of the primary drying endpoint during the model validation experiments. The dried end product had an elegant product appearance and an acceptable residual moisture content ($0.99 \pm 0.28\%$).

Bibliography

- [1] J. C. Kasper and W. Friess. The freezing step in lyophilization: Physico-chemical fundamentals, freezing methods and consequences on process performance and quality attributes of biopharmaceuticals. *Eur. J. Pharm. Biopharm.*, 78:248–263, 2011.
- [2] V. R. Koganti, E. Y. Shalaev, M. R. Berry, T. Osterberg, M. Youssef, D. N. Hiebert, F. A. Kanka, M. Nolan, R. Barrett, G. Scalzo, G. Fitzpatrick, N. Fitzgibbon, S. Luthra, and L. Zhang. Investigation of design space for freeze-drying: use of modeling for primary drying segment of a freeze-drying cycle. *AAPS PharmSciTech*, 12:854–861, 2011.
- [3] S. L. Nail and J. A. Searles. Elements of Quality by Design in development and scale-up of freeze-dried parenterals. *BioPharm Int.*, 21:44–52, 2008.
- [4] R. Bogner and M. J. Pikal. The Incredible Shrinking Design Space: Using Risk Tolerance to Define Design Space for Primary Drying. *Notes of Freeze Drying of Pharmaceuticals and Biologicals Conference, Garmisch-Partenkirchen*, pages 184–198, 2010.
- [5] A. Giordano, A. A. Barresi, and D. Fissore. On the use of mathematical models to build the design space for the primary drying phase of a pharmaceutical lyophilization process. *J. Pharm. Sci.*, 100:311–324, 2011.
- [6] L. N. Mockus, T. W. Paul, N. A. Pease, N. J. Harper, P. K. Basu, E. A. Oslos, G. A. Sacha, W. Y. Kuu, L. M. Hardwick, J. J. Karty, M. J. Pikal, E. Hee, M. A. Khan, and S. L. Nail. Quality by design in formulation and process development for a freeze-dried, small molecule parenteral product: a case study. *Pharm. Dev. Technol.*, 16:549–576, 2011.
- [7] D. Fissore, R. Pisano, and A. A. Barresi. Advanced approach to build the design space for the primary drying of a pharmaceutical freeze-drying process. *J. Pharm. Sci.*, 100:4922–4933, 2011.
- [8] R. Pisano, D. Fissore, A. A. Barresi, P. Brayard, P. Chouvenc, and B. Woinet. Quality by design: optimization of a freeze-drying cycle via design space in case of heterogeneous drying behavior and influence of the freezing protocol. *Pharm. Dev. Technol.*, 18:280–295, 2013.

- [9] S. Mortier, P. J. Van Bockstal, J. Corver, I. Nopens, K. Gernaey, and T. De Beer. Uncertainty analysis as essential step in the establishment of the dynamic Design Space of primary drying during freeze-drying. *Eur. J. Pharm. Biopharm.*, 103:71–83, 2016.
- [10] D. E. Overcashier, T. W. Patapoff, and C. C. Hsu. Lyophilization of protein formulations in vials: Investigation of the relationship between resistance to vapor flow during primary drying and small-scale product collapse. *J. Pharm. Sci.*, 88:688–695, 1999.
- [11] S. Rambhatla, R. Ramot, C. Bhugra, and M. J. Pikal. Heat and mass transfer scale-up issues during freeze drying: II. Control and characterization of the degree of supercooling. *AAPS PharmSciTech*, 5:54–62, 2004.
- [12] W. Y. Kuu, L. M. Hardwick, and M. J. Akers. Rapid determination of dry layer mass transfer resistance for various pharmaceutical formulations during primary drying using product temperature profiles. *Int. J. Pharm.*, 313:99–113, 2006.
- [13] S. M. Patel, S. Chaudhuri, and M. J. Pikal. Choked flow and importance of Mach I in freeze-drying process design. *Chem. Eng. Sci.*, 65:5716–5727, 2010.
- [14] R. Bird, W. Stewart, and E. Lightfoot. *Transport phenomena*. John Wiley & Sons, New York, 2006.
- [15] J. Brenner. *Design specifications for wet-bulb aspirator apparatus*. PhD thesis, University of Wisconsin-Madison, 2010.
- [16] G. F. Nellis and S. A. Klein. Radiation. In *Heat Transfer*. Cambridge University Press, Cambridge, 2009.
- [17] J. Vercruyssen, M. Toiviainen, M. Fonteyne, N. Helkimo, J. Ketolainen, M. Juuti, U. Delaet, I. Van Assche, J. P. Remon, C. Vervaet, and T. De Beer. Visualization and understanding of the granulation liquid mixing and distribution during continuous twin screw granulation using NIR chemical imaging. *Eur. J. Pharm. Biopharm.*, 2013.
- [18] L. Eriksson, E. Johansson, N. Kettaneh-Wold, J. Trygg, C. Wikström, and S. Wold. *Multi- and megavariable data analysis part 1: Basic principles and applications*. Umetrics, Umeå, 2006.
- [19] S. Pieters, Y. Vander Heyden, J. M. Roger, M. D’Hondt, L. Hansen, B. Palagos, B. De Spiegeleer, J. P. Remon, C. Vervaet, and T. De Beer. Raman spectroscopy and

- multivariate analysis for the rapid discrimination between native-like and non-native states in freeze-dried protein formulations. *Eur. J. Pharm. Biopharm.*, 85:263–271, 2013.
- [20] L. Hansen, T. D. Beer, S. Pieters, Y. V. Heyden, C. Vervaet, J. P. Remon, J. P. Montenez, and R. Daoussi. Near-infrared spectroscopic evaluation of lyophilized viral vaccine formulations. *Biotechnol. Progr.*, 29(6):1573–1586, 2013.
- [21] J. Workman and L. Weyer. *Practical Guide to Interpretive Near-Infrared Spectroscopy*. CRC Press, Boca Raton (FL), 2007.
- [22] X. Tang and M. J. Pikal. Design of freeze-drying processes for pharmaceuticals: practical advice. *Pharm. Res.*, 21:191–200, 2004.

CHAPTER 8

Evaluation of thermal imaging as a non-contact in-line process analytical tool for product temperature monitoring during continuous freeze-drying

8.1 Introduction

Product appearance is an important CQA of freeze-dried drug products. Loss of cake structure (i.e., cake collapse) should be avoided for aesthetic purposes and to ensure fast reconstitution of the dried product [1]. Therefore, the product temperature at the sublimation interface T_i should be kept below the critical product temperature $T_{i,crit}$ during the entire primary drying process [2]. $T_{i,crit}$ is defined as the eutectic temperature T_e or the collapse temperature T_c for crystalline and amorphous products, respectively. In general, T_c lies a few degrees above the glass transition temperature of the maximum freeze-concentrated formulation T'_g as the high viscosity of the glass near T'_g limits molecular motion [2]. Mechanistic models allow the determination of the optimal combination of shelf temperature T_s and chamber pressure P_c to avoid exceeding $T_{i,crit}$ while maximizing the primary drying efficiency [3–8]. The development of this optimal dynamic profile of T_s and P_c requires the reliable measurement of T_i .

In batch freeze-drying, T_i is generally measured using resistance temperature detectors (RTDs) or, preferentially, thermocouples [9]. RTDs provide a mean readout for the complete area of the detection element, which is partially in contact with dried material during the majority of the primary drying process, leading to unreliable data. Thermocouples

are preferred as the temperature is measured at the point where the two thin wires, made of different metals or metal alloys, are connected, making them less unreliable compared to RTDs in measuring T_i . The invasive character of both RTDs and thermocouples alters the process conditions compared to in the absence of these sensors. During the freezing step, the insertion of the temperature sensors induces ice nucleation, i.e., a lower degree of supercooling, resulting in larger ice crystals [10]. Besides faster drying kinetics due to the reduced product resistance in the monitored vials, the presence of these sensors adds to the heat transfer, contributing to the increased sublimation rate [11]. Therefore, the monitored vials containing a temperature sensor are not representative for the whole batch [12–16]. The response of the thermocouple is also highly dependent of its position in the ice because of the temperature gradient across the frozen product [9]. Deviations in its positioning and the gradual downward movement of the sublimation front add to the high uncertainty on the measurement of the correct value of T_i .

In the previous chapter, a mechanistic model was developed which allowed the computation of the optimal dynamic temperature profile of the IR heater to maximise the primary drying efficiency while maintaining an elegant product appearance. The development of the optimal IR heater profile for a specific formulation requires the reliable measurement of T_i . Thermocouples are unsuitable to measure T_i during the continuous primary drying step. The spinning of the glass vials makes it impossible to insert thermocouples in the frozen product layer during the continuous freezing step. Trying to assess the product temperature through measuring the temperature of the glass wall is compromised by poor contact due to rotation of the vial.

Thermal imaging allows non-contact temperature measurements based on the detection of IR radiation emitted by an object and its conversion to a thermal image, displaying the spatial temperature distribution. Previously, this technique has been considered for in-line temperature monitoring during batch freeze-drying [17]. The IR camera was implemented on the top of the freeze-dryer which required customization of the equipment by removing a part of the radiation shield to visualize the vials on the top shelf. From the position where the IR camera was installed, only the top of the cake was visualized. As the sublimation front moves gradually downwards during primary drying, most of the time the temperature of the dried product is measured, which is not representative for T_i . In addition, it is not possible to quantify the temperature gradient over the dried product layer. Consequently, thermal imaging is incompatible with batch freeze-drying, as illustrated in figure 8.1 (Top). In the continuous freeze-drying concept, the vials are not packed on shelves, but

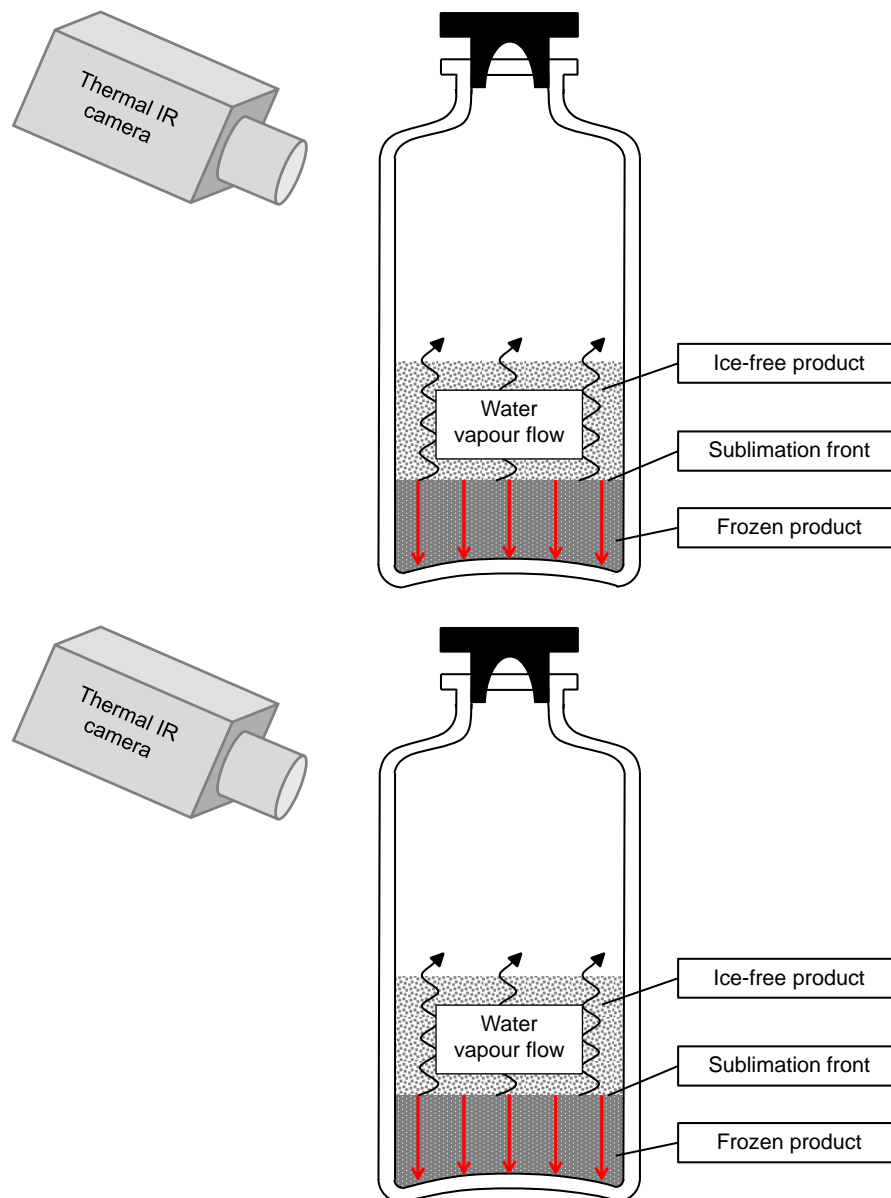


Figure 8.1: Illustration of the compatibility of thermal imaging with batch (top) and continuous (bottom) freeze-drying; The direction of the sublimation front during primary drying is indicated by the red arrows

freely rotating in front of an individual IR heater, forming a long line of vials (Chapter 5). The product is spread over the entire wall of the spin frozen vial, which allows complete visualisation by the IR camera (Figure 8.1, bottom). The sublimation front moves from the centre of the vial towards the glass wall during the continuous primary drying step.

Hence, after compensation for the temperature gradient over the glass wall and the ice layer, T_i can be continuously monitored from the very beginning of the primary drying step until the end.

The global objective of this study was to evaluate the feasibility of thermal imaging for continuous real-time measurement of the temperature at the sublimation front T_i during the entire primary drying stage. In a first step, the implementation of the IR camera in the prototype is described via a model-based design approach. Secondly, the temperature gradient over the thin glass wall of the vial and the ice layer was calculated to accurately measure T_i . Finally, the use of thermal imaging was evaluated for two different applications: the determination of the endpoint of primary drying and the calculation of the dried product mass transfer resistance R_p .

8.2 Model-based design of thermal camera set-up

The freeze-drying of parenteral (bio-)pharmaceuticals needs to meet the Good Manufacturing Practice (GMP) standards for the aseptic production of parenteral drug products. This implies that all product contact areas need to be sanitized and sterilized using Cleaning-in-Place (CIP) and Sterilization-in-Place (SIP) procedures. Since the thermal IR camera is not compatible with such processes, it must be positioned outside the continuous freeze-drying equipment, more specifically, the primary drying unit (Figure 8.2). Hence, the temperature of the spin frozen vials during primary drying was monitored through a window consisting of a material which is highly transparent for the electromagnetic radiation emitted by the vials. The radiation spectrum of an object is highly dependent on its temperature. This relation is given by Planck's law, which describes the spectral radiance B_λ (W/sr/m³) in function of wavelength λ (m) and the absolute temperature T (K) of the object [18]:

$$B_\lambda(\lambda, T) = \frac{2hc^2}{\lambda^5} \frac{1}{e^{\frac{hc}{\lambda k_B T}} - 1} \quad (8.1)$$

with h the Planck constant (6.63×10^{-34} J s), c the speed of light (3.00×10^8 m/s) and k_B the Boltzmann constant (1.38×10^{-23} J/K). As the vial temperature should be monitored during both the primary and secondary drying phase, B_λ was calculated for a vial temperature which can vary from approximately -50°C to 50°C . For each temperature in this interval, B_λ is plotted in function of λ in the 1.0×10^{-6} m to 25.0×10^{-6} m region, as given in figure 8.3 (Left). These spectra were then compared to the transmission prop-

erties of different window materials. Taking other properties into account as well, e.g., the mechanical resistance of the window material to the vacuum in the drying chamber, germanium was selected because of its good transmission properties in the spectral region of interest. A germanium disk with a thickness of 3 mm and an anti-reflectance coating was implemented in the drying module via a plastic interface and rubber rings, leading to an IR transparent window with a diameter of 30 mm. The spectral transmittance of the germanium IR window in function of the wavelength $T_B(\lambda)$ and the influence of this window on the radiation spectrum are plotted in the middle and right part of figure 8.3, respectively. It should be noted that $T_B(\lambda)$ and $B_\lambda(\lambda, T)$ are only plotted between 7.0×10^{-6} m to 14.0×10^{-6} m as only for this spectral region the transmittance data were provided by the supplier of the IR window. Due to the high $T_B(\lambda)$ of germanium, $B_\lambda(\lambda, T)$ is only slightly reduced, illustrating the good transmission properties of the material, making it suitable as IR window. As $B_\lambda(\lambda)$ depends on the temperature T of the measured object, i.e., the spin frozen vial, and T_B changes for λ , T_B also changes with T (Figure 8.3). Therefore, the transmittance of the germanium window is experimentally determined in function of the vial temperature, i.e., $T_B(T)$ (Section 8.3.3).

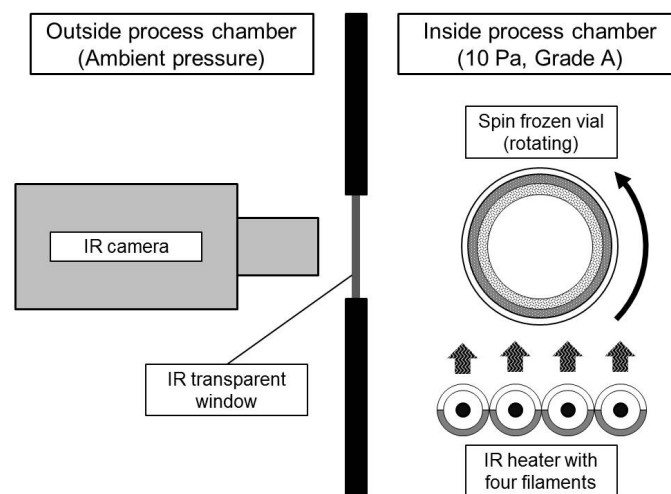


Figure 8.2: Illustration of the IR camera set-up (top view) during primary drying with the rotating spin frozen vial and the IR heater inside the vacuum chamber and the IR camera positioned outside measuring through an IR window at an angle of 90°

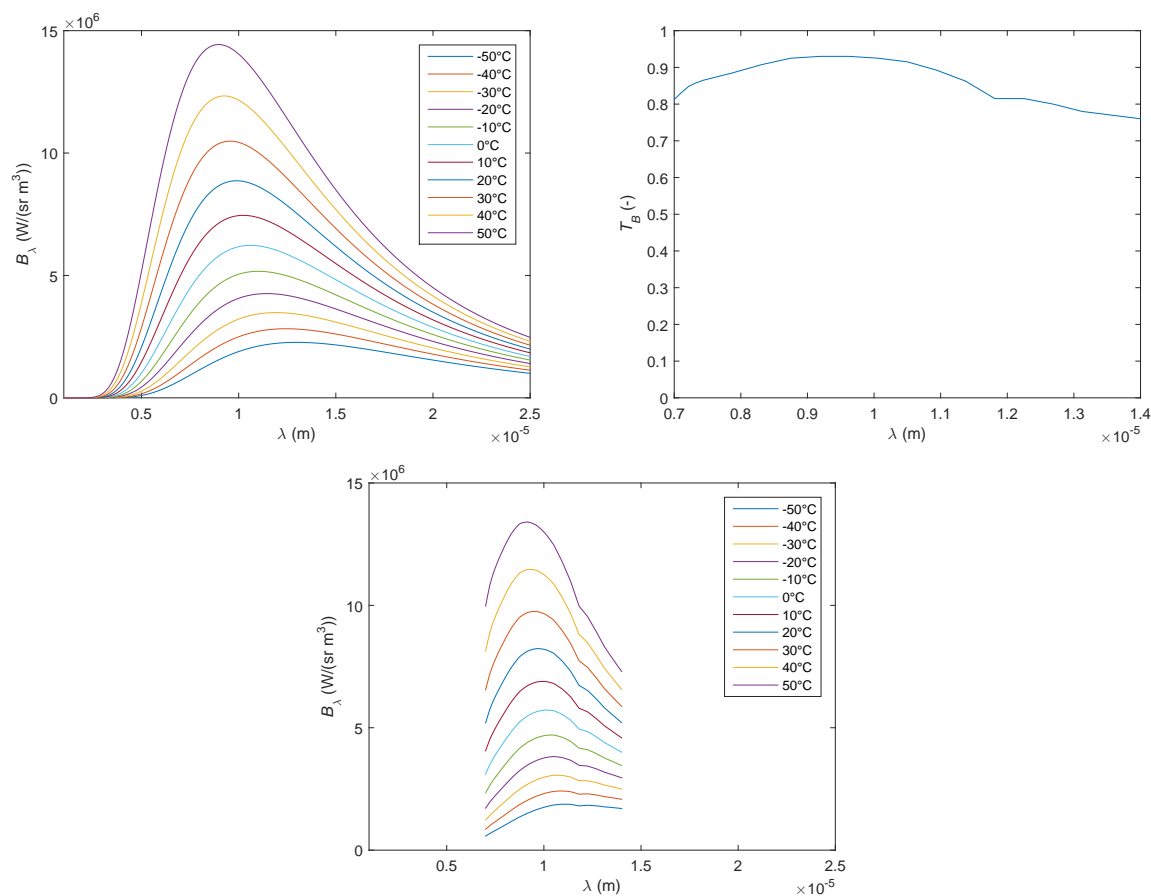


Figure 8.3: The spectral radiance B_λ emitted by glass vials in function of the wavelength λ for a vial temperature varying from -50°C to 50°C , in the absence (top left) and presence (bottom) of the germanium IR window between the vial and the IR camera; the transmission of the germanium window in function of the wavelength $T_B(\lambda)$ is plotted on the top right

8.3 Materials and methods

8.3.1 Experimental freeze-drying set-up

A 10 mL type I glass vial (Schott, Müllheim, Germany) was filled with 3.9 mL of an aqueous 3 mg/mL sucrose (Sigma-Aldrich, Saint Louis, MO, USA) solution and spin frozen as previously described (Chapter 6). The glass vial was positioned in a vial holder and vertically rotated along its longitudinal axis at approximately 2900 rpm. The solution was consequently spread uniformly across the entire vial wall after which the rotating vial was

immersed into liquid nitrogen for 40 ± 5 s, leading to complete solidification of the product. Within 15 ± 5 s after spin freezing, the vial was transferred from the liquid nitrogen to the drying chamber of an Amsco FINN-AQUA GT4 freeze-dryer (GEA, Köln, Germany), to avoid exceeding T'_g of the formulation. The vacuum chamber of this pilot-scale batch freeze-dryer is used as a model for the primary drying module of the continuous freeze-drying technology. The shelves in the drying chamber were cooled at a fixed temperature of -10°C to minimize its radiation contribution to the spin frozen vial during drying. The vial was hung in front of one IR heater (Weiss Technik, Zellik, Belgium) at a distance of 4 cm measured from the centre of the vial until the heated filaments of the IR heater, without making contact with the shelf (Figure 8.2). To achieve a homogeneous radiation energy transfer, the spin frozen vial was continuously rotating at 5 rpm. After placing the vial in the drying chamber, the pressure was immediately lowered to 13.3 Pa. Within 5 minutes, the pressure was below the triple point of water. After 17 minutes, the desired pressure was reached and the IR heater was activated. Primary drying was conducted at a constant electric power input P_e of 7 W, supplied by the Voltcraft PPS-11360 power supply (Conrad Electronic, Hirschau, Germany) to the IR heater. The amount of ice sublimed during the initial pressure decrease, i.e., the 17 min lasting period between activating the vacuum pump and the IR heaters, was gravimetrically determined in triplicate (Chapter 7).

8.3.2 Thermal imaging

The temperature of the spin frozen vials was continuously monitored using a FLIR A655sc IR camera (Thermal Focus, Ravels, Belgium) equipped with a 45° lens and an uncooled micro-bolometer as detector. The thermal IR camera was placed in front of the germanium window, as illustrated in figure 8.2. The spin frozen vial was slowly rotating at a distance of 350 ± 10 mm of the camera. The depth of field far and near limit were approximately 380 and 320 mm, respectively. Hence, each object situated between these limits was in focus. The IR heater providing the energy for ice sublimation, was positioned at an angle of 90° to the thermal camera (Figure 8.2). Thermal images were recorded with an image size of 640 x 480 IR pixels. Pixels from the surrounding IR window interface which did not contain any relevant information were removed from the thermal images. At the specified measuring distance, the width of the vial (24 mm) took up approximately 80 pixels, leading to a spatial resolution of 0.30 mm. The thermal resolution of the IR camera is 30 mK Noise Equivalent Temperature Difference (NETD). Each minute a thermal image was recorded via the FLIR ResearchIR MAX software (Thermal Focus, Ravels, Belgium).

Data processing was conducted using the same software. The emissivity of the glass vial was 0.93.

8.3.3 Experimental determination of transmittance of germanium IR window

The spectral transmittance of the germanium IR window in function of the vial temperature $T_B(T)$ was experimentally verified by comparing thermal images with thermocouple data. A glass vial completely filled with water was frozen using liquid nitrogen (without spinning) and hung in the drying chamber after freezing. Before freezing, a thermocouple was inserted in the glass vial, hence, completely immersed in ice. Based on the principle that ice temperature is related to its vapour pressure, the temperature of the ice was varied over the range of interest to monitor the temperature during primary drying. The pressure in the drying chamber was initially decreased until 10 Pa which allowed to measure the temperature starting from a lower limit of approximately $-40\text{ }^\circ\text{C}$. The pressure in the drying chamber was increased in discrete steps of 0.25 to 0.50 Pa until 70 Pa, which was associated with a gradual increase in temperature until approximately $-24\text{ }^\circ\text{C}$. At each pressure level, after sufficient equilibration, the temperature of the vial $T_{v,o}$ was measured with the thermal IR camera, positioned in front of the IR window. These measurements were correlated with the thermocouple output, allowing to estimate the transmittance of the germanium window in function of the temperature of the glass vial. As will be discussed in further sections, for this experiment, the temperature gradient over the glass wall and the ice layer was assumed to be negligible, due to the very limited energy input to the vial, as no additional heating but the radiation contribution of the surroundings was provided.

8.3.4 Calculation of temperature gradient over glass wall and ice layer

The IR camera measures the temperature of the outer side of the vial wall although the temperature at the sublimation front during primary drying is critical and, thus, of interest. Hence, the accurate measurement of the temperature at the sublimation interface T_i requires an appropriate compensation for the temperature gradient over the glass wall and the ice layer, which are in close contact with each other (Figure 8.4). Due to the endothermic nature of the sublimation process, the radiation energy provided by the IR heaters during primary drying is completely consumed for ice sublimation and T_i remains constant. Therefore, the system can be assumed to be at steady-state. Hence, the temperature gradient can be quantified by Fourier's law of thermal conduction, which states that the rate of heat flow per unit area is proportional to the temperature gradient [18].

After integrating from the outer radius of the glass vial $r_{v,o}$ to the inner radius $r_{v,i}$ for the specific cylindrical geometry (Figure 8.4), the one-dimensional heat conduction over the glass wall of the vial is given by [18]:

$$P_{tot} = 2\pi k_{glass} k \frac{(T_{v,o} - T_{v,i})}{\ln\left(\frac{r_{v,i}}{r_{v,o}}\right)} \quad (8.2)$$

with P_{tot} the total power provided to the spin frozen vial (W), k_{glass} the thermal conductivity of glass (1.05 W/(m K)), k the height of the spin frozen product (m), $T_{v,o}$ the temperature measured at the outer side of the vial wall (K), $T_{v,i}$ the temperature at the inner side of the vial wall (K), $r_{v,i}$ the inner radius of the glass vial (m) and $r_{v,o}$ the outer radius of the glass vial (m). The temperature gradient over the thin ice layer is also calculated via equation 8.2, in which $T_{v,o}$ and $T_{v,i}$ are replaced by $T_{v,i}$ and T_i (K) and $r_{v,o}$ and $r_{v,i}$ by $r_{v,i}$ and the sum of the radius from the centre of the vial to the border of the spin frozen layer $r_{p,i}$ (m) and the thickness of the dried product layer l (m), respectively (Figure 8.4). Also, the thermal conductivity of ice k_{ice} (2.18 W/(m K)) is taken into account instead of k_{glass} . Due to the close contact between the ice layer and the vial wall, the thermal contact resistance between the glass and ice can be ignored [9].

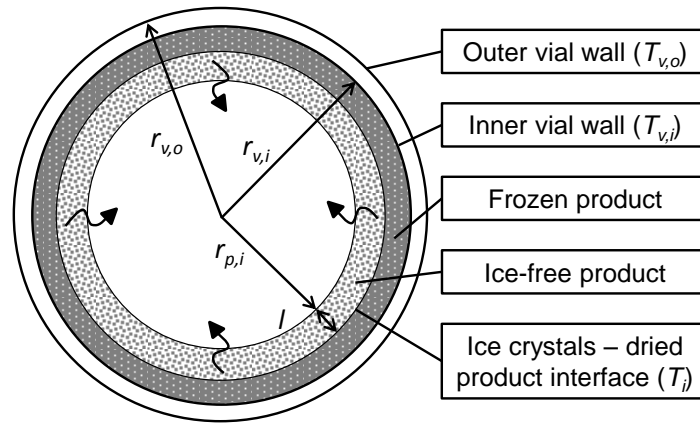


Figure 8.4: Illustration of a cross section of a spin frozen vial during primary drying with specified temperatures and radii

The power provided by the IR heater to the spin frozen vial during primary drying P_{rad} is calculated via the Stefan-Boltzmann law [18]:

$$P_{rad} = A_{rad} F \sigma (\epsilon T_{rad}^4 - a T_{v,o}^4) \quad (8.3)$$

with A_{rad} the surface area of the IR heater (m²), F the view factor (-), σ the Stefan-Boltzmann constant (5.67 x 10⁻⁸ W/(m² K⁴)), ϵ the emission coefficient of the IR heater

(-), T_{rad} the temperature of the IR heater (K) and a the absorptivity of the glass vial (-). In general, a is estimated as the value of ϵ for a given surface, in this case the glass vial [18]. F is defined as the percentage of total radiation which leaves the surface of the IR heater and goes directly to the target surface, i.e., the spin frozen vial [19]. F is computed based on a Monte Carlo method previously described (View factor paper). Finally, the radiation energy provided by the surrounding surfaces (e.g., the chamber walls and door) to the spin frozen vial P_{sur} was experimentally determined as described in previous chapter 7. Hence, P_{tot} was compensated for this additional energy contribution following equation 8.4:

$$P_{tot} = P_{rad} + P_{sur} \quad (8.4)$$

8.3.5 Determination of dried product mass transfer resistance

During primary drying, the sublimation front gradually moves from the centre of the vial towards the glass wall, leaving a porous product matrix (Figure 8.4). The water vapour generated at this sublimation interface escapes through this porous structure before reaching the condenser. The flow of water vapour through the pores is restricted by the dried product mass transfer resistance R_p . Exceeding this mass flow limit is associated with a local increase in vapour pressure at the sublimation interface $P_{w,i}$ due to the saturation of the pores. As T_i is in equilibrium with $P_{w,i}$, T_i will then also increase. However, T_i should be maintained below $T_{i,crit}$ during the entire primary drying step to avoid collapse of the product. Therefore, the accurate determination of R_p is essential for the development of the optimal freeze-drying cycle (i.e., the optimal dynamic IR heater temperature profile) for a specific formulation, allowing a maximum primary drying efficiency while yielding a decent cake aspect (Chapter 7).

The dried product mass transfer resistance R_p (m/s) is correlated to the ratio of the vapour pressure gradient between the sublimation interface and the drying chamber and the mass flow rate by the following equation:

$$R_p = \frac{A_p(P_{w,i} - P_{w,c})}{\dot{m}_{sub}} \quad (8.5)$$

with A_p the product surface area available for sublimation (m^2), $P_{w,i}$ the vapour pressure of ice at the sublimation interface (Pa), $P_{w,c}$ the partial pressure of water in the drying unit (Pa) and \dot{m}_{sub} the sublimation rate during primary drying (kg/s). $P_{w,c}$ is considered to be equal to the overall pressure in the drying unit P_c , as the gas composition in the primary drying unit consists almost entirely of water vapour, similar to batch freeze-drying

[5]. The system was assumed to be at steady-state (Section 8.3.4), hence, \dot{m}_{sub} is directly linked to P_{tot} . This relation is given by:

$$\dot{m}_{\text{sub}} = \frac{P_{\text{tot}}M}{\Delta H_s} \quad (8.6)$$

where M is the molecular weight of water (0.018 kg/mol) and ΔH_s is the latent heat of ice sublimation (51139 J/mol). P_{tot} is determined via the Stefan-Boltzmann law, based on the measurement of $T_{v,o}$ using the IR camera, including the compensation for P_{sur} (Section 8.3.4). Alternatively, \dot{m}_{sub} can also be determined via a gravimetric procedure, requiring a series of experiments. $P_{w,i}$ is in equilibrium with T_i , calculated by the following empirical equation [20]:

$$P_{w,i} = 3.6 \cdot 10^{12} e^{-\frac{6145}{T_i}} \quad (8.7)$$

where T_i is determined based on the measured value of $T_{v,o}$, taking the temperature gradient over the glass wall and the ice layer into account (Section 8.3.4). A_p of the spin frozen layer is calculated by:

$$A_p = 2\pi(r_{p,i} + l)k \quad (8.8)$$

where $r_{p,i}$ is given by:

$$r_{p,i} = \sqrt{r_{v,i}^2 - \frac{V}{\pi k}} \quad (8.9)$$

with V the filling volume (m³). Due to the cylindrical shape of the cake, A_p increases with the gradual movement of the sublimation interface from the inside of the vial towards the vial wall (Figure 8.4).

R_p is formulation specific and is strongly influenced by the size of the pores in the dried product layer, which is mainly determined by the freezing procedure and the degree of supercooling during this freezing step [21, 22]. In addition, as the path of water vapour originating from the sublimation front and flowing through the pores of the dried product layer prolongs with the primary drying progress, R_p generally increases with the corresponding increase in l . This relation is given by the following empirical equation [23]:

$$R_p = R_{p,0} + \frac{A_{R_p}l}{1 + B_{R_p}l} \quad (8.10)$$

where $R_{p,0}$ (m/s), A_{R_p} (1/s) and B_{R_p} (1/m) are constants describing R_p in function of the thickness of the dried product layer l . R_p is calculated in function of drying time t for a specified time interval Δt (e.g., 60s) via equation 8.5. The increase in the dried layer

thickness Δl (m) is calculated for the same Δt by:

$$\Delta l = \frac{\dot{m}_{\text{sub}} \Delta t}{A_p \rho_{\text{ice}} \phi} \quad (8.11)$$

with ρ_{ice} the density of ice (kg/m^3) and ϕ the volume fraction of ice (-). Equation 8.11 is fitted to the experimental R_p data in function of l via non-linear regression, resulting in the R_p constants.

8.3.6 NIR spectroscopy

Diffuse reflectance NIR spectra were continuously in-line collected with an Antaris™ II Fourier-Transform NIR spectrometer (Thermo Fisher Scientific, Erembodegem, Belgium), equipped with a quartz halogen lamp, a Michelson interferometer and an InGaAs detector. The fibre optic probe was implemented in the drying chamber at a distance of 0.5 ± 0.1 mm near the middle of the vial without hampering or disturbing the rotation of the vial. As drying progresses from the centre of the vial to the inner vial wall, in-line NIR spectroscopy allowed the detection of complete ice removal, i.e., the endpoint of primary drying. Every 20 seconds a NIR spectrum was collected in the $4500\text{--}10000\text{ cm}^{-1}$ region with a resolution of 16 cm^{-1} and averaged over 4 scans. The illumination spot size obtained with the NIR probe was approximately 28 mm^2 . Due to rotation of the vial during the measurements, each spectrum was collected at a different position of the cake on a specific height. It was assumed that this monitored part is representative for the whole cake.

8.3.7 Multivariate data analysis

The collected NIR spectra during each validation run were analysed with the help of the multivariate data analysis software SIMCA (Version 14.0.0, Umetrics, Umeå, Sweden). The NIR spectra collected before activation of the heaters were removed from each dataset. The Savitzky-Golay filter was applied to smooth the spectra: a quadratic polynomial function was fitted to a moving sub-model, each containing fifteen data points. Additionally, SNV preprocessing was applied to eliminate the additive baseline offset variations and multiplicative scaling effects in the spectra which may be caused by small variations in distance between the NIR probe and the rotating glass vial and possible differences in product density [24]. PCA was then used for the analysis of the preprocessed and mean-centred NIR spectra.

PCA is an unsupervised multivariate projection method which extracts and displays the variation in the data set [25, 26]. The original variables, e.g., the individual wave numbers of the NIR spectra, are replaced by a new set of latent variables, named PCs. These PCs are sequentially acquired by an orthogonal, bilinear decomposition of the data matrix. Each component explains most of the remaining variability in the data. PCs are composed of a score and a loading vector. The score vector contains a score value for each spectrum, which describes its quantitative relation to the other spectra. The loading vector provides qualitative information about which spectral features present in the original observations are captured by the corresponding component.

8.3.8 Determination of the glass transition temperature

The T_g' of the 3 mg/mL sucrose formulation was determined via MDSC using a differential scanning calorimeter Q2000 (TA instruments, Zellik, Belgium). Hermetically sealed aluminium pans (TA instruments, Zellik, Belgium) were filled with approximately 12 mg of the formulation. The DSC cell was constantly purged with dry nitrogen at a flow rate of 50 mL/min. The sample was initially cooled until -90°C . This temperature was maintained for 5 minutes. Subsequently the temperature was linearly increased until 0°C at a heating rate of $2^\circ\text{C}/\text{min}$. The modulation amplitude and period were set at 0.212°C and 40 seconds, respectively. The analysis was conducted in duplicate. The thermal images were analysed with TA Instruments Universal Analysis 2000 version 4.7A (TA Instruments, Zellik, Belgium).

8.4 Results and discussion

8.4.1 Transmittance of germanium IR window

The experimentally verified spectral transmittance T_B through the germanium IR window is plotted in function of the vial temperature $T_{v,o}$ in figure 8.5. The transmittance T_B increases with $T_{v,o}$. The spectral radiance profile $B_\lambda(\lambda)$ emitted by the glass vials changes with $T_{v,o}$ (Figure 8.3 left). In turn, the transmittance of IR radiation by the germanium window depends on the wavelength of the radiation. The top of the IR radiation spectrum shifts to a lower wavelength for a higher temperature of the glass vials. From figure 8.3 (middle), it can be observed that the transmission of germanium is higher at a lower wavelength. Hence, the transmittance of the IR radiation spectrum emitted by the glass vial is higher for a higher temperature of this vial.

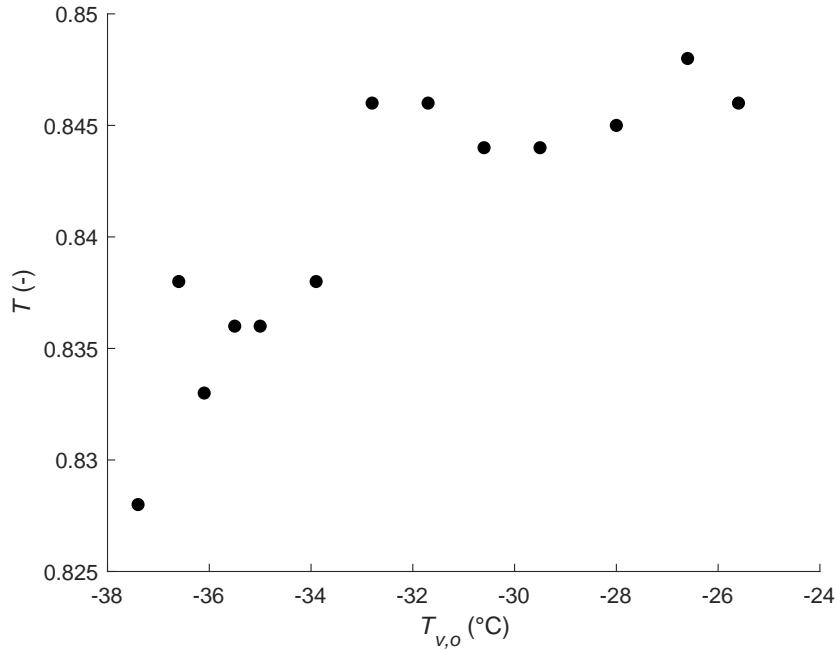


Figure 8.5: Spectral transmittance T_B of the germanium IR window in function of the vial temperature $T_{v,o}$

A quadratic model was fitted to the experimental T_B data in function of $T_{v,o}$. A t -test indicated that the quadratic term is significant at the 5% significance level. The RMSECV for quadratic model was 0.002951. Based on these findings, the relation between T_B and $T_{v,o}$ for the temperature range under study was described by the following (empirical) quadratic equation:

$$T_B = -0.0001734T_{v,o}^2 + 0.08508T_{v,o} - 9.593 \quad (8.12)$$

with $T_{v,o}$ expressed in K.

8.4.2 Analysis of thermal images

The thermal images obtained at different time points during the primary drying of a spin frozen vial are plotted in figure 8.6. The top left thermal image in figure 8.6 shows a spin frozen vial under constant vacuum (13.3 Pa), just before activation of the IR heater. Generally, the measured temperature $T_{v,o}$ was approximately -37°C . In the middle (black arrow in left thermal image in figure 8.6) and at the edge of the vial (red arrows in left thermal image in figure 8.6), thin bands are present with temperature values deviating

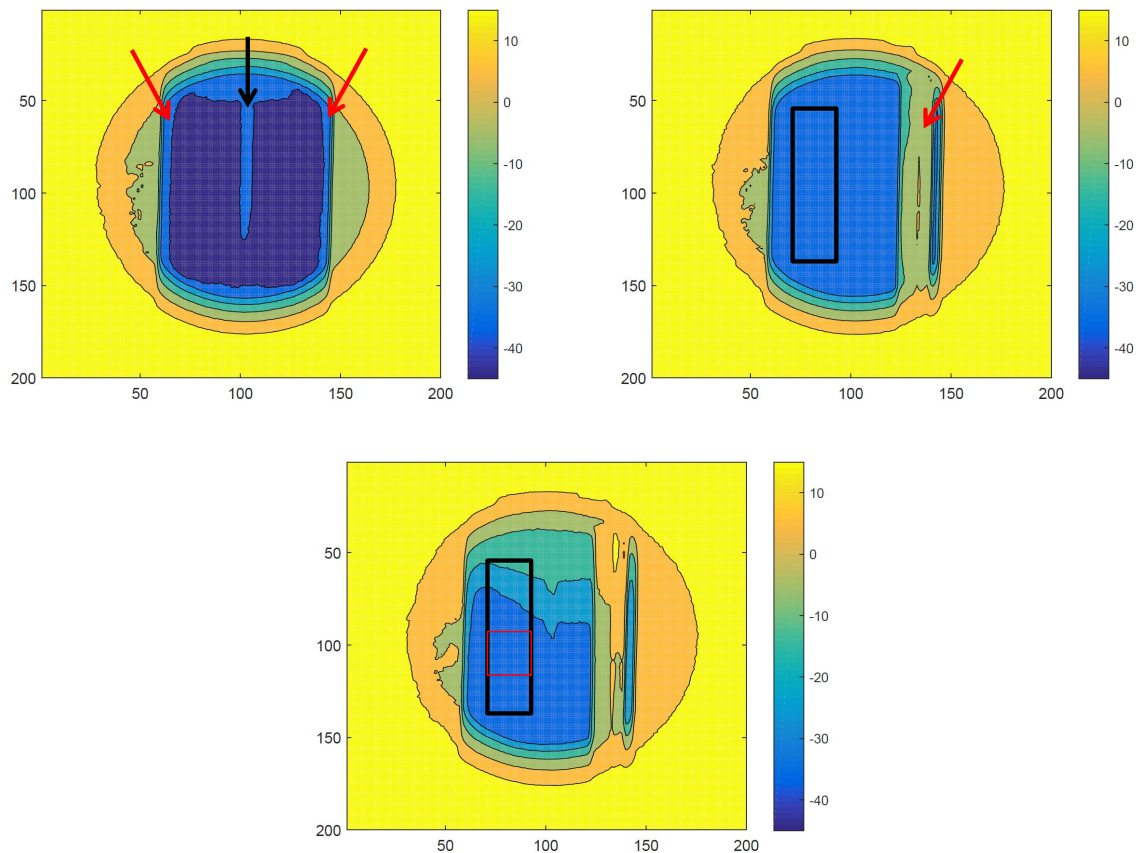


Figure 8.6: Thermal images of a spin frozen vial just before activation of the IR heaters (top left), after 20 min (top right) and after 100 min of primary drying (bottom); the arrows indicate regions on the vial wall which suffer from external reflectance, while the red and black rectangle indicate the region of interest for temperature monitoring

from the rest of the glass surface. These bands remained in the same position despite the rotation of the spin frozen vial, indicating they originated from external factors instead of being a characteristic of the monitored vial itself. Both bands originated from reflectance inherent to the experimental set-up and resulted in a higher value for $T_{v,o}$. These observations were present in each thermal image recorded during the entire drying process. The deviating temperature data in these points do not represent a correct measurement of T_i , hence, these regions were excluded from further analysis.

The top right thermal image in figure 8.6 was captured 20 min after activating the IR heater. $T_{v,o}$ had raised to approximately -33°C , as the increased energy input lead to a

higher sublimation rate, associated with a local increase in $P_{w,i}$ and, naturally, T_i (Section 8.3.5). The emitted radiation energy reflected on the vial side facing the IR heater (red arrow in middle thermal image in figure 8.6), leading to unreliable $T_{v,o}$ data in that position. In combination with the previous findings, the region of interest for the correct and reliable measurement of $T_{v,o}$ was situated on the vial side facing away from the IR heater, as indicated by the black rectangle.

The third thermal image (Figure 8.6) was obtained after 100 min of primary drying. A steep increase in $T_{v,o}$ towards approximately -20°C at the top part of the vial indicated ice removal was complete as the provided radiation energy is no longer consumed for ice sublimation. Instead, the energy is used to heat up the glass vial and its content, associated with higher values for $T_{v,o}$. As $T_{v,o}$ at the middle and bottom of the vial remained approximately -32.5°C , the thermal image indicates that primary drying was finished earlier in the top part of the spin frozen layer compared to the bottom part. This observation can be explained by the difference in product layer thickness between top and bottom of the cake, originating from the spin freezing step. Fast rotation of the vial results in a thin layer with a parabolic shape of the liquid surface. The inherent deviation in layer thickness between the top and the bottom of the vial is calculated by:

$$\Delta L_{tot} = \frac{kg}{\omega^2 r_{p,i}} \quad (8.13)$$

with ΔL_{tot} the deviation to the average thickness of the spin frozen layer (m), g the gravitational acceleration (9.81 m/s^2) and ω the angular velocity (rad/s). For the maximum rotation speed of the current experimental set-up (2900 rpm), the relative deviation in layer thickness between the cake at the top and the bottom of the vial is 29.68%. By increasing the rotation speed to 7000 rpm, which will be possible in the future continuous freeze-drying manufacturing equipment, this relative deviation can be minimized until 5.00%, intended as maximum allowable deviation in layer thickness between top and bottom. The rotation speed can be adapted in the continuous freeze-drying prototype to assure this condition is met, without being harmful for biopharmaceuticals.

8.4.3 Temperature monitoring

The temperature of the glass vial $T_{v,o}$ is plotted in function of (primary) drying time t in figure 8.7. In the top part of figure 8.7, the temperature trajectory is plotted for each individual pixel from the rectangle indicated in black in the bottom thermal image from

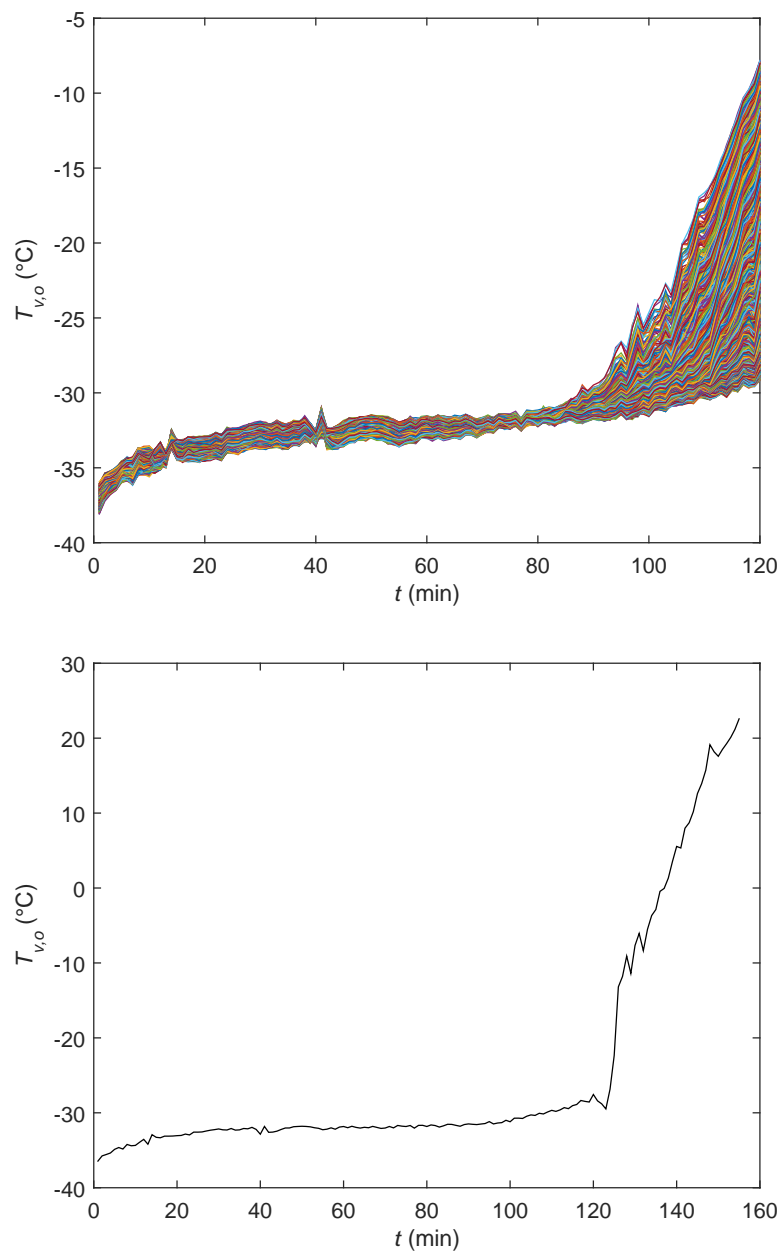


Figure 8.7: The temperature at the outer vial wall $T_{v,o}$ in function of drying time t : at the top, the temperature profiles for each individual pixel within the black rectangle drawn on the vial shown in the bottom image of figure 8.6; at the bottom, the mean value for $T_{v,o}$ calculated from the red rectangle drawn on the vial shown in the bottom image of figure 8.6

figure 8.6. $T_{v,o}$ is equal for the complete vial during most of the primary drying step, while towards the end, $T_{v,o}$ starts to increase at different timings depending on the location on the vial. The analysis of the thermal images indicated primary drying was finished earlier at the top of the cake compared to the bottom, which was attributed to the deviation in layer thickness between top and bottom (Section 8.4.2). For further calculations, the mean value of $T_{v,o}$ was calculated for the square region indicated in red in the bottom thermal image from figure 8.6. This region was located in the middle of the vial, where the layer thickness approaches the average theoretical value of the spin frozen product layer.

Initially, $T_{v,o}$ increases a few degrees until a plateau value is reached after approximately 25 min. This gradual temperature rise is caused by the increase in R_p , as will be discussed in section 8.4.5. Only after approximately 100 min, $T_{v,o}$ again starts to rise, followed by a steep increase after 124 min. As observed in the right thermal image in figure 8.6, a steep increase in $T_{v,o}$ indicates that the amount of ice is diminishing as the provided energy is no longer consumed for sublimation but to heat up the glass vial. As confirmation, the primary drying endpoint was determined via the NIR spectroscopy method as described in chapter 6 and 7. This method is based on PCA to analyse the NIR spectra which were collected in-line during the drying stage. This way, the primary drying endpoint was estimated to be reached after 128 min (data not shown). This value is in accordance with the data obtained by the IR camera and confirms the applicability of thermal imaging to determine the primary drying endpoint.

Via NIR spectroscopy, the primary drying progress is monitored at one specific height of the rotating vial while thermal imaging provides a two-dimensional image with additional spatial information. Hence, thermal imaging allows the monitoring of the drying behaviour for the complete spin frozen layer. Even multiple vials of the continuous belt could be monitored at once, offering a huge advantage to NIR spectroscopy, making use of a single probe at a fixed position in the drying chamber. Multipoint NIR spectroscopy could offer an alternative for the monitoring of multiple vials, while NIR chemical imaging could be applied to image the complete vial [27]. However, it is practically not possible to implement NIR chemical for in-line measurements. NIR spectroscopy and thermal imaging are highly complementary as the first can provide detailed in-line information about several CQAs as residual moisture content, protein conformation or the solid state of different components (e.g., mannitol) while the latter is an essential tool regarding product appearance by monitoring T_i (Section 8.4.4) [27–30]. Eventually, the combination of both

thermal imaging and NIR spectroscopy will be implemented in the continuous freeze-drying equipment for optimal real-time process monitoring and control.

8.4.4 Temperature gradient over glass wall and ice layer

The temperature at the sublimation front T_i is calculated based on the measured temperature at the outer vial wall $T_{v,o}$ via Fourier's law of thermal conduction (Section 8.3.4). $T_{v,o}$ and T_i are plotted in function of t in figure 8.8. During primary drying, the lowest temperature is situated at the sublimation interface. Hence, T_i is constantly lower than $T_{v,o}$ and energy is transferred from the outer glass wall towards the sublimation front. With the progress of primary drying, the ice layer thickness gradually decreases. Provided that the energy flux remains constant, the absolute temperature difference between $T_{v,o}$ and T_i also decreases (Figure 8.8). At the start of the primary drying step, the temperature gradient over the glass wall and ice layer was 0.88°C . With the gradual decrease in ice layer thickness, the temperature gradient over the glass wall at the end of primary drying was 0.47°C .

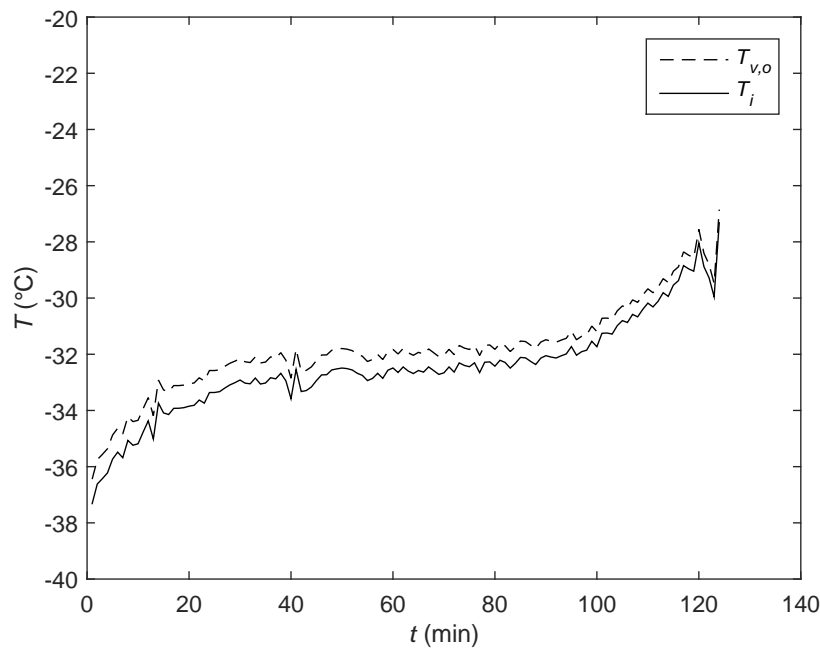


Figure 8.8: The temperature at the outer vial wall $T_{v,o}$ (dashed line) and the temperature at the sublimation front T_i (solid line) in function of primary drying time t

After approximately 100 min of primary drying, $T_{v,o}$ increases with a few degrees (Figure 8.8), despite primary drying is only finished after 124 min (Figure 8.7). The NIR data indicate that traces of ice are still present at the time this small increase in temperature occurs (NIR data not shown). Possibly, the remaining low amount of ice might not sufficiently cool the glass vial which might cause the gradual increase in $T_{v,o}$. Hence, from this moment on, the assumption of a system under steady-state in calculating the temperature gradient over the glass wall (and remaining ice layer) via Fourier's law of thermal conduction, might not be longer valid. Therefore, T_i might be overestimated for the few last minutes of the primary drying stage. Towards the end, the obtained T_i exceeds T'_g of the formulation, i.e., -32.5°C , while no macroscopic collapse was observed, which might confirm this hypothesis.

8.4.5 Dried product mass transfer resistance

Based on the measurement of T_i , the dried product mass transfer resistance R_p is calculated using equation 8.5 and plotted in function of the dried layer thickness l in figure 8.9. The R_p profile has a similar shape as the T_i curve. R_p is plotted starting at a dried layer thickness of 0.0001 m because of ice sublimation during the initial pressure decrease in the drying chamber (Chapter 6). The steep increase in R_p at a dried layer thickness of approximately 0.0014 m is caused by the small increase in temperature after approximately 100 min of primary drying, as extensively described in the previous section. At this very end of primary drying, it was hypothesized that T_i was overestimated, in turn leading to an overestimation of R_p . Therefore, this last part of the R_p profile, indicated by the vertical line in figure 8.9), was not included for the fitting of equation 7.3 to the R_p data.

Via non-linear regression, $R_{p,0} = -9.22 \cdot 10^3 \text{ m/s}$ (95% confidence interval $[-2.10 \cdot 10^4 \text{ m/s } 2.60 \cdot 10^3 \text{ m/s}]$), $A_{R_p} = 4.22 \cdot 10^8 \text{ 1/s}$ ($[2.79 \cdot 10^8 \text{ 1/s } 5.65 \cdot 10^8 \text{ 1/s}]$) and $B_{R_p} = 3.48 \cdot 10^3 \text{ 1/m}$ ($[2.50 \cdot 10^3 \text{ 1/m } 4.46 \cdot 10^3 \text{ 1/m}]$) were calculated. The 95% confidence interval for $R_{p,0}$ included zero, indicating that at the start of primary drying ($l = 0$), R_p was minimal as no pores were present to limit the mass flow. Often, $R_{p,0}$ is assumed to be zero because of the theoretical absence of any product resistance when sublimation is initiated [31]. This condition was not imposed for the regression analysis, as this point was situated outside the experimental region, but the $R_{p,0}$ coefficient seems to confirm this theory.

With the increase in l , R_p increased towards a plateau value as B_{R_p} is significantly different from zero. This behaviour has been observed before for pure sucrose formulations and

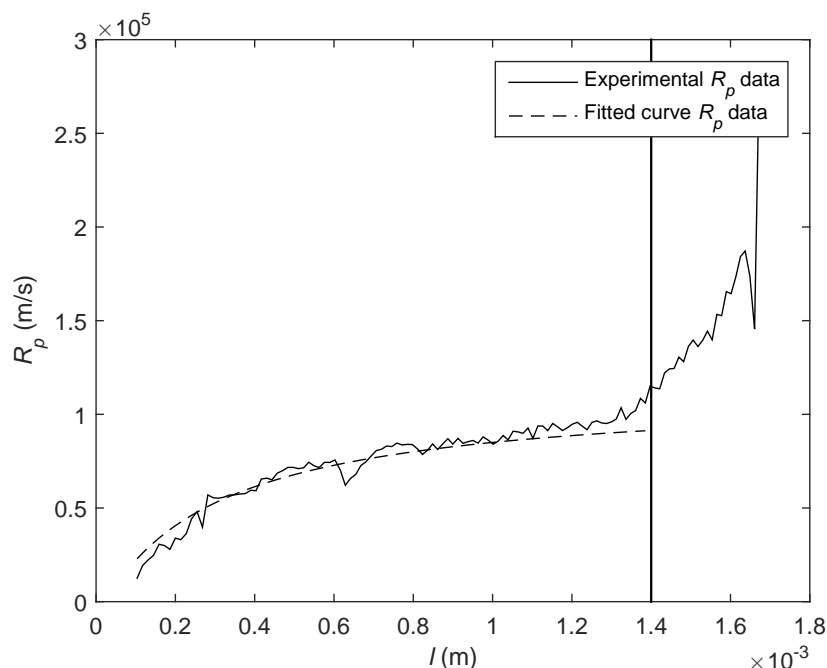


Figure 8.9: The dried product mass transfer resistance R_p (m/s) in function of the dried layer thickness l (m); the R_p data on the right side of the vertical line were not included to the fitting of the curve

is attributed to the onset of microcollapse because of the very low T'_g of the formulation (-32.5°C) [6, 21, 31–33]. The R_p profile starts to level when T_i approaches T'_g of the formulation, which might confirm the occurrence of microcollapse.

The results indicate that thermal imaging is a suitable technique to determine R_p in function of l for spin frozen vials. This is an important step regarding the development and optimization of the primary drying process conditions (i.e., the dynamic IR heater profile) for the continuous freeze-drying of a wide range of products (Chapter 7). In addition, the proposed procedure allows the development of a standardized method to evaluate the influence of different process and formulation parameters on R_p , which will lead to new insights in the development of the continuous freeze-drying technology.

8.5 General conclusion

Non-invasive thermal imaging was shown to be particularly suitable for in-line measurement of T_i during the primary drying step of the continuous freeze-drying concept, as opposed to the invasive temperature sensors applied during batch freeze-drying. As the sublimation

front in spin frozen vials moves in the direction of the glass wall towards the thermal IR camera, T_i could be monitored during the entire primary drying step, after compensating for the temperature gradient over the glass wall and ice layer via Fourier's law of thermal conduction. Based on the monitoring of T_i , thermal imaging allowed the detection of the primary drying endpoint in spin frozen vials, confirmed by NIR spectroscopy. In addition, this technique allowed the measurement of the dried product mass transfer resistance R_p in function of the dried layer thickness l , essential for the optimization of the dynamic IR heater profile during the continuous freeze-drying of a specific product. The developed procedure can be applied as a standardized method to evaluate the impact of several process parameters on R_p , offering essential information for the further development of the continuous freeze-drying technology.

Bibliography

- [1] V. R. Koganti, E. Y. Shalaev, M. R. Berry, T. Osterberg, M. Youssef, D. N. Hiebert, F. A. Kanka, M. Nolan, R. Barrett, G. Scalzo, G. Fitzpatrick, N. Fitzgibbon, S. Luthra, and L. Zhang. Investigation of design space for freeze-drying: use of modeling for primary drying segment of a freeze-drying cycle. *AAPS PharmSciTech*, 12:854–861, 2011.
- [2] J. C. Kasper and W. Friess. The freezing step in lyophilization: Physico-chemical fundamentals, freezing methods and consequences on process performance and quality attributes of biopharmaceuticals. *Eur. J. Pharm. Biopharm.*, 78:248–263, 2011.
- [3] R. Bogner and M. J. Pikal. The Incredible Shrinking Design Space: Using Risk Tolerance to Define Design Space for Primary Drying. *Notes of Freeze Drying of Pharmaceuticals and Biologicals Conference, Garmisch-Partenkirchen*, pages 184–198, 2010.
- [4] L. N. Mockus, T. W. Paul, N. A. Pease, N. J. Harper, P. K. Basu, E. A. Oslos, G. A. Sacha, W. Y. Kuu, L. M. Hardwick, J. J. Karty, M. J. Pikal, E. Hee, M. A. Khan, and S. L. Nail. Quality by design in formulation and process development for a freeze-dried, small molecule parenteral product: a case study. *Pharm. Dev. Technol.*, 16:549–576, 2011.
- [5] D. Fissore, R. Pisano, and A. A. Barresi. Advanced approach to build the design space for the primary drying of a pharmaceutical freeze-drying process. *J. Pharm. Sci.*, 100:4922–4933, 2011.
- [6] A. Giordano, A. A. Barresi, and D. Fissore. On the use of mathematical models to build the design space for the primary drying phase of a pharmaceutical lyophilization process. *J. Pharm. Sci.*, 100:311–324, 2011.
- [7] S. Bosca, D. Fissore, and M. Demichela. Risk-Based Design of a Freeze-Drying Cycle for Pharmaceuticals. *Ind. Eng. Chem. Res.*, 54:12928–12936, 2015.
- [8] S. Mortier, P. J. Van Bockstal, J. Corver, I. Nopens, K. Gernaey, and T. De Beer. Uncertainty analysis as essential step in the establishment of the dynamic Design Space of primary drying during freeze-drying. *Eur. J. Pharm. Biopharm.*, 103:71–83, 2016.

- [9] S. Nail, S. Tchessalov, E. Shalaev, A. Ganguly, E. Renzi, F. Dimarco, L. Wegiel, S. Ferris, W. Kessler, M. Pikal, G. Sacha, A. Alexeenko, T. N. Thompson, C. Reiter, J. Searles, and P. Coiteux. Recommended Best Practices for Process Monitoring Instrumentation in Pharmaceutical Freeze Drying 2017. *AAPS PharmSciTech*, 18:2379–2393, 2017.
- [10] S. M. Patel, T. Doen, and M. J. Pikal. Determination of end point of primary drying in freeze-drying process control. *AAPS PharmSciTech*, 11:73–84, 2010.
- [11] A. A. Barresi, R. Pisano, D. Fissore, V. Rasetto, S. A. Velardi, A. Vallan, M. Parvis, and M. Galan. Monitoring of the primary drying of a lyophilization process in vials. *Chem. Eng. Process.*, 48:408–423, 2009.
- [12] A. I. Liapis, M. J. Pikal, and R. Bruttini. Research and Development Needs and Opportunities in Freeze Drying. *Drying Technol.*, 14:1265–1300, 1996.
- [13] X. Tang and M. J. Pikal. Design of freeze-drying processes for pharmaceuticals: practical advice. *Pharm. Res.*, 21:191–200, 2004.
- [14] P. Chouvinc, S. Vessot, J. Andrieu, and P. Vacus. Optimization of the Freeze-Drying Cycle: A New Model for Pressure Rise Analysis. *Drying Technol.*, 22:1577–1601, 2004.
- [15] S. Schneid and H. Gieseler. Evaluation of a new wireless Temperature Remote Interrogation System (TEMPRIS) to measure product temperature during freeze drying. *AAPS PharmSciTech*, 9:729–739, 2008.
- [16] S. A. Velardi, V. Rasetto, and A. A. Barresi. Dynamic parameters estimation method: Advanced manometric temperature measurement approach for freeze-drying monitoring of pharmaceutical solutions. *Ind. Eng. Chem. Res.*, 47:8445–8457, 2008.
- [17] H. Emteborg, R. Zeleny, J. Charoud-Got, G. Martos, J. Lüddeke, H. Schellin, and K. Teipel. Infrared thermography for monitoring of freeze-drying processes: Instrumental developments and preliminary results. *Journal of Pharmaceutical Sciences*, 103:2088–2097, 2014.
- [18] R. Bird, W. Stewart, and E. Lightfoot. *Transport phenoma*. John Wiley & Sons, New York, 2006.
- [19] G. F. Nellis and S. A. Klein. Radiation. In *Heat Transfer*. Cambridge University Press, Cambridge, 2009.

- [20] D. E. Overcashier, T. W. Patapoff, and C. C. Hsu. Lyophilization of protein formulations in vials: Investigation of the relationship between resistance to vapor flow during primary drying and small-scale product collapse. *J. Pharm. Sci.*, 88:688–695, 1999.
- [21] S. Rambhatla, R. Ramot, C. Bhugra, and M. J. Pikal. Heat and mass transfer scale-up issues during freeze drying: II. Control and characterization of the degree of supercooling. *AAPS PharmSciTech*, 5:54–62, 2004.
- [22] W. Y. Kuu, L. M. Hardwick, and M. J. Akers. Rapid determination of dry layer mass transfer resistance for various pharmaceutical formulations during primary drying using product temperature profiles. *Int. J. Pharm.*, 313:99–113, 2006.
- [23] R. Pisano, D. Fissore, A. A. Barresi, P. Brayard, P. Chouvinc, and B. Woinet. Quality by design: optimization of a freeze-drying cycle via design space in case of heterogeneous drying behavior and influence of the freezing protocol. *Pharm. Dev. Technol.*, 18:280–295, 2013.
- [24] J. Vercruyssen, M. Toiviainen, M. Fonteyne, N. Helkimo, J. Ketolainen, M. Juuti, U. Delaet, I. Van Assche, J. P. Remon, C. Vervaet, and T. De Beer. Visualization and understanding of the granulation liquid mixing and distribution during continuous twin screw granulation using NIR chemical imaging. *Eur. J. Pharm. Biopharm.*, 2013.
- [25] L. Eriksson, E. Johansson, N. Kettaneh-Wold, J. Trygg, C. Wikström, and S. Wold. *Multi- and megavariable data analysis part 1: Basic principles and applications*. Umetrics, Umeå, 2006.
- [26] S. Pieters, Y. Vander Heyden, J. M. Roger, M. D’Hondt, L. Hansen, B. Palagos, B. De Spiegeleer, J. P. Remon, C. Vervaet, and T. De Beer. Raman spectroscopy and multivariate analysis for the rapid discrimination between native-like and non-native states in freeze-dried protein formulations. *Eur. J. Pharm. Biopharm.*, 85:263–271, 2013.
- [27] A. Kauppinen, M. Toiviainen, O. Korhonen, J. Aaltonen, J. Paaso, M. Juuti, and J. Ketolainen. In-Line Multipoint Near-Infrared Spectroscopy for Moisture Content Quantification during Freeze-Drying. *Anal. Chem.*, 85:2377–2384, 2013.
- [28] T. R. M. De Beer, M. Wiggenshorn, R. Veillon, C. Debaq, Y. Mayeresse, B. Moreau, A. Burggraev, T. Quinten, W. Friess, G. Winter, C. Vervaet, J. P. Remon, and W. R. G. Baeyens. Importance of Using Complementary Process Analyzers for the

- Process Monitoring, Analysis, and Understanding of Freeze Drying. *Anal. Chem.*, 81:7639–7649, 2009.
- [29] T. R. M. De Beer, P. Vercruyssen, A. Burggraef, T. Quinten, J. Ouyang, X. Zhang, C. Vervaet, J. P. Remon, and W. R. G. Baeyens. In-Line and Real-Time Process Monitoring of a Freeze Drying Process Using Raman and NIR Spectroscopy as Complementary Process Analytical Technology (PAT) Tools. *J. Pharm. Sci.*, 98:3430–3446, 2009.
- [30] S. Pieters, T. De Beer, J. C. Kasper, D. Boulpaep, O. Waszkiewicz, M. Goodarzi, C. Tistaert, W. Friess, J. P. Remon, C. Vervaet, and Y. Vander Heyden. Near-infrared spectroscopy for in-line monitoring of protein unfolding and its interactions with lyoprotectants during freeze-drying. *Anal. Chem.*, 84:947–955, 2012.
- [31] A. Konstantinidis, W. Kuu, L. Otten, S. Nail, and R. Sever. Controlled Nucleation in Freeze-drying: Effects on Pore Size in the Dried Product Layer, Mass Transfer Resistance, and Primary Drying Rate. *J. Pharm. Sci.*, 100:3453–3470, 2011.
- [32] W. Kuu, K. O’Brien, L. Hardwick, and T. Paul. Product mass transfer resistance directly determined during freeze-drying cycle runs using tunable diode laser absorption spectroscopy (TDLAS) and pore diffusion model. *Pharm. Dev. Technol.*, 16:343–357, 2011.
- [33] R. Chen, N. K. H. Slater, L. A. Gatlin, T. Kramer, and E. Y. Shalaev. Comparative rates of freeze-drying for lactose and sucrose solutions as measured by photographic recording, product temperature, and heat flux transducer. *Pharm. Dev. Technol.*, 13:367–374, 2008.

CHAPTER 9

Summary and general conclusion

Freeze-drying is a well-established formulation technique to improve the stability of biopharmaceuticals which are unstable in aqueous solution. Conventional pharmaceutical freeze-drying is a batch-wise process during which all vials are processed through a sequence of consecutive steps, i.e., freezing, primary drying and secondary drying, until the dried end product is obtained. However, this inefficient batch approach is inherently associated with several disadvantages, as discussed in **chapter 1**. The freezing step is uncontrolled due to the stochastic nature of ice nucleation resulting in different ice crystal sizes and corresponding pore sizes for each vial in the batch. During the primary drying step, vials placed at the edge of the shelves receive additional energy radiated from the warmer surroundings. Both this uncontrolled freezing and uneven heat transfer lead to different process conditions for each individual vial in the batch. Product quality is only tested on a limited fraction of vials, before releasing the complete batch. The uncontrolled vial-to-vial variation and quality approach do not meet the most recent guidelines issued by the regulatory authorities regarding Quality-by-Design (QbD) and Process Analytical Technology (PAT) which state that quality should be guaranteed by building it into the product instead of elaborate off-line testing.

The objectives of this thesis are outlined in **chapter 2**. The first objective was to optimize the primary drying step of a batch freeze-drying process, which is considered the most time-consuming, through mechanistic modelling. Due to the inherent disadvantages related to batch freeze-drying, as confirmed by the experiments regarding the first objective, the second (main) objective was to develop and evaluate a continuous freeze-drying concept for unit doses as alternative for the current state-of-the-art batch process.

In **chapter 3**, the determination of the dynamic Design Space of the primary drying step during batch freeze-drying is described. The batch freeze-drying process is regulated by the (dynamic) settings of the adaptable process parameters shelf temperature T_s and chamber pressure P_c . To obtain an elegant dried product appearance, the product temperature at the sublimation interface T_i should be kept below the critical temperature $T_{i,crit}$ during the entire primary drying step. Mechanistic modelling of the primary drying step allows the computation of the optimal combination of T_s and P_c in function of the primary drying time to maximise the sublimation efficiency while simultaneously minimising and controlling the risk of cake collapse. An uncertainty analysis (UA) was conducted on the mechanistic primary drying model to construct the dynamic Design Space for the primary drying step of a freeze-drying process, allowing to quantitatively estimate and control the risk of cake collapse, i.e., the Risk of Failure (RoF). The propagation of the error on the estimation of the thickness of the dried layer L_{dried} as function of primary drying time was included in the UA. The constructed dynamic Design Space and the predicted primary drying endpoint were experimentally verified for different RoF acceptance levels (1%, 25%, 50% and 99% RoF), defined as the chance of macroscopic cake collapse in one or more vials. An acceptable cake structure was only obtained for the verification runs with a preset RoF of 1% and 25%. The run with the nominal values for the input variables (RoF of 50%) led to collapse in a significant number of vials. For each RoF acceptance level, the experimentally determined primary drying endpoint was situated below the computed endpoint, with a certainty of 99%, ensuring sublimation was finished before secondary drying was started. The uncertainty on the model input parameters demonstrates the need of the UA for the determination of the dynamic Design Space to quantitatively estimate the risk of batch rejection due to cake collapse.

In **chapter 4**, a Global Sensitivity Analysis (GSA) was applied on the validated mechanistic primary drying model to evaluate how the uncertainty in the output of this model can be apportioned to different sources of uncertainty in the model input. Both a regression-based and variance-based GSA were conducted to estimate the impact of several model input parameters on two output variables, the product temperature at the sublimation front T_i and the sublimation rate \dot{m}_{sub} . T_s was identified as most influential parameter on both T_i and \dot{m}_{sub} , followed by P_c and the dried product mass transfer resistance α_{Rp} for T_i and \dot{m}_{sub} , respectively. The GSA findings were experimentally validated for \dot{m}_{sub} via a Design of Experiments (DoE) approach. The results indicated that GSA is a very useful tool to evaluate the impact of different process variables on the model outcome, leading to essential process knowledge, without the need for time-consuming experiments.

Chapter 5 focused on the current change in mindset in the pharmaceutical industry and the incentives to shift from batch manufacturing to continuous processing. The history of continuous freeze-drying is briefly summarized, with special attention for the lacking aspects which are indispensable for the continuous freeze-drying of (bio-)pharmaceutical unit doses. The proposed continuous freeze-drying concept for unit doses, resolving the disadvantages related to the batch process, is elaborately described. This continuous concept is initiated by rapidly spinning the vials along their longitudinal axis while the flow of a cold gas cools and freezes the solution. This spin freezing step allows flexible and standardized freezing of the sterile glass vials containing the aqueous drug formulation. Consequently, a thin product layer spread over the entire inner vial wall is formed, with an increased surface available for sublimation compared to conventional frozen vials. During primary drying of these spin frozen vials, the energy transfer is provided via non-contact infrared (IR) radiation. Each vial is slowly rotated along its longitudinal axis in front of an individual temperature-controlled IR heater, guaranteeing an efficient and homogeneous energy transfer. In addition, the drying trajectory can be individualized and optimized for each single spin frozen vial. The consecutive process steps in the continuous concept are separated by space, instead of the separation by time characteristic for batch processes. The modules for each specific process step are connected through load-lock systems which allow vial transfer without disturbing the specific conditions of pressure and temperature in each chamber.

In **chapter 6**, the applicability of non-contact IR radiation was examined as an efficient heat transfer during drying is essential for the continuous processing of spin frozen vials. The impact of several process and formulation variables upon the mass of sublimed ice after 15 minutes of primary drying (i.e., sublimation rate) and the total drying time was examined. Two experimental designs were conducted in which electrical power to the IR heaters, distance between the IR heaters and the spin frozen vial, chamber pressure, product layer thickness and five model formulations were included as factors. A near-infrared NIR spectroscopy method was developed to determine the endpoint of both primary and secondary drying. The sublimation rate was mainly influenced by the electrical power to the IR heaters and the distance between the IR heaters and the vial. The layer thickness had the largest effect on total drying time. The chamber pressure and the five model formulations had no significant impact on sublimation rate and total drying time, respectively. The results showed that IR radiation is suitable to provide the energy transfer during the continuous processing of spin frozen vials.

In **chapter 7**, a mechanistic model was developed which allows the computation of the optimal, dynamic IR heater temperature in function of the primary drying progress to maximise the drying efficiency while avoiding cake collapse. In addition, the primary drying endpoint could also be predicted based on the applied dynamic IR heater temperature. The model was validated by drying spin frozen vials containing the model formulation (3.9 mL in 10 mL vials) according to the computed IR heater temperature profile. In total, 6 validation experiments were conducted. The primary drying endpoint was experimentally determined via in-line NIR spectroscopy and compared with the endpoint predicted by the model (50 minutes). The mean ratio of the experimental drying time to the predicted value was 0.91, indicating a good agreement between the model predictions and the experimental data. The end product had an elegant product appearance (visual inspection) and an acceptable residual moisture content (Karl Fischer).

The standard temperature sensors applied in batch freeze-drying provide unreliable temperature data due to their invasive character. In addition, these sensors are incompatible with the continuous freeze-drying concept based on spinning the vials during freezing. Therefore, in **chapter 8**, the feasibility of in-line non-invasive IR thermography was evaluated to measure T_i during continuous freeze-drying of unit doses. The sublimation front moves from the inner side of the spin frozen cake towards the glass wall in the direction of the IR camera. Via Fourier's law of thermal conduction, the temperature gradient over the vial wall and ice layer was quantified, which allowed the constant monitoring of T_i . Based on these IR thermography measurements, the IR energy transfer was computed via the Stefan-Boltzmann law and the R_p profile was determined. This procedure allows the determination of the optimal dynamic IR heater temperature profile for the continuous freeze-drying of several products. In addition, the endpoint of primary drying was detected via IR thermography and confirmed by in-line NIR spectroscopy. Both applications show that IR thermography is a suitable and promising PAT tool for non-invasive in-line temperature measurements during continuous freeze-drying, with an enormous potential for process monitoring and control.

In the closing **chapter 10**, a detailed outline of the social and economic context is provided in which the research of this thesis fits. Here, the focus is on the future challenges of the pharmaceutical industry and the valorization potential of the proposed continuous freeze-drying technology. The next steps in the valorization trajectory are emphasized.

CHAPTER 10

Broader international context, relevance, and future perspectives

10.1 Broader international context and relevance

Biological drug products like therapeutic proteins and vaccines are considered the key driver of growth in the pharmaceutical industry. Influential biopharmaceutical companies predict a compound annual growth rate (CAGR) of 4.4% for biological therapeutics compared to small-molecules with a growth rate below 1% [1]. Coming from US\$ 33 billion sales in 2005, to US\$ 82 billion in 2010 and US\$ 109 billion in 2012, IMARC expects the global biopharmaceutical market to exceed sales worth US\$ 166 billion by 2017. The market is currently dominated by monoclonal antibodies (50%), followed by recombinant proteins and vaccines.

With the first patents on biologics (e.g., EPO) being expired, the market for biosimilars produced by generic companies is getting traction and is expected to become one of the fastest growing market segments in life sciences. The global biosimilar market, estimated at US\$ 2 billion in 2012 and expected to touch US\$ 2.7 billion in 2013, is further projected to reach US\$ 19.4 billion by 2018, exhibiting a CAGR of 36.6% over the period 2009 to 2018. This growth can be attributed to some of the top selling biologicals coming off-patent over the next years [2].

Biopharmaceuticals often provide a formulation challenge due to water-mediated degradation pathways [3]. Freeze-drying is commonly applied to improve the stability of these products during storage and distribution by removing the aqueous solvent. Approximately

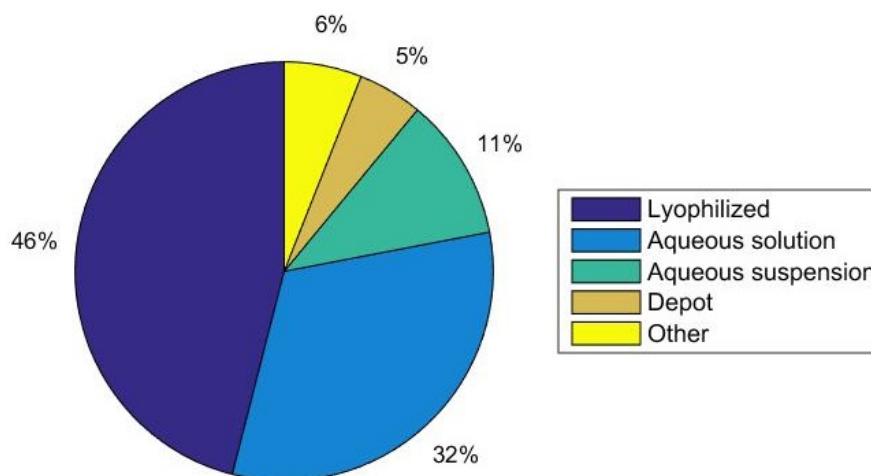


Figure 10.1: FDA-approved protein, peptide, vaccines (including viral and bacterial), oligonucleotide, and cell-based products grouped according to dosage form [3]

46% of the FDA approved biopharmaceuticals are freeze-dried, indicating it is the most common formulation strategy for the currently marketed products (Figure 10.1).

Conventional pharmaceutical freeze-drying of unit doses is a batch-wise process. However, as extensively discussed in the introductory chapter of this thesis, batch freeze-drying is associated with several disadvantages:

- **High production cost:** need for large equipment with high operational, maintenance, energy and infrastructure costs because of the high standards of cleanliness and sterility, which are mandatory in the production of biopharmaceuticals.
- **Time-consuming:** the whole freeze-drying cycle may last 1 to 7 days depending on the product properties. One important cause is the inefficient energy supply from shelves to vials during drying.
- **Issues during scale-up:** lab-scale → pilot-scale → production scale. Each step requires complete re-optimization and re-validation of the freeze-drying cycle to meet GMP standards due to differences in energy transfer between different equipment scales.
- **Impaired quality:** Uncontrolled freezing and uneven heat transfer during drying results in uncontrolled vial-to-vial variability of end product quality within a batch

and between batches (up to 40 000 vials/batch). Poor quality control as only a small fraction of the processed vials is assessed prior to batch release; no in-line process monitoring and control at the scale of the individual vial. Furthermore, since the handling equipment before (filling) and after (capping, packaging) freeze-drying is continuously operated by nature, buffer systems are necessary, increasing the risk of product contamination.

- **No flexibility:** only large batches can be produced. A batch freeze-dryer is commonly designed, optimized and validated to process only the largest applicable amount of vials of one specific product.

Investment in innovative freeze-drying technologies would be desired, however, there are a few industrial bottlenecks. First, the pharmaceutical industry is very conservative. Therefore, they look at innovative manufacturing equipment as a potential regulatory hazard, not as a business opportunity. Second, the market of pharmaceutical freeze-drying equipment is a niche market. As such, innovation is less considered as a strategy to gain market share. Lastly, the pharmaceutical equipment manufacturers have a strong engineering tradition, but lack hands-on experience with drug formulations, which hampers innovation capabilities. The link between equipment design and drug formulation (development) is often missing in order to improve the processing efficiency. The scientific multidisciplinary nature related to the freeze-drying process is one of the biggest hurdles for gaining knowledge in the area of the physical and chemical phenomena occurring during freeze-drying.

In the near future, the pharmaceutical industry has to face multiple challenges. Despite the industrial bottlenecks, five major drivers are demanding a more efficient and better controllable pharmaceutical freeze-drying technology for unit doses:

- **Cost-cutting:** Big pharma is forced to implement dramatic cost-cutting strategies to compete with the generics industry. In addition, local governments are increasingly demanding low-cost drugs from a health economics perspective (e.g., Kiwi model, Model of pay-for-cure). As such, reducing manufacturing costs has become a priority.
- **Regulatory pressure:** In 2004, the FDA published its PAT guideline as a signal to the pharmaceutical industry to tackle the control problem in their manufacturing processes. The document states that the desired goal of the PAT framework is to design and develop fundamentally understood processes that can consistently ensure a predefined quality at the end of the manufacturing process. To meet this requirement, a guaranteed quality at the scale of the individual freeze-dried vial is needed.

The uncontrolled vial-to-vial variability observed in traditional batch freeze-drying is thus in conflict with this guideline.

- **Ageing population:** Need for new types of drugs and more medication per capita, but also a need for more personalized, targeted and tailor-made drug products. This requires manufacturing technologies that allow to produce in a flexible, cost-efficient and high-quality manner.
- **Growth of biopharmaceuticals:** In contrast to traditional small molecules, therapeutic proteins/peptides represent a significant and increasing portion. It is expected that the share of biopharmaceuticals in future new drug products will continue to increase.
- **High value, low volume products:** Personalized medicine selects the appropriate and optimal therapy depending on the patient's genome. This new trend mainly emerges within the field of oncology, but also for autoimmune diseases. More general, there is an emerging trend towards tailored therapies depending on gender or race. In addition, there is the growing need for medicines for rare diseases, known as orphan drugs. Except for the high value they represent due to the technological challenges during development, the batch-size is generally rather limited. The current batch freeze-driers have no flexibility to vary the size of batches, nor the ability for automated process control, leading to strong delays in the development of these orphan drug products.

The proposed continuous freeze-drying technology offers advantages in terms of cost-cutting, quality control, capacity/flexibility and regulatory compliance. This way, the technology directly addresses the main needs created by the current trends in the biopharmaceutical market and the subsector of pharmaceutical manufacturing:

- **Lower production cost:** A cost reduction of up to 50% can be realized by implementing continuous pharmaceutical freeze-drying due to the need of less equipment, lower space requirements, lower energy needs, faster GMP upscaling and a more efficient production process (faster production, no batch losses).
- **Superior quality:** The control of process conditions at a single vial level is a unique feature of our technology. This allows us to better control the critical process and product parameters, resulting in a better quality of the biopharmaceutical end-product and much less inter-vial variability. This achieved by in-line process monitoring and control.

- **Higher capacity and flexibility:** As illustrated by the above described by the market projection figures for biopharmaceuticals and biosimilars for the coming years, the biopharmaceutical manufacturing sector is facing capacity problems. Shifting to a continuous processing could offer a solution as it offers i) a more easy and faster scale-up; ii) higher throughput (continuous production strategies); and iii) a more flexible use of equipment (use of same machine for multiple products).
- **Regulatory compliance:** The continuous technology allows to monitor and control the freeze-drying process at the scale of the individual vial and, hence, consistently guarantee the predefined quality of the end product. In addition, the work in this thesis is a first significant step towards the complete fundamental understanding of the continuous freeze-drying process. This approach is in line with the PAT guideline issued by FDA in 2004, in contrast to traditional batch freeze-drying associated with the uncontrolled vial-to-vial variability.

10.2 Future perspectives

10.2.1 Research initiatives

The research in this thesis was the first step in assessing all the aspects concerning the continuous freeze-drying technology. The reported results pave the path for further investigation regarding each individual process step and how they interact, for instance, the evaluation of the influence of cooling rate during spin freezing on ice crystal size and its impact on the consecutive drying steps. Other studies will focus on the continuous freeze-drying of several therapeutic proteins or viral and bacterial vaccine formulations to evaluate the remaining activity and viability upon reconstitution.

During the development of the mechanistic primary drying model describing the IR energy transfer during continuous freeze-drying (Chapter 7), inherently, a few assumptions and simplifications were included. Additionally, some input variables and process parameters are an estimation of the actual value, associated with a certain measurement error. These uncertainties propagate to the model output, which might explain the small deviation between the experimental primary drying time and the model predictions. Similar to the primary drying model developed for batch freeze-drying (Chapter 3), an uncertainty analysis will be conducted on the model describing the IR energy transfer during continuous freeze-drying. The uncertainty analysis will estimate and quantify the uncertainty for each

input variable and process parameter in the model, leading to the quantification and control of the risk of cake collapse for the resulting dynamic IR heater profile.

Continuous manufacturing requires real-time monitoring and control of Critical Process Parameters (CPPs) and CQAs. For this reason, in-line NIR spectroscopy and IR thermography were evaluated and considered very promising. Both techniques prove to be highly complementary. NIR spectroscopy can provide detailed in-line information about several CQAs as residual moisture content, protein conformation or the solid state of different components (e.g., mannitol). In turn, IR thermography allows real-time monitoring of the product temperature at the sublimation interface T_i . Moreover, the IR thermography application offers the opportunity to control T_i during the continuous primary drying step, hence, guaranteeing a good cake aspect. Based on this measuring principle, a method will be developed to control T_i by adapting the IR energy transfer, i.e., the temperature of the IR heater, making use of a feedback control system. More specifically, when it is detected that T_i threatens to exceed the critical product temperature $T_{i,crit}$, the temperature of the IR heater will be lowered to avoid the risk of cake collapse. This approach will allow to standardize the drying behaviour for each spin frozen vial and will offer a significant added value during the valorization of the continuous freeze-drying technology (see further).

Further research will also focus on the implementation of additional PAT tools to monitor the continuous freeze-drying process. As the presence of ice overwhelms the spectra, NIR spectroscopy is suitable to detect the endpoint of primary drying. However, no information regarding the solutes, e.g., protein structure or polymorphic state of the solutes like mannitol, is provided. For this reason, the implementation of Raman spectroscopy should be considered as the Raman spectra are not affected by the presence of ice. Hence, this technique could provide information regarding protein structure or solid state during freezing, annealing and primary drying.

10.2.2 Valorization

The first part of this closing chapter focused on the future challenges for the pharmaceutical industry and the drivers for a more efficient and better controllable freeze-drying technology. This thesis describes how the proposed continuous concept addresses these needs. Lab-scale research modules were developed to conduct the many tests as a proof-of-feasibility to support these claims.

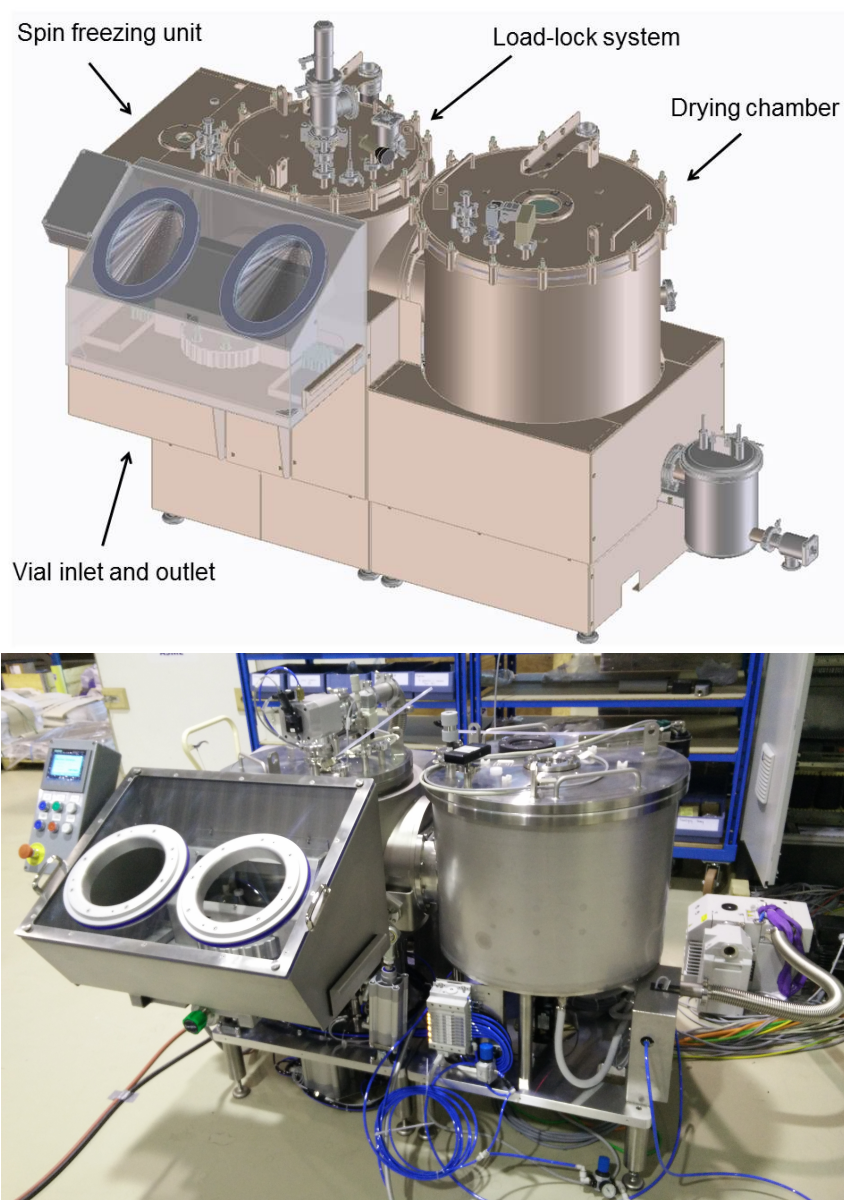


Figure 10.2: 'GMP-like' prototype of the continuous freeze-drying technology

In a next step, the individual steps of the continuous freeze-drying concept are integrated in one continuous line. Currently, a '**GMP-like**' prototype is being developed. The design of this prototype is given in figure 10.2, in which the different units are indicated. A central load-lock system will be used to transfer the vials between the vial inlet and outlet, the spin freezing unit and the drying module, all having different conditions of pressure and temperature. Required process monitoring and control systems will be implemented. The pilot continuous freeze-drying system will be part of a test facility which allows end-

users to test the capabilities of this new system with their own products. This approach will also allow us to gain in-depth insights into the needs and expectations of end-users, providing valuable information for further improvement of the system. In addition, the different research initiatives defined above will be elaborated using this prototype.

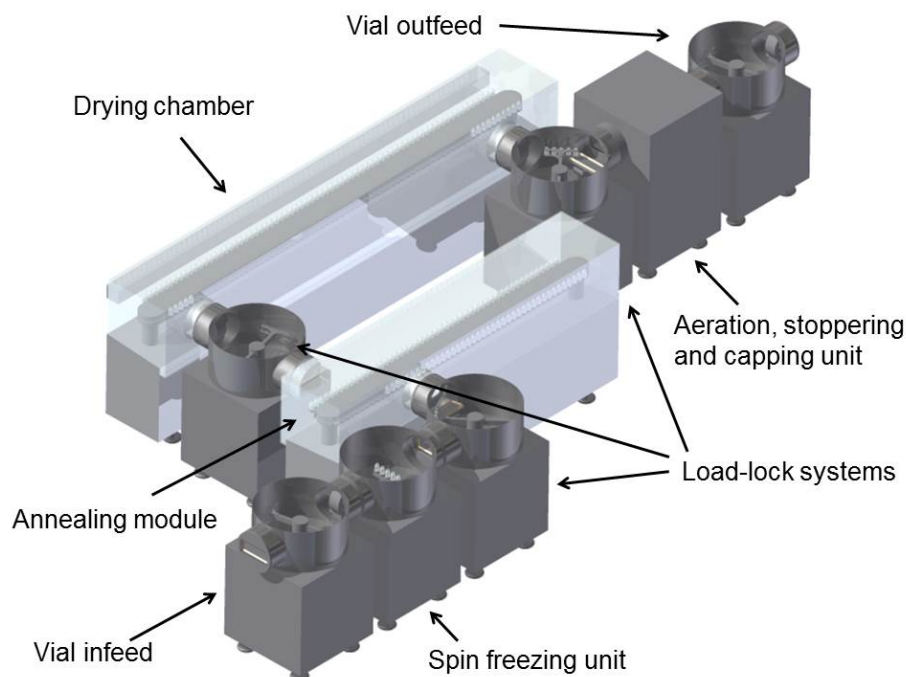


Figure 10.3: 'GMP' prototype of the continuous freeze-drying technology

By the end of 2019, it is aimed to develop a '**GMP**' **prototype** integrated in a production facility (Figure 10.3). To switch from the 'GMP-like' prototype to a GMP system, some adaptations have to be considered:

- **Integration in clean room:** The vial infeed to the continuous freeze-drying system has to be aligned with the automated filling line. Similarly, the vial outfeed should be integrated with the capping and packaging equipment.
- **CIP and SIP:** The (continuous) freeze-drying of parenteral drug products needs to meet the GMP standards for aseptic production. Appropriate facilities for conducting CIP and SIP need to be provided, including the adaptation of the design, e.g., a sloped bottom for drainage of the cleaning water.
- **Relocation of IR heaters:** In the 'GMP-like' prototype, the IR heaters are placed inside the drying chamber, directly heating the spin frozen vials. However, these

radiators are incompatible with the mandatory CIP and SIP procedures for aseptic pharmaceutical manufacturing. Therefore, the IR heaters have to be relocated to outside the drying chamber. There, they will be placed behind an appropriate IR transparent window to radiate the spin frozen vials inside the drying module.

Recent years, the mindset of the pharmaceutical industry has changed towards continuous manufacturing, highly encouraged by the regulatory authorities. This is illustrated by the recent introduction of two solid drug products on the market, i.e., Orkambi® (Vertex Pharmaceuticals) and Prezista® (Johnson & Johnson), which are produced by continuous manufacturing. Driven by the current mindset and the huge potential of the continuous freeze-drying technology, it is our ambition and ultimate goal to assist in the launch of a new commercial drug product produced using the continuous freeze-drying technology.

Bibliography

- [1] S. Shepherd. <http://www.gtai.de/GTAI/Content/EN/Meta/Events/Invest/2012/Reviews/Chemical-healthcare/Downloads/Breakfast-seminar-presentation-stephanie-shepard.pdf>, 2012.
- [2] <http://www.imarcresearch.com/>.
- [3] H. R. Constantino and M. J. Pikal. *Lyophilization of Biopharmaceuticals*. AAPS Press, Arlington (VA), 2004.

Nederlandse samenvatting

Biofarmaceutische geneesmiddelen zoals therapeutische proteïnen of vaccins van virale of bacteriële oorsprong hebben vaak een beperkte stabiliteit wanneer geformuleerd als een waterige oplossing. Vriesdrogen wordt vaak toegepast om de stabiliteit van deze producten te verzekeren tijdens distributie en bewaring. Het solvent waarin de biofarmaceutische formulatie is opgelost, meestal water, wordt verwijderd door initieel de waterige formulatie in te vriezen, vervolgens het gevormde ijs te laten sublimeren bij verlaagde druk tijdens de primaire droogstap en tot slot residueel (niet-ingevroren) vocht te verwijderen via desorptie en diffusie tijdens de secundaire droogstap, ook onder vacuüm. Uiteindelijk wordt een gedroogd product met een gegarandeerde stabiliteit verkregen.

Traditioneel farmaceutisch vriesdrogen is een inefficiënt batch proces dat inherent gepaard gaat met verschillende nadelen, zoals beschreven in **hoofdstuk 1**. Bepaalde nadelen zijn kenmerkend voor (farmaceutische) batch processen in het algemeen, zoals een lange procestijd (zeker bij batch vriesdrogen kan dit oplopen tot verschillende dagen), een lage flexibiliteit en de opschalingsproblematiek. Daarnaast zijn er ook nadelen specifiek aan batch vriesdrogen, met name het ongecontroleerde invriezen en de inhomogene energie transfer tijdens het drogen. Deze kunnen tot een ongecontroleerde variabiliteit van het eindproduct leiden, tussen de flesjes van eenzelfde batch en tussen verschillende batches. De kwaliteit wordt maar op een fractie van de flesjes van een gevriesdroogde batch bepaald alvorens deze vrij te geven. Deze ongecontroleerde productvariabiliteit en kwaliteitsbenadering strookt niet met de recente richtlijnen van de regelgevende instanties (EMA en FDA) inzake *Quality-by-Design* (QbD) en Proces Analytische Technologie (PAT), waarbij de kwaliteit van elk eindproduct gegarandeerd dient te worden door deze in te bouwen tijdens het proces.

De doelstellingen van deze thesis worden beschreven in **hoofdstuk 2**. Het eerste objectief

bestaat erin om de primaire droogstap van een batch vriesdroogproces te optimaliseren via mechanistische modellen. Omwille van de inherente nadelen gerelateerd aan batchvriesdrogen, is de tweede (voornaamste) doelstelling om een continu en gecontroleerd vriesdroog concept voor eenheidsdosissen te ontwikkelen en te evalueren als alternatief voor het huidige batch proces.

In **hoofdstuk 3** wordt de bepaling van de dynamische *Design Space* voor de primaire droogstap tijdens batch vriesdrogen beschreven. Het proces wordt gestuurd door het dynamisch instellen van de te regelen proces parameters, i.e., plaattemperatuur T_s en kamerdruk P_c . Om een gedroogd product met een goede structuur te verkrijgen, dient de producttemperatuur aan het sublimatiefront T_i tijdens de gehele primaire droogstap onder de kritische temperatuur $T_{i,crit}$ gehouden te worden. Het mechanistisch modelleren van de primaire droogstap laat toe om de optimale combinatie van T_s en P_c te bepalen in functie van de primaire droogtijd om zo de sublimatie efficiëntie te maximaliseren en tegelijkertijd het risico op verlies van productstructuur te minimaliseren en te controleren. Een onzekerheidsanalyse werd uitgevoerd op het mechanistische primair drogen model om de dynamische *Design Space* te bepalen voor de primaire droogstap van het batch vriesdroogproces, wat toelaat om het risico op verlies van productstructuur kwalitatief in te schatten en te controleren, i.e., het risico op falen (RoF). De accumulatie van de fout op de berekening van de dikte van de gedroogde laag L_{dried} in functie van de primaire droogtijd werd geïncorporeerd in deze onzekerheidsanalyse. De dynamische *Design Space* en het voorspelde eindpunt van primair drogen werden experimenteel geverifieerd voor verschillende RoF acceptatie niveaus (1%, 25%, 50% and 99% RoF), gedefinieerd als de kans op macroscopisch verlies van productstructuur in één of meerdere flesjes. Een aanvaardbare productstructuur werd enkel verkregen bij de verificatie experimenten met een RoF van 1% en 25%. De run met de nominale waarden voor de input variabelen, i.e., RoF van 50%, resulteerde in structuurverlies bij verschillende flesjes van de batch. Voor elk RoF acceptatieniveau bevond het experimenteel bepaalde eindpunt van de primaire droogstap zich voor het berekende eindpunt, met een zekerheid van 99%, waardoor primair drogen steeds klaar was alvorens over te gaan naar de secundaire droogstap. De onzekerheid op de model input parameters toont de nood aan een onzekerheidsanalyse voor de bepaling van de dynamische *Design Space* om het risico op afkeuring van de batch omwille van product collaps in te schatten.

Voortbouwend op het voorafgaande hoofdstuk, wordt in **hoofdstuk 4** de toepassing van een globale sensitiviteitsanalyse (GSA) op het gevalideerde mechanistische primair drogen

model beschreven om na te gaan hoe de onzekerheid op de output van het model kan toegeschreven worden aan de verschillende bronnen van onzekerheid bij de model input. Zowel een GSA gebaseerd op regressie als op variantie werden uitgevoerd om de impact van verschillende input parameters van het model na te gaan op twee output variabelen, i.e., de producttemperatuur aan het sublimatiefront T_i en de sublimatiesnelheid \dot{m}_{sub} . De plaattemperatuur T_s werd gidentificeerd als de meest invloedrijke parameter op zowel T_i als \dot{m}_{sub} , gevolgd door P_c en de weerstand van de droge productlaag α_{Rp} op respectievelijk T_i en \dot{m}_{sub} . De resultaten van de GSA werden experimenteel geverifieerd voor \dot{m}_{sub} via een experimenteel ontwerp (DoE). De resultaten duiden erop dat de GSA een nuttige tool is om de impact van verschillende proces variabelen op de model output te evalueren, wat leidt tot essentiële proceskennis, zonder het uitvoeren van tijdrovende experimenten.

Hoofdstuk 5 focust op de huidige verandering in manier van denken in de farmaceutische industrie en de drijfveren om van batch naar continue processen over te gaan. De geschiedenis van continu vriesdrogen wordt geschetst, met extra aandacht voor de ontbrekende aspecten bij eerder voorgestelde concepten die onontbeerlijk zijn voor het continu vriesdrogen van biofarmaceutische eenheidsdosissen. Het voorgestelde continue vriesdroog concept, dat een oplossing biedt voor de nadelen geassocieerd met batch vriesdrogen, wordt gedetailleerd beschreven. Bij dit concept wordt tijdens het invriezen het flesje met de geneesmiddel formulatie snel geroteerd om de verticale as zodanig dat het ingevroren product een dunne uniforme laag vormt die verspreid is over de volledige glaswand. Voor het afkoelen en invriezen wordt gebruik gemaakt van een steriel, inert en koud gas (bv. stikstofgas). Deze spin vriesstap laat toe om de met geneesmiddel formulatie gevulde flesjes op een flexibele en gestandaardiseerde manier in te vriezen. Tijdens het primair drogen van deze spin gevroren flesjes, wordt de energie transfer voorzien via contactloze infrarood (IR) straling. Elk flesje draait langzaam rond om zijn verticale as voor een individuele temperatuur gecontroleerde IR straler, waardoor een uniforme energie transfer naar de gehele glaswand van het flesje gegarandeerd wordt. Op deze manier kan het droogtraject voor elk spin gevroren flesje geïndividualiseerd en geoptimaliseerd worden. De modules voor elke specifieke processtap zijn verbonden via een load-lock systeem dat transfer van de flesjes toelaat zonder de specifieke druk en temperatuur condities in elke kamer te verstoren.

In **hoofdstuk 6** wordt de toepasbaarheid van contactloze IR straling geëvalueerd omdat een efficiënte energie transfer essentieel is voor het continue primair drogen van spin gevroren flesjes. De impact van verschillende proces en formulatie gerelateerde parameters op de hoeveelheid gesublimeerd ijs na 15 minuten primair drogen, i.e., de sublimatiesnel-

heid, en totale droogtijd werd onderzocht. Twee experimentele ontwerpen werden uitgevoerd waarbij het elektrisch vermogen naar de IR stralers, de afstand tussen de IR stralers en het spin gevoren flesje, de druk in de kamer, de dikte van de product laag en vijf verschillende model formulaties werden gencludeerd als factors. Een methode gebaseerd op NIR spectroscopie werd ontwikkeld om het eindpunt van zowel de primaire als de secundaire droogstap te bepalen. De sublimatiesnelheid werd voornamelijk beïnvloed door het elektrisch vermogen naar de IR stralers en de afstand tussen de IR stralers en het spin gevoren flesje. De dikte van de product laag had het grootste effect op de totale droogtijd. De kamerdruk en de vijf verschillende model formulaties hadden geen significante impact op respectievelijk de sublimatiesnelheid en de totale droogtijd. Deze resultaten tonen aan dat IR straling geschikt is om de energie transfer tijdens continu primair drogen van spin gevoren flesjes te verzorgen.

In **hoofdstuk 7** werd een mechanistisch model ontwikkeld dat toelaat om het optimale dynamische temperatuur traject van de IR straler in functie van de primaire droogtijd te bepalen om zo de droog efficiëntie te maximaliseren en tegelijkertijd het risico op product collaps te minimaliseren. Daarnaast laat het model toe om het eindpunt van primair drogen te bepalen op basis van dit temperatuur traject. Het model werd gevalideerd door spin gevoren flesjes met een bepaalde model formulatie te drogen op basis van het berekende temperatuur traject van de IR straler. In totaal werden zes validatie experimenten uitgevoerd. Het eindpunt van primair drogen werd experimenteel bepaald via de ontwikkelde NIR spectroscopie methode en vergeleken met het voorspelde eindpunt, dat op 50 minuten lag. De gemiddelde verhouding tussen de experimentele droogtijd en de voorspelde waarde was 0,91, wat op een goeie overeenkomst wijst tussen de voorspellingen van het model en de experimentele data. Het verkregen eindproduct had een goede productstructuur (visuele inspectie) en een aanvaardbaar residueel vochtgehalte (Karl Fischer).

De standaard temperatuur sensors die bij batch vriesdrogen gebruikt worden leiden tot onbetrouwbare temperatuur data omwille van hun invasieve karakter. Daarnaast zijn deze sensoren incompatibel met het continue vriesdroogconcept waarbij de flesjes roteren tijdens het drogen. In **hoofdstuk 8** werd de toepasbaarheid van *in-line* niet-invasieve thermische beeldvorming gevalueerd om T_i te meten tijdens continu vriesdrogen van eenheidsdosissen. Het sublimatiefront beweegt van de binnenkant van het flesje naar de glaswand, in de richting van de thermische IR camera. Via de wet van Fourier die de warmteoverdracht via geleiding beschrijft, kan de temperatuur gradiënt over de glaswand van het flesje en de ijslaag gekwantificeerd worden, wat toelaat om T_i continu te monitoren. Op basis van deze

thermische beeldvorming werd de IR energie transfer berekend op basis van de Stefan-Boltzmann vergelijking en kon het profiel van de weerstand van het gedroogde product R_p in functie van de dikte van de droge laag bepaald worden. Deze methode laat toe om het optimale dynamische temperatuur traject van de IR straler in functie van de primaire droogtijd te bepalen voor verschillende producten. Daarnaast werd het eindpunt van primair drogen bepaald via de IR thermografie methode en werd dit bevestigd door *in-line* NIR spectroscopie. Beide toepassingen tonen aan dat thermische beeldvorming een geschikte en veelbelovende PAT tool voor niet-invasieve *in-line* temperatuur metingen tijdens continu vriesdrogen, met een enorm potentieel voor proces monitoring en controle.

In het laatste **hoofdstuk 10** wordt een gedetailleerd overzicht geschetst van de sociale en economische impact van het onderzoek beschreven in deze thesis. De focus ligt op de toekomstige uitdagingen van de maatschappij en de farmaceutische industrie en het valorisatie potentieel van de voorgestelde continue vriesdroog technologie. De vervolgstappen van het valorisatie traject worden hierin toegelicht met het ontwikkelen van een prototype dat aan de GMP standaarden voldoet.

Curriculum vitae

Personal information

Surname: Van Bockstal
First names: Pieter-Jan Pierre
Address: Hazelaarlaan 15
8790 Waregem
GSM: +32-(0)495-13 09 82
Date of birth: July 30th, 1990
Place of birth: Lokeren
Nationality: Belgian
E-mail: PieterJan.VanBockstal@UGent.be
pieterjanvb101@hotmail.com

Education

2013 - Present: Doctor of Pharmaceutical Sciences (PhD)
Promoter: Prof. Thomas De Beer
Laboratory of Pharmaceutical Process Analytical Technology
Ghent University, Belgium

2011 - 2013: Master of Science in Drug Development
Ghent University, Belgium

2008 - 2011: Bachelor of Science in Pharmaceutical Sciences
Ghent University, Belgium

2002 - 2008: Degree Sciences - Mathematics
Sint-Teresiacollege, Eksaarde (Lokeren), Belgium (2002 - 2006);
Sint-Lodewijkscollege, Lokeren, Belgium (2006 - 2008)

Language skills

Native language: Dutch
Other languages: English (Fluently)
French (Basic)
German (Notions)

Publications in peer reviewed journals

Developing a framework to model the primary drying step of a continuous freeze-drying process based on infrared radiation.

Van Bockstal P.J., Corver J.*, Mortier S.T.F.C., De Meyer L., Nopens I., Gernaey K.V., De Beer T. (2018) *European Journal of Pharmaceutics & Biopharmaceutics*, doi: 10.1016/j.ejpb. 2018.02.025.

*Shared first authorship

The relevance of shear, sedimentation and diffusion during spin freezing, as potential first step of a continuous freeze-drying process for unit doses.

Lammens J., Mortier S.T.F.C., De Meyer L., Vanbillemont B., **Van Bockstal P.J.**, Van Herck S., Corver J., Nopens I., Vanhoorne V., De Geest B.G., De Beer T., Vervaet C. (2018) *International Journal of Pharmaceutics*, doi: 10.1016/j.ijpharm. 2018.01.009.

Polymorphism of indomethacin in semicrystalline dispersions: formation, transformation and segregation.

Van Duong T., Ludeker D., **Van Bockstal P.J.**, De Beer T., Van Humbeeck J., Van den Mooter G. (2018) *Molecular Pharmaceutics*, doi: 10.1021/acs.molpharmaceut. 7b00930.

Global Sensitivity Analysis as Good Modelling Practices tool for the identification of the most influential process parameters of the primary drying step during freeze-drying.

Van Bockstal P.J., Corver J., Mortier S.T.F.C., Nopens I., Gernaey K.V., De Beer T. (2018) *European Journal of Pharmaceutics & Biopharmaceutics*, 123, 108-116.

Quantitative risk assessment via uncertainty analysis in combination with error propagation for the determination of the dynamic Design Space of the primary drying step during freeze-drying.

Van Bockstal P.J., Mortier S.T.F.C., Corver J., Nopens I., Gernaey K.V., De Beer T. (2017) *European Journal of Pharmaceutics & Biopharmaceutics*, 121, 32-41.

Modelling the primary drying step for the determination of the optimal dynamic heating pad temperature in a continuous pharmaceutical freeze-drying process for unit doses.

De Meyer L., Lammens J., Mortier S.T.F.C., Vanbillemont B., **Van Bockstal P.J.**, Corver J., Nopens I., Vervaet C., De Beer T. (2017) *International Journal of Pharmaceutics*, 532, 158-193.

Formulation optimization of freeze-dried long-circulating liposomes and in-line monitoring of the freeze-drying process using an NIR spectroscopy tool.

Sylvester B., Porfire A., **Van Bockstal P.J.**, Porav S., Achim M., De Beer T., Tomută I. (2017) *Journal of Pharmaceutical Sciences*, 107, 139-148.

Mechanistic modelling of infrared mediated energy transfer during the primary drying step of a continuous freeze-drying process.

Van Bockstal P.J., Mortier S.T.F.C., De Meyer L., Corver J., Vervaet C., Nopens I., De Beer T. (2017) *European Journal of Pharmaceutics & Biopharmaceutics*, 114, 11-21.

In-line monitoring of compaction properties on a rotary tablet press during tablet manufacturing of hot-melt extruded amorphous solid dispersions.

Grymonpré W., Verstraete G., **Van Bockstal P.J.**, Van Renterghem J., Rombouts, P., De Beer T., Remon J.P., Vervaet, C. (2017) *International Journal of Pharmaceutics*, 517, 348-358.

Noncontact infrared-mediated heat transfer during continuous freeze-drying of unit doses.

Van Bockstal P.J., De Meyer L., Corver J., Vervaet C., De Beer T. (2017) *Journal of Pharmaceutical Sciences*, 106, 71-82.

A comparative study between melt granulation/compression and hot melt extrusion/injection molding for the manufacturing of oral sustained release thermoplastic polyurethane matrices.

Verstraete G., Mertens P., Grymonpré W., **Van Bockstal P.J.**, De Beer T., Boone M.N., Van Hoorebeke L., Remon J.P., Vervaet, C. (2016) *International Journal of Pharmaceutics*, 513, 602-611.

Hydrophilic thermoplastic polyurethanes for the manufacturing of highly dosed oral sustained release matrices via hot melt extrusion and injection molding.

Verstraete G., Van Renterghem J., **Van Bockstal P.J.**, Kasmi S., De Geest B.G., De Beer T., Remon J.P., Vervaet, C. (2016) *International Journal of Pharmaceutics*, 506, 214-221.

Impact of vacuum-induced surface freezing on inter- and intra-vial heterogeneity.

Oddone I., **Van Bockstal P.J.**, De Beer T., Pisano R. (2016). *European Journal of Pharmaceutics & Biopharmaceutics*, 103, 167-178.

Uncertainty analysis as essential step in the establishment of the dynamic Design Space of primary drying during freeze-drying.

Mortier S.T.F.C., **Van Bockstal P.J.**, Corver J., Nopens I., Gernaey K.V., De Beer T. (2016) *European Journal of Pharmaceutics & Biopharmaceutics*, 103, 73-83

Comparison of metoprolol tartrate multiple-unit lipid matrix systems produced by different technologies.

Aleksovski A., **Van Bockstal P.J.**, Roškar R., Sovány T., Regdon G. Jr, De Beer T., Vervaet C., Dreu R. (2016) *European Journal of Pharmaceutical Sciences*, 88, 233-245.

Continuous manufacturing of delta mannitol by cospray drying with PVP.

Vanhoorne V., **Van Bockstal P.J.**, Van Snick B., Peeters E., Monteyne T., Gomes P., De Beer T., Remon J.P., Vervaet, C. (2016) *International Journal of Pharmaceutics*, 501, 139-147.

In-line near infrared spectroscopy during freeze-drying as a tool to measure efficiency of hydrogen bond formation between protein and sugar, predictive of protein storage stability.

Mensink M.A., **Van Bockstal P.J.**, Pieters S., De Meyer L., Frijlink H.W., van der Voort Maarschalk K., Hinrichs W.L., De Beer T. (2015) *International Journal of Pharmaceutics*, 496, 792-800

Evaluation of spin freezing versus conventional freezing as part of a continuous pharmaceutical freeze-drying concept for unit doses.

*De Meyer L., **Van Bockstal P.J.**, Corver J., Vervaet C., Remon J.P., De Beer T. (2015) International Journal of Pharmaceutics, 496, 75-85.*

Publications in non peer reviewed journals

A continuous and controlled pharmaceutical freeze-drying technology for unit doses
Van Bockstal P.J., Corver J., De Beer T. (2017) *European Pharmaceutical Review, issue 6*

A dynamic Design Space for primary drying during batch freeze-drying
Mortier S.T.F.C., **Van Bockstal P.J.**, Nopens I., De Beer T., Gernaey K.V. (2016) *Chimica Oggi - Chemistry Today, 34, 59-61*

Presentations at conferences

Oral presentations

Mechanistic modelling of the infrared mediated heat transfer during the primary drying step of a continuous freeze-drying concept for unit-doses

Van Bockstal P.J., Mortier S.T.F.C., De Meyer L., Corver J., Nopens I., Gernaey K.V., De Beer T.

International Society of Lyophilization - Freeze-drying, Inc.; Havana (Cuba), 24-28 April 2017

Mechanistic modelling of the IR energy transfer during the continuous freeze-drying of unit-doses

Van Bockstal P.J., De Meyer L., Mortier S.T.F.C., Corver J., Vervaet C., De Beer T.

10th PSSRC annual symposium, Copenhagen (Denmark), 5-8 July 2016

Infrared mediated heat transfer during continuous freeze-drying of unit-doses

Van Bockstal P.J., De Meyer L., Corver J., Vervaet C., Remon J.P., De Beer T.
9th PSSRC annual symposium, Ghent (Belgium), 16-18 September 2015

Near-infrared spectroscopy for in-line lyoprotection evaluation of proteins during freeze-drying

Van Bockstal P.J., Vervaeet C., Remon J.P., De Beer T.

8th PSSRC annual symposium, Ljubljana (Slovenia), 16-17 September 2014

Near-infrared spectroscopy for in-line lyoprotection evaluation of proteins during freeze-drying

Van Bockstal P.J., Vervaeet C., Remon J.P., De Beer T.

Workshop on continuous pharmaceutical manufacturing, Kuopio (Finland), 20-22 August 2014

Poster presentations

Non-contact infrared mediated heat transfer during continuous freeze-drying of unit-doses

Van Bockstal P.J., De Meyer L., Corver J., Vervaeet C., Remon J.P., De Beer T.

Freeze-drying of Pharmaceuticals & Biologics, Breckenridge (USA), 12-15 July 2016

An innovative continuous freeze-drying concept for unit-doses

Van Bockstal P.J., De Meyer L., Corver J., Vervaeet C., Remon J.P., De Beer T.

Biopharmacy Day, Leuven (Belgium) 23 November 2015

Infrared mediated heat transfer during continuous freeze-drying of unit-doses

Van Bockstal P.J., De Meyer L., Corver J., Vervaeet C., Remon J.P., De Beer T.

International Society of Lyophilization - Freeze-drying, Inc., Barcelona (Spain), 6-10 July 2015

Dr. Thomas Jennings Award - Poster prize

Attended courses, conferences and workshops

Course: Technology Transfer Skills, November 2017, Ghent University, Ghent (Belgium)

Workshop: Application of Modelling to Lyophilization Process Design & Scale Up and Process validation approaches (International Society of Lyophilization - Freeze-drying, Inc.), 25 April 2017, Havana (Cuba)

Course: How to change/adapt our chemometrics to imaging, 913 May 2016, Ghent University, Ghent, Belgium

Workshop: Quality by Design and Infrastructure Design and Organization (International Society of Lyophilization - Freeze-drying, Inc.), 7 July 2015, Barcelona (Germany)

Course: Leadership foundation, 23-25 June 2015, Ghent University, Ghent (Belgium)

Conference: Freeze-drying of Pharmaceuticals & Biologics, 24-26 September 2014, Garmisch-Partenkirchen (Germany)

Course: Modulated Differential Scanning Calorimetry (MDSC) Training Course, 13 March 2014, TA Instruments, Zellik (Belgium)

Course: Differential Scanning Calorimetry (DSC) Training Course, 25-26 February 2014, TA Instruments, Zellik (Belgium)

Course: Multivariate Data Analysis, November 2013, Ghent University, Ghent (Belgium)

Course: Design of Experiments, October 2013, Ghent University, Ghent (Belgium)

